Universitat Autònoma de Barcelona

Doctoral Thesis

Measuring and Estimating Solar Direct Normal Irradiance using LIDAR, Solar Station and Satellite Data in Qatar

Author:
Dunia Antoine Bachour

Supervisor:
Prof. Mokhtar Chmeissani Raad

Tutor:
Prof. Enrique Fernández Sánchez

A thesis submitted in fulfilment of the requirements for the degree of Doctor of Philosophy

in the

Institut de Física d'Altes Energies,
Departament de Física

July 2015

Acknowledgements

Thank you to all who contributed to make my thesis work possible and continually encouraged me through this journey:

I would like to express my sincere gratitude to the Qatar Foundation and the Qatar Environment and Energy Research Institute, where I have conducted my research work during these 4 years. I would like to thank Dr. Rabi Mohtar and Dr. Mohammad Khaleel for giving me the opportunity to pursue my PhD studies.

I would like to express all my gratitude to my thesis advisor, Dr. Mokhtar Chmeissani. I am indebted and thankful for the opportunity and help he offered me to register for my doctoral studies in UAB. I was delighted, Mokhtar, to collaborate with you in QEERI and to work together on the installation of the lidar and the first high precision solar radiation monitoring station in Qatar. I am thankful for all the support, trust and motivation you gave me during these years.

It was a great pleasure to work side by side with my colleague Dr. Daniel Pérez Astudillo in QEERI, with whom I shared memorable moments and I enjoyed learning and discussing on a daily basis matters related to the solar radiation field and also to other fields in Physics. I really appreciate your readiness Daniel to always help and share your wide knowledge. I am very fortunate to have met such a bright person like you and deeply thank you for all your encouragement, inspiration and friendship. *Muchas gracias, Daniel*.

I would like to thank in QEERI: Dr. Ahmed Ennaoui and Dr. Nouar Tabet for their support, Dr. Luis Martin Pomares for sharing his knowledge in the solar resource assessment field, the Solar Atlas Team and all those who gave me helpful advice during my work. Also, I thank the Qatar Meteorological Department for providing their historical solar radiation data.

Thank you to all my friends and cousins in Qatar who were present by my side during good and bad moments. Special thanks to Fouad, Jihad, Ghada, Manale, Richard, Rouba and Chadi.

And words cannot express my appreciation and love for my family, who have been

always loving and supportive. Thank you for my sisters Maria and Randa, and their families Raymond, Gerard, Marwan, Ghiwa, Joe and Roy. Thank you to my uncle Maurice and all my family in Lebanon. For my lovely husband and kids, I am so blessed to have you in my life. Thank for your love, patience and understanding. Thank you Ayman for your care and for all the support you gave me to achieve my thesis and for patiently taking care of the kids during my absence. Thank you Joe for being so sweet, caring and for being the great big brother that you are. Thank you Jad for being so cute and making me laugh during stressful moments. Thank you Mateo for being a healthy, happy and sweet baby. Thank you for all the wonderful moments that we share and will always have together.

Finally I would like to deeply thank my parents, Antoine and Rose, who always supported me and encouraged me throughout my life. Thank you mom for all the love, help, and sacrifices, without you I would have never been able to achieve anything in my life. And for you my father, you sadly left us just before the completion of this work, I wish you were here with me, I love you and miss you desperately and heartily dedicate my thesis to you.

...In memory of my father.

Contents

List of Figures

Page

List of Tables

Page

Abbreviations

ABL	Atmospheric Boundary Layer
ACR	Active Cavity Radiometer
ACRIM	Active Cavity Radiometer Irradiance Monitor
AOD	Aerosol Optical Depth
ARF	Aerosol Radiative Forcing
AU	Astronomical Unit
AWS	Automatic Weather Stations
BHI	Beam Horizontal Irradiance
BL	Boundary Layer
BSRN	Baseline Surface Radiation Network
CERES	Clouds and the Earth's Radiant Energy System
CPV	Concentrated Photovoltaic
CSP	Concentrated Solar Power
DHI	Diffuse Horizontal Irradiance
DNI	Direct Normal Irradiance
ERBS	Earth Radiation Budget Satellite
FOV	Field Of View
GCC	Gulf Cooperation Council
GHI	Global Horizontal Irradiance
GMT	Greenwich Mean Time
HA	Hour Angle
IRENA	International Renewable Energy Agency
ISO	International Standards Organization
LIDAR	LIght Detection And Ranging
LST	Local Solar Time
LSTM	Local Standard Time Meridian
LT	Local Time
MBE	Mean Bias Error

MISR	Multi-angle Imaging SpectroRadiometer
MODIS	MODerate resolution Imaging Spectroradiometer
NASA	National Aeronautics and Space Administration
PBL	Planetary Boundary Layer
PMOD	Physikalisch-Meteorologisches Observatorium Davos
PV	Photovoltaic
QEERI	Qatar Environment and Energy Research Institute
QMD	Qatar Meteorological Department
QNFSP	Qatar National Food Security Programme
RMSE	Root Mean Square Error
SoHO	Solar and Heliospheric Observatory
SORCE	SOlar Radiation and Climate Experiment
TIM	Total Irradiance Monitor
TSI	Total Solar Irradiance
TCTE	TSI Calibration Transfer Experiment
TST	True Solar Time
UTC	Universal Time Coordinated
WCRP	World Climate Research Programme
WMO	World Meteorological Organisation
WRC	World Radiation Center
WRDC	World Radiation Data Center

Introduction

The electromagnetic radiation emitted by the sun is a crucial source of energy on the earth's surface, playing an important role in the weather, climate and different biological processes on earth. The earth's atmosphere affects the amount of solar radiation that reaches the surface of the planet, due to absorption and scattering. This results in changing the amount and characteristics of the solar radiation available at ground level: the solar radiation reaching a horizontal surface, called global horizontal irradiance (GHI), is composed of the radiation coming directly from the sun disk, known as direct or beam irradiance, and the scattered or diffuse irradiance, coming from the sky dome. These components can be harvested by different technologies, to produce heat or electricity. The direct component is the main gauge of projects based on concentrating technologies such as concentrated solar power (CSP) and concentrated photovoltaic (CPV), while GHI is the required parameter for photovoltaic (PV) projects. Being the fuel of such systems and an important parameter for climate and atmospheric studies, it is vital to conduct an accurate assessment of the solar resources available at ground level. This allows for reliable planning and implementation of solar energy-based projects, and also provides precious information for any other scientific or technical fields requiring the study and analysis of solar radiation.

Of particular interest to this work is the direct component of the solar radiation emanating directly from the sun disk and reaching the earth's surface on a plane normal to the sun rays, called DNI, the direct normal irradiance. The amount of DNI at ground level is affected by:

- the amount of incoming radiation at the top of the atmosphere, which depends on the sun-earth distance and varies around 6.7% between the closest and the farthest points;
- the distance traversed by the sun rays from the top of the atmosphere to the ground level, that is, the air mass or thickness of the atmosphere along the path of the sun rays to the ground;

- the atmospheric constituents that intercept the solar radiation along its path, scattering and absorbing part of it, thus reducing its magnitude on the ground level.

Due to these dependencies, the direct solar radiation is more abundant in regions with these characteristics: low latitudes, long sunshine durations, clear or cloudless skies most of the time, i.e., small cloud cover, and obviously, clean sky conditions, that is, low pollution and low levels of aerosols in the atmosphere.

The main objective of this research work is to accurately measure the solar radiation in Doha, Qatar, and to show how the atmospheric conditions, in a region located at low latitudes, can attenuate the direct solar radiation reaching the earth surface. Indeed, Qatar has, on daily basis, long hours of sunshine and usually the sky is cloudless most of the year. However, the high amounts of aerosols present in the atmosphere, whether of natural or anthropogenic nature, have a definite effect on the direct solar radiation, which shows values lower than what could be expected in such a region of the world. In this work, the effect of aerosols on the direct component of the solar radiation is quantified by the use of a lidar-ceilometer device which measures the backscatter profiles of the atmosphere. The comparison of backscatter and solar radiation measurements constitutes the essence of this work, and demonstrates that lidar-ceilometer devices, normally used for determining cloud heights or boundary layer heights in the atmosphere, can also be considered as prospective tools for aerosol estimation in the solar resource assessment field.

Research context

Given its geographic location, in the Sun Belt region of the world, Qatar has plenty of solar radiation resources: sunny conditions most of the time with an average sunshine duration of 9.2 hours per day and limited cloud cover during the year [1]. The country has already set several plans and targets for harvesting solar energy as an alternative to fossil fuels, a solution for diversifying its energy resources and reducing its carbon emissions [2].

To efficiently use the solar resource, it is essential to perform an estimation of the available solar radiation and evaluate its spatial and temporal variabilities. This can be done in terms of solar maps, which provide a clear representation on grid cells of the spatial variations of solar radiation in a country or a region. Such solar maps can assist and guide in the process of setting national solar energy targets, based on realistic figures of the resources. In addition, this will play a major role in selecting the most appropriate technology, qualifying a site, and optimising the design of solar power plants.

When it comes to the implementation and deployment of utility-scale solar energy-based projects, more in-depth assessment of solar resources and site-specific data are crucial. This assessment constitutes the primary step and includes the precise knowledge of the available solar energy at the site and over time. Apart from energy production, solar radiation data is needed in other fields such as atmospheric sciences, climate change studies, meteorology, etc.

An accurate method for characterising the solar radiation is through the use of high quality ground measurements of solar radiation. A sufficient number of ground stations measuring DNI, GHI and DHI (diffuse horizontal irradiance) over the whole area of interest and for at least one complete solar cycle of 11 years is ideally required for this purpose. In practice, however, this is usually not possible and is not the case in most areas of the world. The alternative solution is to use reliable long-term satellite-derived solar radiation data validated against ground measurements in the region, and combine it with short-term ground-measured solar radiation data, if available [3].

The existing satellite-based solar maps for Qatar, described in Section 3.3, are informative and give a first insight on the availability of solar radiation in the country. However, their reliabilities have not been assessed with ground-measured solar radiation data in Qatar. Global solar radiation has been measured in several locations in the country since 2007. These GHI data samples are of unknown quality, but if filtered with quality control checks, they can be considered of value to validate or calibrate the modelled global solar radiation. Yet, ground-measured DNI data are not available for Qatar and the only available DNI data are derived from satellite observations. A serious problem of the modelled DNI is the disagreement between the different available databases, leading to high uncertainties. In Europe, for instance, relative standard deviations of 17% have been found between different datasets of modelled DNI data [4]. The evaluated differences between modelled datasets can reach as much as approximately 30% in many regions, as stated in [5]. Indeed, by its nature, being the component of solar radiation that arrives to the earth's surface directly from the sun, DNI is highly influenced by the atmospheric contents along its path, i.e., small changes of the atmospheric conditions have a strong influence on its attenuation. This fact adds more challenges to achieving high accuracy and low uncertainty in DNI modelling, given the constantly changing atmospheric conditions.

In a clear sky, the more radiatively active atmospheric constituents are aerosols, water vapour and ozone. Aerosols are the main contributor to the extinction of the direct beam [6]. Their concentrations exhibit large variation in space and time. Errors in the determination of aerosol data give uncertainties in the order of 15 to 20% on a mean

annual basis in satellite-derived DNI [7]. Therefore, accurate aerosol determination is critical for modelling the direct component of solar radiation.

In general, the extinction factor due to aerosols is represented by the aerosol optical depth (AOD) parameter, which is a measure of the total extinction of sunlight over the vertical path, as it passes through the atmosphere. Commonly, AOD is either determined by spectral solar attenuation of sunphotometer measurements [8], or estimated using satellite sensors [9, 10], or modelled using chemical-transport models [11]. The ground-based data present the most accurate option for AOD determination. However, they are generally limited in spatial and temporal coverage. Satellite observations, in contrast, provide long-term and uninterrupted spatial coverage, but they provide data with lower spatial and temporal resolutions and show high uncertainties when compared to ground measurements [12], specially over regions with high dust and aerosol loads [13]. In addition, several studies show significant differences between the data sets produced by the different sources, a factor which presents a particular challenge in the estimation of the direct component of solar radiation [14].

In order to summarise the current situation and put things into perspective, the major points to retain are listed below. From this list it is easy to define and prioritise the research opportunities:

- Qatar is considered a potentially good location for solar energy-based projects in general, and CSP systems in particular, since it is located at low latitudes and has long hours of sunshine and low cloudiness most of the time.
- DNI being the fuel of CSP, there is a need to have accurate and reliable data of DNI for project planning, design and implementation.
- Ground-measured DNI data is so far not available, and the only option is to rely on modelled DNI data.
- Differences exist between modelled DNI datasets from different sources, see Section 1.5 for some available databases.
- The main input parameter affecting the modelled DNI in clear-sky conditions is aerosol data.
- AOD is normally used to describe the solar radiation extinction due to aerosols.
- Ground data of AOD are generally scarce, and unavailable for Qatar.
- AOD data derived from satellite observations or chemical transport models show discrepancies and high uncertainties.

- The uncertainties are even more accentuated in extreme atmospheric conditions, such as those in Qatar, characterised by high aerosols loads.

In view of the above-mentioned points, it was deemed necessary to address these challenges in a direct and concise manner, covering these gaps, which are particular to the region under study, while developing a research concept that can be applicable to other regions.

To that end, this thesis work presents an analysis of the characteristics of solar radiation and backscatter profiles of the atmosphere in Doha, Qatar. It introduces a new model to derive DNI in clear sky conditions from lidar-ceilometer measurements. It also tackles a new approach of evaluating local aerosol data from the backscatter profile measurements, which can be ultimately used in solar radiation modelling. This analysis was possible through: the study of one year of measurements with a high-quality solar radiation monitoring station collecting the three components of solar radiation (DNI, GHI and DHI) at 1-minute temporal resolution, and the measurements of a lidar-ceilometer pointing vertically upwards and profiling with high temporal resolution (36 s) the backscattering properties of the atmosphere. The model for DNI derivation was developed by combining DNI and backscatter measurements, where aerosol information was represented by the integration of the backscatter signal of the lidar-ceilometer over the vertical column. This new suggested model for DNI retrieval has been evaluated and the results have been compared with those of satellite models and shows good, and in some cases even better, results. An important application emerged from the suggested analysis, and consists of using the lidar signal to indirectly calibrate AOD retrieval methods. This is important to elucidate the limitation of DNI models in extreme conditions of high aerosol loads. The retrieval of aerosol data from backscatter measurements presents high temporal resolution (hourly, as opposed to daily or monthly-averaged AOD data) and high spatial resolution (local measurements, in contrast to a minimum of 100×100 km^2 grid cells generally used in solar radiation modelling). Local measurements allow to capture the high spatial and temporal variability of aerosols, a feature of high importance when modelling aerosols in a country like Qatar. Indeed, large amounts of aerosols are present in the atmosphere of Qatar and dust storms can strike suddenly, making significant changes in the local aerosol regime. Thus, the use of aerosol data as derived from the ceilometer could present an alternative for solar radiation modelling or satellite data calibration, in regions prone to dust and aerosols.

Through the correlation study of the direct normal irradiance with the backscatter profiles of the atmosphere over Doha, Qatar, it is demonstrated here that apart from its normal use for cloud and boundary layer monitoring, lidar-ceilometer devices can also be

ultimately used for deriving DNI and for calibrating satellite- and model-derived DNI. The radiative effect of aerosols, instead of being presented by the usual AOD parameter, is evaluated by the integration of the backscatter signal of the lidar-ceilometer over the vertical column. This method, although promising, is still yet to be validated and consolidated with more data and, most importantly, should be derived with a more physically sound approach, a concept guiding the future perspectives of this thesis work.

Thesis outline

The thesis work, as highlighted and presented in this introduction, is divided as per the following structure:

- Chapter 1 - Overview on Solar Radiation.
  Within this chapter, solar radiation at the top of the atmosphere, the effects of the earth's atmosphere on the attenuation of solar radiation, and solar radiation components at the ground level are discussed. Methods of measuring and modelling solar radiation are also described with examples of use of solar radiation as a renewable source of energy.

- Chapter 2 - Atmospheric Properties and Lidar Techniques.
  This chapter briefly introduces the atmospheric structure and properties with further description of the troposphere, its Atmospheric Boundary Layer (ABL) and the influence of aerosols on the earth's radiation budget. Light-matter interaction within the atmosphere is shortly discussed along with the theories of interactions of molecules and particles with light (Rayleigh and Mie theories, respectively). Descriptions of the lidar technique and the elastic backscatter lidar are also given.

- Chapter 3 - Solar Energy in Qatar.
  Qatar's geographic location and climate along with the plans for the introduction of solar radiation in the energy production mix of the country is briefly discussed in this chapter. The existing solar maps and solar resource assessment efforts undertaken in Qatar are also presented.

- Chapter 4 - Instrumentation.
  The experimental setup used in this thesis work is shown here, including descriptions of the ceilometer used for the measurement of the backscatter coefficient of aerosols in the atmosphere, the solar radiation monitoring station used for the measurements of solar radiation, and their respective data acquisition systems.

- Chapter 5 - Solar Radiation Data Analysis.
  The analysis of historical global solar radiation data is shown first in this chapter. The analysis of one year of solar radiation measured at the experimental site is then presented. This includes the hourly, daily and monthly averages as well as frequency distributions of solar irradiance values. The atmospheric conditions of the site are also studied through two indices: the clearness index and diffuse ratio.
- Chapter 6 - Correlation of DNI with backscatter.
  This chapter is mainly dedicated to present the method and results of the correlation between the lidar backscatter and solar radiation measurements. This includes first the analysis used to find the atmospheric height used for the integration of the backscatter signal. The methodology for the correlation is then described along with the validation of the proposed model and an example of application using the aerosol information extracted from lidar measurements for the calibration of satellite-derived solar data.
- Chapter 7 - Conclusions.
  Conclusions about the main results found in this thesis work are summarised in this chapter.
- Chapter 8 - Future work.
  Perspectives are discussed here with potential expansion of the work for a better application and use of the presented results.

Chapter 1

Overview on Solar Radiation

This chapter provides insight on the key characteristics of solar radiation. It discusses the basic definition of solar radiation, the effects of the earth's atmosphere on the transmission of solar radiation, and solar radiation components at ground level. It also covers most aspects of solar radiation measurement methods, comprising a description of the radiometric sensors and their principles of operation. A brief discussion of the setup and operation of a solar radiation monitoring station is presented. Also outlined, are methods of solar radiation modelling as well as the use of satellite images for solar radiation estimation. Finally, the use of solar energy as a clean and renewable energy source is addressed, with examples of its application.

1.1 Introduction to solar radiation

The sun is the fundamental source of almost all the energy on earth and the main driver of its climate system. Solar radiation emanating from the sun constitutes a crucial component of the earth's global energy balance and drives different systems, such as the atmospheric and hydrological processes. According to a NASA facts document [15], every square metre on earth receives approximately, on average over a year, 342 W of solar energy, equivalent to a power of 4.4×10^{16} W for the whole planet (excluding waters). To put this number in perspective, about 44 million large (1×10^{9} W) electric power plants are needed to equal this amount of energy.

The sun is a star, basically a ball of gas composed of about 92% hydrogen (H_2) and about 8% helium (He). It has a surface temperature of around 5000 K, with its core reaching between 8 and 40 million K [16]. Due to the high temperatures and pressures in its interior, nuclear fusion reactions occur, causing it to emit enormous amounts of electromagnetic radiation that travels into space at the speed of light. The earth is the

third closest planet to the sun, at a mean distance of around 150 million kilometres, completing an elliptical orbit, with small eccentricity, in about 365 days.

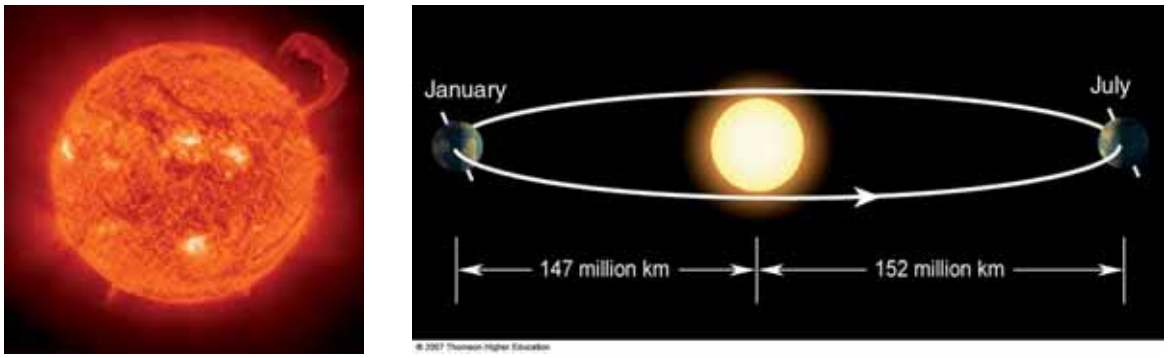

Figure 1.1: Left: the sun (photo: NASA/European Space Agency). Right: the earth's orbit around the sun (not to scale).

The electromagnetic radiation emitted by the sun ranges from very-short-wavelength gamma rays to long-wavelength radio waves in the electromagnetic spectrum, with a dominant portion emitted in the visible range around 0.48 μm. The total amount of solar radiation, integrated over all wavelengths, received on a plane perpendicular to the sun's rays at the top of the earth's atmosphere, at the mean sun-earth distance of 1 astronomical unit (AU), is called the *extraterrestrial solar irradiance*, usually referred to as the total solar irradiance (TSI), previously known as solar constant. Measurements of TSI from space-borne instruments in the late 1970s indicate that TSI varies over time and presents periodic components, the main one being the 11-year solar cycle (or sunspot cycle). The Active Cavity Radiometer Irradiance Monitor-I (ACRIM-I) was the first instrument, in 1979, to show that the total solar irradiance from the sun is not a constant. From 1984 on, TSI has also been measured by the Earth Radiation Budget Satellite (ERBS) instrument. Second and third ACRIM instruments have also been measuring TSI, in addition to the VIRGO on the NASA/ESA Solar and Heliospheric Observatory (SoHO). The SOlar Radiation and Climate Experiment (SORCE) satellite, launched in 2003, continues to produce TSI measurements through the Total Irradiance Monitor (TIM). More recently, the TSI Calibration Transfer Experiment (TCTE) instrument was launched into orbit in 2013, and has been providing TSI data since December 2013.

Different composite records of TSI are available and differ in their absolute scale and temporal variations due to calibration and degradation problems of spaceborne radiometers. Figure 1.2 shows, for instance, the most recent version (as of this writing) of the composite provided by the 'Physikalisch-Meteorologisches Observatorium Davos' of the World Radiation Center (PMOD/WRC), compared with two other composites [17]. The

composites present space-based measurements of TSI since 1980, normalised to 1 AU and covering three and a half 11-year solar cycles.

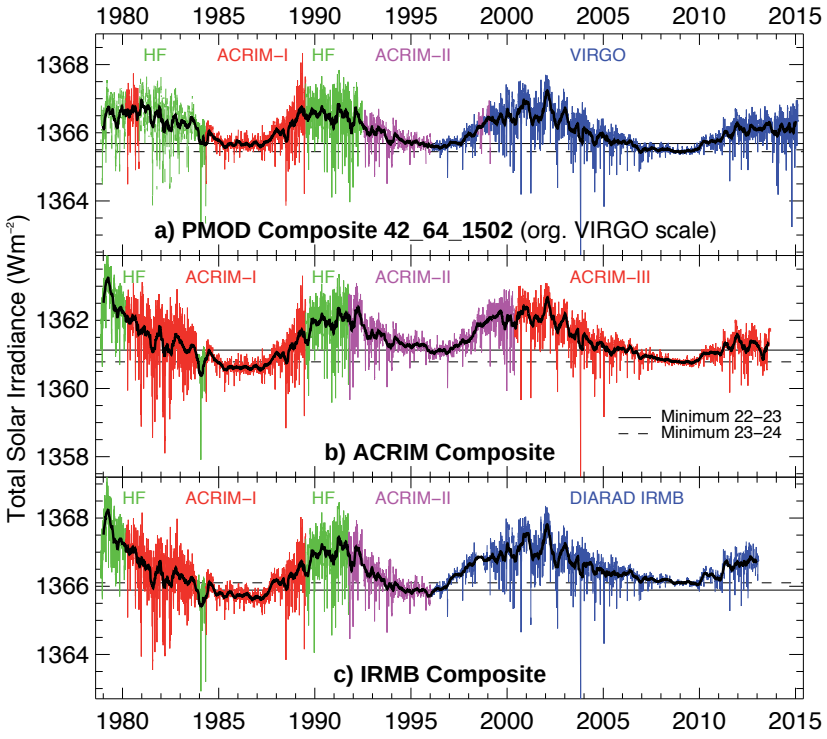

Figure 1.2: Composite measurements of TSI based on satellite-based radiometers (colour-coded) and model results produced by the World Radiation Center and two other composites, showing TSI variations for three solar cycles [17].

The typical variation in annual mean TSI is estimated to be around 0.1% between the minimum and the maximum of the 11-year cycle of the sun due to changing numbers and strength of sunspots and other phenomena, depending on solar activity. In general, this variation is stable and is considered negligible, so the term 'solar constant' is given to a long-term average of the TSI. The World Meteorological Organisation (WMO) has recommended a solar constant value of 1367 W/m^2. The American Society for Testing and Materials (ASTM) gives the value of 1366.1 W/m^2 to the solar constant, based on 25 years of data [18]. Gueymard, in a study in 2004 [18], reported that TSI measurements have an inherent absolute uncertainty of at least 0.1%, or 1.4 W/m^2, and he confirmed in the same study a solar constant value of 1366.1 W/m^2. Therefore, it can be assumed that the differences between the measured TSI values given above were not of high significance. More recently, measurements of the SORCE satellite indicate a slightly lower value, of approximately 1361 W/m^2 [19].

In the following chapters of this work, the TSI given by $I_0 = 1367\ W/m^2$ has been

used, as recommended by the WMO. TSI, or solar constant, as discussed above, refers to the solar radiation flux at the top of the atmosphere at the mean value of the sun-earth distance, R_0, of 1 AU. However, since the distance R between the sun and the earth varies during the year by 1.67% from their mean separation, the solar radiation flux at the top of the atmosphere, DNI_0, varies during the year over a range of about 6.7% (inversely proportional to the square of the distance from the sun). The correction factor is related to the eccentricity of the earth's orbit, and is given by the following equation:

$$\frac{DNI_0}{I_0} = \left(\frac{R_0}{R}\right)^2 \sim 1 + 0.033 \cos\left(\frac{2\pi n}{365}\right), \tag{1.1}$$

where n is the day of the year, from 1 to 365. In the literature, other approximation equations can be found, some more accurate, some less. For instance, the one given by Spencer in terms of a Fourier series expansion is more accurate. However, Equation 1.1 is considered accurate enough for most applications of solar resource assessment, and is used in the current work [16].

The spectral distribution of the extraterrestrial solar radiation is shown in Figure 1.3 (yellow curve). This distribution is similar to that of a black body with a temperature of 5778 K, with a spectral range of about 300 to 4000 nm, referred to as the short-wave solar radiation. The integrated energy over the same region is the broadband or total solar radiation.

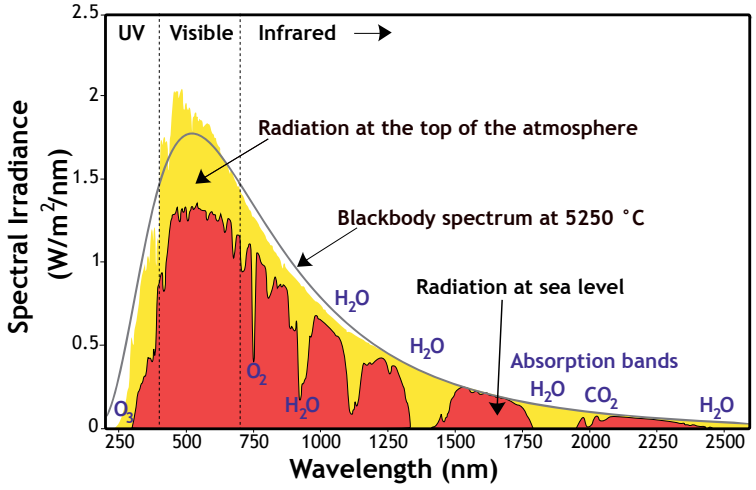

Figure 1.3: Spectral distribution of solar radiation at both the top of the earth's atmosphere and at sea level. Image adapted from Nick84, Wikimedia commons.

1.2 Solar radiation at the earth's surface

The amount of incoming solar radiation at the earth's surface is affected by the atmospheric composition, which intercepts the radiation along the way from the top of the atmosphere to the surface. As will be seen in Chapter 2, the atmosphere contains about 78% nitrogen, 21% oxygen and 1% argon in its lowest part. Other trace gases and water vapour are also found in low concentrations, but have a large influence on the radiation budget. A thin layer of ozone is present in the stratosphere and has a major role in the absorption of the ultraviolet wavelengths. In addition, atmospheric aerosol particles whether of natural sources such as dust, sea-salt spray, biological decay, chemical reactions of atmospheric gases, etc. or anthropogenic, i.e., human-induced such as from agriculture, transport, industrial emissions, etc., have a high impact on solar radiation. After penetrating the earth's atmosphere, the extraterrestrial solar radiation encounters these atmospheric constituents and its intensity is attenuated due to scattering and absorption processes that take place on its path before reaching the ground.

Scattering is due to radiation interaction with air molecules, water vapour and aerosols. It depends on the number of particles and the size of the particle relatively to the wavelength. Air molecules, for instance, scatter radiation as described by the Rayleigh theory, more significantly at shorter wavelengths, i.e., the ultraviolet and visible ranges, and there is little scattering in the infrared range, see Section 2.2.1. For larger particle sizes, such as dust and water vapour, the scattering process is more complex. For these cases, the Mie theory is applied. It describes the scattering of radiation by sphere-shaped objects, see Section 2.2.1. A different approach commonly used to explain the process of scattering by aerosols is described by the Ångström turbidity equation [16], which gives the atmospheric turbidity and its wavelength dependence:

$$\tau_{a,\lambda} = \exp(-\beta\lambda^{-\alpha}m), \tag{1.2}$$

where $\tau_{a,\lambda}$ is the transmission function, β is the Ångström turbidity coefficient, depending on the aerosol loading in the atmosphere and typically ranging between 0 (very clean atmosphere) and 0.4 (high aerosol amounts) [20], α is the wavelength exponent and depends on the size distribution of the aerosols, λ is the wavelength of the radiation in micrometres and m is the air mass along the path of the radiation, that is, the path length that solar radiation takes through the atmosphere normalised to the shortest possible path length when the sun is directly overhead.

Absorption of solar radiation is selective and is mostly due to ozone, water vapour and carbon dioxide in the atmosphere. Ultraviolet radiation is mainly absorbed by ozone,

but also by sulphur dioxide, nitrogen dioxide and trace gases. In the visible range, there is little absorption. Water vapour and carbon dioxide absorb strongly the solar radiation in the infrared range.

All these wavelength-dependent processes change the spectrum of the radiation that reaches the ground. For instance, the extraterrestrial radiation reaching the outer atmosphere at solar zenith angle of zero (see Section 1.2.1), decreases by about 30% on a very clear day to nearly 90% on a very cloudy day. The typical spectral distribution of the radiation at the earth's surface is shown by the red curve of Figure 1.3. Approximately half of the solar radiation at ground level is in the visible portion of the spectrum. The attenuation of the extraterrestrial solar radiation below 300 nm is mainly caused by the absorption by the ozone layer present in the stratosphere. The attenuation in the visible range is mainly due to Rayleigh and Mie scattering by gas molecules. Several strong absorption bands are seen in the infrared region of the spectrum due to water vapour and CO_2, which are responsible for the absorption of all solar radiation above 2500 nm. The spectrum of the solar radiation at the earth's surface depends upon the changing characteristics of the atmosphere, the surface composition, location, solar zenith angle and the air mass from the top of the atmosphere to the ground.

1.2.1 Sun position and sun angles

For the vital task of calculating the solar radiation intensity on any specified point on earth, it is necessary to know not only the properties of the atmosphere, but also the position of the sun in the sky, for any location on earth, at any time of the day. Two movements govern the variations of the sun's position in the sky:

- The earth's rotation around its axis, which modulates the variations through the day, from sunrise to sunset.
- The earth's revolution around the sun in an elliptic orbit, which modulates the variations through the year.

Moreover, the tilt of the earth's axis of rotation, as well as the geographic latitude of the location of interest, play an important role in calculating the position of the sun in the sky.

In order to find the sun's position for a given point on earth at a given time, several sun angles can be defined using different coordinate systems. Given that the sun's position needs to be known on the 'sky dome' seen by an observer on the surface of the earth, as shown in Figure 1.4, it is convenient to use a spherical coordinate system, with the observer's location as the origin of the coordinates.

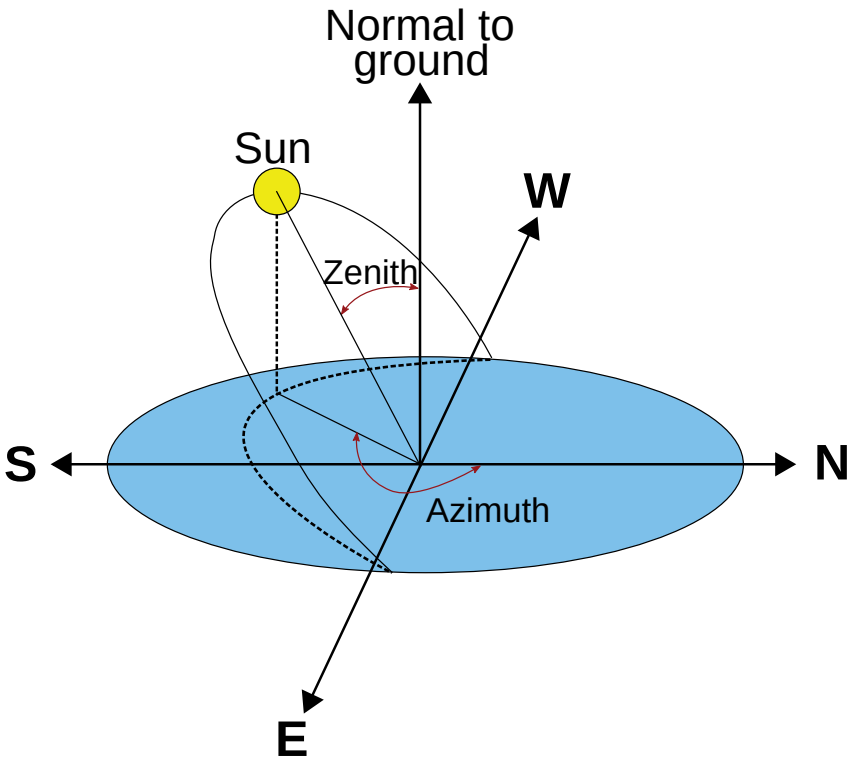

Figure 1.4: Angles used to describe the position of the sun in the sky of an observer at the earth's surface.

The radial distance to the sun is used to retrieve the solar radiation value at the top of the earth's atmosphere, using Equation 1.1. What remains to be determined are two coordinates, i.e., the position of the sun on the imaginary hemispherical surface of the sky dome, given by the azimuth and zenith angles. The azimuth angle indicates in which cardinal direction the sun is located, like a compass direction, with North as the reference, and varying between 0° and 360°. The zenith angle is measured between the vertical overhead and the line to the centre of the sun, and is the complement of the solar elevation angle (elevation of the sun from the horizontal). However, for the purposes of this thesis work, only the zenith angle and the radial distance to the sun are needed and discussed here. The solar zenith angle at any moment and location is interrelated by trigonometric relationships with a number of other angular quantities that take into account the location, time of the day, and time of the year. The solar zenith angle, θ_z, as used in this thesis work, is estimated using the following expression:

$$\cos(\theta_z) = \sin\phi \cdot \sin\delta + \cos\phi \cdot \cos\delta \cdot \cos(ha), \tag{1.3}$$

where ϕ is the latitude of the location of interest, on earth (-90 to 90 degrees), δ is the *declination angle* of the sun, and ha is the *hour angle* of the sun.

The sun's declination and hour angle describe the movement of the sun in the sky due to the earth's rotation and translation, and are more conveniently defined in an equatorial coordinate system (with origin at the earth's centre and projecting the earth's equator onto the celestial sphere). This system is independent from the position of the observer on earth but depends on the time of observation.

- The hour angle (ha) is the conversion of the true solar time (tst) into an angle in degrees corresponding to the angular motion of the sun along its path in the sky. The solar time is the apparent time and path of the sun in the sky relative to a specified location on earth. Solar time is different from the local time due to the orbital eccentricity of the earth and human adjustments such as time zones and daylight savings. Solar noon is when the sun is in its highest position in the sky. The hour angle is 0° at solar noon and each hour away from solar noon corresponds to a movement of the sun in the sky of 15°, with the hour angle negative before noon and positive after noon. Below are the steps required for the calculation of the solar hour angle in degrees.

  First, in order to calculate the local solar time, the local standard time should be corrected accounting for:

  - The time zone correction, which is the relationship between the local time zone, known as the Local Standard Time Meridian (LSTM), and the local longitude. The LSTM is related to the time zone of the location and is calculated in degrees by multiplying 15 degrees per each hour of difference between the local time and Greenwich Time. The time zone correction is expressed by:

    $$tz_{corr} = 4 \cdot (\Lambda - 15 \cdot tz), \tag{1.4}$$

    where Λ is the local longitude in degrees and tz is the timezone in hours from Greenwich Mean Time (GMT). Both longitude and tz are defined as positive to the east. The factor '4' seen in this equation comes from the conversion of degrees to minutes, the earth rotating 1° every 4 minutes.
  - The eccentricity of the earth's orbit around the sun and the tilt of the earth's rotational axis with respect to the plane of its orbit. To correct for both effects, an empirical equation called the 'equation of time' is calculated in minutes:

    $$\begin{aligned} eqtime \;=\; & 229.18 \cdot \big[0.000075 + 0.001868 \cdot \cos(\gamma) - 0.032077 \cdot \sin(\gamma) \\ & -0.014615 \cdot \cos(2\gamma) - 0.040849 \cdot \sin(2\gamma)\big], \end{aligned} \tag{1.5}$$

where γ is the fractional year in radians, given by:

$$\gamma = \frac{2 \cdot \pi}{365} \cdot \left(day - 1 + \frac{hour - 12}{24} \right) \tag{1.6}$$

From these two adjustments the time offset is calculated, in minutes, by:

$$t_{offset} = eqtime + tz_{corr} \tag{1.7}$$

and the true solar time, or local solar time (LST), can be expressed, in minutes, by using the time offset to adjust the local time (LT) in minutes, following the equation:

$$tst = LT + t_{offset} \tag{1.8}$$

Finally, the hour angle in degrees is given by

$$ha = \frac{tst}{4} - 180 \tag{1.9}$$

- The declination angle is the angle between a line joining the centre of the sun with the centre of the earth and a plane passing through the earth's equator. The seasonal variation of the declination angle is due to the tilt of the earth's axis of rotation by 23.45° with respect to the plane of its orbit, and to the translation of the earth around the sun. The declination is zero at the equinoxes, positive during the northern hemisphere's summer and negative during the northern hemisphere's winter. It reaches a maximum of 23.45° at the summer solstice and a minimum of -23.45° at the winter solstice.

  Several expressions can be used to calculate the sun declination. The formula used in this thesis is (δ in degrees):

$$\delta = 23.45 \cdot \sin\left(360 \cdot \frac{284 + n}{365} \right), \tag{1.10}$$

  where n is the day of the year, with the first of January being $n = 1$.

1.2.2 Solar radiation components

Solar radiation reaching the earth's surface includes two components: beam and diffuse. The beam radiation comes from the direction of the sun, with no scattering or absorption, and is called *direct normal irradiance* (DNI) when seen on a plane perpendicular to the

sun's rays. The part of the incident radiation scattered as it passes through the earth's atmosphere, received on a horizontal plane, is called *diffuse horizontal irradiance* (DHI), and includes radiation scattered from the earth's surface and from the atmosphere. *Global horizontal irradiance* (GHI) is the total amount of sunlight on a horizontal surface. In addition to the direct and diffuse components, the total or global solar radiation striking a surface has a contribution from reflected radiation, coming from any other surface. However, this contribution is small, unless the receiving surface is tilted at a steep angle from the horizontal and the ground is highly reflective. In this case, the *global tilted irradiance* (GTI) is defined as the total irradiance that falls on a tilted (non-horizontal) surface.

Direct Normal Irradiance

DNI is defined as 'the energy flux density of the solar radiation incoming from the solid angle subtended by the sun's disc on a unit area of a surface perpendicular to the rays' [21]. Another definition, from the WMO, states that DNI is the amount of radiation from the sun and a narrow annulus of sky as measured with a pyrheliometer (see Section 1.3.1) designed with a field of view (FOV) of about 5° [22]. Given the sun's apparent diameter of around 0.5° as seen from the earth, this means that DNI is the solar radiation arriving directly to the ground from the solar disc and close circumsolar region around it. This region is caused by the forward scattering of solar radiation by atmospheric particles, appearing to come from the solar aureole. DNI depends on the amount of incident energy at the top of the atmosphere and on the extinction properties of the atmospheric constituents, independently of whether the extinction is caused by scattering or absorption. The beam (direct) component incident on a horizontal surface, denoted as *beam horizontal irradiance* (BHI), is the direct component multiplied by the cosine of the angle of incidence at which it falls on the horizontal surface. On a typical clear day, approximately 70% of the extraterrestrial direct normal irradiance passes through the atmosphere without undergoing scattering or absorption. DNI is the fuel of the concentrating solar energy conversion systems such as concentrating solar power and concentrating photovoltaic. Plants utilising these technologies require the detailed analysis and knowledge of DNI.

Diffuse Horizontal Irradiance

DHI is the radiation that reaches ground level after being scattered by the atmospheric constituents (aerosols, molecules, clouds). Part of the incident radiation is scattered by the earth's surface and re-scattered again by the atmosphere, which results in an

additional contribution to the diffuse irradiance. To be more specific, DHI is the solar radiation arriving on a horizontal surface from all parts of the sky dome except directly from the sun, i.e., excluding DNI. At a certain air mass, the amount of the diffuse component in a clear sky depends on the atmospheric constituents as well as on the albedo of the underlying surface. During cloudy conditions, the diffuse component is usually high. Modelling the diffuse radiation is complicated due to complex light-atmosphere interactions, the varying compositions of the clouds and the complex optical properties of the ground.

Global Horizontal Irradiance

GHI is the total hemispherical solar radiation on a horizontal surface, received from the entire 2π solid angle of the sky dome. It represents the sum of the direct and diffuse horizontal components or, in other words, the sum of the direct normal irradiance projected on a horizontal surface and the diffuse horizontal irradiance:

$$GHI = DNI \cdot \cos(\theta_z) + DHI = BHI + DHI, \tag{1.11}$$

where θ_z is the solar zenith angle calculated for the date and time of measurement at a specific location. This relation is fundamental for most solar radiation measurement applications, such as data quality controls and atmospheric radiative transfer models. GHI is of particular interest for photovoltaic systems.

1.2.3 Solar radiation units

Solar radiation components are in general expressed in terms of irradiance and irradiation. Irradiance is the intensity of solar radiation or rate of solar energy received per unit area and unit time. It is measured with the unit of Watts[i] per square metre, W/m^2. Insolation or irradiation is the solar radiation intensity per unit area integrated over a specified period of time, that is, 1 hour, 1 day, 1 month, or even 1 year, and can be expressed in Joule per square metre, J/m^2, or Watt-hour per square metre, Wh/m^2. Daily and yearly insolation totals are commonly given in $kWh/m^2/day$ and $kWh/m^2/yr$, respectively.

[i] 1 Watt is equal to 1 Joule per second, 1 $W = 1\ J/s$.

1.3 Ground measurements of solar radiation

1.3.1 Solar radiation sensors

Accurate measurements of solar radiation are essential for many applications. One can cite: atmospheric physics research, climatic change studies, solar energy-based project design and implementation, development and validation of solar radiation estimation models, solar resource forecasting techniques, etc. Radiometry is the used technique for the measurement, and commonly a specific radiometer is used to measure each of the solar radiation components specified in Section 1.2.2. DNI is usually measured by a pyrheliometer mounted on a sun tracker, while GHI and DHI are measured by pyranometers. The most frequently used sun radiometers are made with thermal sensors based on the thermoelectric effect. The irradiance in W/m^2 is determined by using a sensor calibration factor. In general, the spectral sensitivity of this type of radiometers is almost constant over the solar spectral range, which makes the measurements of solar radiation nearly independent of its wavelengths.

The thermoelectric principle involves the interconversion of heat energy and electrical energy. The energy conversion can be reversible or irreversible. The Seebeck, Peltier and Thomson effects are examples of reversible thermoelectric effects, with most practical applications in radiometry limited to the Seebeck effect. The Joule effect, on the other hand, is a very well known irreversible thermoelectric effect in which an electric current is irreversibly transformed into heat, using the electrical resistance of the conductor.

Thermopile sensors have been extensively used in the most common radiometers and are based on the Seebeck effect, in which a difference of voltage is created between two metallic conductors when their junctions are kept at different temperatures. Thermopiles consist of a series of thermocouples (junctions between two different metals) connected together usually in series or, less commonly, in parallel. When thermal radiation is absorbed by the active thermocouple junctions (the hot junctions), it increases their temperature, creating thus a differential temperature between these junctions and the reference junctions (the cold ones) kept at a fixed temperature. This produces a voltage difference directly proportional to the induced temperature difference. Inside a radiometer, the active junctions are placed underneath a black coating surface and are heated by the solar radiation absorbed by the blackened receiver. The passive junctions are mounted close to the sensor housing, so that they keep the same temperature of the housing. Blackened coatings are the most commonly used receiver surface in thermopile-based sensors. Black-and-white coatings can also be used, in which the hot junctions are placed beneath the black coating and the cold junctions are bonded to the white coating. The detection

of thermal energy is based on the difference of absorptivity of colour variations over the receiving surface. With this design, there is no need to use a large thermal mass to maintain the stability of the cold junctions, since the white coating provides the 'absolute' temperature of the cold junctions. However, the white coating may turn yellow with time due to solar radiation, and this causes a decrease in its sensitivity and makes it necessary to re-calibrate more frequently the sensors based on this design. Figure 1.5 shows a typical construction of a thermopile, with an illustration of a black-and-white coating.

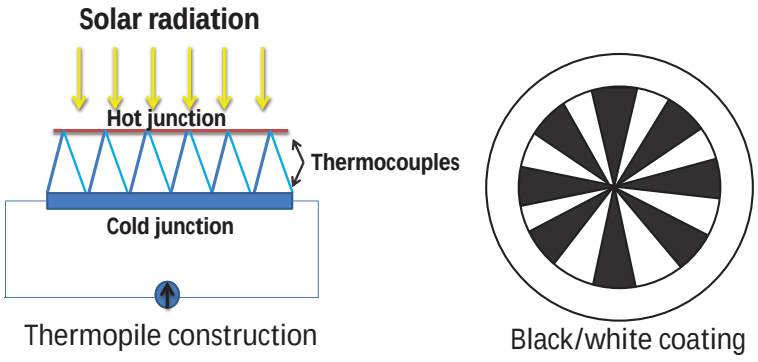

Figure 1.5: Thermopile principle of operation and illustration of a black/white coating.

A more recent radiometry method used for solar radiation is based on Peltier element sensors. The Peltier effect is the reverse of the Seebeck effect, where heat is liberated or absorbed if an electrical current flows across a junction of two different semi-conductors. Figure 1.6 shows the construction and the arrangement of a Peltier element, which consists of multiple semiconductors of two different materials, n-type and p-type semiconductors, in an alternating arrangement. For solar radiation measurement applications, the top side of the Peltier element is heated by the solar radiation and the bottom side is connected to the radiometer body. A current is then applied in order to equalise the temperature of the two sides. The applied current is proportional to the absorbed solar radiation. In practical applications, Peltier-based sensors are more stable than thermopiles and present better performance in terms of response time and linearity, but are more expensive [23]. In all cases, the engineering of radiometers is very delicate due to several considerations, specially given that the radiometers have to be placed outdoors and must withstand any kind of weather, from extreme temperatures, to wind, dust, rain, and snow.

An economical alternative to radiation sensors based on the thermoelectric principle are radiation sensors based on the photoelectric principle, mainly used for measuring radiation in specific spectral ranges. The photoelectric effect is the emission of electrons

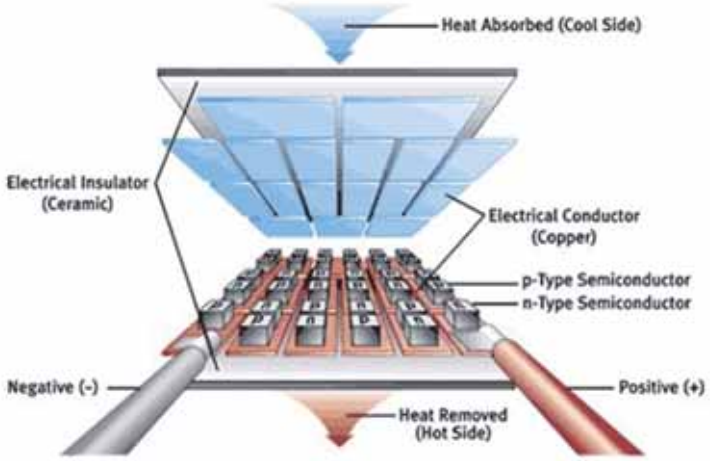

Figure 1.6: Peltier element principle of operation.

from a metal, when incident light radiates upon the metal. The absorption of the photons within the metal results in the transition of electrons to a higher energy level and electrons can escape from the metal as free electrons. In the case of a semiconductor device, the excited electrons remain within the material and increase its conductivity. The typical sensing elements based on the photoelectric effect and used in radiometry are photodiodes characterised by their small size and relatively high output signal. See Figure 1.7 for some photodiode sensors currently provided by different manufacturers. A photodiode is a semiconductor device made of a junction of oppositely doped regions (p-n junction). The absorption of photons results in the creation of electron-hole pairs in the depletion region of the p-n junction. The built-in electromagnetic field of this region sweeps these free carriers from the junction, thus producing a photocurrent proportional to the incident radiation. Apart from being less expensive and requiring lower maintenance compared to thermopile detectors, the main advantage of using photodiode sensors in solar energy measurements is their faster response time, which is around 10 μs, while the thermopile response time ranges between 1 and 10 s [24]. However, photodiodes have a limited spectral response and their sensitivity is wavelength-dependent, so depending on the application and the required spectral ranges, different types of materials can be used.

Pyrheliometer

A pyrheliometer is the instrument developed for the measurement of the direct normal irradiance from the sun. A field pyrheliometer is usually mounted on a two-axis automatic solar tracking system which allows the instrument to permanently point towards

Figure 1.7: Examples of photodiode-based sensors from different manufacturers, used for solar radiation measurements.

the sun throughout the daylight period. The main elements of a pyrheliometer consist of a collimating tube, a blackened detector placed near the base of the tube, a flat protective window, aperture rings and alignment aids. A typical construction of a pyrheliometer is shown in Figure 1.8. The detector is in general a multi-junction thermopile, with a black-painted coating serving as the sensing element, to fully absorb solar radiation in the wavelength range from 280 nm to 3000 nm. The black surface absorbs the solar energy and warms up the thermopile. The produced thermal energy causes a temperature difference between the receiver and the reference temperature inside the tube. The induced temperature difference generates an output voltage proportional to the incident radiation and given by the sensitivity of the device. For the optical geometry within a pyrheliometer, the WMO recommends an angular aperture of 5°, in order to limit the measurements to radiation coming directly from the sun disc plus radiation coming from a small circumsolar region around it. The alignment with the axis of the sun beam should have 0.1° or better of pointing accuracy, and the slope angle, an important angle for the tracking accuracy, should be 1°, as advisable by the Baseline Surface Radiation Network (BSRN) (see Section 1.3.4). Temperature compensation is usually incorporated in high performance sensors to minimise sensitivity to ambient temperature fluctuations, and desiccants are used to prevent condensation and keep the instrument dry. The instantaneous voltage value from the sensor is read with a data acquisition system, and a data logger provides the DNI values in W/m^2 by taking into account the sensitivity of the instrument.

An absolute cavity radiometer (ACR) is a sophisticated type of pyrheliometer of a

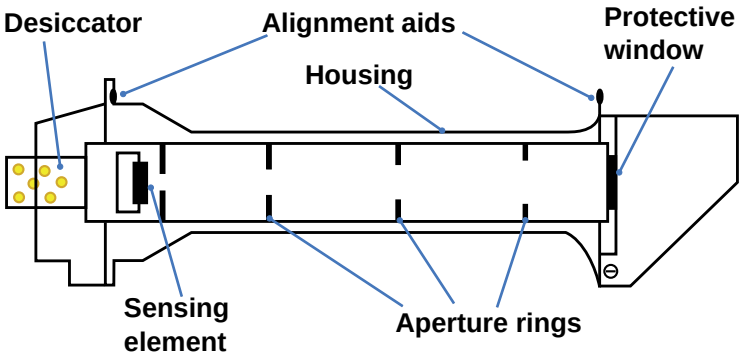

Figure 1.8: Construction of a typical pyrheliometer.

primary standard quality. It is an electrically self-calibrating instrument. By design, it has no protective window, and therefore is sensitive to all wavelengths available from the direct sun beam. Its use is limited to fully attended operation under clear sky conditions and is not suitable for continuous and unattended operation in all weather conditions. An ACR has a cavity with a precision aperture operating in two arrangements: the 'active cavity' mode, which heats up when exposed to the sun, and the 'passive cavity' mode, when the cavity is shaded from the sun beam and acts as a compensating mode. The temperature rise induced by absorption of sunlight in the active cavity is matched to the temperature rise induced by an electrical current through the cavity walls in the passive cavity. The ACR is the basis for the World Radiometric Reference (WRR), the internationally recognised detector-based measurement standard for DNI [25]. They are also used as a reference for the calibration of field and reference pyrheliometers. Figure 1.9 shows a PMOD/WRC absolute cavity radiometer system with its control unit.

Figure 1.9: Absolute cavity radiometer from PMOD/WRC.

Pyranometer

A pyranometer is the instrument used for the measurement of global and diffuse solar radiation in the spectral range of 300 nm to 3000 nm. It is placed horizontally and has an almost complete hemispherical field of view of 2π steradian. For measuring the diffuse horizontal irradiance, a suitable shading device is used in addition, in order to eliminate the contribution of the direct radiation. This shading device can be manual, such as a shadow ring which requires periodic manual adjustment for the declination angle of the sun, or automatic, i.e., a shadow ball or disk mounted on an automatic solar tracker like the one used for the pyrheliometer. As specified by the WMO and the international ISO 9060 standards, pyranometers are required to have sensors characterised by their non-selective spectral response, which is the case of thermoelectric sensors. The main components of a pyranometer are the detector, the hemispherical dome(s) and the housing. Figure 1.10 shows a typical pyranometer construction. The sensing element of the detector can have a black or a black-and-white coating, and the dome(s) protects the receiver from dirt and weather. The housing serves as the sensor thermal reference with the principle similar to that of a pyrheliometer. The pyranometer can house a desiccator for keeping the instrument dry and a thermistor as temperature compensation system. Some pyranometer systems have ventilation units with heaters which continuously blow air to help reduce dew and frost in the early morning but also dust in case the instrument is located in a dusty environment. The whole system is protected by a removable sun shield, which limits the viewing angle to 180°. An important feature of the pyranometer is the 'zero offset' type A, which is the false signal generated on the detector by the thermal radiation emitted by the dome after it gets heated by the incoming radiation. This effect is generally reduced by using two domes in the construction of a pyranometer. Black-and-white coatings have lower thermal offsets than the fully black-coated surface, but they require calibration more frequently due to a reduced long-term stability.

As seen in Section 1.3.1, photodiodes generate a photocurrent in response to incident radiation, in proportion to incident light. Therefore, silicon photodiode-based pyranometers are also used for measuring the global horizontal irradiance. They are placed underneath a diffuser to provide a good directional response. However, they do not meet the international standards in terms of spectral sensitivity and range. Figure 1.11 shows the construction of a silicon photodiode-based pyranometer as designed by [24] and which incorporates all necessary electronics for conditioning, control and communications. The spectral response of silicon pyranometers has a limited range in comparison to the thermopile type, as depicted in Figure 1.12. This smaller spectral responsivity to the solar spectrum contributes to the low accuracy of silicon photodiode-based detectors, so their

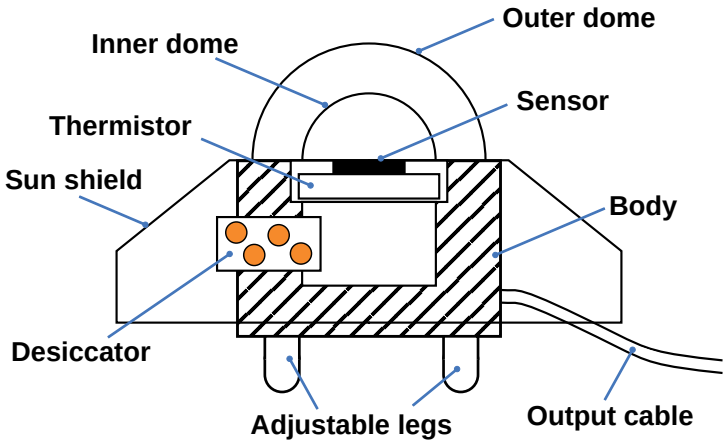

Figure 1.10: A typical thermoelectric pyranometer.

use is usually limited to simple and low-cost applications.

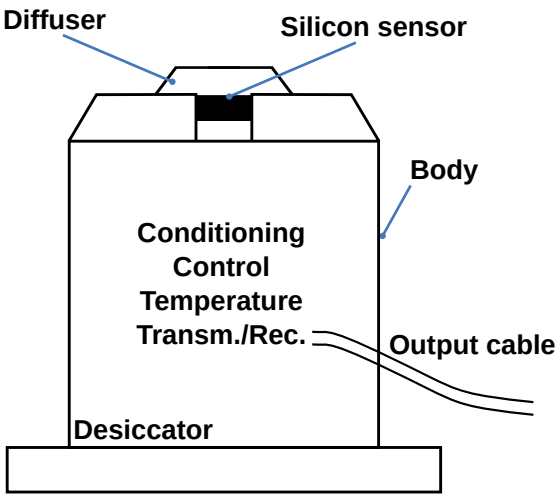

Figure 1.11: Example construction of a silicon photodiode pyranometer as given by [24].

Rotating shadowband radiometer

An alternative method that allows to obtain all components with one sensor (with less accuracy, though) is the use of a rotating shadowband radiometer (RSR), see Figure 1.13. This instrument consists of a silicon photodiode pyranometer (described in the previous paragraph) and a shading band rotating with a constant speed at defined time intervals. When unshaded, the photodiode measures GHI, and when the band completely shades the detector from the sun, DHI is measured, taking advantage of the fast response time of the sensor. The horizontal component of DNI is then calculated as the difference of

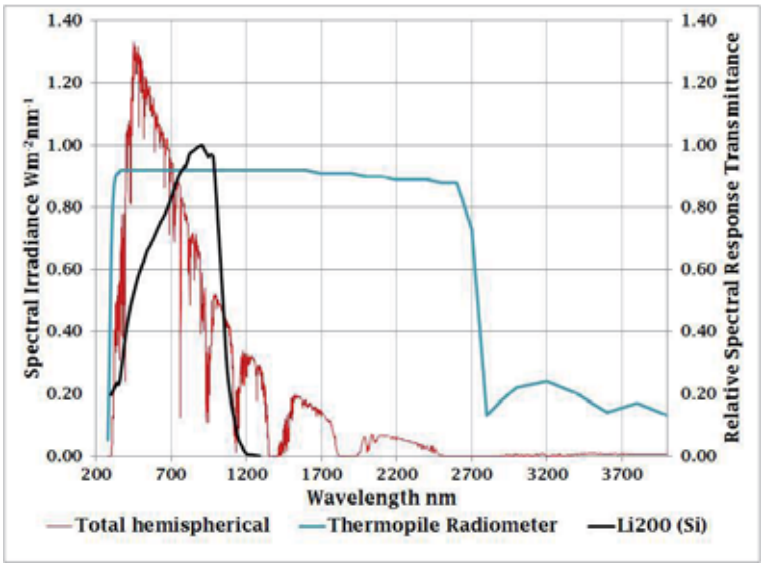

Figure 1.12: Spectral response of silicon (black line) and thermopile (blue) pyranometers, compared to the solar spectrum at ground level (red) [26].

these two measurements and DNI is obtained by dividing the horizontal beam radiation by the cosine of the zenith angle at that moment (cf. Equation 1.11). This measurement includes many uncertainties, such as the temperature dependency of the photodiode, its spectral response, etc. Nevertheless, it is a less expensive method to obtain DNI and DHI without using a tracker.

1.3.2 Radiometer calibration

Calibrating an instrument is determining a relation between its input and output values. Pyranometers and pyrheliometers are calibrated in W/m^2 and their sensitivity is in general in the region 5–20 $\mu V W^{-1} m^2$. The World Radiometric Reference is the internationally accepted traceable reference for all radiometer measurements. It is used as a standard for calibrating solar radiometers and to ensure homogeneity of solar radiation measurements around the world. The WRR is produced by a group of absolute cavity radiometers, the World Standard Group (WSG), maintained and operated at the World Radiation Center (WRC) by the Physical Meteorological Observatory, Davos (PMOD), in Switzerland [22]. Every five years, an International Pyrheliometer Comparison (IPC) is held at the PMOD/WRC to transfer the WRR to the participating reference ACR instruments, using the sun as the source. The transfer of WRR from the WSG is described in [27].

Reference pyrheliometers are calibrated by direct comparison with absolute cavity radiometers traceable to the WRR. The calibration is similar to the transfer of the WRR

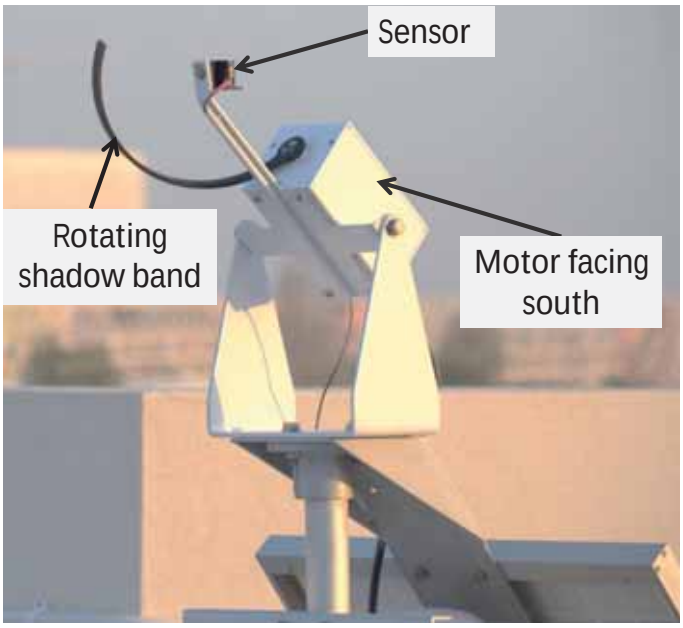

Figure 1.13: Rotating Shadowband Radiometer installed at QEERI's site.

to the ACR radiometers [28]. The average sensitivity, ratio of the voltage signal of the test pyrheliometer to the ACR beam irradiance (in units of $\mu V W^{-1} m^2$), is calculated for a large range of irradiance levels and solar geometries.

Reference pyranometers are calibrated against a reference ACR by using Equation 1.11 [29] and the 'sun and shade' method described in [30], where the pyranometer is first exposed to the full hemispherical radiation to generate an output voltage V_g and then it is shaded, so it responds only to the diffuse sky radiation, and generates the output voltage V_d. The sensitivity can then be calculated from the direct beam radiation measured by the ACR:

$$Sensitivity = \frac{V_g - V_d}{DNI \cdot \cos(\theta_z)} \tag{1.12}$$

The calibration methodology of field instruments is performed in laboratories, in comparison with a reference instrument of the same type and using artificial sources of light. The calibration method is described in [31] for field pyranometers and in [32] for field pyrheliometers.

1.3.3 Radiometer properties and classifications

Radiometer measurement errors and uncertainty depend on several factors and properties characteristic of the radiometer in use. These properties define the relationship of input values (radiation intensity) to output values (induced voltage), and the most important are the following:

- **Non-linearity of response** is the change in sensitivity related to the level of the incident radiation. It is evaluated as the percentage deviation from the responsivity at 500 W/m^2 due to any change of irradiance within the range 100 to 1100 W/m^2. This effect is mainly attributed to convective and radiative heat losses at the black-painted surface.
- **Temperature response** is the change in the sensitivity due to any change in ambient temperature. The manufacturer provides in general a temperature response curve for the specific model of the radiometer.
- **Zero offsets** are the result of the measuring principle of the radiometer. The radiometer temperature varies in proportion to the ambient temperature and causes thermal currents inside the instrument, called 'zero offset type B'. It is quantified in ISO 9060:1990 as the response in W/m^2 to a 5 K/hr change in ambient temperature. The 'zero offset type A' only affects pyranometers and is described in Section 1.3.1.
- **Response time** is the time required by the radiometer to respond to changes in the incident radiation. In general, it is the time for the output to reach 95% (sometimes $1 - 1/e$, 63%) of the final value after a step-change in the irradiance.
- **Non-stability** is the sensitivity drift with time, quoted as the percentage change of sensitivity over a period of one year of operation of the instrument. This effect is mostly due to degradation by UV radiation of the black absorber coating on the thermopile surface. Most manufacturers recommend recalibration every two years.
- **Directional response** (for pyranometers) is the relative deviation of the measured value from the ideal value, relative to the angle of incidence of the solar radiation. Ideally, a sensor should report an intensity value proportional to the cosine of the zenith angle of the incident radiation, called the 'cosine response'.
- **Spectral selectivity** is the variation of the dome transmittance and absorption coefficient of the black detector coating with wavelength, and is commonly specified as % of the mean value.
- **Tilt response** (for pyranometers) is the percentage deviation from the responsivity at 0 degrees tilt (horizontal) due to changes in tilt from 0 degrees to 90 degrees at 1000 W/m^2.

- **Resolution** is the smallest change in the amount of radiation that the instrument can detect.

Classifications and specifications for solar irradiance measurement devices have been established by ISO 9060/1990 [33] and WMO [22], based on the characteristics listed above and on the estimated measurement uncertainty of each instrument and their quality. Tables 1.1 and 1.2 list the WMO characteristics for pyrheliometers and pyranometers, respectively. Tables 1.3 and 1.4 list the ISO specifications for these radiometers. From the highest quality to the lowest, three classes are distinguished: secondary standard, first class and second class. Various models of instruments are available in the market. These specifications and classifications should be examined in detail in order to get the required quality of instruments for a particular application.

Characteristic	High quality	Good quality
Response time	$< 15\ s$	$< 30\ s$
Zero offset	$2\ W/m^2$	$4\ W/m^2$
Resolution	$0.051\ W/m^2$	$1\ W/m^2$
Stability	0.01%	0.05%
Temperature response	1%	2%
Non-linearity	0.02%	0.05%
Spectral sensitivity	0.05%	1.0%
Tilt response	0.02%	0.05%
Achievable uncertainty, 95% conf. level		
1-min totals		
Percent	0.9	1.8
kJ/m^2	0.56	1
Wh/m^2	0.16	0.28
1-h totals		
Percent	0.7	1.5
kJ/m^2	21	54
Wh/m^2	5.83	15

Table 1.1: WMO characteristics of operational pyrheliometers for DNI measurements [22].

Characteristic	High quality	Good quality	Moderate quality
Response time	$< 15\ s$	$< 30\ s$	$< 60\ s$
Zero offset			
Response to 200 W/m^2 net thermal radiation (ventilated)	7 W/m^2	7 W/m^2	7 W/m^2
Response to 5 K/h change in ambient temperature	2 W/m^2	2 W/m^2	2 W/m^2
Resolution	1 W/m^2	5 W/m^2	10 W/m^2
Stability	0.08%	1.5%	3%
Directional response	10 W/m^2	20 W/m^2	30 W/m^2
Temperature response	2%	4%	8%
Non-linearity	0.05%	1%	3%
Spectral sensitivity	2%	5%	10%
Tilt response	0.5%	2%	5%
Achievable uncertainty, 95% C.L.			
Hourly totals	3%	8%	20%
Daily totals	2%	5%	10%

Table 1.2: WMO characteristics of operational pyranometers for GHI and DHI measurements [22].

Specification	Class of pyrheliometer		
	Secondary standard	First class	Second class
Response time	$< 15\ s$	$< 20\ s$	$< 30\ s$
Zero offset	$\pm 2\ W/m^2$	$\pm 4\ W/m^2$	$\pm 8\ W/m^2$
Resolution	$\pm 0.5\ W/m^2$	$\pm 1\ W/m^2$	$\pm 5\ W/m^2$
Stability	$\pm 0.5\%$	$\pm 1\%$	$\pm 2\%$
Non-linearity	$\pm 0.2\%$	$\pm 0.5\%$	$\pm 2\%$
Spectral selectivity	$\pm 0.5\%$	$\pm 1\%$	$\pm 5\%$
Temperature response	$\pm 1\%$	$\pm 2\%$	$\pm 10\%$
Tilt response	$\pm 0.2\%$	$\pm 0.5\%$	$\pm 2\%$
Traceability	With a primary std. pyrheliometer	With a secondary std. pyrheliometer	With a first class pyrheliom. or better

Table 1.3: ISO specifications for pyrheliometers used for DNI measurements [33].

Specification	Class of pyranometer		
	Secondary standard	First class	Second class
Response time	$< 15\ s$	$< 30\ s$	$< 60\ s$
Zero offset			
Response to 200 W/m^2 net thermal radiation (ventilated)	$\pm 7\ W/m^2$	$\pm 15\ W/m^2$	$\pm 30\ W/m^2$
Response to 5 K/h change in ambient temperature)	$\pm 2\ W/m^2$	$\pm 4\ W/m^2$	$\pm 8\ W/m^2$
Resolution	$\pm 1\ W/m^2$	$\pm 5\ W/m^2$	$\pm 10\ W/m^2$
Stability	$\pm 0.8\%$	$\pm 1.6\%$	$\pm 2\%$
Non-linearity	$\pm 0.2\%$	$\pm 0.5\%$	$\pm 2\%$
Directional response	$\pm 10\ W/m^2$	$\pm 20\ W/m^2$	$\pm 30\ W/m^2$
Spectral selectivity	$\pm 2\%$	$\pm 5\%$	$\pm 10\%$
Temperature response	$\pm 2\%$	$\pm 4\%$	$\pm 8\%$
Tilt response	$\pm 0.5\%$	$\pm 2\%$	$\pm 5\%$

Table 1.4: ISO specifications for pyranometers used for GHI and DHI measurements [33].

1.3.4 Solar radiation monitoring station

Reliable data of solar radiation is key for any solar energy-based project. Direct ground measurements of solar radiation are the most accurate method for knowing the amount of incoming solar radiation at a certain location. For this purpose, installing a solar monitoring station to measure the different components of solar radiation simultaneously in a unique system is fundamental. This system consists of a set of solar sensors mounted on an automatic two-axis sun tracker which provides a stable platform where all sensors are placed in optimum positions and, most importantly, moves horizontally in the azimuth direction and vertically in the zenith direction, following the path of the solar disc, in a way to continuously point to the sun from sunrise to sunset. This offers an uninterrupted measurement of solar radiation through the following sensors (described above): one pyrheliometer for direct normal irradiance, one pyranometer for global horizontal irradiance and another pyranometer for diffuse horizontal irradiance with a shading assembly mounted in a way to shade the dome of the pyranometer and block the direct radiation. A solar station can also host a pyrgeometer (for far infrared long-wave radiation), UV radiometer, albedometer or other sensors.

A number of considerations should be taken into account before installing a solar monitoring station:

- The site should be easily accessible for periodic maintenance of the instruments, including frequent cleaning of the domes and changing the desiccants.
- The site should be free from any obstructions to the sun path through the year and to the horizon in all directions, in order to obtain a clear hemispherical field of view. The rule of thumb is that the distance d from an obstruction to the instrument should be at least ten times the elevation h of the obstruction, $d \geq 10 \times h$.
- Noise from cabling should be limited between the sensors and the data acquisition system.
- Cleaning and inspection of the alignment of instruments should be performed regularly.
- Instruments should be re-calibrated at least every two years or as advised by the manufacturer.

In order to characterise solar radiation in terms of its temporal and spatial distribution, it is important to operate continuously a network of monitoring stations in different locations, at adequate distance from each other. However, such a project requires a large amount of resources and has very high costs in terms of investment and maintenance. This limits the implementation of a network of measuring stations, restricting the number of stations to be deployed. Therefore, and in order to obtain a global coverage of solar radiation, classical statistical techniques, that is, interpolation and extrapolation, have been developed to estimate the solar radiation at any point. The simplest method is to extrapolate the data by using measured values from the closest ground station. This method is not very accurate and may introduce errors which increase with the distance from the closest station. Better results can be achieved by using spatial interpolation methods, such as the weighted interpolation where the data are weighted proportionally to the inverse squared distance of the surrounding stations, or by using the so-called Kriging technique, where the weights are determined so that the root mean square errors are minimal. Usually, however, the number of available nearby ground stations is not sufficient to get reliable interpolations and, moreover, it has been shown that daily measurements of solar radiation can be trustable up to a maximum radius of around 30 km [34].

An example of a high quality solar radiation monitoring network is the Baseline Surface Radiation Network (BSRN) of the World Climate Research Programme (WCRP) [35]. This network is part of a project designated for detecting important changes in the earth's radiation field at the earth's surface related to climate changes. Currently, about 58 stations are located in contrasting climatic zones, covering a latitude range from 80°N

to 90°S. The World Radiation Data Centre (WRDC) of the WMO [36], on the other hand, is an online database maintained by the Russian Federal Service for Hydrometeorology and Environmental Monitoring, and serves as a central depository for solar radiation data collected at over one thousand measurement sites throughout the world. In Qatar, the Qatar Meteorological Department (QMD) currently operates a network of 12 automated weather stations (AWS) distributed in coastal and inland locations throughout the country, and most of these stations have been collecting global horizontal irradiation data from as early as 2007, along with meteorological parameters. For more details on the QMD network, see Section 5.1.

1.4 Solar radiation modelling

Although ground measurements of solar radiation, if the used instrumentation is well maintained and regularly calibrated, represent the most accurate option for the knowledge of solar radiation data, they are not always available, and solar radiation monitoring networks have limited coverage. In the absence of ground measurements, models have been developed for the estimation of solar radiation. These models can be based on empirical approaches, using meteorological parameters or atmospheric constituents or a more readily available solar radiation component. They can also be quasi-physical and physical, considering the radiative extinction processes in the atmosphere. Artificial Neural Network models have also been developed for solar radiation estimation.

1.4.1 Empirical models

Empirical methods use a relationship between the atmospheric transmissivity and other meteorological parameters and are mostly based on measured radiation data at specific sites. Meteorological parameters used to model solar radiation may include sunshine duration, temperature, cloud cover, precipitation and humidity. The accuracy of the model depends on the used parameters and the way they are implemented in the model.

The first empirical model for estimating global solar radiation was developed by Ångström and is based on the hours of sunshine duration, using data generally available in many locations [37]. Several regression models, based on the Ångström model, have been proposed, with a resulting linear equation given by:

$$\frac{H}{H_0} = a + b\frac{S}{S_0}, \tag{1.13}$$

where H and H_0 are, respectively, the monthly averages of daily global radiation and

of daily extraterrestrial radiation on the horizontal surface, S and S_0 are the monthly averages of daily hours of bright sunshine and of maximum possible daily sunshine hours (the day length), a and b are empirical constants depending on the location.

It was found that this linear-type equation cannot be applicable for particular days with extreme values, leading to overestimation of the total radiation on cloudless days when $\frac{S}{S_0} = 1$ and on overcast days when $\frac{S}{S_0} = 0$. A quadratic form was then suggested for the relationship between the ratio of daily global to extraterrestrial radiation and actual to maximum possible hours of sunshine greater than zero. Others suggest multi-linear regression equations with combinations of one or more weather parameters such as temperature, relative humidity, and relative sunshine duration [38]. The Ångström-type empirical models were reviewed by Gueymard et al. in [39], covering the errors coming from instrumental measurements of S and the effects of seasonal and climate variability.

Another empirical method which has been extensively used is the air temperature-based model [40], since air temperature measurements are available at many locations from the majority of meteorological stations. The method is based on the calculation of the difference between the maximum and minimum temperatures, which has different range on clear days than on overcast or rainy days.

Of particular interest to this work is the direct normal irradiance. Many empirical models have been developed to derive DNI by statistical means from other, more readily available data. One approach is to use the global solar radiation in order to estimate the direct component, through an empirical relationship between the global and direct clearness indices or transmittances, K_t and K_n [41]. The global clearness index K_t is defined as the ratio of global horizontal radiation at the earth's surface (GHI) to the global horizontal radiation at the top of the atmosphere. The direct clearness index K_n is the same ratio but for the beam (direct) components. Another empirical approach for direct normal radiation estimation is to correlate the diffuse ratio to K_t. The diffuse ratio is the fraction of the radiation on a horizontal plane which is diffuse, i.e., the ratio DHI/GHI. Many well-known models have been proposed based on this correlation. To cite, Orgill and Hollands in 1977 [42], Erbs in 1982 [43] and Reindl et al. in 1999 [44]. Each of these models is derived from a different data set of ground measurements. In general, all the cited models are almost identical and give similar results for practical purposes. Below is the equation of the diffuse fraction as given by the Erbs correlation

for hourly radiation and clearness index:

$$\frac{DHI}{GHI} = \begin{cases} 1 - 0.09K_t, & \text{if } K_t \leq 0.22 \\ 0.9511 - 0.1604K_t + 4.388K_t^2 - 16.638K_t^3 + 12.336K_t^4, & \text{for } 0.22 < K_t \leq 0.08 \\ 0.165, & \text{for } K_t > 0.8 \end{cases} \tag{1.14}$$

The main limitation of any empirical-based solar radiation model is that it is site-dependent. However, in most of the cases the overall equation of any of these models can be applied with revised coefficients and constants depending on the particular location.

1.4.2 Quasi-physical and physical models

The Direct Insolation Simulation Code (DISC) is a quasi-physical model developed by E. Maxwell [45]. It makes use of the global horizontal irradiance measurements, but also needs the sun zenith angle, day of the year, and the site's average atmospheric pressure as inputs for the estimation of the direct radiation. The algorithm uses physical principles for the improvement of the empirical relationship between the global and direct clearness indices. The DirInt model developed by Richard Perez is an improved version of the DISC model, based on binning the zenith angle, the global clearness index K_t, and dew point temperature in a way to have an indication of the sky condition. This method results in finding a coefficient from a four-dimensional look-up table to be used to improve the estimation of DNI by the DISC model. In the DirIndex model, the same approach as in DirInt is used but taking into account the atmospheric turbidity, which has a high influence on the beam irradiance [46].

Physical models are based on codes which model the transfer of solar radiation through the atmosphere. As mentioned before, solar radiation traversing the atmosphere is absorbed and scattered by the atmospheric constituents, which are highly variable in space and time. This makes it very complex to model the radiative transfer and requires various input parameters, each of them describing the atmospheric extinction sources in the path of the direct beam. The spectral distribution of the extraterrestrial direct beam radiation and the modification of its spectrum due to the wavelength dependence of the scattering and absorption processes, lead to a complex calculation of DNI. Spectral models span from the very complex 'line-by-line' models to the less complex spectral band models such as MODTRAN, and are mostly used in atmospheric sciences.

In most solar applications, physical models are based on the calculation of the physical extinction of radiation through the atmosphere by means of a broadband approach

starting with clear-sky models, which estimate the solar radiation on clear days, and then deriving the solar radiation in all weather conditions. In a study in 2003 [47], Gueymard cites twenty one basic clear-sky models that predict DNI for clear days using a broadband scheme. Apart from solar position geometry, which is common to all models, different atmospheric inputs are used depending on the model. These may include: local air pressure, precipitable water, ozone column, NO_2 abundance in the troposphere or in the stratosphere or the total NO_2 abundance, broadband aerosol optical depth, Ångström's turbidity coefficient, and the Ångström wavelength exponent. All these factors are translated into a total transmittance function, which affects the broadband extraterrestrial beam radiation, to give DNI:

$$DNI = DNI_0 \cdot T, \tag{1.15}$$

where T is the overall transmittance comprising the Rayleigh, ozone, water, aerosol, and mixed gas transmittances. The individual transmittances can instead be included in a multiplicative way, such as:

$$DNI = DNI_0 \cdot T_r \cdot T_a \cdot T_w \cdot T_o \cdot T_g \tag{1.16}$$

When the input parameters are correctly determined, clear-sky DNI can be estimated with 1% difference from measurements [48]. However, this is not always the case and input parameters are not always accurately specified, in particular aerosol transmission.

1.4.3 Artificial Neural Network models

Estimation of solar radiation is also possible using Artificial Neural Network (ANN) approaches. These are statistical-based models relying on machine learning. They consist of a set of processing units or 'neurons' connected together and forming a network. These units are trained with a number of inputs and outputs weighted by the connection strengths between the units, in order to approximate a non-linear relationship between them. After this machine learning process, and given a new set of inputs, the ANN can then predict the corresponding output. In the case of solar radiation modelling using the ANN technique and due to the direct correlation between the solar radiation and the atmospheric conditions, the meteorological parameters and atmospheric constituents are taken as inputs to the ANN model. These may include ambient temperature, relative humidity, sunshine hours, evaporation, wind speed, cloud cover, air molecules, water vapour, ozone, carbon dioxide, dust, etc. Several ANN-based models have been developed for the estimation of global horizontal radiation using ground-based meteorological

measurements as inputs [49, 50]. Satellite observations can also be used as ANN inputs for the estimation of the global [51] or the direct [52] solar radiation.

1.5 Satellite-derived solar data

Methods based on satellite observations represent an alternative for the estimation of solar radiation and are widely used [53, 54, 55]. Solar energy-based projects commonly use long-term satellite data in combination with high-quality short-term solar ground measurements for solar resource assessment purposes. According to Zelenka et al. [56], hourly irradiation data derived from satellites are considered the most accurate option for solar radiation prediction in locations at distances greater than 25 km from a ground station. Meteorological satellites scan the earth's surface, and based on the produced images it is possible to retrieve the solar radiation components at ground level with relatively high spatial and temporal resolution. For instance, the satellites of the Meteosat Second Generation (MSG) provide images of Europe, Africa and the North Atlantic since 2004, with a temporal resolution of 15 minutes and spatial resolution of approximately 1 $km \times 1$ km at sub-satellite point. Imagers on-board the satellite observe the earth in different spectral channels and provide information and data of the state of the atmosphere.

Several methods exist for deriving solar radiation from satellite observations. They can be divided into empirical or physical methods. The empirical methods consist of establishing relationships between satellite- and ground-based observations to give an (empirical) estimation of solar radiation. Physical methods use satellite information directly to determine the atmospheric properties, for the estimation of the surface solar radiation. Improvements in many aspects of the modelling processes have led to the derivation of solar radiation from satellite images using both empirical and physical information in a hybrid approach [57].

There are two types of meteorological satellites:

- Polar-orbiting weather satellites, thus called because by circling the earth they pass over the poles. They are located at low altitudes, around 850 km above the ground, offering higher resolution information. With the polar satellites, every location on earth can be observed twice each day. This low temporal resolution limits their operational use for the estimation of surface solar radiation. Several countries operate polar-orbiting meteorological satellites, such as NOAA by the United States and the European Metop-A and Metop-B satellites. Russia has the Meteor and Resurs series of satellites. Recently, the Advanced Very High Resolution Radiometer (AVHRR), on board the polar-orbiting NOAA and Metop satellites,

provides information several times a day, which allows the solar radiation estimation with higher confidence, as studied by Karlsson et al. in [58].

- Geostationary weather satellites are suspended at the same place above the equator at an altitude of about 36000 km. Since they orbit the earth in the same direction and speed as the earth's rotation, they remain stationary as viewed from the earth's surface and thus provide continuous information of the entire hemisphere seen by the satellite. Several geostationary meteorological satellites are in operation covering the whole world except the poles and include the United States Geostationary Operational Environmental System (GOES), the European Meteosat Missions, the Indian INSAT, the Japanese MTSAT, the Russian new-generation weather satellite Elektro-L1, and the Chinese Feng-Yun geostationary satellites. In general, geostationary satellites are the most used for the derivation of solar radiation data due to the high temporal resolution that they can offer.

The basis of satellite-based methods is the equation of energy conservation, taking into account the interaction of the extraterrestrial radiation with the atmospheric constituents before reaching the earth's surface. When the solar radiation traverses the atmosphere, it is partly reflected back to space and partly absorbed by the atmosphere. The remaining part which reaches the ground is partly absorbed by the earth's surface and partly reflected back (affected again by atmospheric diffusion and absorption) to space as the surface albedo. The satellite sensor measures the radiation backscattered by the earth-atmosphere system. Following this energy conservation scheme and by knowing the absorbed energy and the surface albedo, the solar radiation on the earth's surface can be derived. The extraterrestrial radiation is retrieved by astronomical equations and the reflected radiation is measured by the satellite radiometers. For more details on the expression of energy conservation for the derivation of solar radiation at the earth's surface, see [59].

In the following, one renowned method, Heliosat, is briefly described in order to give an overview on the derivation of solar radiation from satellite observations. Heliosat is developed and continuously improved by the Centre for Energy and Processes, École des Mines de Paris/Armines, France. Originally, the model was developed by Cano et al. [53], and has been followed by different versions for model improvement. The original concept consists of statistically determining the global solar irradiance from the amount of cloud cover over a given area and time. This includes the derivation of a cloud cover index n for each pixel of the original satellite image, as follows:

$$n = \frac{\rho - \rho_g}{\rho_c - \rho_g}, \tag{1.17}$$

where ρ is the albedo measured by the satellite, ρ_c is the cloud albedo of a heavily overcast sky, and ρ_g is the ground albedo, associated to a clear, clean and dry sky. The cloud cover index ranges from 0 to 1.

The first version, Heliosat-1, as defined by Diabate et al. [60], considers a linear correlation between the cloud cover index n and the instantaneous clearness index K_t:

$$K_t = an + b, \tag{1.18}$$

where a and b are empirical parameters. Heliosat-1 uses numerical counts of the satellite images for the calculation of the albedos, so that ρ is measured by the digital counts of the sensor, ρ_c represents the maximum count, and ρ_g represents the minimum count. The Heliosat-2 version uses calibrated radiances instead of the digital counts and considers atmospheric extinction and cloud extinction separately. The clear-sky solar irradiance is derived from the European Solar Radiation Atlas (ESRA) model [61], taking the Linke turbidity as input parameter; the Linke turbidity factor being the number of clear and dry atmospheres needed to give the optical thickness of the atmosphere due to both the absorption by the water vapour and absorption and scattering by the aerosol particles.

The Heliosat-3 version is based on a radiative transfer code, the SOLIS model scheme. It uses as inputs the atmospheric parameters information (clouds, ozone, and water vapour, and aerosols) derived from the Second Generation of the Meteosat satellite databases MSG or other platforms.

Heliosat-4 is the newest version of the Heliosat method, created by MINES ParisTech and the German Aerospace Centre DLR (Deutsches Zentrum für Luft- und Raumfahrt). It is based on a fully physical model using an approximation of the libRadtran radiative transfer model. It is composed of the McClear model for clear-sky irradiances and the McCloud model for calculating the extinction of irradiance due to clouds. Inputs to Heliosat-4 are atmospheric products derived from the MACC database, ground albedo derived from the MODIS data, and cloud properties derived from images of the Meteosat satellites. For more information on the Heliosat-4 method, see [62].

Direct and diffuse irradiances are in general derived from the satellite-derived global irradiance by using the separation or decomposition models as discussed in Section 1.4.1. However, there are other methods to derive the direct normal irradiance directly from the satellite images. These methods are usually based on a clear sky model where DNI under clear-sky conditions follows Equation 1.16. DNI for cloudy conditions is estimated by multiplying DNI_{clear} by a transmission coefficient of clouds. The transmittances for the attenuation by gases, ozone, water vapour and aerosols, are determined from different meteorological satellites or other sources. The transmission coefficient of clouds

is function of a cloud index derived from the infrared (IR) and visible (VIS) channels of the Meteosat satellite images, see for instance the Solar Energy Mining (SOLEMI) method of DLR [63].

In all cases, the estimation of solar radiation from satellite images should be validated and calibrated with high-quality ground data covering different time periods and ground areas. Statistical parameters like MBE (mean bias error) and RMSE (root mean square error) are used to quantify the accuracy of the assessment of the satellite models. In [59], a table summarising the results of the accuracy of the satellite models in terms of MBE and RMSE from several studies, shows that the RMSE of the global hourly radiation lies between 17–25%, and between 10–15% for the daily estimations. Larger errors are found for DNI, due to the high dynamicity of this component. Task 36 of Solar Heating and Cooling – International Energy Agency [64] proposes a standardisation of procedures for benchmarking and ways to improve the quality of satellite estimations. Several web-based services and databases offering solar radiation information from satellite observations are currently available, either from commercial providers [65, 66, 67, 68, 69], or for free [70, 71]. For more details on different satellite models available, see the NREL Best Practices Handbook [72].

1.6 Solar radiation as renewable source of energy

The clean and plentiful resource of solar energy can be gathered with solar collectors and converted into another form of energy such as heat or electricity. This can be possible through passive solar techniques and measures to trap and store the solar radiation, such as effective spaces design, building orientation towards the sun and selection of materials with good thermal properties, but also through active solar techniques using solar energy conversion systems. Solar photovoltaic (PV) and concentrating photovoltaics (CPV) directly convert solar energy into electricity, while Concentrating Solar Power (CSP) systems convert the solar energy into heat, then the heat is transformed into electricity.

The conversion of solar energy to electricity by using PV devices is based on the photoelectric effect: the direct creation of an electric current in a semiconductor material upon exposure to light. The smallest unit of a PV system is a cell. Cells are wired together to produce PV modules, and modules are assembled together to form a panel. A group of panels creates an array, and a group of arrays forms the array field of a PV facility. The chain is illustrated in Figure 1.14.

PV cells are made of thin layers of positive- and negative-type semiconductors, forming a p-n junction and creating an electric field. A typical silicon PV cell is composed of an

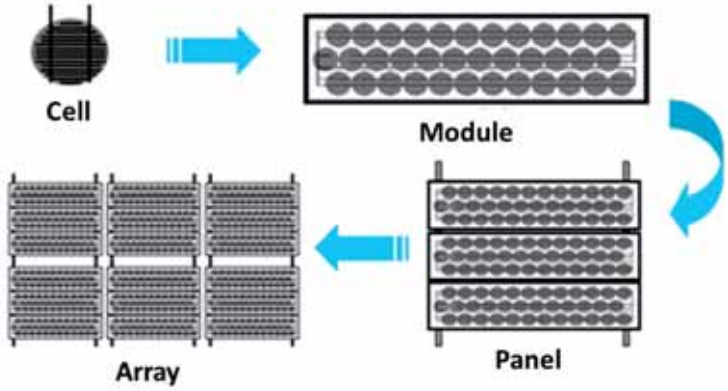

Figure 1.14: From PV solar cell to PV solar arrays. Image credit: Florida Solar Energy Center website.

ultra-thin layer of phosphorus-doped (n-type) silicon on top of a thicker layer of boron-doped (p-type) silicon. The n-type layer contains a surplus of free electrons while the p-type layer has positive charged particles, or 'holes', caused by a deficit of free electrons. An electric field is created between these two layered semiconductors, near the top surface of the cell, the p-n junction. When sunlight strikes the surface of the cell, the energy absorbed from the sunlight causes the electrons of the atoms of the cell to become free and travel randomly. These free electrons, guided by the existing electric field of the p-n junction, generate a higher flow of electric field, which results in a current when the solar cell is connected to an external electrical load.

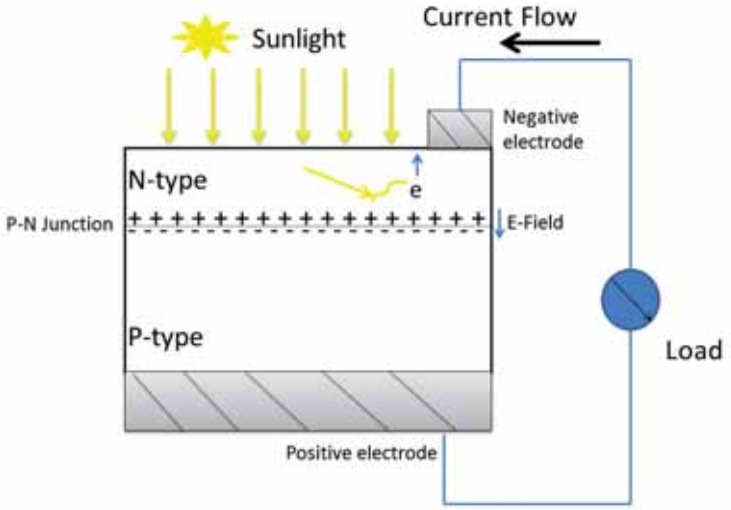

Figure 1.15: Principle of operation of a PV solar cell.

Many factors affect the amount of current generated by a PV cell, such as its efficiency,

its size and the intensity of the incident solar radiation. The most common type of materials used for PV cells are semi-conductor crystalline silicon and quartz. Other materials, manufactured in thin films and incorporated into modules, include amorphous silicon, cadmium telluride or copper indium di-selenide. Typically, silicon modules have efficiencies of $\sim$ 12–16%, while thin-film modules have efficiencies of $\sim$ 9–13%, depending on the technology [73].

Similarly to the conventional PV systems, CPV also uses the photovoltaic effect to directly convert sunlight into electricity, except that they make use of lenses and mirrors to concentrate the direct solar radiation onto a smaller area of multi-junction solar cells, thus increasing the efficiency level to about 40%. CPV uses solar trackers to automatically follow the sun. For more information on CPV systems, see [74].

Solar thermal collectors, on the other hand, receive the solar radiation from the sun and convert it into heat which can be used for many purposes such as water heating, space heating and cooling, and heating fluids to high temperature. The solar collectors can be either concentrating or non-concentrating.

The most common type of non-concentrating collectors are flat-plate collectors and operate at low and medium temperatures. They are usually employed for swimming pool heating or heating water or air for residential and commercial use. A common design of a flat-plate collector is illustrated in Figure 1.16 and consists of an absorber that intercepts and absorbs the solar energy, a transparent cover to reduce heat loss from the absorber, and a heat-transfer fluid (air or water) circulating through tubes to transfer the heat from the absorber to a heat-insulating backing.

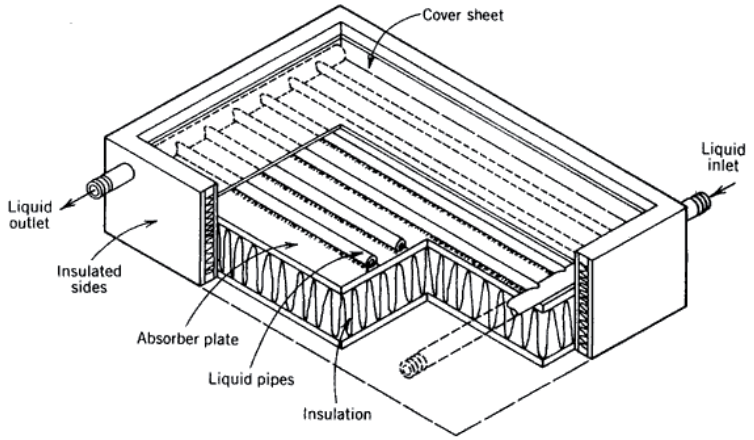

Figure 1.16: A liquid flat-plate collector [75].

Concentrating collectors are high-temperature collectors which concentrate sunlight using mirrors or lenses. They are generally used to heat a fluid to produce steam and operate a turbine for electricity generation in solar thermal power plants. The heat is

converted into mechanical energy as it is transferred from the fluid to water to produce steam, which drives a turbine to generate electricity through a conventional generator coupled to the turbine. CSP plants have the advantage that they can be equipped with a heat storage system, which allows the supply of heat and electricity at night or under cloudy skies. The four main types of concentrator systems for solar thermal power plants are: Parabolic Trough, Fresnel Reflector, Solar Tower and Solar Dish, see Figure 1.17.

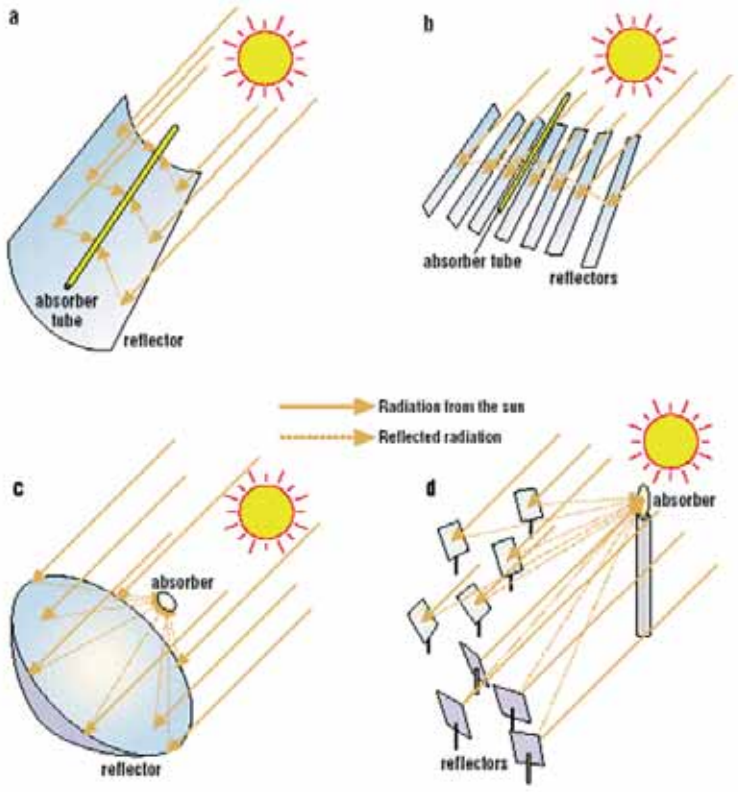

Figure 1.17: Concentration of sunlight using (a) parabolic trough collector, (b) linear Fresnel collector, (c) central receiver system with dish collector, and (d) central receiver system with distributed reflectors [76].

Each type has its own design in terms of mirror and receiver configuration, type of heat transfer fluid used and whether or not the system involves heat storage. For Parabolic Trough and Fresnel Reflector, the maximum achievable temperature is about 550 $°C$, since the mirrors concentrate the sun's rays on a focal line. For the Solar Tower and Solar Dish, sunlight is concentrated on a single focal point, which can reach higher operating temperatures (800–1000 $°C$). The Parabolic Trough system is currently the most commercially mature technology according to [77].

Chapter 2

Atmospheric Properties and Lidar Techniques

This chapter provides basic information on the atmospheric structure and properties. The atmospheric boundary layer (ABL), the lowest part of the troposphere, is described in more detail. Aerosols and their influence on the earth's radiation budget are discussed. A short description of the interaction of light with atmospheric constituents is given, including the theories of scattering of light by molecules and particles: the Rayleigh and Mie theories. Finally, since lidar has been proven to be an effective tool for profiling the atmosphere and detecting aerosol layers, this chapter gives also an overview about the lidar technique, with an expanded description of the elastic backscatter lidar.

2.1 Atmospheric structure

The earth's atmosphere is a relatively thin layer of gases that surrounds the earth. The mass of the atmosphere is around 5×10^{18} kg, and 99% of this mass is within the first 30 km from the earth's surface. In the atmosphere, both pressure and density decrease with height. Temperature has, however, a varying profile; it may decrease, increase or remain relatively constant with height, dividing the atmosphere into five main layers. The troposphere is the lowest and major part of the atmosphere, since it contains up to 75% of the mass of the atmosphere, and most of the atmospheric aerosols and water vapour. Within it, day-to-day weather phenomena occur and molecules and particulates are well mixed. This layer extends from the earth's surface up to about 10 km in mid-latitudes and to about 15 km at the equator. Within this layer, temperature decreases with height at a constant rate. The lowest part of the troposphere is the Atmospheric Boundary Layer (ABL), also called the planetary boundary layer (PBL), or sometimes simply boundary

layer (BL), where most of the human activities take place. This sublayer will be further described in Section 2.1.2. The stratosphere starts at around 10–15 km, reaching 50 km above the surface (at mid-latitudes) and containing the ozone layer. It is a stable and stratified layer where the temperature increases with increasing altitude. This is due to the absorption of ultraviolet (UV) solar radiation by the ozone layer. Molecules dominate in this layer; however, in the lower part of the stratosphere, particulates can also be present mainly from aircraft engine exhaust or volcanic eruptions. In the middle of the atmosphere, is the mesosphere, where the air is thin and the temperature decreases with altitude due to little absorption of solar energy at this level. A high concentration of ions is present at the upper level of this layer. Above the mesosphere lays the thermosphere, from around 80 km up to 400 km, where a significant temperature inversion is observed. It is a relatively warm layer because of the presence of oxygen, which absorbs the UV energy from the sun. The exosphere is the top layer of the atmosphere and the farthest away from the surface. It extends from approximately 500 km to about 1000 km, but it doesn't have clear boundaries, i.e., lower and upper limits. Molecule concentrations in this layer are small, so they do not collide with each other, and can escape to outer space. These various atmospheric layers are depicted schematically in Figure 2.1.

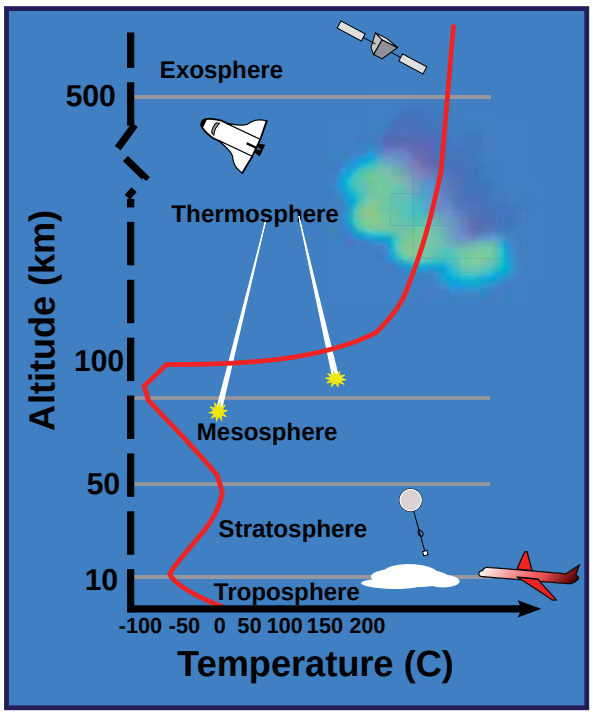

Figure 2.1: The major layers within the atmosphere, based on the vertical distribution and variations of the temperature (red line) in the atmosphere.

2.1.1 Composition of the atmosphere

The composition of the atmosphere can be divided into a 'clean dry' component, water vapour, and aerosols. Table 2.1 lists the major gaseous components of the atmosphere with their proportions. As shown, the atmosphere is mainly composed of nitrogen (N_2, 78% by volume), oxygen (O_2, 21% by volume), and argon (Ar, 1% by volume). The remaining components, although present in small amounts, play an important role in the earth's energy balance through the different radiative processes and their efficiency in trapping the solar radiation. These gases are called greenhouse gases and the most important are carbon dioxide and ozone. Water vapour is also an important greenhouse gas; it accounts for roughly 0.25% of the atmospheric mass and its concentration in the atmosphere is highly variable among different regions. Aerosols account for only a minute fraction of the mass of the atmosphere. Yet, they have a high influence on the energy balance of the earth, and affect the hydrological cycle and the abundance of greenhouse and reactive trace gases.

Constituent	Molecular weight [g/mol]	Fractional concentration by volume
Nitrogen (N_2)	28.013	78.08%
Oxygen (O_2)	32.000	20.95%
Argon (Ar)	39.95	0.93%
Water vapour (H_2O)*	18.02	0–5%
Carbon dioxide (CO_2)*	44.01	380 ppm
Neon (Ne)	20.18	18 ppm
Helium (He)	4	5 ppm
Methane (CH_4)*	16.04	1.75 ppm
Krypton (Kr)	83.80	1 ppm
Hydrogen (H_2)	2.02	0.5 ppm
Nitrous oxide (N_2O)*	56.03	0.3 ppm
Ozone (O_3)*	48	0–0.1 ppm

Table 2.1: Major gaseous constituents of the earth's atmosphere, up to an altitude of 105 km, with respect to dry air [78].

* The so-called greenhouse gases.

2.1.2 Atmospheric boundary layer

As seen in Section 2.1, the troposphere extends from the ground up to an average of 10 to 15 km. The atmospheric or planetary boundary layer is the lowest part of the troposphere, where human and other living organisms are present and where almost all of the energy, water vapour and aerosols are created and transported to the upper atmosphere. Stull [79] defines the boundary layer as "that part of the atmosphere that is directly influenced by the presence of the earth's surface, and responds to surface forcings with a timescale of about an hour or less". Kaimal and Finnigan [80] describe this layer as the "lowest 1–2 km of the atmosphere, the region most directly influenced by the exchange of momentum, heat, and water vapour at the earth's surface". The ABL is influenced by the earth's surface through several forcings like friction, pollutant emissions and heat and cooling fluxes on the ground. Depending on the forcing, the ABL depth can range from hundreds to even several thousand metres from the surface level [81]. Moreover, the depth of the ABL is influenced by the location, topographical features on the ground, season, time of the day and weather. The top of the ABL shows a sharp increase in temperature and drop in the concentration of particulates and water vapour. It is separated from the 'free atmosphere' above it by the capping inversion, a stable layer of warm air above cool air, that prevents convection and dynamic liftings, trapping pollutants in the ABL. Being influenced by the solar heating, the ABL height varies during one day and several sublayers are found within it:

Surface layer is the layer closest to the surface; its height ranges from 50 to 100 m, about 10% of the ABL height. The surface layer is characterised by large gradients of atmospheric properties: temperature, moisture, wind speed and trace gas concentrations.

Convective boundary layer, also called the mixing layer, is the layer where particles are well mixed due to surface-air interaction in mechanical and thermal forms. After sunrise, solar heating causes thermals of warm air to rise upwards until their temperatures drop to the same temperature of the surrounding air.

Residual layer is the layer of particles being left from the previous convective layer after sunset or from long-range transportation of winds.

The study of the diurnal variation of the ABL plays a crucial role in the determination of atmospheric pollutants' dispersion pathways and their chemical properties. At night, a more stable layer grows and forms the nocturnal boundary layer around sunset, in which mixing is caused by wind friction. The highest stable nocturnal boundary layer is less

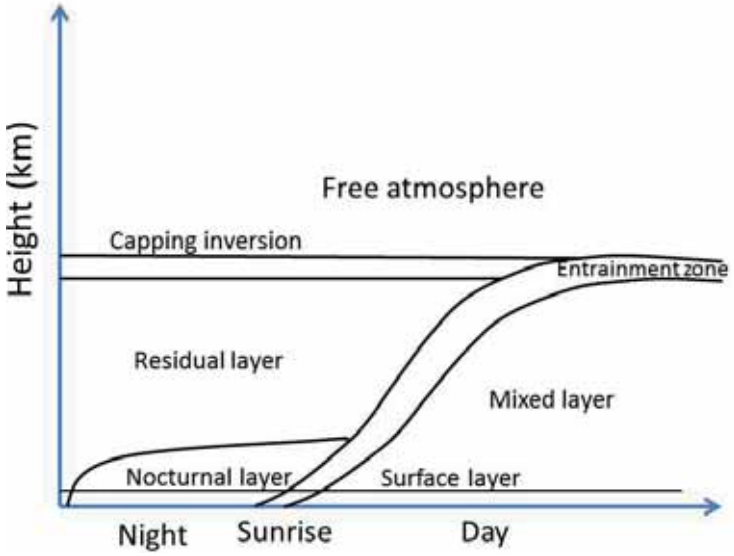

Figure 2.2: Diurnal evolution of the atmospheric boundary layer.

than 400 to 500 m in height, see [82]. Absence of convection during the night creates vertical stratification. Figure 2.2 shows the typical evolution of the atmospheric boundary layer. Examples of the formation of these layers and their evolution with time during a day are given in Figure 4.7, discussed in Chapter 4. The figure shows the formation and evolution of the boundary layer and other layers in the atmosphere for several days, as acquired by the Lidar-ceilometer installed at the QEERI facility in Doha, Qatar.

2.1.3 Aerosols in the troposphere

Atmospheric aerosols play an important role in the atmospheric radiative transfer. They have large influence on climate change and the earth's radiation budget [83], despite being only a minor constituent of the atmosphere, as discussed in Section 2.1.1. An aerosol is defined in its simplest form as a collection of solid or liquid particles suspended in a gas [84]. Atmospheric aerosols are a complex and dynamic mixture of solid and liquid particles originating from natural and anthropogenic sources as primary emissions, i.e., introduced directly into the atmosphere, or secondary, i.e., formed in the atmosphere through chemical reactions. This includes a wide range of phenomena such as dust, fume, smoke, mist, fog, haze and clouds. Aerosols exhibit large diversity in terms of their properties. Depending on the sources and the meteorological processes, aerosols vary in shape, chemical composition, lifetime, transformation and removal mechanisms, physical and optical properties.

Various distributions have been used to fit the aerosol size distribution, such as the

power law, the modified gamma and the log-normal distributions [85]. Their sizes can cover a wide range, from few nanometres to tens of micrometres. Particles of diameter $d < 2.5\ \mu m$ are considered in the fine mode. Particles of diameter $d > 2.5\ \mu m$ represent the coarse mode. Fine mode is divided into the nuclei mode ($0.005\ \mu m < d < 0.1\ \mu m$) and accumulation mode ($0.1\ \mu m < d < 2.5\ \mu m$). Although this classification is important, there is no strict scientific classification of aerosols; they can be also classified based on their physical form and method of generation. In climate models, for instance, aerosols are subdivided into different types based on the properties of their components. Components may include soil particles, sulphates and nitrates, soot, sea-salt particles, desert dust and sulphate droplets. Table 2.2 shows the different types of aerosols along with their properties which represent average conditions, as detailed in [86]. N is the number concentration, r_{eff} is the effective radius describing the mean size of the particle ensemble, ssa is the single-scattering albedo defined as the ratio of total scattering to extinction of the particle, g is the asymmetry parameter, which is a measure of the light scattered toward the forward direction compared to the light scattered toward the back direction, and å is the Ångström exponent describing the spectral slope of the optical coefficients.

Aerosol type	N cm^{-3}	r_{eff} μm	ssa 0.55 μm	g 0.55 μm	å 0.35–0.55 μm	å 0.55–0.8 μm
Cont. clean	2600	0.247	0.972	0.709	1.10	1.42
Cont. average	15,300	0.204	0.925	0.703	1.11	1.42
Cont. polluted	50,000	0.150	0.892	0.698	1.13	1.45
Urban	158,000	0.139	0.817	0.689	1.14	0.43
Desert	2300	1.488	0.888	0.729	0.20	0.17
Marit. clean	1520	0.445	0.997	0.772	0.12	0.08
Marit. polluted	9000	0.252	0.975	0.756	0.41	0.35
Marit. tropical	600	0.479	0.998	0.774	0.07	0.04
Arctic	6600	0.120	0.887	0.721	0.85	0.89
Antarctic	43	0.260	1.000	0.784	0.34	0.73
Stratosphere	3	0.243	1.000	0.784	0.74	1.14

Table 2.2: Aerosol types and their properties.

Aerosol properties change in time and alter the chemical composition of the atmosphere. Their impact on climate change is noticeable through the variability of the global annual air surface temperature [87]. Aerosols interact with the climate system in

many ways, including the direct effect where they interfere with incoming and outgoing radiation by scattering and absorption processes, the semi-direct effect where aerosols potentially impact cloud formation, and the indirect effect by changing the microphysical structure of clouds within the atmosphere. These effects are quantified in terms of aerosol radiative forcing (ARF), defined as the difference between atmospheric radiative fluxes when aerosols are present and when aerosols are absent. The direct ARF, which is of interest for this study, can be derived through models based on the optical properties, the size distribution and the atmospheric concentration of aerosols [88, 89]. However, these estimates are not of high confidence due to large uncertainties in the determination of the spatial and temporal distribution, as well as of the optical properties, of aerosols in the vertical air-column. Satellite observations are also used to estimate the ARF using modern instruments such as the MODerate resolution Imaging Spectroradiometer (MODIS), the Multi-angle Imaging SpectroRadiometer (MISR) or the Clouds and the Earth's Radiant Energy System (CERES). All these methods have been applied for the estimation of the aerosol radiative forcing of both natural and anthropogenic aerosols in [90, 91], for example.

The main optical parameter used to characterise the interaction of aerosols with radiation is the aerosol optical depth (AOD, τ), defined as the magnitude of solar radiation extinction by aerosols, integrated in the vertical column. Another quantity used to describe how aerosols influence the radiative balance is the single-scattering albedo, which describes the capability of aerosols to absorb radiation. Aerosol optical parameters can be determined using lidar observations. Lidar-measurement techniques have been widely investigated for the characterisation of the temporal and spatial distribution of aerosols affecting the optical characteristics of the atmosphere [92, 93]. This thesis work is based on the use of a lidar-ceilometer device for the derivation of aerosol backscatter profiles; backscatter measurements are then used for a correlation study with solar radiation measurements.

2.2 Propagation of light in the atmosphere

In a turbid atmosphere, the constituents of the atmosphere (particles and molecules) contribute to the extinction of light energy from a beam through the following processes:

- Scattering by atmospheric molecules such as oxygen and nitrogen.
- Scattering and absorption by particles in the atmosphere such as dust, mist and water droplets.

- Absorption by molecules such as ozone, carbon dioxide or water vapour.

To quantify these effects, some simplifications are necessary. When a narrow parallel incident beam of light with a radiant flux $I_{0,\lambda}$ (radiant energy per unit time) passes through a turbid layer of a geometric thickness H, the resulting radiant flux I_λ decreases depending on the optical transparency of the the layer H given by its transmittance $T(H)$:

$$T(H) = \frac{I_\lambda}{I_{0,\lambda}} \tag{2.1}$$

$T(H)$ represents a measure of the turbidity of the layer H and ranges from 0 for a totally absorbing medium to 1 where no absorption or scattering occurs when the light beam passes through the layer. In a heterogeneous medium, the transmittance is given by:

$$T(H) = \exp\left[-\int_0^H \alpha(r,\lambda)dr\right], \tag{2.2}$$

and the total extinction of the collimated beam, referred to as the Beer-Lambert law, is

$$I_\lambda = I_{0,\lambda} \cdot \exp\left[-\int_0^H \alpha(r,\lambda)dr\right], \tag{2.3}$$

where $\alpha(r,\lambda)$ is defined as the probability of a photon to be scattered or absorbed, and thus represents the extinction coefficient of the medium. The integral of $\alpha(r,\lambda)$ over the thickness H constitutes the optical depth of the layer and determines how much light is removed from the beam after it passes the layer H:

$$\tau = \int_0^H \alpha(r,\lambda)dr \tag{2.4}$$

The extinction coefficient α is the sum of the scattering and absorption coefficients by both molecules (subscript m) and particles (subscript p):

$$\alpha(r,\lambda) = \alpha_m(r,\lambda) + \alpha_p(r,\lambda) \tag{2.5}$$

For a number N_p of particles having the same size, with A being the geometric cross section area of one particle, the extinction coefficient can be written as:

$$\alpha(r,\lambda) = N_p Q_{ext} A, \tag{2.6}$$

where Q_{ext} is the extinction efficiency defined as the ratio of the total energy flux attenuated by a particle to the total energy flux incident on the particle.

The extinction of light in the atmosphere is not as straightforward as the explanations given above. However, it is sufficient to understand the transmission and backscatter terms that are part of the lidar equation (Section 2.3.2), and to understand the processes behind the interaction of the lidar laser light and the solar radiation with the atmospheric components. For more detailed and complete information on the subject, [94, 95] can be consulted. This thesis work is focused on elastic lidar techniques, which involve radiation elastically scattered from atoms or molecules with no change of light wavelength. Therefore, the following discussion about scattering will cover mainly elastic scattering processes, with a brief explanation of absorption and inelastic processes.

2.2.1 Elastic scattering

Photon scattering is a process in which incident electromagnetic radiation interacts with the electric field of a scattering particle. If the interaction is elastic, the particle considered as point source re-emits a fraction of the incident light in all directions, with the same wavelength of the incoming light. Atmospheric scattering of light by molecules and particles is mostly elastic; the contributions of processes such as fluorescence or inelastic (Raman) scattering are small.

The scattering depends on the difference of the refractive index of the scatterer and that of the surrounding medium. The index of refraction m is a complex number represented by:

$$m = n - ik \tag{2.7}$$

The real part n of the refraction index is related to the scattering properties and describes the velocity change of electromagnetic waves in a medium relatively to vacuum. The imaginary part k is related to absorption properties of particles and molecules.

In addition, the amount of scattered energy depends strongly on the relation between the size of the particle and the wavelength of the radiation, more precisely the ratio of particle size to the wavelength of the incident light. This ratio is represented by the so-called 'size parameter'. For instance, for a spherical particle, the size parameter is defined as the ratio of the particle circumference to the incident wavelength:

$$\phi = 2\pi\rho/\lambda, \tag{2.8}$$

where ρ is the particle radius. It should be noted that the size parameter is well-defined for spherical particles but, in general, particles can have very irregular shapes. However,

using this parameter gives a rough idea of how the particle size and the wavelength compare. Based on the size parameter, three regimes are considered:

- If $\phi \ll 1$, the scattering is referred to as Rayleigh scattering, for which there is a simple theory that will be further discussed below. The particle is much smaller than the wavelength. This is the case of the scattering of visible light ($0.4-0.7\ \mu m$) by atmospheric molecules.
- If $\phi \sim 1$, i.e., particle sizes are comparable or similar to the light wavelength, the process is referred to as Lorenz-Mie scattering, which applies to scattering from spherical particles. This regime is very complex and requires the solution of the Maxwell equations. The Mie theory includes also the solution of the Rayleigh scattering.
- If $\phi \gg 1$, i.e., particle sizes are much larger than the wavelength of light, the scattering can be regarded in the geometric optics regime. The scattering process is still complex because of reflection on the surface and refraction in the interior but it can be calculated using for instance the ray tracing method, which relies on approximate solutions to Maxwell's equations.

Scattering involves the dispersion of the light beam in all directions. The intensity of the directional scattering is function of the angle between the incident light beam direction and the scattering direction. To describe the angular distribution of scattered energy, the phase function P_θ is defined as the ratio of the energy scattered in the direction θ to the total scattered energy in all directions. In general, if a narrow light beam of wavelength λ of a spectral irradiance E_λ encounters a differential volume of a scatterer and is scattered in the direction θ, the radiant spectral intensity of the scattered light $I_{\theta,\lambda}$ can be written as:

$$I_{\theta,\lambda} = \beta_{\theta,\lambda} E_\lambda, \tag{2.9}$$

where $\beta_{\theta,\lambda}$ is a directional scattering coefficient for the direction θ relative to the direction of the incident light. The total volume scattering coefficient β is obtained by integrating over all solid angles (4π) and the phase function per unit volume can thus be written as:

$$P_\theta = \frac{\beta_\theta}{\beta} \tag{2.10}$$

The phase function determines the probability of scattering into a specific direction; it will be shown that small particles scatter almost equally in both forward and backward directions. For particles of larger sizes, more energy is scattered in the forward direction,

and secondary maxima and minima appear at different scattering angles. For more in-depth understanding of the scattering theory of photons with matter, the reader is referred to [94, 96, 95].

Rayleigh scattering

Atmospheric Rayleigh scattering is always attributed to molecules. Particles that are very small in size relatively to the wavelength of the incident radiation, i.e., atmospheric molecules of the order of Ångström, usually oxygen and nitrogen, scatter more effectively at shorter wavelengths and the intensity is the same for both forward and backward directions. As discussed above, the molecular angular scattering coefficient $\beta(\theta, \lambda)_m$ describes the amount of light at a wavelength λ which is scattered in a given direction θ. For Rayleigh scattering, this is given by:

$$\beta(\theta, \lambda)_m = \frac{\pi^2(n^2-1)^2 N}{2N_s^2\lambda^4}(1+\cos^2\theta), \tag{2.11}$$

where θ is the angular direction relative to the direction of the incident light, n is the real part of the refractive index, N is the number density (number of molecules per unit volume) at the existing pressure and temperature, N_s is the number density of molecules at standard conditions, and λ the wavelength of light. As can be seen in this angular scattering coefficient, the Rayleigh-scattered intensity (see Equation 2.9) varies inversely as the fourth power of wavelength, that is, as λ^{-4}. This means that shorter wavelengths are more effectively scattered than longer wavelengths.

By integrating over the total solid angle 4π, the total Rayleigh molecular volume scattering coefficient β, which defines the total intensity of light removed from an incident light beam after scattering, can be derived from Equation 2.11, giving:

$$\beta_m = \frac{8\pi^3(n^2-1)^2 N}{3N_s^2\lambda^4} \tag{2.12}$$

With Equations 2.11 and 2.12, the molecular phase function P_θ (cf. Equation 2.10) is then:

$$P_\theta = \frac{3}{16\pi}(1+\cos^2\theta) \tag{2.13}$$

Based on the symmetry of this phase function, the amount of light scattered in the forward direction is equal to the amount scattered in the backward direction, see Figure 2.3.

The molecular cross section σ_m, which specifies the amount of scattering due to a single molecule, can be derived from the molecular scattering coefficient β_m and the

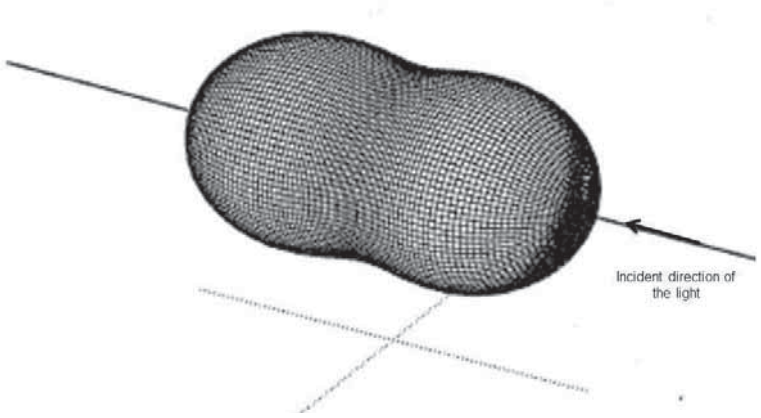

Figure 2.3: Angular dependency of Rayleigh scattering, showing that forward- and back-scattering intensities are twice as high as those of directions perpendicular to the incident radiation.

molecular density:

$$\sigma_m = \frac{\beta_m}{N} \tag{2.14}$$

Thus, the total molecular scattering cross section σ_m is given by:

$$\sigma_m = \frac{8\pi^3(n^2-1)^2}{3N_s^2\lambda^4} \tag{2.15}$$

Mie scattering

Rayleigh scattering describes only scattering processes for molecules and particles that are smaller in size compared to the wavelength of the incident light. Larger particles, such as haze or dust particles of the order of nanometres to micrometres, are comparable in size to the wavelength of the incident sunlight: the particle sizes may range from 0.1 to 10 times the wavelength of the incident radiation. In this case, the scattering process becomes practically independent of wavelength and the angular distribution of the scattered light becomes more complex. One of the first theories developed to provide an analytical solution to this type of interaction is the Mie scattering theory, proposed by Gustav Mie in 1908 [97]. The Mie theory assumes that the scatterer is a sphere characterised by a single index of refraction for a given wavelength and embedded in a homogeneous medium. It calculates the scattered electromagnetic field at all points within the particle (internal field) and at all points of the homogeneous medium in which the particle is embedded. Although this theory includes the solution of the Rayleigh scattering, it is normally only used to describe the scattering caused by particles with

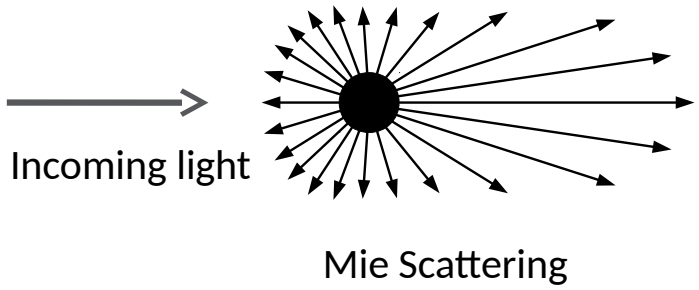

Figure 2.4: Example of the angular dependency of Mie scattering intensity, showing that forward-scattering is much more intense than back-scattering, with other peaks observed at different angles.

sizes similar to the wavelength of the radiation.

The total particulate scattering coefficient is the product of the particulate number density N_p and the single particle cross section σ_p, in analogy to molecular scattering:

$$\beta_p = N_p \sigma_p \tag{2.16}$$

By defining the scattering efficiency parameter, Q_{sc}, as the ratio of the particulate scattering cross section σ_p to the geometric cross sectional area of the scattering particle, i.e.,

$$Q_{sc} = \frac{\sigma_p}{\pi \rho^2}, \tag{2.17}$$

the total particulate scattering coefficient can be written as:

$$\beta_p = N_p \pi \rho^2 Q_{sc} \tag{2.18}$$

The factor Q_{sc} depends on the size parameter ϕ (Equation 2.8) and the index of refraction, and is given analytically for a spherical particulate by:

$$Q_{sc} = \frac{2}{\phi^2} \sum_{m=1}^{\infty} (2m+1) \left(|a_m|^2 + |b_m|^2 \right), \tag{2.19}$$

where a_m and b_m are coefficients of the amplitude functions of the scattered waves, obtained by applying boundary conditions. Figure 2.4 shows a sample scattering function of the Mie theory.

The Mie theory provides analytical solutions and calculates the scattering and absorption cross sections for homogeneous spherical particles of sizes comparable to the

wavelength of the incident light. However, this is only applicable to spherical particles and relatively simple shapes such as ellipsoids. For non-spherical particles, the T-matrix method is applied [98]. For complex-shaped particles, numerical methods are used to solve the Maxwell equations, such as the Discrete Dipole Approximation (DDA) method [99].

2.2.2 Inelastic scattering

While elastic scattering processes are predominant in the atmosphere, inelastic processes may also happen, in which the incident radiation interacts with the molecules of the atmosphere, resulting in scattered radiation shifted in frequency by an amount that is characteristic of each molecule. Inelastic scattering involves the excitation of the vibrational and rotational modes of a molecule. When the molecule deexcites, it emits photons with energy similar to its vibrational or rotational energy amplitudes, which is less than the incident energy. This effect, known as Raman scattering, is important for the application of Raman lidars, as will be discussed in Section 2.3.

2.2.3 Absorption

Absorption is another process that affects the propagation of light in the atmosphere; the absorbed energy is converted to another form of energy. This is translated into absorption bands in the electromagnetic spectrum, where each band constitutes a range of wavelengths within which the energy is absorbed by a specific constituent in the atmosphere: water vapour, carbon dioxide, oxygen, ozone and nitrous oxide. Absorption happens when incident radiation having the same resonant energy of an atom or molecule, is absorbed by the atom or molecule, producing an excited state. In this case, the energy is not reemitted with the same wavelength but is rather transformed into heat motion and consequently radiated at longer wavelengths. Infrared and other radiation of shorter wavelength than visible light are more affected by absorption processes than by scattering in the atmosphere.

2.3 Introduction to lidar

LIDAR, LIght Detection And Ranging, is an active remote-sensing and range-resolved measurement technique widely used to profile the atmosphere. Its operation consists of emitting laser pulses into the atmosphere and measuring the backscattered light. The

basic principle behind a lidar is to measure the time the light takes to return to the lidar, using the simple equation:

$$Distance = \frac{Speed\ of\ Light \times Time\ of\ Flight}{2} \tag{2.20}$$

The backscattered signal measured by the lidar provides as well certain properties of the atmosphere, as a function of time and distance from the device. This information is highly valuable for atmospheric research studies, specially given that atmospheric constituents such as aerosols and clouds are measured with high temporal and spatial resolution. Other atmospheric properties such as temperature, pressure, humidity or wind can also be determined. The application depends on how the lidar is set to measure the different interaction processes of the emitted light with the molecules and particulates in the atmosphere, thus classifying lidar techniques into different types.

The most common type of lidar is the elastic backscatter lidar, which basically consists of a short-pulsed laser light of single wavelength and a detector measuring the elastically (with the same wavelength) backscattered light from the atmospheric constituents. The information extracted from the elastic lidar measurements is normally the location of aerosols and clouds in the atmosphere. The elastic type of lidar is the one used in this work and will be described with more details in the next sections.

Another type of commonly used lidar is the Raman lidar, which usually emits one laser wavelength, but detects two or more wavelengths separately, since it makes use of the inelastic scattering processes of light by atmospheric molecules. The inelastic Raman scattering, as described in Section 2.2.2, involves the excitation of several rotational and vibrational molecular energy levels, resulting in a shift of the wavelength of the scattered light relative to the incident light. The amount of this shift in the Raman-scattered radiation is characteristic of the interacting molecules. This property allows to provide additional information about the constituents of the atmosphere, such as the detection of specific polluting gases or the remote sensing of the atmospheric water vapour component.

The same set of principles, discussed at length in Section 2.3.1, that explain the elastic lidar are valid for the Raman lidar, with the difference that a Raman lidar presents several detection channels; in general, one for the measurement of the water vapour, one for the nitrogen Raman signals and one for the elastic signal. Therefore, in order to sense the atmospheric gases that interact with the lidar's wavelength via the Raman scattering process, Raman lidars operate with a pulsed laser beam usually in the ultraviolet or near the ultraviolet wavelengths. Additional technical specifications are also required, such as a higher power of laser transmitter and a highly efficient receiving and detection system, since the Raman backscatter signals have low intensity. Figure 2.5 shows an

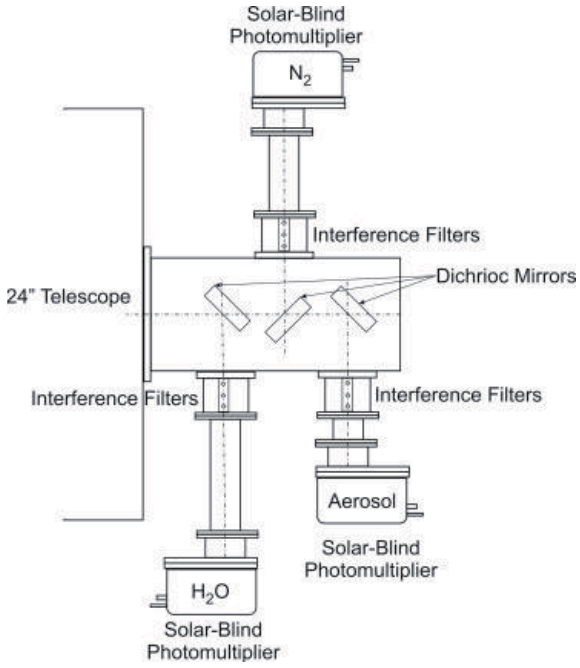

Figure 2.5: Schematic diagram of the optic system of a Raman lidar: beam splitters, filters, and lenses that separate the light at the back of the telescope [100].

example of the design of an optical analyser system typical of Raman lidars [100]. This diagram describes a Raman lidar installed at the Los Alamos National Laboratory. The beam splitters, filters, and lenses are located at the back of the telescope that collects the photons backscattered from the atmosphere. The beam splitters are used to separate three different wavelengths of the backscattered light: the elastically-scattered wavelength (248 nm), the nitrogen Raman-scattered wavelength (263 nm), and the water vapour Raman-scattered wavelength (273 nm). In each direction, interference filters are used to block undesired wavelengths and allow only the required wavelengths. Figure 2.6 shows the telescope used by the Barcelona IFAE-UAB team for the building of their Raman lidar. The system will be installed and operated at the Cherenkov Telescope Array (CTA) site, for better characterisation and monitoring of the atmospheric conditions above the experiment site.

The main drawback of the Raman lidar technique is that it involves the inelastic scattering with the atmospheric molecules, a process much less frequent than the elastic one in the atmosphere. This results in a small backscattered signal and requires the use of photon counting detection techniques in order to obtain signals at long ranges. In addition, it limits the use of Raman lidars during daytime due to the high background noise coming from the photons of the sun. The limited amount of the returned light

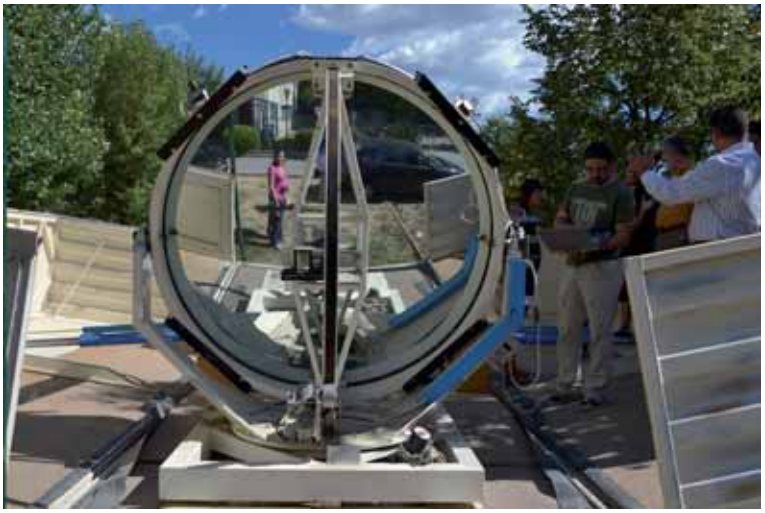

Figure 2.6: Photo of the telescope (parabolic solid-glass mirror of 1.8 m diameter) used by the Barcelona IFAE-UAB team to build their Raman lidar.

signal results also in the use of large telescopes and thus large lidar systems. Despite these limitations, Raman lidars are considered efficient systems for the estimation of atmospheric extinction.

Other types of lidar instruments are available, such as the differential-absorption lidar, known as DIAL, the Doppler lidar and the fluorescence lidar. With the DIAL type of lidar, the detection of a defined chemical constituent of the atmosphere is possible. DIAL lidars operate with two wavelengths in a way that one is more strongly absorbed than the other by the gas of interest. The concentration of the examined gas is determined from its differential absorption cross sections. Doppler lidar measures the wind speed along the lidar sightline by measuring the frequency shifts of the backscattered light. The fluorescence lidar senses layers in the upper atmosphere to detect resonance scattering of free metallic atoms and ions abundant in the upper layer.

Lidar-ceilometers are compact lidar systems based on the elastic backscatter lidar technique, and they are of particular interest for this work, to study atmospheric aerosols. Therefore, the next sections will focus on elastic lidar techniques and their principle of operation.

2.3.1 Basic principle of elastic lidar

Elastic backscatter lidars have proven to be effective tools for monitoring aerosol sources, transport and dilution as well as distribution and microphysical properties of clouds in the atmosphere [101, 102]. An elastic lidar-ceilometer system operates by emitting a laser

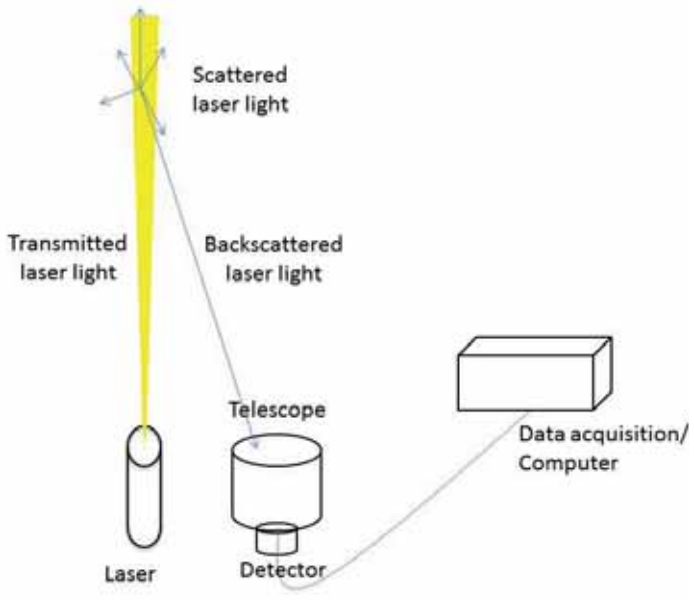

Figure 2.7: Schematic representation of a lidar system's working principle.

pulse upwards into the atmosphere. The emitted light interacts with the constituents of the atmosphere and is scattered in all directions. The lidar measures the elastically backscattered light, which is the light reflected backwards along its original path and has the same wavelength of the emitted laser pulse.

The system can be described by two major components: the transmitter and the receiver. It should be noted that these two basic components are common to all lidar systems discussed in Section 2.3, with difference in the configuration and the design of these components, depending on the application. Other devices are also part of a lidar system, as schematically illustrated in Figure 2.7. In the case of an elastic lidar, the transmitter consists of a laser source of short, strongly focused and monochromatic light pulses of one wavelength, to be sent in the vertical direction into the atmosphere. The receiver, where the backscatter signal is captured, consists of a telescope, an optical analysing system, a detector and a data acquisition system. The telescope collects the light backscattered from the atmosphere and directs it to the detection unit. The optical analysing system, depending on the application, transmits the light to the detector in a certain passband around the wavelength of interest and suppresses light outside this band. The detector transforms the received optical signal into an electrical signal. A data acquisition system digitises and processes the electrical signal; the intensity of the backscattered light is recorded as a function of distance from the lidar.

Depending on the application, each of the lidar elements can have different parameters and configurations, which set the resolution, range and characteristics of a lidar

system. For instance, the laser source can have one or more wavelengths usually ranging from about 250 nm to 11 μm, with specific spectral properties in terms of pulse width, mean power, spatial, and temporal characteristics; the length of the laser pulse sets the minimum range resolution of a lidar. The Nd:YAG laser type is widely used as a source of light in the lidar techniques; however, other types of laser can also be used, such as solid state lasers (ruby laser, 694.3 nm), gas lasers (CO_2, 9–11 μm) and semiconductor lasers (GaAs, 820 nm) [86]. Different types of refractive and reflective telescopes can be chosen but preferably the telescope should have a small field of view in order to limit the detection of multiple scattering and reduce background light from the atmosphere. Another design consideration is the geometric arrangement of the emitter and receiver optical axes relative to each other: either coaxial or biaxial; the chosen arrangement determines the minimum distance from which the backscatter signal can be fully detected. The commonly used photodetectors for recording the spectrally selected optical lidar signals are photomultiplier tubes (PMTs) or avalanche photodiodes (APDs). A photomultiplier tube is an electron tube composed of a photocathode, a series of dynodes, and an anode. When incident light hits the photosensitive material of the cathode, it causes the release of electrons as a consequence of the photoelectric effect. These electrons are attracted and accelerated towards a series of dynodes, where electrons are multiplied by the secondary emission process; the result is an amplified electrical current. On the other hand, an avalanche photodiode is a highly sensitive semiconductor, commonly made of silicon, with a p-n junction that also converts light to electricity through the photoelectric effect. It is operated at a high reverse-bias voltage so that charges are rapidly swept from the depletion region.

The methods used for processing the output signal can be divided into analogue and digital modes, depending on the intensity of the incident light and the bandwidth of the output processing circuit. The analogue mode uses direct, high-speed digitisation of the signal, which increases the near-field spatial resolution. This is useful for the ABL observations. The photon counting mode is used for longer range soundings. For more details, see [100].

All of the mentioned options and lidar design configurations are carefully chosen to pursue specific measurement tasks and ensure the required accuracy in the measurement of the atmospheric property of interest.

2.3.2 Lidar equation

To quantitatively describe the relation between the received range-resolved backscattered signal and atmospheric parameters, the common form of the single-scattering elastic

backscatter lidar equation takes into account the initial laser power, the efficiency and geometry of the lidar system, and atmospheric parameters including the light propagation in the atmosphere and the interaction processes. The fundamental equation of elastic lidar techniques is written as:

$$P(R,\lambda) = P_0(\lambda)\frac{c\tau_0}{2}A\eta\frac{O(R)}{R^2}\beta(R,\lambda)\exp\left[-2\int_0^R \alpha(r,\lambda)dr\right], \tag{2.21}$$

where $P(R,\lambda)$ is the detected power of the backscattered light received at time t from a distance $R = ct/2$ from the instrument, $P_0(\lambda)$ is the average power of the emitted laser pulse, c is the velocity of light, τ_0 is the temporal pulse duration, A is the area of the primary receiver optics responsible for the collection of backscattered light, η is the overall system efficiency, $O(R)$ is the overlap function between the laser beam and the receiver field of view, equal to 1 for a complete overlap, and $\beta(R,\lambda)$ and $\alpha(R,\lambda)$ are, respectively, the volume backscatter and attenuation coefficients of the atmosphere at wavelength λ, caused by aerosols and molecules.

Different signal inversion algorithms have been developed for solving the lidar equation. The main output is the retrieval of the range-resolved profile of the two aerosol optical parameters: backscatter and extinction. The principle of the inversion algorithm is based on the natural logarithm of the range-corrected signal, defined as

$$S(R) = \ln[R^2 \cdot P(R)] \tag{2.22}$$

The differential form of Equation 2.22 is:

$$\frac{dS}{dR} = \frac{1}{\beta}\frac{d\beta}{dR} - 2\alpha \tag{2.23}$$

To find a solution to the lidar equation, which has two unknown functions, it is usual to define or assume a functional relationship between β and α whenever $d\beta/dR \neq 0$; this relationship is called the lidar ratio, and is given by:

$$\frac{\alpha}{\beta} \tag{2.24}$$

Alternatively, if $d\beta/dR = 0$ for an assumption of a homogeneous atmosphere, the attenuation coefficient is directly derived from the slope of the signal $S(R)$, which is the basis of the slope method:

$$\alpha = -\frac{1}{2}\frac{dS}{dR} \tag{2.25}$$

Assuming that the atmosphere is homogeneous over short distances, the slope method can also be applied by using it consecutively to successive range intervals. In practice, and

under unstable sky conditions of dense cloud, fog, smoke, or dust, high fluctuations in the backscatter coefficient are observed and dominate the lidar signal so that the application of the slope method is not valid.

Under inhomogeneous atmospheric conditions, an empirical power law that relates β and α is assumed:

$$\beta = const \cdot \alpha^k, \tag{2.26}$$

where k depends on the lidar's wavelength and various properties of the aerosol. The reported values of k range generally between 0.67 and 1. By applying this relationship, Equation 2.23 becomes solvable:

$$\frac{dS}{dR} = \frac{k}{\alpha}\frac{d\alpha}{dR} - 2\alpha \tag{2.27}$$

The above differential equation, known as the Bernoulli equation, can be solved by introducing a new function as the inverse of α and by starting the integration from a reference range R_0 which is the near end ($R \geq R_0$). A well-known form of the solution, referred to as the forward integration method, may be obtained:

$$\alpha(R) = \frac{\exp\left(\dfrac{S(r) - S_0}{k}\right)}{\dfrac{1}{\alpha_0} - \dfrac{2}{k}\displaystyle\int_{R_0}^{R} \exp\left(\frac{S(r) - S_0}{k}\right) dr} \tag{2.28}$$

This solution (forward integration) tends to be numerically unstable. A restatement of the Bernoulli equation was introduced by Klett [103] in order to get a more reasonably stable solution for application on real data. The Klett method is based on a backward integration scheme which starts from a reference range R_m at the remote end ($R < R_m$) of the measuring range. The backward integration method leads to the solution:

$$\alpha(R) = \frac{\exp\left(\dfrac{S(r) - S_m}{k}\right)}{\dfrac{1}{\alpha_m} - \dfrac{2}{k}\displaystyle\int_{R}^{R_m} \exp\left(\frac{S(r) - S_m}{k}\right) dr} \tag{2.29}$$

Chapter 3

Solar energy in Qatar

This chapter provides an overview about Qatar's geographic location and climate. It also describes the steps that the country is undertaking in its transition towards the inclusion of renewable energy resources, solar in particular, in its energy production mix. What is of interest for this thesis work is the solar resource assessment in Qatar, which is addressed herein with examples of the existing solar maps and their corresponding data.

3.1 Background about Qatar

Qatar is a small peninsula located in an arid region, lying on the western coast of the Arabian Gulf, between the latitudes 24° and 27° N, and longitudes 50° and 52° E, with a total area of around 11500 km^2, extending about 160 km north-south, and an east-west width between 55 and 90 km. It is surrounded by the waters of the Arabian Gulf from all sides except for the south, where it shares borders with the Kingdom of Saudi Arabia. The island of Bahrain is 30 km away from the northwest coast of Qatar. The land is mostly flat with an approximate average altitude of 5 m above sea level and a highest altitude of 103 m. The terrain is sandy with barren land and scarce vegetation. The climate is of desert type with very hot and humid summers extending from April to September and mild winters from November to February with negligible precipitation. Heavy dust storms occasionally strike Qatar throughout the year, being in close proximity to the large desert area of Saudi Arabia, which is an extensive source of dust and sand in the Arabian Peninsula.

Being located in a strategic region of the world, one of the most energy-rich regions, Qatar has plentiful resources of oil and natural gas [104], and currently relies on burning those resources for electricity production. The main uses for electricity in the country are aimed to overcome the hot and humid environment and the scarcity of water, and include

an intensive use of air-conditioning, and tap/potable water production through sea-water desalination. Compared to other countries, Qatar has a high electric power consumption; for the year 2010, the electricity consumption per capita in Qatar was 15.075 $kWh/year$, compared to 8.022 in Saudi Arabia, 5.707 in Spain, 8.337 in Japan, 3.476 in Lebanon and 1.916 in Mexico, as reported in [105]. This energy consumption is growing at a fast rate, see Figures 3.1 and 3.2 for the electricity and water consumption in Qatar, respectively, per capita and per year, taken from the 2012 statistics report [106] of the national utility company, Kahramaa (the Qatar General Electricity and Water Corporation).

This growth in energy consumption is mostly due to the rapidly growing population, but also due to large investments and development of infrastructure in the country in all sectors. Recently, additional investment in infrastructure has taken place since Qatar was selected to host the football World Cup in 2022. As a result, huge power generation and desalination capacities are being developed by Kahramaa, in order to ensure sufficient supply of power and water to meet the expected growth in demand.

However, the energy mix should be mitigated at some point in order to address the challenges of energy security and environmental sustainability, specially given that Qatar is rated as one of the world's top countries regarding carbon dioxide emissions. In fact, Qatar is accountable for the world's highest per capita emission of CO_2[i]. According to the World Bank data (2010) [105], CO_2 emissions in Qatar are about 40.3 tonnes per person, almost 10 times the global average (4.6 tonnes per capita). Moreover, an energy conservation plan is needed not only because the hydrocarbon resources are finite, but also from economical and financial points of view. Hence the need for the country to examine its energy strategy and to improve its green credentials by diversifying its sources of energy, not only relying on its current resources of oil and gas. Renewable energy resources are indeed alternatives to fossil fuels and can help in covering the growing energy needs of Qatar, addressing at the same time the concerns about environmental impacts.

3.2 Solar energy projects in Qatar

Qatar has expressed interest in increasing power generation from renewable energy sources and has set targets to generate electricity with renewable energy facilities. The use of renewable energy sources is clearly encouraged in the Qatar National Vision 2030 [107], aiming at achieving environmental sustainability. The commitment towards sustainable and responsible development is also clear in the National Development Strategy (2011-

[i] A big portion of the emissions comes from burning the fossil fuels for electricity production.

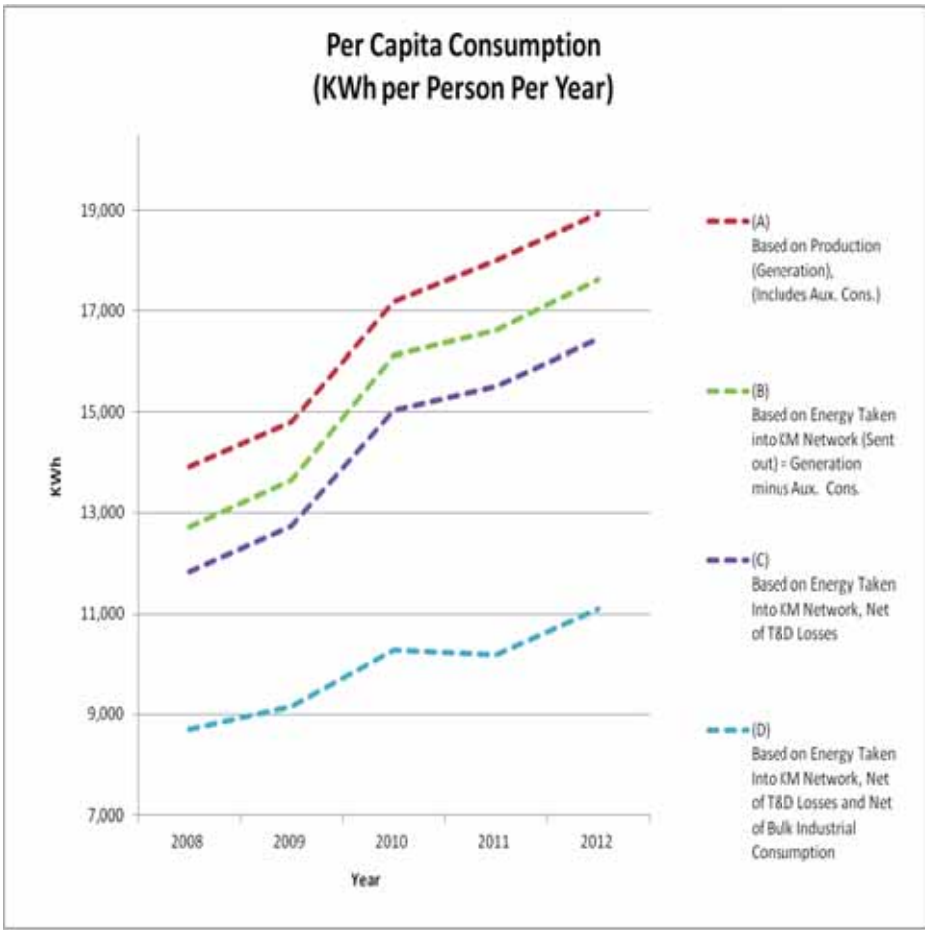

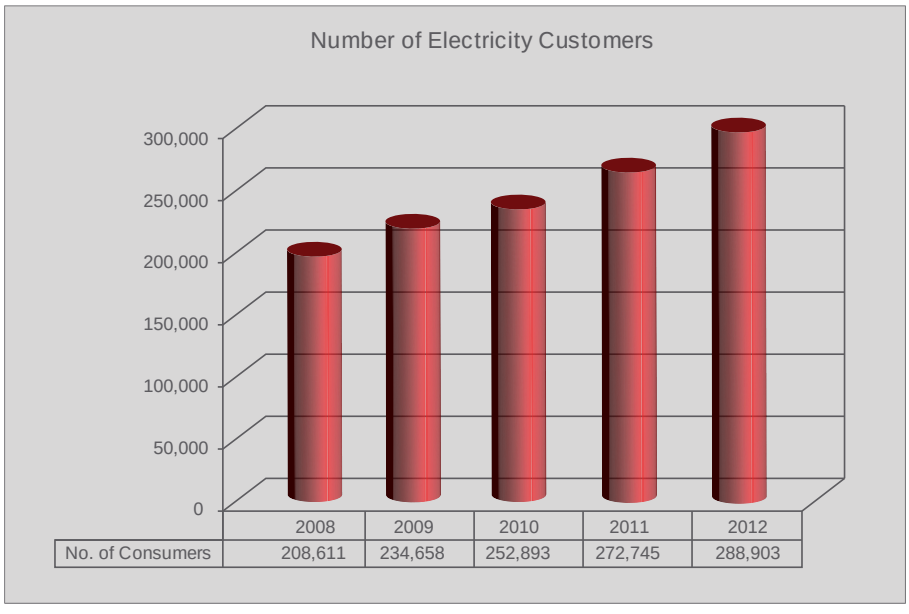

Note that "Consumers" as used in this context is the number of customers registered with KAHRAMAA, not Qatar's population.

Figure 3.1: Electricity consumption per capita and per year, for Qatar until year the 2012 [106].

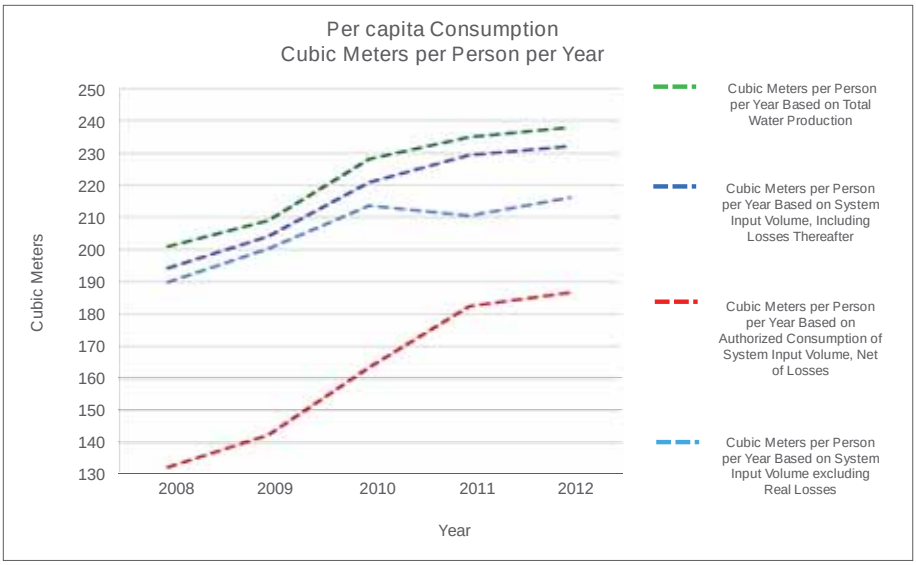

Calculation is net of forwarding and distribution losses.

Table WT14 Number of Water Customers

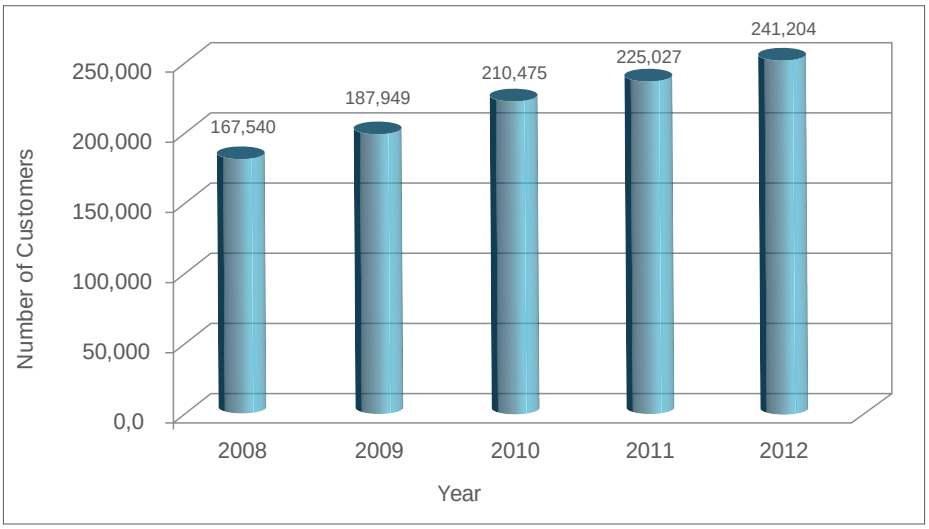

The average growth on the number of water customers from 2008 to 2012 is 10.1%

Figure 3.2: Water consumption per capita and per year, for Qatar until the year 2012 [106].

2016) [2]. The country has therefore announced huge investment and utilities in renewable energy. Given that solar energy is abundantly available in Qatar, solar energy-based projects and solutions come at the first stage of exploitation as renewable energy alternatives in the country. Technology-specific targets using solar energy resources have been set, see Table 3.1 summarising these targets for some of the Arab countries in the GCC (Gulf Cooperation Council) region [108]. Different plans have been announced in this regard. For instance, according to the National Research Strategy, about 2% of Qatar's

total electricity production is planned to come from solar resources by the year 2018. Kahramaa is planning to replace 10% of the total energy used for electricity generation and water desalination with solar power by 2018. As presented in the last Qatar Solar Summit (November 2014), the latest figures about Qatar's targets in terms of electricity production are: installing 1.8 GW of solar capacity by 2020, generating 20% of its energy from renewables by 2030, and powering by solar energy 80% of Qatar's total water desalination. Table 3.2 shows the general solar technology targets set for 2020 and 2030 at different GCC countries, as reported in [108].

Country	Solar-CSP	Solar-PV
Qatar	N/A	100 MW by 2015 and 640 MW by 2020
Saudi Arabia	25000 MW by 2032	16000 MW by 2032
UAE, Dubai	1% of electricity installed capacity	5% of electricity installed capacity
UAE, Abu Dhabi	7% of electricity generation	N/A
Bahrain	N/A	N/A
Oman	N/A	N/A

Table 3.1: Technology-specific targets in GCC countries [108].

Country	2020 target	2030 target
Qatar	6% of electricity generation	20% of electricity generation
Saudi Arabia	N/A	30% of electricity generation
UAE, Dubai	1% of electricity installed capacity	5% of electricity installed capacity
UAE, Abu Dhabi	7% of electricity generation	N/A
Bahrain	N/A	5% of electricity generation
Oman	N/A	N/A

Table 3.2: Solar energy targets in GCC countries [108].

Large-scale solar projects have been planned by several agencies in Qatar such as Kahramaa, the Qatar National Food Security Programme (QNFSP), and the 2022 World Cup Bid Committee (now the Supreme Committee for Delivery & Legacy). In January 2010, Qatar announced the plans to have a 1 billion-USD solar power plant project with an aim to generate at least 100 MW of solar power within five years. Qatar Foundation has hugely invested in a plant to produce polycrystalline silicon, the refined raw material for solar cells. Qatar Solar Technologies (QSTec) is expected to be in operation sometime in 2015 and would be the first operational polycrystalline silicon plant in the region. The successful bid to host the football World Cup 2022, awarded to Qatar on the 2nd December 2010, includes plans for sustainable practices in the construction and operation

of football stadiums, such as using solar energy for powering the stadiums, see Figure 3.3, as well as significant upgrades to the Qatari public transportation network by integrating solar technology. In November 2014, during the Qatar Solar Summit, Kahramaa announced that it is developing a 5–10 MW pilot project for the current year (2015), which is expected to cost up to 34 million USD.

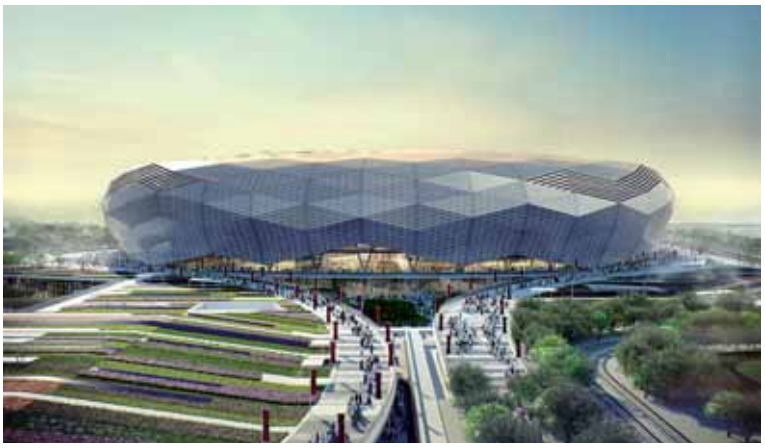

Figure 3.3: The Qatar Foundation stadium design for the World Cup 2022 [109].

Applications of solar energy in Qatar started as early as in 1984, with a study describing a solar pilot project [110]. The project consisted of testing benches for thermal collectors (low and high temperatures), tests for photovoltaic cells and panels, a flat plate thermal collecting/concentrating system, a solar pond energy collection and storage system, a heliostat mounted on a two-axis tracking system, a flat thermo-photovoltaic hybrid concentrating collecting system, a thermal solar distillation desalination unit, and a small experimental farm that makes use of sand, sea-water and solar energy. In 1990, another effort in solar energy was led by a Qatar University research team and consisted of making a solar pond to be used for water desalination. Research activities related to solar energy in Qatar continue to this day with small-scale university projects, research, development and demonstration work in this field with several practical uses such as lighting, cooling, water heating, water desalination, the operation of meteorological stations, etc. The Qatar National Convention Centre (QNCC), for instance, hosts 3500 m^2 of solar panels on its roof (see Figure 3.4), providing 12.5% of the overall energy demand [111].

In addition, the Qatar Science and Technology Park (QSTP) hosts a 35000-square metre Solar Test Facility (STF) in Qatar Foundation premises, to test photovoltaic cell solar power technologies and other sustainable energy technologies like solar thermal, with the main goal of studying the efficiency of such power generation systems in the harsh climatic conditions of the region, see Figure 3.5. The tests include the effects of heat, humidity and dust on the performance of the different technologies. The STF is

Figure 3.4: Photovoltaic panels on the roof top of the Qatar National Convention Centre.

a joint collaboration project between QSTP, GreenGulf, and Chevron. Another joint collaboration, among QSTP, Fraunhofer I.W.S., and Texas A&M University in Qatar, is the Qatar Solar Carbon Black Project, which aims to build and test several generations of smart solar reactors that produce high-grade carbon and co-products from natural gas without greenhouse gas emissions.

Figure 3.5: Solar Test Facility at Qatar Science & Technology Park. Image courtesy of Benjamin W. Figgis (QEERI).

Despite the stated plans, the ambitious targets set and the willingness to diversify its energy supply by using renewable energy and solar in particular, solar energy-based projects in Qatar are still at their infancy stages and large-scale projects have not yet been implemented, in contrast to other projects in the region, see Table 3.3. For instance, the United Arab Emirates (UAE) had 33 MW of installed solar PV capacity in 2013, while Saudi Arabia followed with 19 MW. The UAE inaugurated as well the world's largest stand-alone CSP plant, Shams 1 (100 MWe), in January 2013 [112]. A main reason behind Qatar's lag could be that, unlike the other Arab countries in the region, Qatar does not have a dedicated entity that coordinates renewable energy matters and

strategy and devoted to streamline the promotion and implementation of renewable energy projects. Examples are Masdar City in the UAE and the King Abdullah City for Atomic and Renewable Energy (K. A. CARE) in Saudi Arabia. In Qatar, activities and large-scale projects related to renewable energy are so far handled by the renewable energy units of Qatar Petroleum and Kahramaa. Research and development, on the other hand, are handled by Universities' departments, such as the College of Engineering at Qatar University, and research institutes such as the Qatar Environment and Energy Research Institute (QEERI) of Qatar Foundation, which was launched in 2011 and is committed to develop knowledge and address research and development in critical energy and environmental challenges.

Country	Solar-CSP	Solar-PV
Qatar	N/A	1.2 MW
Saudi Arabia	N/A	19 MW
UAE	100 MW	33 MW
Bahrain	N/A	5 MW
Oman	N/A	0.5 MW

Table 3.3: Solar energy installed capacity in GCC countries, until the end of 2013 [108].

3.3 Available solar resource in Qatar

By taking a first glance on existing solar data for Qatar, the solar conditions in the country seem in general favourable for both concentrated using DNI resources and PV applications using GHI resources. Focusing on DNI in particular and given its geographic location and climatic conditions, Qatar is expected to have high DNI resources, and thus high potential for solar thermal power plants. Indeed, according to a study published in 2005 by the German Aerospace Center (DLR) about the total yield of the solar thermal potential [113], building a solar thermal power plant in 1 km^2 of desert land in North Africa can yield up to 200 to 300 $GWhe/year$ and can produce 165,000 m^3 freshwater per day by desalination. This is equivalent to a 50 MW coal or gas plant, or 500,000 bbl of oil per year, and allows to avoid 200,000 tons of CO_2 emissions per year, see Figure 3.6 which explicitly shows the large potential of using thermal solar technology in an area with high DNI resources.

Therefore, considering these figures, harvesting solar radiation using solar thermal technology seems to be promising and may be one of the viable and practical solutions in

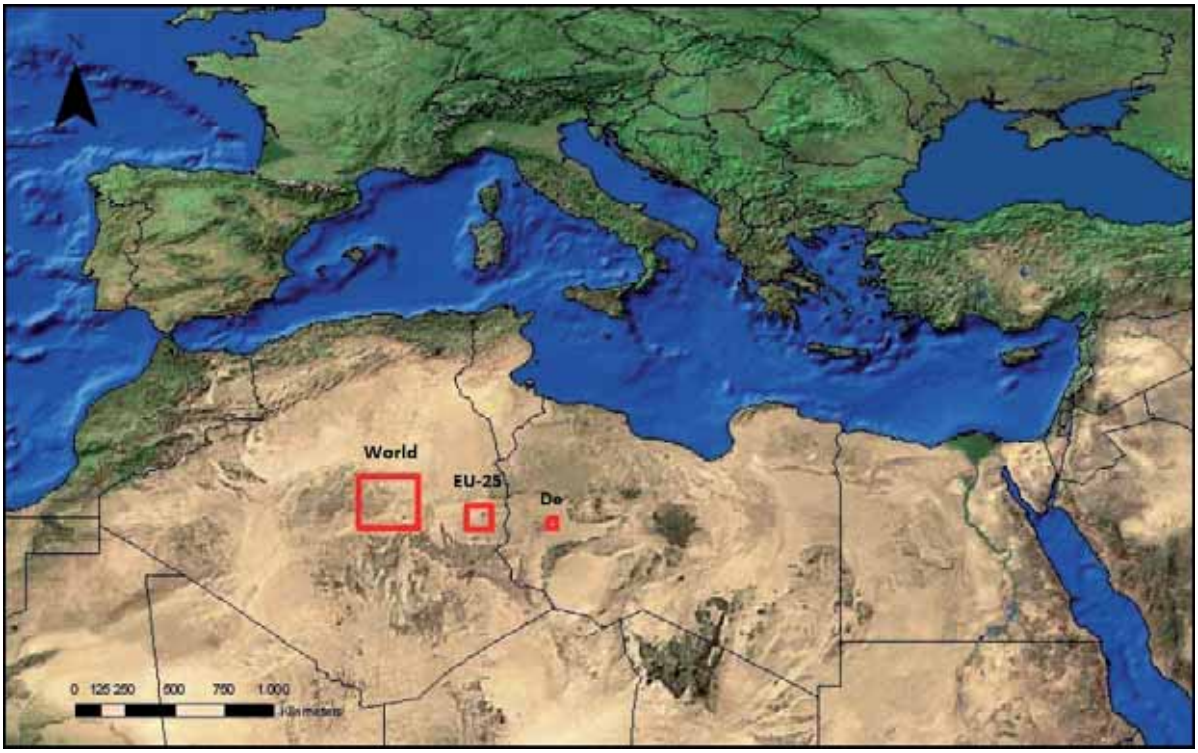

Figure 3.6: Requirements in terms of theoretical space for a solar thermal power plant to meet the electricity demand of the world (254 $km \times 254$ km), Europe (110 $km \times 110$ km) and Germany (45 $km \times 45$ km) [113].

a country like Qatar, where there is an urgent need for the country to diversify its energy resources and reduce its CO_2 emissions.

Looking to the existing solar resource estimations in Qatar, an old study used ground measurements of GHI to validate some of the methods of prediction of global solar radiation. The found total incident GHI over Doha for 8 years was 6983 $MJ/m^2/year$, or 1940 $kWh/m^2/year$ [1]. The International Renewable Energy Agency (IRENA) has published in [108] the annual average solar radiation values for Qatar estimated from satellite data for the year 2005. Direct Normal Irradiance was reported as 2200 $kWh/m^2/year$ for the country. As a reference, DNI exceeding 1800 $kWh/m^2/year$ is generally considered a good technical potential for CSP. The reported global horizontal radiation was 2140 $kWh/m^2/year$, indicating that Qatar is also attractive for PV technology. For comparison with estimated solar energy potential in other Arabian Gulf countries, see Table 3.4 [108].

A more recent study was conducted by GeoModel Solar in 2012 [114] to evaluate the PV power production potential in most of the countries of Europe, the Middle East and North Africa. The study offers information on long-term annual averages of GHI and DNI derived from the SolarGIS satellite-based solar radiation database. The covered period is

Country	GHI ($kWh/m^2/year$)	DNI ($kWh/m^2/year$)
Qatar	2140	2200
Saudi Arabia	2130	2500
UAE	2120	2200
Bahrain	2160	2050
Oman	2050	2200

Table 3.4: Estimated solar energy potentials in some Arabian Gulf countries [108].

of 18 years, from 1994 to 2010, in 15-minute time-steps, with a spatial resolution of 9 arc-sec (approx. 250 m). Results for Qatar give a mean annual GHI of 2134 $kWh/m^2/year$ and DNI of 1836 $kWh/m^2/year$.

The currently available solar maps for Qatar are either maps based solely on satellite-derived solar data or solely on limited available ground measurements.

3.3.1 Satellite-derived maps

A DNI solar map of Qatar was provided within the MED-CSP study of DLR about Concentrating Solar Power for the Mediterranean Region. The map shows the potential sites for CSP in Qatar, deducted from the DNI values estimated in $kWh/m^2/year$ for the year 2002 using satellite data, see Figure 3.7 on the left. The aim of the study was to demonstrate how the CSP plants could meet the electrical and water demand for the GCC countries by 2050 based on the consumption of the year 2000. DNI was estimated for all areas of Qatar that are not excluded from the land resource assessment; this excludes sites that are unsuitable for the deployment of solar fields due to several reasons, such as ground structure, water bodies, slope, dunes, protected or restricted areas, etc. For more details on this work, see [115]. Another solar map was disseminated by the Qatar National Food Security Programme, QNFSP, and shows annual DNI averages from 7 years of satellite-derived values, from 1999 to 2005, see Figure 3.7 on the right [116].

It can be noted that both maps, although derived from the same source, do not show the same absolute or even relative values. Both maps were calculated in different periods of time: the map on the left shows the DNI values of the single year 2002, whereas the map on the right shows the average DNI values for a period of 7 years. Also, the model used to derive DNI has improved to better resolution, as seen by the reduction of the pixel sizes on the right-hand side map.

More recently, QNSFP has awarded DLR a project to study the solar potential for sustainable electricity production and water desalination in Qatar. The plan was to

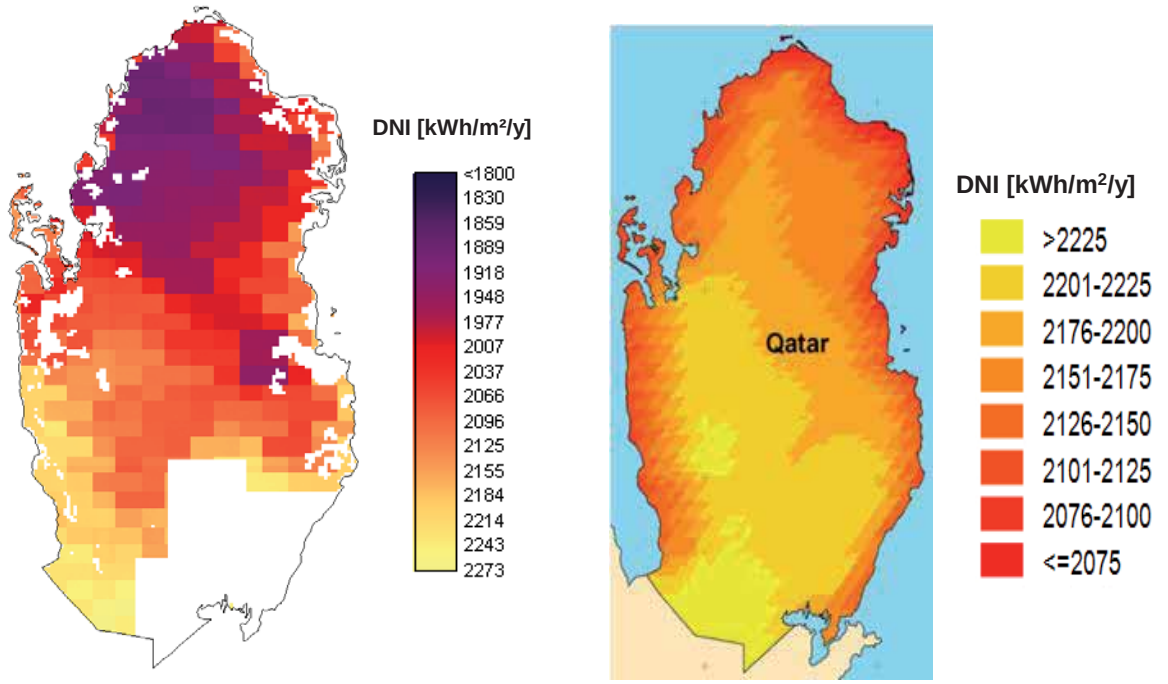

Figure 3.7: DNI solar maps for Qatar from DLR. On the left, a map for the year 2002 for the study of solar thermal electricity generating potentials in Qatar [115]. On the right, a map for the period 1999-2005 [116].

combine accurate ground measurements, to be taken at several locations within Qatar, and long-term historical satellite data (20 years) using the DLR service SOLEMI, in order to have reliable information on GHI and DNI, to be then combined with data on land use, infrastructure, soil condition, etc. within a Geographical Information System (GIS) in order to identify suitable regions for future solar power plants in Qatar. The project started in 2012. However, there is no access to information about the status of the project.

High spatial ($3\times3\ km^2$) and temporal (15-min) resolution satellite-derived solar maps for Qatar can be purchased from any of the commercial satellite data providers, see Section 1.5 for currently available services. One of these commercial companies, GeoModel Solar, has published maps of DNI and GHI for several countries that can be downloaded for free from their website; see Figure 3.8 for the SolarGIS DNI map of Qatar. Data can also be obtained for free from several databases available on the internet, but at lower resolution [70]. Maps of Qatar could also be derived from the solar mapping domain of the neighbouring countries [117, 118].

On a larger regional scale, the Global Atlas for Renewable Energy, led by IRENA,

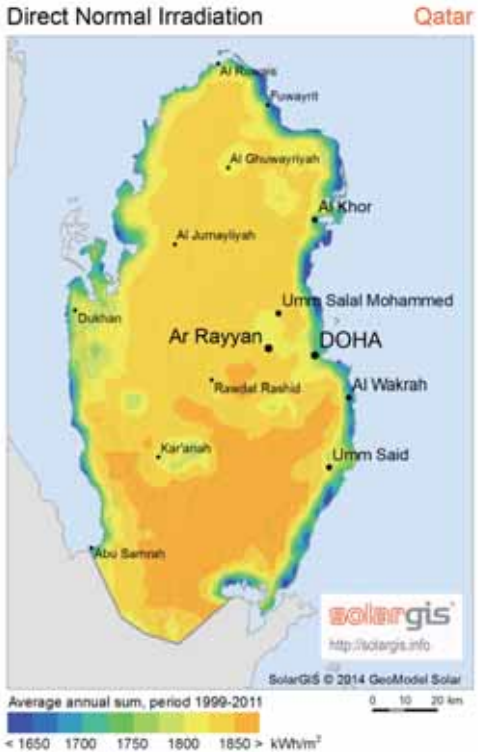

Figure 3.8: DNI solar map of Qatar by SolarGIS model from GeoModel Solar.

provides high-resolution and long-term solar resource maps. The database also includes information on protected areas, roads or infrastructures, which enables to highlight potential sites for developing solar projects and to undergo pre-feasibility studies. The information provided using this database can be considered as a first estimation before the initiation and the development of any solar-based project in the region, allows to formulate policies in the renewable energy sector, and stimulates investment. The Solar Atlas for the Mediterranean countries (Solar-Med-Atlas), although providing solar maps for the Arab countries, does not have coverage of Qatar and the GCC area. Both the Solar-Med-Atlas and the Global Atlas for Renewable Energy provide basic information on solar radiation. Commercial companies and service providers focus more on customised solutions and the provision of data time series and consultancy services for specific sites and projects.

3.3.2 Ground measurement-derived maps

Currently, the only available direct measurements of solar resource throughout Qatar consist of GHI data, being collected by the Qatar Meteorological Department (QMD), which operates a network of 12 automatic weather stations (AWS) distributed across the country, see Figure 3.9. Looking at the spatial distribution of the stations across the

country, the station locations are mostly coastal and may not cover all possible solar climates in Qatar, since stations are missing inland or in the centre of the country.

Figure 3.9: Network of monitoring stations in Qatar, operated by QMD.

Table 3.5 lists the QMD AWS locations with their starting dates of operation: the oldest stations were installed in 2007 and the newest in 2011.

Using ground measurements of GHI available from the QMD network, annual GHI solar maps over Qatar were derived based on daily GHI data, for the period from 2007 to 2012 in [119]. In that study, several maps were obtained using the mentioned dataset and showing the spatial variation of annual GHI in Qatar. It is worth mentioning that the information about instrument maintenance and calibration was unknown. Figure 3.10 shows a map produced by taking the complete dataset of the 12 stations for their full periods of operation. The QMD network provides priceless first-hand information on the solar resources in Qatar.

3.3.3 Summary

The existing solar maps for Qatar are informative and give first insight about the solar resources available in the country. Satellite-derived maps have to be validated with ground measurements in order to assess their respective accuracy, the correctness of the model used and its validity in the region. In terms of ground measurements, there is still a need

Station location	Operating since	Valid days (%)
1. Abu Samra	2007	95
2. Al Ghuwayriya	2009	98
3. Al Karanaah	2009	70
4. Al Khor	2007	97
5. Al Ruwais	2007	94
6. Al Shehaimiya	2011	100
7. Al Wakrah	2009	99
8. Doha	2008	93
9. Dukhan	2007	96
10. Qatar University	2007	99
11. Turayna	2011	99
12. Ummsaid	2007	99

Table 3.5: Solar monitoring stations collecting GHI in Qatar, with year of operation start and percentage of days with daily values reported until 31 December 2012.

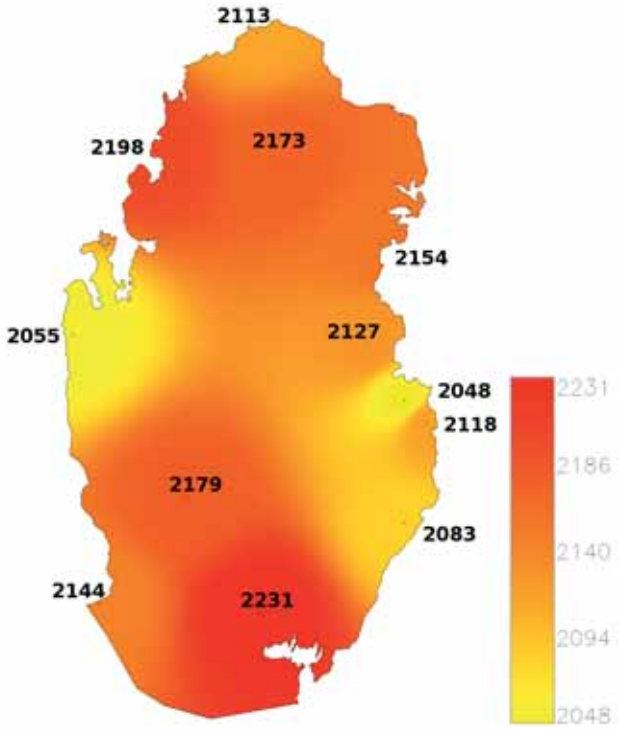

Figure 3.10: GHI solar map (values in $kWh/m^2/year$) based on daily ground measurements of GHI.

in Qatar to have precise measurements on the direct and the diffuse solar radiation, in addition to the existing global radiation measurements.

Chapter 4

Instrumentation

This chapter presents the experimental setup with descriptions of all the instruments used to collect the data used in this thesis. This includes a CL51 lidar ceilometer, from Vaisala, used for the measurement of the backscatter coefficient of aerosols in the atmosphere, and a Kipp & Zonen solar radiation monitoring station comprising several radiometers, used for solar radiation measurements. In addition, the data acquisition system along with examples of measurements as acquired by both systems are described. Details about the experimental site and the features considered for its selection are also given.

4.1 Lidar-ceilometer

Previous studies have demonstrated that lidar systems are suitable devices for the detection of aerosol layers and their boundaries [120, 121]. The system works by transmitting a laser pulse vertically into the atmosphere to measure the backscattered signals as explained in Section 2.3. The number of backscattering particles at a certain height from the lidar determines the strength of the backscattered signal; for instance, higher amounts of aerosols in the atmosphere will result in stronger backscatter signals. The distance is determined by measuring the time of flight (TOF), i.e., the time between the transmission of the pulse and the reception of the signal. A ceilometer is a compact lidar system, commercially available and designed in a way to operate continuously with little maintenance required. The primary use of a ceilometer is the detection of the heights of the cloud base in the fields of aviation and meteorology. Beyond cloud detection, ceilometers are also used for the determination of the boundary layer height and the characterisation of its structure [122], monitoring of dust and volcanic ash clouds [123], and the estimation of particulate matter (PM) concentration [124]. In this thesis work, however, the lidar-ceilometer is not used for the determination of the height of the cloud base or the

boundary layer, but rather to measure the backscatter as a function of height in order to get a quantitative indication on the amount of aerosols in the atmosphere. Below is a description of the used ceilometer and its main specifications.

4.1.1 Vaisala ceilometer CL51

The detection of aerosols in the atmosphere was achieved with the CL51, an elastic lidar-ceilometer commercially available from Vaisala, which in its customary usage provides measurements of cloud heights and vertical visibility, through the acquisition of vertically-resolved backscatter profiles of the atmosphere, including aerosols.

The CL51 unit was installed in December 2012 on the rooftop of the Qatar Environment and Energy Research Institute (QEERI) building in Doha. It has been operational since then as part of the solar resource assessment and air quality monitoring facilities at QEERI. A special platform was made for fixing it to the roof, to ensure its stability against wind. The system is installed in one corner of the roof with no obstructions in its field of view. The CL51 ceilometer consists of a shielding cabinet and a measurement unit as shown in Figure 4.1.

Figure 4.1: Vaisala Ceilometer CL51, as installed at the QEERI facility in Doha, Qatar.

Inside the shield, there is a blower/heater to remove any excess of dust on the window, and to ensure reliable operation in precipitation and extreme temperatures. The interior

of the measurement unit of the CL51 is shown in Figure 4.2 and includes mainly the transmitter, the receiver, and the optical unit, for which the generic descriptions are given in Section 2.3.1.

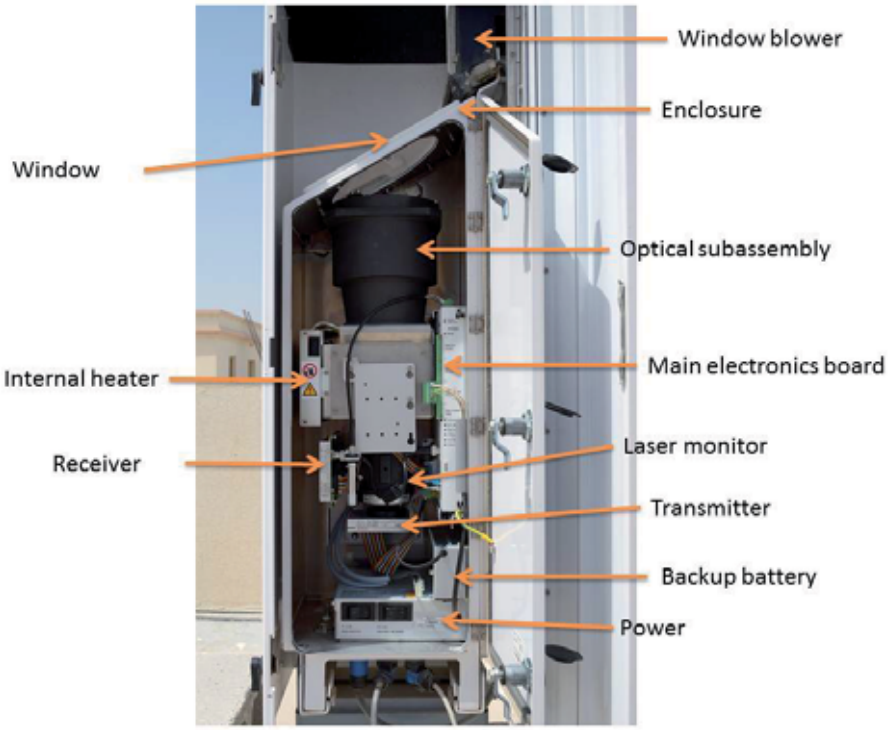

Figure 4.2: Vaisala Ceilometer CL51, measurement unit main parts.

The CL51 uses an Indium Gallium Arsenide (InGaAs) pulsed diode laser to emit short and powerful laser pulses of 910 nm wavelength and 3 μWs energy, into a selectable vertical or near-vertical (12 degrees from the vertical) direction. The emission frequency is 6.5 kHz, while the pulse duration is 110 ns. As per the lidar principle, the CL51 measures the intensity of the directly backscattered light as a function of time. It detects the elastically backscattered light, i.e., the return signal is measured at the same wavelength of the transmitted beam. The resulting backscatter profile represents the signal strength versus height.

The backscattered light is collected by the lens of the receiving optics. The CL51 has a single-lens optical design [125], i.e., the same lens is used for the transmission and the reception of light. A schematic representation of this optical concept is shown in Figure 4.3. The collimation of the outgoing laser beam is done by the centre of the lens, and the outer part of the lens is used to focus the backscattered light onto the receiver. This is possible through an inclined mirror with a hole in the centre. This arrangement ensures a full overlap for the collection of aerosol backscatter in the near range and at the same

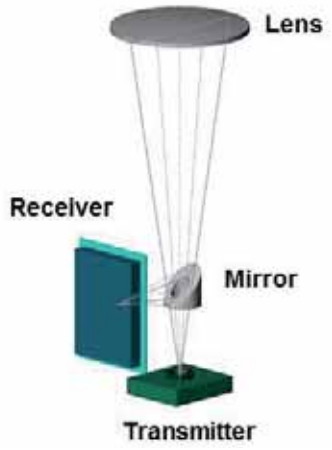

Figure 4.3: Vaisala Ceilometer CL51, optical configuration. Image: Vaisala.

time makes the receiver practically blind to the light reflected by the lens. The good overlap between the transmitted laser beam and the receiver field of view decreases the effect of multiple scattering. The main characteristics and specifications of the CL51 are listed in Table 4.1.

Property	Value
Backscatter profiling range	15 km
Cloud reporting range	13 km
Reported vertical resolution	10 m
Measuring interval	6 s
Reporting interval	36 s
Laser type	InGaAs diode
Laser wavelength	910 nm
Laser beam width at 7.5 km height	3 m
Laser beam width at 15 km height	6 m
Receiver	Silicon avalanche photodiode
Pulse rate	6.5 kHz

Table 4.1: Specifications of the Vaisala ceilometer CL51 installed at the QEERI facility.

No specific maintenance is carried out on the CL51 other than daily cleaning of the window so that it is kept clean, a requirement common to all optics.

4.1.2 Operating principle of CL51

The basic operating principle of the CL51 consists of the measurement of the time taken by the pulse of light from its emission by the transmitter, through its way up to any

obstruction in the atmosphere until its detection by the receiver. This is schematically illustrated in Figure 4.4. In this illustration, the obstruction is depicted by three layers of cloud shapes. The basic formula relating the time delay t with the height h of the backscatterer is given by:

$$h = \frac{ct}{2}, \tag{4.1}$$

where c is the speed of light. For instance, a backscatter signal from a height of 7.5 km will be received after 50.2 μs.

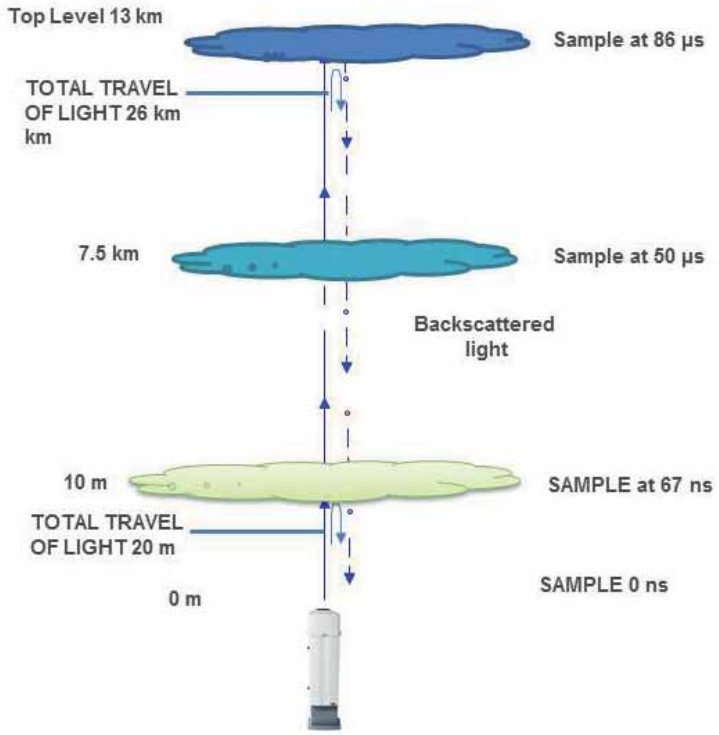

Figure 4.4: Vaisala Ceilometer CL51, principle of operation.

An example of measured signal as a function of height is shown in Figure 4.5 and gives information about the presence of particles in the atmosphere which scatter the light back from a certain height. The CL51 detection of the received light is based on the photocurrent technique. The return signal is digitally sampled every 67 ns, which gives an adequate spatial resolution of 10 m for atmospheric measurements, up to 100 μs after each pulse, providing a full range of operation up to 15 km. In the configuration of the CL51, the transmitted laser power is low by design for safety and economic reasons, according to the manufacturer; this makes the noise coming from the ambient light stronger than the backscatter signal specially at the top heights. In order to reduce the noise, a signal-to-noise ratio (SNR) improvement technique was adopted by Vaisala, and consists of sending

a large number of laser pulses and summing, for each height, all the return signals; the noise, being random, adds up to a constant value lower and distinguishable from the real signals, thus improving the SNR. Additional processing of the backscatter profile provides the cloud base height detection. The detection of a cloud by the CL51 consists of the identification of cloud droplet scattering that reduces the visibility to less than 100 m [126]. The CL51 cloud reporting range is up to 13 km, and it can detect up to three layers of clouds in a simultaneous way. In case of precipitation or fog obscuring the cloud base, the CL51 reports vertical visibility.

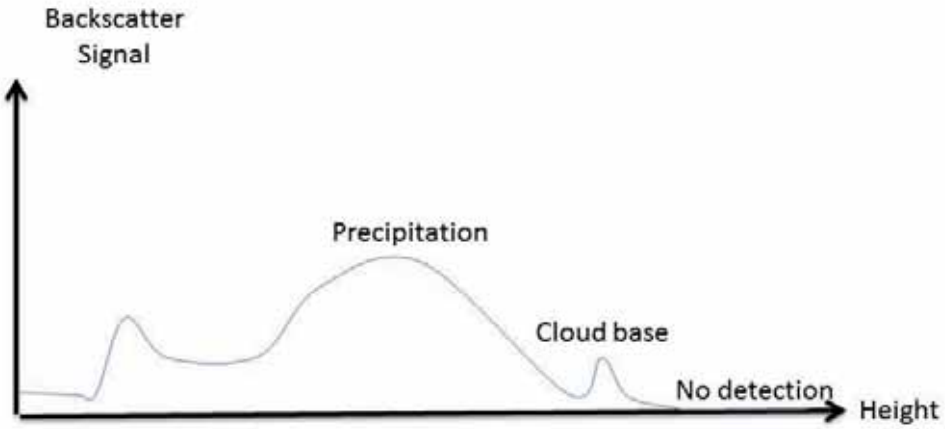

Figure 4.5: Example of a ceilometer measurement signal.

Based on the lidar equation (Equation 2.21), the instantaneous return signal power can be derived. This is given by:

$$P_r(Z) = E_0 \frac{c}{2} \frac{A}{Z^2} \beta(Z) \exp\left[-2 \int_0^Z \sigma(Z')dZ'\right], \tag{4.2}$$

where $P_r(Z)$ is the instantaneous power received from distance Z, E_0 is the effective pulse energy taking all optics attenuation into account and given in Ws, c is the speed of light in m/s, A is the receiver aperture in m^2, Z is the distance in m, $\beta(Z)$ is the volume backscatter coefficient at distance Z in $m^{-1}srad^{-1}$ which represents the part of light reflected back towards the receiver from a distance Z, and the exponential term is the attenuation of the light from the two-way travel of the light: the transmitted and backscattered light. The return signal is multiplied with the square of the height in order to have a normalised signal and to eliminate the height dependence of the power of the return signal. This normalisation, however, accentuates the noise with increasing height since the noise is height-independent. In the processing of the CL51 data and in order to solve the lidar equation, the backscatter coefficient is considered proportional to the

extinction coefficient and expressed as follows:

$$\beta(Z) = k\sigma(Z), \tag{4.3}$$

where k is the proportionality constant in $1/srad$, also known as lidar ratio.

For solving the lidar equation for the CL51, it is assumed that the lidar ratio k remains constant with height, specially since it is needed to have accurate estimates of the extinction profile. In many cases, it has been demonstrated that k is equal to 0.03, smaller in high humidity conditions (around 0.02), and bigger (up to 0.05) in low humidity conditions [126]. However, in precipitation conditions, k can have a wider range of values.

4.1.3 Maintenance

The CL51 is a self-operating device and once installed, there is basically no need for adjustments in the field. The embedded software of the CL51 includes self-monitoring controls and functions meant for testing and maintenance purposes and gives continuous status information. This includes internal tests of the laser power, receiver sensitivity, internal voltages, window contamination, internal temperatures, etc.. Any failure of these tests will indicate an error in the status message with the error type and information. The CL51 is fitted with a maintenance terminal connection; in case any maintenance is needed it is possible to connect a serial cable to the ceilometer maintenance port and a terminal computer in order to access the CL51 maintenance open command. A built-in tilt angle sensor detects the angle of deviation from the vertical; this automatic tilt angle measurement triggers a correction of the tilt accordingly. As seen in Figure 4.2, the CL51 is also fitted with a window blower which runs when the system detects contamination of the window; the blower only removes small contamination from the window and dries off rain drops. The proper functioning of the blower is automatically checked once an hour. The only daily maintenance activities carried out on the CL51 are: the manual cleaning of the window so that it is kept clean, as applicable to all optics, and the checking on the proper operation of the blower. Additional controls carried out daily include inspection of the data acquisition software to look for any data interruption caused by data transmission or collection failure, and checking the data message for alarms and warnings.

4.1.4 Data collection

For the data acquisition, the CL51 was connected to a PC through an RS-232 serial cable. Two supporting software packages can be used with the CL51: CL-VIEW, a graphical

user interface for collected data, and BL-VIEW, the boundary layer analysis tool.

The CL-VIEW software is a graphical presentation program for cloud height and backscatter profile data as measured by the ceilometer. It is used for collecting, storing and presenting the data acquired by the CL51. In its online mode, CL-VIEW collects the data from the ceilometer via the serial line and stores them on the computer hard disk according to the selected options. The data are displayed instantaneously in graphical form on the screen. CL-VIEW can also be used to examine stored data, in its offline mode. In Figure 4.6, an example is shown of the so-called 'cloud intensity' graph and a backscatter data profile collected at the experimental site in Doha, Qatar, on 07/Jun/2013, during the normal operation of the CL51. The plot on the left corresponds to the cloud intensity graph and is used for the cloud height determination. The horizontal axis in the plot presents the time and the vertical axis is the altitude. Each point reflects the place of the backscatter identified by the current time. The darkness in the colour of the points identifies the intensity of the backscatter at the corresponding height. The plot on the right is the backscatter profile; this can be presented as an instantaneous or as averaged mode. The horizontal axis is the backscatter intensity and the vertical axis is the altitude. In the offline mode of CL-VIEW, each data file contains all information about the backscatter coefficients acquired as a function of height and time and are used for the further analysis of the atmospheric backscatter coefficient, of interest in this work.

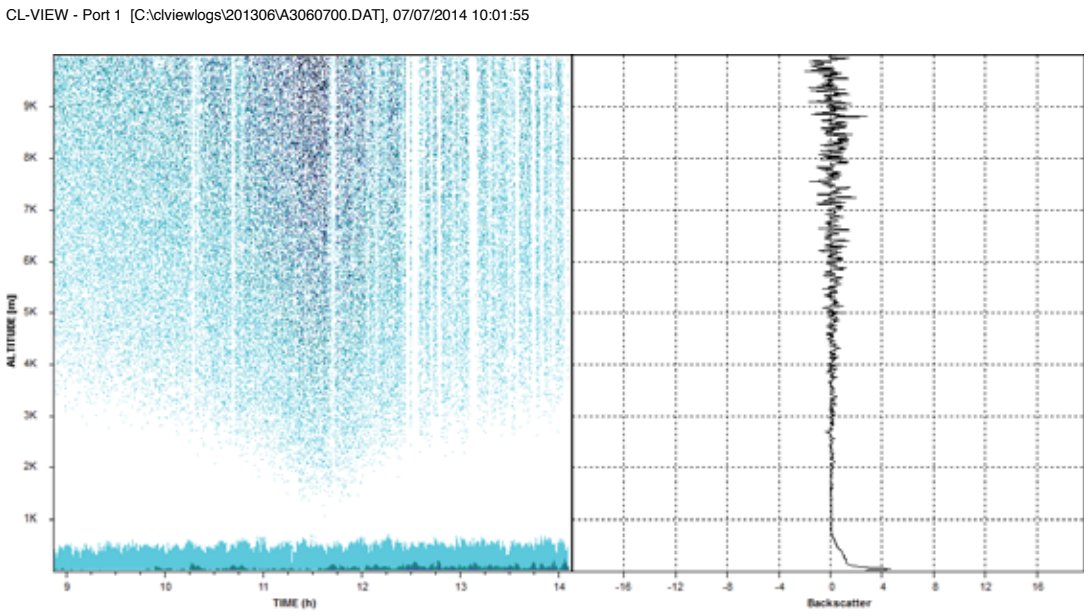

Figure 4.6: CL-VIEW cloud and backscatter intensity graphs as measured by the Vaisala Ceilometer CL51. Data collected on 07/Jun/2013.

BL-VIEW is a software tool used for boundary layer reporting and analysis. It can be

used instead of CL-VIEW for collecting, storing, and presenting the data acquired by the CL51. BL-VIEW analyses the ceilometer backscatter profile data according to default parameters and reports the height of the planetary boundary layer and of other aerosol layers from ground level (the height of the ceilometer) up to 4 km. Indeed, the measured backscatter profile gives information about the presence of aerosols in the atmosphere which are mainly emitted at the surface and have in general a higher concentration within the boundary layer than in the free troposphere. Therefore, a sharp gradient in the aerosol concentration detected by the backscatter signal indicates the height of the boundary layer and separates it from the relatively clean free troposphere. The algorithm uses an enhanced gradient method approach. The standard gradient method consists of searching for strong gradients or local gradient minima in the backscatter profile [127]. The most pronounced of the found minima is reported as the boundary layer height by the method, and the other minima can be reported as residual or additional layers. The BL-VIEW algorithm involves: cloud and precipitation filter, noise- and range-dependent time- and height-averaging intervals, and signal strength-dependent detection thresholds. Averaging in time and height is applied in order to reduce sensitivity to noise and weather conditions. Additional filters are also applied for the enhancement of the retrieval of the boundary layer specially in situations when weather conditions such as precipitation or fog prevent the detection of boundary layer height [128]. BL-VIEW can report up to three layer heights in a single vertical measurement. Figure 4.7 shows samples of BL-VIEW backscatter profiles for cloudless days, as measured by the CL51, over Doha for several days in different months, covering varying degrees of dust in the atmosphere. Each of these plots displays the evolution of the backscatter signal during one full day, from midnight to midnight. The colours represent the intensity of the signal (left side scale), from dark blue for the lowest and red for the highest intensities. The vertical axis on the right side indicates the height above ground level from 0 to 4000 m. The black squares are layer boundaries found by the gradient algorithm of BL-VIEW. For instance, on 12 January and 26 March, the PBL is relatively well defined since a layer can be found with an evolution through the day from sunrise to sunset as per the definition of the boundary layer. On the 2nd of January, the boundary layer can still be found but other layers are also evident. On the 27th of May, the boundary layer is being pushed down by a thick layer of dust on top of it. On the 12th and 22nd of May, the dust layer is so dense and dominant that the boundary layer signal cannot be differentiated from other layers. Many days in April and May 2013 were loaded with heavy dust and the corresponding BL-VIEW graphs are similar to the ones seen in this figure, with the dust layer extending above 4000 m. An attempt was made [129] to compare the boundary

layer height with DNI measurements at noon. The study had inconclusive results because the BL height could not be identified with BL-VIEW from other dust layers, which often extended above 4 km, in many days.

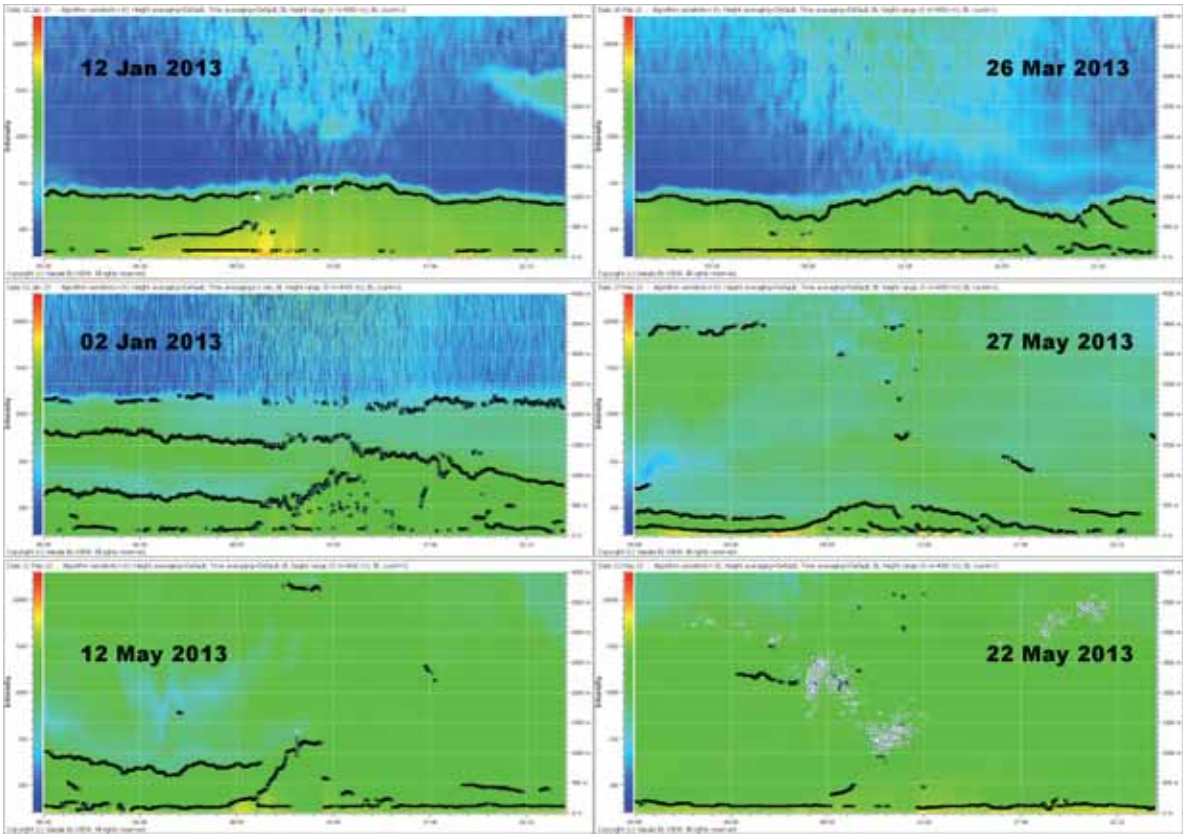

Figure 4.7: Samples of backscatter profiles as displayed by BL-VIEW.

4.1.5 Data used

Different intensity profiles can be recorded by the CL51 depending on the constituents of the atmosphere, like dust, fog, haze, rain, etc. These profiles provide information on the height of the cloud base as a function of time, given by CL-VIEW, and data on the evolution and structure of the boundary layer height, given by BL-VIEW. Of most importance for this work are the backscatter coefficients retrieved by the ceilometer, which are recorded as a function of time and height according to Equation 4.2. The data analysis presented here uses the CL51 signal describing the backscatter properties of the atmosphere. These signals are represented as a two-dimensional dataset of backscatter coefficient values, reported in time every 36 s, and height up to 15 km in 10-m steps.

4.2 Solar radiation instruments

For the precise measurements of solar radiation, a Kipp & Zonen solar radiation monitoring station has been installed in QEERI's facilities and is acquiring data since December 2012. This monitoring station consists of a SOLYS 2 sun tracker which hosts all the instruments for solar radiation measurements: one CHP1 pyrheliometer for the measurement of direct normal irradiance mounted in a way to follow the sun rays all through the day and all through the year, and two CMP11 pyranometers, one shaded for the measurement of the diffuse horizontal radiation and one unshaded for the measurement of the global horizontal radiation, both mounted on a horizontal platform which ensures the mechanical stability and proper levelling of the instruments. Another instrument, a CGR4 pyrgeometer, was also mounted on the monitoring station for measuring the infrared radiation. However, the CGR4 measurements are not used in the scope of this work. The Kipp & Zonen type of station is widely used for high quality solar measurements and was selected for its high performance and reliability and its compliance with the requirements of the BSRN, which uses Kipp & Zonen sun trackers and radiometers in many of their stations installed worldwide. Figure 4.8 shows the complete monitoring station with all the mounted accessories and instruments as installed and operating at QEERI's facility. Below is a description of each of these instruments.

4.2.1 SOLYS 2 sun tracker

The SOLYS 2 is a fully automatic two-axis sun tracker, used as a platform for positioning the radiometers that need to follow the movement of the sun in the sky. It has an integrated GPS receiver; the measurement site's latitude, longitude and time were automatically configured by the GPS during installation and the time is being regularly updated by the GPS to avoid any internal clock drift. An on-board program, the Michalsky algorithm [130], uses this information to calculate regularly the position of the sun throughout the day. The pointing accuracy of the SOLYS 2 is 0.1°, which meets the BSRN requirements. As additional control for the accuracy of the tracking, the SOLYS 2 was fitted with a sun sensor kit consisting of a four-quadrant photodiode sensor within a weather resistant enclosure. This sensor provides active tracking, and corrections to the tracking algorithm, in case the mounting of the tracker is not stable or exhibits movement. For the installation of the tracker, the tripod stand with levelling feet was bolted on a firm and stable base. The levelling and alignment adjustments were aided by an integrated bubble level on the top of the tracker. The obstacle-free operating area of SOLYS 2, including all accessories, ensures a proper movement for the SOLYS 2 and

Figure 4.8: Solar radiation monitoring station as installed at the QEERI facility in Doha, Qatar.

prevents any blocking, with respect to both the azimuth and zenith axes, throughout the year. On the sides of the tracker there are plates with zenith adjustment for the mounting of the pyrheliometer, so that it points precisely to the sun, and for the shading assembly which serves to ensure blocking the direct radiation from reaching the pyranometer measuring the diffuse radiation. On the top, a horizontal platform is fitted in order to conveniently mount the other radiometers. The tracker uses stepping motors controlled by micro-processors to make the horizontal (azimuth) and vertical (zenith) movements in a way to follow the solar arc. The main specifications of the SOLYS 2 system are summarised in Table 4.2.

4.2.2 CHP1 pyrheliometer

For measuring DNI, the Kipp & Zonen CHP1 pyrheliometer was used; this device complies with the ISO and WMO performance criteria for First Class Normal Incidence Pyrheliometers, classifications described in Section 1.3. It is calibrated by Kipp & Zonen upon manufacturing and a calibration certificate traceable with the WRR (World Radiometric Reference) is supplied with the instrument, indicating the sensitivity of the pyrheliometer, which is the constant proportionality ratio between the voltage output

Property	Value
Pointing accuracy	$< 0.1°$
Torque	20 Nm
Angular velocity	$5°/s$
Rotation	110° zenith and 540° azimuth
Over rotation and damage protection	Physical limits stop
Operating temperature range	-40 $°C$ to 50 $°C$ (AC power with heater)
Bubble level accuracy	$< 0.1°$
Supply voltage	28–30 VDC (nominal 24 DC)
	90–264 VAC (50/60 Hz)

Table 4.2: Main specifications of Kipp & Zonen SOLYS 2, installed at the QEERI facility.

and an absolute irradiance level. The sensitivity used hereby, as given by the calibration certificate from Kipp & Zonen, is 7.75 $\mu V/(W/m^2)$, valid for an ambient temperature of 22 $\pm$ 2 $°C$ and a normal incident radiation of 500 W/m^2. This factor is determined indoors in Kipp & Zonen laboratories by comparing the CHP1 against a reference pyrheliometer of similar type, in a horizontal parallel beam of light from a xenon lamp. The used reference pyrheliometer is fully characterised in terms of linearity, temperature dependence and directional response and is regularly calibrated outdoors, using the sun as source, at the World Radiation Centre in Davos, Switzerland with a calibration accuracy of $\pm$0.5%. The CHP1 measures the irradiance resulting from the radiant flux from a solid angle of 5°. Figure 4.9 shows the CHP1 as mounted on the SOLYS 2 at QEERI. The CHP1 has a flat window made of quartz, which ensures that 97 to 98% of the solar radiation spectrum will be transmitted across the window to reach the detector. A rain shield cover protects the window. The instrument temperature is measured through 2 thermistors placed inside the device assembly. The two alignment aids on the pyrheliometer tube are used for checking the alignment the CHP1 with the axis of the direct beam of the sun. The detection in the CHP1 is based on the thermoelectric effect described in Section 1.3.1. It consists of the thermopile with black surface coating on the top, with a spectral selectivity of less than 2%. The optical configuration of the CHP1 complies with the WMO recommendations; it consists of a field stop, sets of blackened baffles and an aperture stop, defining the CHP1 field of view of 5° and slope angle of 1°. The detector sits behind the aperture stop. The interior of the CHP1 tube, which surrounds and holds this assembly, is blackened. For the prevention of dew on the inner sides of the window in case moisture enters the radiometer body, a screw-in drying cartridge is mounted in the radiometer housing and filled with silica gel.

Figure 4.9: Kipp & Zonen CHP1 pyrheliometer used at the solar radiation monitoring station installed at the QEERI facility.

The parameters characterising the response of the CHP1 are provided in Table 4.3, which also summarises its main specifications. Kipp & Zonen expects a maximum uncertainty of 2% for hourly totals and 1% for daily totals for the CHP1 pyrheliometer.

4.2.3 CMP11 pyranometer

The pyranometers used for measuring global and diffuse solar radiation are the CMP11 model from Kipp & Zonen, which fully complies with the requirements of ISO 9060:1990 for a Secondary Standard Pyranometer; the two units are shown in Figure 4.10. The CMP11 is calibrated in accordance with ISO 9847 for the calibration of field pyranometers by comparison to a reference pyranometer and is supplied with the calibration certificate. The CMP11 pyranometer is designed for measuring the short-wave total solar irradiance, which is the sum of the direct and diffuse solar radiation, on a plane surface in W/m^2. Like the CHP1, the CMP11 uses the thermoelectric effect and has a 32-junction thermopile sensing element, with a non-spectrally selective black surface coating on the top of it. It is also fitted with a built-in passive temperature compensation system with a standardised linear function. The sensing element characterises the detector in terms of response time, linearity and measurement range. The detector is shielded by two glass domes

Property	Value
ISO Classification	First class
Response time (95%)	5 s
Zero offsets due to temperature change (5 K/hr)	± 1 W/m^2
Non-stability (change/year)	$\pm 0.5\%$
Non-linearity (0 to 1000 W/m^2)	$\pm 0.2\%$
Temperature dependence of sensitivity	0.5% (-20 $°C$ to 50 $°C$)
Sensitivity	7 to 14 $\mu V/(W/m^2)$
Impedance	10 to 100 Ω
Operating temperature	-40 $°C$ to 80 $°C$
Spectral range	200 to 4000 nm
Typical signal output for atmospheric applications	0 to 15 mV
Maximum irradiance	4000 W/m^2
Expected daily uncertainty	$\pm 1\%$
Full opening view angle	$5° \pm 0.2°$
Slope angle	$1° \pm 0.2°$
Required tracking accuracy	$\pm 0.5°$

Table 4.3: Main specifications of Kipp & Zonen CHP1, installed at the QEERI facility.

for additional protection of the sensing element and the black painted coating. The glass domes are designed to minimise errors in measurement at all incident angles (the directional response) and allow the transmittance of 97 to 98% of the solar radiation spectrum. A built-in bubble level is used for checking the alignment of the instrument. The CMP11 is placed horizontally on the mounting stand through its three feet, of which two are adjustable in order to properly level the detector surface; this is achieved by turning the two adjustable feet to bring the bubble of the spirit level centrally within a marked ring. A sun shield is used to cover the housing and reduce solar heating. No power is required for the operation of the CMP11; the radiation absorbed by the sensing element produces a small analogue output voltage. Similarly to the CHP1, the CMP11 has a removable drying cartridge filled with self-indicating silica gel desiccant used to absorb the humidity within the radiometer so that the detector and electronics of the CMP11 are kept dry. For the diffuse measurements, a shading mechanism consisting of a small sphere mounted on an articulated assembly was installed on the SOLYS 2 sun tracker. The sphere casts a shadow adjusted properly upon installation to cover the pyranometer dome completely. For improving the accuracy of the measurements and to better adapt to the dusty and humid weather conditions of Qatar, both CMP11

pyranometers, for global and diffuse measurements, were fitted with ventilation units running continuously to keep the domes cleaner. This decreases the level of dirt and condensation on the dome and lowers the thermal offset in the dome, characteristic of the pyranometer. All instruments were grounded for lightning and signal noise protection.

Figure 4.10: Kipp & Zonen CMP11 pyranometers used at the solar radiation monitoring station installed at the QEERI facility. Note the shadow covering the sensor of the left pyranometer, in order to measure DHI.

The physical properties are listed in Table 4.4; they are similar to those for the CHP1, except for the zero offset A and the directional response, which only apply to the CMP11 pyranometer.

Based on many years of field measurements, Kipp & Zonen empirically determines uncertainty figures of their pyranometers, for typical operating conditions. For a high quality pyranometer the WMO expects maximum uncertainty totals of 3% in the hourly radiation. In the daily total an uncertainty of 2% is expected, since some response variations cancel each other out if the integration period is long [22].

The sensitivity of the CMP11 measuring the global radiation in the QEERI station is 8.78 $\mu V/(W/m^2)$ and the sensitivity of the CMP11 measuring the diffuse radiation is 8.47 $\mu V/(W/m^2)$ at normal incidence on horizontal pyranometer, obtained by comparison to a reference pyranometer's readings, and supplied on the calibration certificate. The calibration procedure is carried out indoors in Kipp & Zonen laboratories following [31], and is based on a side-by-side comparison of the CMP11 pyranometer with a reference pyranometer under a stable artificial sun corresponding to a metal-halide high-pressure gas discharge lamp; the irradiance at the radiometers is approximately 500 W/m^2. The reference pyranometers used by Kipp & Zonen are regularly calibrated outdoors at the WRC, using the 'continuous sun-and-shade' method. They are also fully characterised

Property	Value
ISO 9060:1990 classification	Secondary standard
Spectral range	285 to 2800 nm
Sensitivity	7 to 14 $\mu V/(W/m^2)$
Impedance	10 to 100 Ω
Expected output range (0 to 1500 W/m^2)	0 to 20 mV
Maximum irradiance	4000 W/m^2
Response time (63%)	< 1.7 s
Response time (95%)	< 5 s
Zero offset A thermal radiation (at 200 W/m^2)	< 7 W/m^2
Zero offset B temperature change (5 K/h)	< 2 W/m^2
Non-stability (change/year)	$< 0.5\%$
Non-linearity (100 to 1000 W/m^2)	$< 0.2\%$
Directional response (up to 80° with 1000 W/m^2 beam)	< 10 W/m^2
Temperature dependence of sensitivity	$< 1\%$
Spectral selectivity (350 to 1500 nm)	$< 3\%$
Temperature response	$< 1\%$ (-10 $°C$ to +40 $°C$)
Field of view	180°
Maximum solar irradiance	4000 W/m^2
Operational temperature range	-40 $°C$ to +80 $°C$
Humidity range 0 to 100% non-condensing	$< 0.2\%$
Tilt response (0° to 90° at 1000 W/m^2)	$< 0.2\%$
Accuracy of bubble level	$< 0.1°$

Table 4.4: Main specifications of Kipp & Zonen CMP11, installed at the QEERI facility.

for linearity, temperature dependence and directional response to enable transfer of the sensitivity under the measurement conditions in Davos to the Kipp & Zonen calibration laboratory conditions. Both radiometers are mounted side-by-side horizontally on a rotating table and the light is restricted to a small cone around the two radiometers and centred on the axis of the table. The reference and test pyranometers interchange their positions through the rotating table in order to correct for any inhomogeneity in the light field. The sensitivity is calculated by comparing the test pyranometer readings to the reference pyranometer readings and the calibration certificate is produced.

4.2.4 Data collection

The data acquisition system is the COMBILOG data logger provided by Kipp & Zonen and manufactured in Germany by Theodor Friedrichs & Co. This logger is placed inside a weatherproof stainless steel enclosure suitable for outdoor use (see Figure 4.11) and can handle up to 8 analogue signal inputs. For the configuration of the present solar station, 6 of these analogue inputs were used. The COMBILOG operates using a 12 V power supply which fits in the same enclosure of the logger and allows the connection to the mains (AC power). A supply of 12 VDC from a solar panel is also used as a back-up supply with a battery placed inside the enclosure for a potentially unreliable supply. The data and configuration in the COMBILOG are non-volatile and are retained if the power goes off. Each time data are downloaded, they are deleted from the internal memory of the logger. Due to this, an external memory card was used as a backup. The sampling happens every second and the stored data are one-minute averages. Although the connection between the COMBILOG and the PC where data are downloaded and monitored can be made wirelessly via a GPRS/GSM modem, in this case it is made through an RS-232 serial cable, since the distance between the PC and the logger is short (less than 10 m). The clock of the data logger is automatically synchronised with the computer clock after each data retrieval, and the PC clock is routinely verified for drifts using the clock of another instrument updated by a GPS receiver.

For the setup and configuration of the logger, a specific MS Windows software (called COMBILOG) is used, where live data can be viewed but not stored at the same time. However, a manual download of the data is possible. Within the software, each measuring channel is defined as a variable in a variable table. The used sensors are selected from an integrated database and the linearisation of the sensor signals is performed automatically. Another software package, COMGRAPH, is used for data logging; COMGRAPH allows the scheduling of automatic downloads of the data and it also produces graphs and basic analysis of the stored data. Data are stored as text files. The data logger uses the instrument calibration factors (sensitivity) embedded in the library of the software to convert the input voltages into radiation values in W/m^2 according to:

$$E = \frac{U}{S}, \tag{4.4}$$

where U is the output signal of the radiometer in μV and S is the sensitivity in $\mu V/(W/m^2)$.

The COMGRAPH software is used for quick visualisation and daily checks of the data. The graphical representation of each of the solar radiation components is shown individually, and there is no means to include the three plots on the same graph. However, for the data analysis done in this thesis, all data are exported to text files, processed and

Figure 4.11: Data logger in its enclosure, for the communication of the solar radiation measurements from the monitoring station installed at the QEERI facility.

cleaned to be used in C++ macros conceived specifically to apply thorough quality check procedures to the data and for the calculation of the hourly, daily and monthly averages of solar radiation, as well as the other analyses. As an example of the data analysis of the three components, profiles of 1-minute DNI, GHI and DHI collected at the experimental site are shown in Figure 4.12, including cloudy days (7–8 May 2013), clear days (9–11 May 2013), one day with haze (6 May) and days with dust (7–9 June 2013).

4.2.5 Installation and operation site

The solar monitoring station was installed on the rooftop of a building of QEERI's offices, at a latitude of 25.33° N and longitude of 51.43° E. The site was carefully prepared before the installation of the monitoring station. The location on the roof where the solar monitoring station is installed was selected to be as much as possible free of obstructions to the hemispherical view as seen from the plane of the detectors of the radiometers, to eliminate any shadow casting upon any of the instruments at any time and enough free space for the movement of the sun tracker. A raised metallic structure was specifically built and serves as a solid and stable horizontal platform for mounting the SOLYS 2 tripod. The dimensions of the base are 1×1 m^2 with 65 cm height. Three holes were

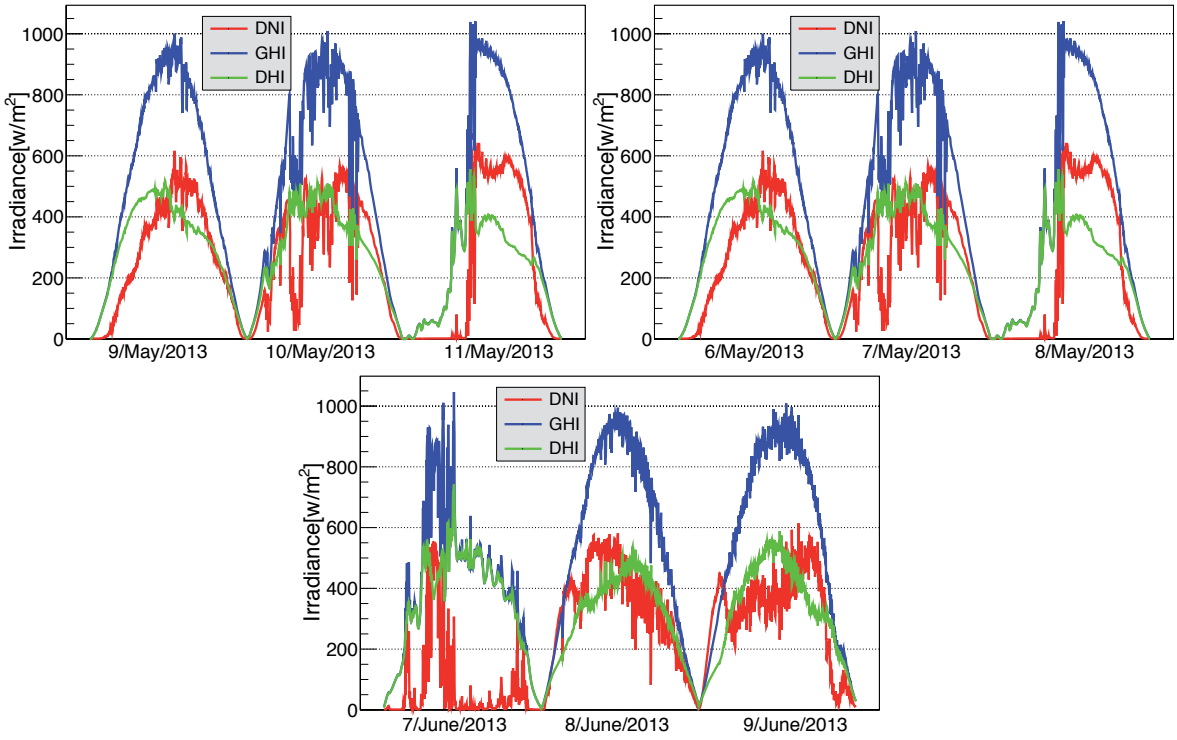

Figure 4.12: Data analysis of DNI, GHI and DHI measured at the experimental site in Doha, Qatar, for clear days (9–11 May), cloudy days (7–8 May), with rain (8 May), with haze (6 May) and days with dust (7–9 June).

drilled for fixing down (bolting) securely the tripod legs of the SOLYS 2 as per the specifications given by the manufacturer. A power connection for the SOLYS 2 was provided. Proper electric grounding was considered for all the instruments during the installation. All the cables connecting the instruments to the data logger are shielded and were provided by the manufacturer.

Daily checks were scheduled for routine maintenance of the instruments; this was possible because of the easy and safe access to the instruments and the near proximity of a control room hosting the PCs of data collection and visualisation. The daily checks include:

- Cleaning the dome of the pyranometers and the window of the pyrheliometer.
- Checking the levelling of the pyranometers and the alignment of the pyrheliometer.
- Checking the levelling of the sun tracker.
- Checking the drying cartridges and that the silica gel is still active.
- Checking the position of the shadow on the pyranometer of the diffuse measurements.

- Checking that the data is properly collected and downloaded from the logger.
- Visual checking of the data in daily profiles to spot any problems.

When the yellow silica gel in the drying cartridge is turned completely transparent, it is replaced by fresh silica gel supplied in small refill packs by Kipp & Zonen. At the same time it is checked that the radiometer mounting is secure and that the cables are in good condition. The replacement of the desiccant by fresh silica was made approximately every 2 to 3 months.

All these checks, as well as any maintenance work or changes done on the instruments, were recorded on a log book kept in the control room, with the date and time and the associated activity performed. This recording is very important, since it helps in the process of identification of problems when bad data are identified and flagged during the data quality control. By examining the log file, any activity that might have influenced the data for the time and date specified by the quality control can be spotted.

4.2.6 Data quality control

While direct measurements are the best method for the knowledge of solar radiation data, errors can be expected, as in any type of measurements. Solar radiation measurements, in particular, are more likely to have errors than the measurements of other meteorological parameters [131], and it is possible to have questionable values even when maintenance and all necessary controls were undertaken prior to the recording of the data. The sources of errors in solar radiation measurements can be divided into two categories: equipment errors and uncertainty, and operation-related problems and errors [132].

In order to make sure that all measured data are reliable, several procedures and software have been developed for post-measurement quality assessment of solar data [133, 134, 135]. For instance, SERI QC [136] is a procedural and software package developed by NREL for quality assessment of data obtained from one-minute to one-hour integrations of the three solar radiation data elements (global horizontal, diffuse horizontal, and direct normal irradiance), defining ranges of acceptable data based on dimensionless parameters normalised with respect to extraterrestrial radiation. The Baseline Surface Radiation Network also has recommendations for radiation data quality checks [137]. The BSRN recommendations were adopted in this research work to ensure the reliability of the acquired data before further processing. The BSRN data quality control includes the following checks:

- Checking whether the measured data do not exceed physically possible limits, which are estimated or defined limits based on basic physical principles. For instance, the

direct normal irradiance should not be less than zero or greater than the extraterrestrial value. The global horizontal irradiance should not be greater than the horizontal component of the extraterrestrial beam. The diffuse irradiance should not exceed the expected Rayleigh diffuse sky. By applying this test, it is possible to spot problems such as the misalignment of the tracker or a dirty pyrheliometer window, and identify thermal offset problems as described in Section 1.3. In some rare situations, the measured value, while correct, may exceed the possible physical limits; this can be due to severe refraction processes, multiple reflections between broken clouds and bright surfaces, inversions, night-time offsets, temperature jumps, etc. [138]. Therefore, a visual inspection and a qualitative assessment of the data is always required for confirmation.

- Checking whether the measured data do not exceed extremely rare limits; these limits have been defined based on the use of meteorological theory and experience, and the analysis of distributions, climatological statistics and extreme weather events [139].
- Checking how the measured data should compare to each other. This consistency check verifies the relationship between the three components (GHI, DHI and DNI) based on Equation 1.11. If the values agree within a few percent, it is likely that the three of them are correct, if not it is likely that one or more of them were poorly measured or the solar tracker was not pointing correctly to the sun. Another test is to check the so-called diffuse ratio, DHI/GHI, to ensure that the diffuse component does not exceed the total radiation.

Table 4.5 resumes the applied physically possible and extremely rare limits tests, and Table 4.6 resumes the consistency checks (the interrelation between the three components and the conditions for the diffuse ratio).

	Min_p	Max_p	Min_e	Max_e
DNI	-4 W/m^2	S_a	-2 W/m^2	$S_a \cdot 0.95 \cdot \mu_0^{0.2} + 10\ W/m^2$
GHI	-4 W/m^2	$S_a \cdot 1.5 \cdot \mu_0^{1.2} + 100\ W/m^2$	-2 W/m^2	$S_a \cdot 1.2 \cdot \mu_0^{1.2} + 50\ W/m^2$
DHI	-4 W/m^2	$S_a \cdot 0.95 \cdot \mu_0^{1.2} + 50\ W/m^2$	-2 W/m^2	$S_a \cdot 0.75 \cdot \mu_0^{1.2} + 30\ W/m^2$

Table 4.5: Quality controls as defined by the BSRN recommendations. The lower physically possible (Min_p) and extremely rare (Min_e) limits, and the corresponding maximum limits (Max_p and Max_e) are defined for DNI, GHI and DHI. S_a is the solar constant adjusted for the earth-sun distance and $\mu_0 = \cos(\theta_z)$ is the cosine of the solar zenith angle.

	Limits
DHI/GHI	< 1.05 for $\theta_z < 75°$ and GHI $> 50\ W/m^2$
DHI/GHI	< 1.10 for $75° < \theta_z < 93°$ and GHI $> 50\ W/m^2$
DHI/GHI	if GHI $< 50\ W/m^2$ the test is not done
GHI/sum	1 ± 0.08 for $\theta_z < 75°$ and GHI $> 50\ W/m^2$
GHI/sum	1 ± 0.15 for $75° < \theta_z < 93°$ and GHI $> 50\ W/m^2$
GHI/sum	if GHI $< 50\ W/m^2$ the test is not done

Table 4.6: Quality controls as defined by the BSRN recommendations for the comparison tests. θ_z is the solar zenith angle and *sum* is $DNI \cdot \cos(\theta_z) + DHI$.

These checks are applied to the measured one-minute data, before any further analysis, in order to ensure the quality of the data and to identify problems. If a one-minute value fails any of these tests, it is flagged accordingly and an investigation is carried out in order to spot the origin of the problem. In the case of this thesis work, this process starts by checking the notes on the log book to see if any particular activity on the instruments or other problems were noted for that specific moment of the day. In addition, a verification was carried out on the daily plots of the data, comparing with the activities on the log book, to identify any problem. The flagged[i] one-minute values are not used in general for the data analysis of the corresponding data set of solar radiation. They can be replaced by an interpolated value or considered as missing value in the calculation of the averages, depending on the problem and the number of consecutive flagged data, see Section 5.2.1. For the data analysis presented in this thesis, the number of flagged entries amounts only to about 1% of the whole sample of data and will be further discussed in Section 5.2.1.

[i] In this document, *flagged* data refers to entries which do not pass the quality tests.

Chapter 5

Solar Radiation Data Analysis

As discussed in Chapter 2, when solar radiation passes through the earth's atmosphere, it is modified by absorption and scattering processes, resulting in different amounts and qualities of solar radiation reaching the earth's surface. This variation depends on the location on earth, and on the incident angle of the solar radiation. For better understanding of the solar energy in Doha, at the experiment site, it is necessary to characterise it and estimate its variations using the past and the current recorded data. A description of the Qatar Meteorological Department's automatic weather stations network is given first. Then, an analysis of the recorded solar data in one of the stations, located in Doha, is presented. Finally, a study of a one-year period of the current solar radiation measured at the QEERI experimental site is shown. This analysis includes the study of hourly, daily and monthly averages as well as frequency distributions of solar irradiance values. Moreover, the clearness index and diffuse ratio are analysed in order to provide insight about the atmospheric conditions in Doha, covering the seasonal variations of solar climate in a one-year period in desert-type conditions. This analysis is important for the knowledge of the characteristics and variations of all components of solar radiation over Doha and is also useful in different fields of application and research, to cite: meteorology, climate studies, material testing, and of course solar energy-based projects.

5.1 QMD Automatic Weather Stations

The Meteorological Department of Qatar operates a network of automatic weather stations distributed across Qatar, measuring solar radiation in the form of global horizontal irradiance. QMD is in charge of the operation and maintenance of the network, which includes periodic cleaning of the instruments and checks on the collected data. Some of the stations are unattended, specially those located deep in the desert, for which the

maintenance is scheduled on a weekly basis. Extra visits and checks are performed after dust storms.

The GHI data are collected and recorded as hourly irradiation totals on the data acquisition system of QMD. However, the data provided to QEERI are daily totals of GHI, for the period from 2007 to 2012, with some number of days that have missing values. The missing values are mainly due to downtime of the stations or data communication issues, according to the QMD technical team.

Solar radiation measured by a well-maintained ground station represents the most adequate way for solar radiation evaluation at a specific location, relevant only within a certain proximity to the ground station, generally up to 25 to 30 km [56]. Beyond this distance, satellite-derived values are more accurate. So if a map of Qatar is to be obtained using only ground stations, a uniform spatial distribution of the stations across the country should be followed, assuming that the mentioned rule of thumb of 30 km between stations is valid in Qatar. The solar radiation variations depend on the geographic and atmospheric characteristics of the location, amongst other parameters. In a flat and small country like Qatar, the application of this rule seems to be feasible. Figure 3.9 shows the sites of the network of AWS installed in Qatar by QMD.

In order to have an idea about how the current network of stations is distributed across Qatar, the distance between all pairs of existing stations of the QMD network is presented. Figure 5.1 shows in a histogram the distance to the closest neighbouring station for each of the 12 stations, in bins of 5 km. Each pair of stations was counted one time. It can be seen that the majority of the inter-station distances are between 25 and 40 km, 2 stations have a neighbour in close proximity (between 5 to 10 km away), for one station the distance to its closest neighbour is within 15 and 20 km, and the biggest inter-station distance is between 50 and 55 km for one station as well. However, a study of the distances is not sufficient to determine whether this network is providing sufficient coverage of solar radiation variations across the country, and additional parameters have to be looked into in order to confirm the same, such as the topography of the country and the existing meteorological and atmospheric conditions.

In general, the relative variation of the daily global solar radiation per distance, between all pairs of stations in Qatar, does not exceed 5.5% on average. This indicates that the distribution of the stations within the existing network provide a good coverage of the possible GHI variability within Qatar and a GHI solar map of Qatar could be produced by interpolating between the measuring points of the existing network. However, to deduce the DNI solar maps using exclusively ground stations, more stations should be added to the existing network, in a way to cover all possible DNI variations, since DNI

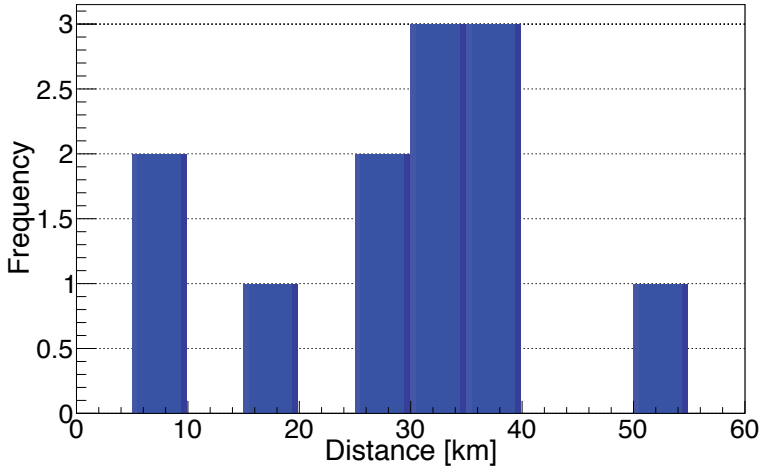

Figure 5.1: Distance in km to the closest neighbouring station for the QMD ground stations.

is more sensitive than GHI to the varying aerosol loads in the atmosphere. Aerosols may change in type and concentration between different areas within Qatar. These areas can be separated as follows: coastal, inland, industrial, unpopulated, and desert zone close to Saudi Arabia. To detect the variations of aerosol from one area to another, and thus DNI, more stations should be added to the existing network and should be located inland and in the centre of Qatar, ensuring a distance not more than 25 to 30 km away from their nearest neighbouring stations.

5.1.1 Historical solar radiation data in Doha

This section focuses on the analysis of daily GHI data taken at the Doha International Airport station of QMD, for the period 2008 to 2012. This data sample is used for cross checking with the solar data collected by the solar monitoring station at QEERI, located around 17 km away from the station of the airport. The analysis includes the inter-annual variability, daily and monthly averages of GHI values, and daily and monthly averages of the clearness index, all of them calculated from the daily total irradiation values provided by QMD. Doha, the capital city of Qatar, is a coastal and expanding city, located on the central east coast of the country. It has a hot and desertic climate with high humidity. The long summer extends from May to September; it is characterised by intense heat with temperatures that can reach 50 °C, and days alternating between dryness and humidity. During winter, temperatures are moderate. Rainfall is rare in Doha, with almost no precipitation during summer, and less than 20 mm during other months. Similarly to the whole country, sudden and violent dust storms occasionally strike Doha, causing a dimming of solar radiation.

The QMD measuring station located at the Doha International Airport (25.246° N, 51.569° E) is near the coast. Like all the other solar radiation monitoring stations installed by QMD in Qatar, the airport station is equipped with a Kipp and Zonen pyranometer of type CM6B. The analysis of the global radiation data is based on the calculations of data provided by QMD as daily total global radiation in J/cm^2. This station started operation in 2008. The percentage of days with available daily values reported until 31 December 2012 is 93%. Due to lack of information about the quality controls and checks of the data, no data-filling procedure was performed. Days with missing values are ignored in the calculations of the averages shown here.

The year-to-year variation of the daily averages of GHI in Doha for 5 years, from 2008 to 2012, in $kWh/m^2/day$, is shown in blue in Figure 5.2; the red line and shaded band represent the average and standard deviation of the 5 years. The calculation of the average Avg_i for the i-th year and standard deviation σ of these averages are done as follows:

$$Avg_i = \frac{1}{N_{i,valid}} \sum_{n=1}^{Ni} GHI_{i,n}, \tag{5.1}$$

$$\sigma = \sqrt{\frac{1}{5} \sum_{i=1}^{5} (Avg_i - AVG)^2}, \tag{5.2}$$

where Avg_i is the average GHI in year i, Ni is the total number of days in year i, $GHI_{i,n}$ is the GHI value on day n of year i, $N_{i,valid}$ is the number of days in year i with *valid* GHI values[i], and AVG is the 5-year average.

In Table 5.1, the calculated daily average of each year is presented with the number of valid days for each year. The year with highest number of missing daily data is the year 2008, with 22% of the 366 days, or about 2.6 (non-consecutive) months; during that year, the data gaps were mostly present in January, February and March, while the other years show better data availability.

To resume the findings: for the 5-year period under study, the average daily GHI value at Doha Airport is 5.611 $kWh/m^2/day$, or a total of 2048 kWh/m^2 per year. It is noticed that the average of the year 2009 is lower by 4% than the 5-year average, a deviation which falls within the common fluctuations of 2 to 7% in annual GHI [140, 141].

Figure 5.3 shows the monthly averages in blue and peaks of daily global radiation per month in red. The thinner lines show the individual years, highlighting in green the years 2008 and 2009, which exhibit lower averages than the longer term 5-year average. The

[i]By valid days, it is meant days with non-missing daily GHI values.

Year	Daily GHI $[kWh/m^2]$	Valid days
2008	5.675	286
2009	5.377	324
2010	5.735	360
2011	5.679	353
2012	5.579	348

Table 5.1: Annual means of daily GHI for Doha International Airport, and the corresponding number of days with non-missing daily GHI values.

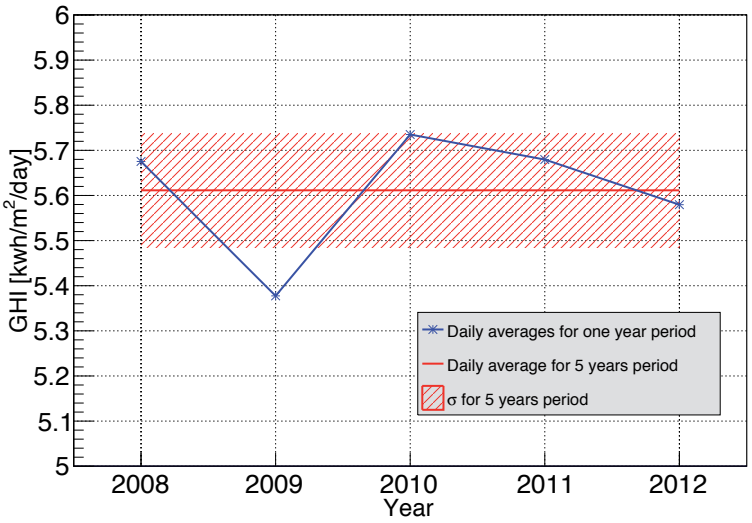

Figure 5.2: Annual variation of daily GHI averages at Doha International Airport.

average for the i-*th* month of the year was calculated as follows:

$$Avg_i = \frac{\sum_{days_i} \sum_{yrs} GHI_{i,yrs}}{N_{i,valid}}, \tag{5.3}$$

which is the sum of the GHI values in month i for the 5 years, divided by $N_{i,valid}$, the total number of days with valid values in month i during the 5-year period.

The figure shows that the monthly averages of GHI are above 6 $kWh/m^2/day$ from April to September. Considering the whole year, the range goes from 4 to 7 $kWh/m^2/day$. The highest average is 6.967 $kWh/m^2/day$, found in June, and the lowest is 3.867 $kWh/m^2/day$, found in December. The highest peak is 8.411 $kWh/m^2/day$, in June, and the lowest peak is 4.77 $kWh/m^2/day$, in December. As seen in Figure 5.2, the year 2009 exhibits a low yearly average compared to other years. In order to understand the month by month contribution to the yearly average of the year 2009, this year is highlighted with a solid green line in Figure 5.3. The averages in July, August, and December have lower values. In August 2009 there are only 6 days of valid daily data; although the

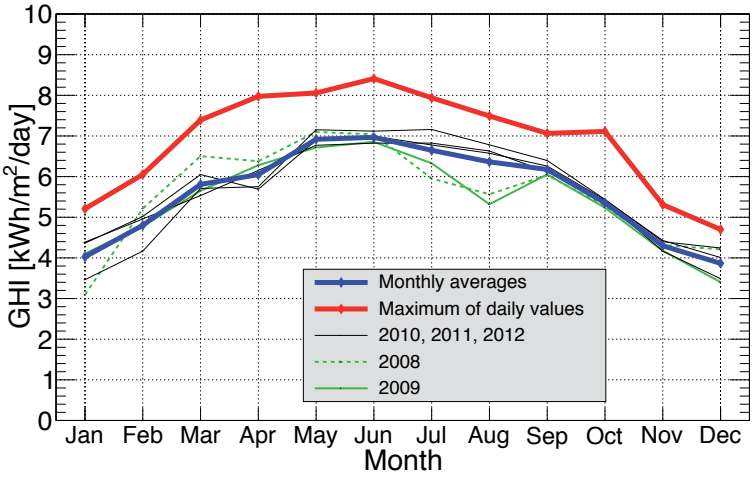

Figure 5.3: Monthly averages and peaks of global radiation at Doha Airport throughout the year.

calculated monthly average only considers the days with non-missing values, the average obtained with these 6 days is not necessarily representative of the whole month. Similarly, the year 2008 (green dashed line) also shows low values in the months of July, August, and January, but the low values are compensated by higher values during the rest of the months.

The daily averages of global radiation for the period from 2008 to 2012 in $kWh/m^2/day$ are shown in Figure 5.4. The average for the i-th day of the year was calculated as follows:

$$Avg_i = \frac{\sum_{n=1}^{Ny} GHI_{i,n}}{Ny_{i,valid}}, \tag{5.4}$$

where $Ny = 5$ is the total number of years and $Ny_{i,valid}$ is the number of years in which day i has valid GHI values.

Similarly to the monthly averages, the daily averages have higher values during summer months. The highest daily average for the period 2008 to 2012 occurs during the month of May and is 7.49 $kWh/m^2/day$, while the lowest average is 3.02 $kWh/m^2/day$, in the month of November. The individual maximum daily values for each month are shown in red in Figure 5.3.

To give more insight about solar radiation at the site, the clearness index was also analysed. This index indicates the atmosphere's effect on the transmission of solar radiation. The monthly average clearness index K is defined [16] as the ratio of monthly average of daily GHI to the monthly average, $\overline{H_0}$, of daily extraterrestrial radiation on a

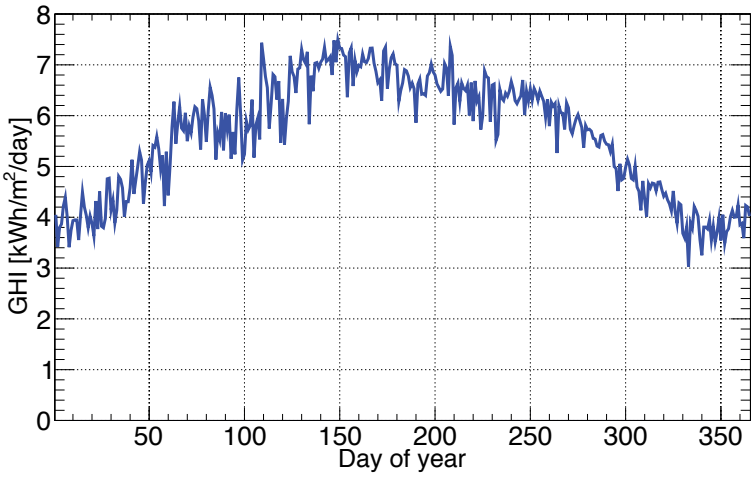

Figure 5.4: Daily averages of global radiation at Doha Airport throughout the year.

horizontal plane (H_0 from Equation 5.6), i.e.,

$$K = \frac{\overline{GHI}}{\overline{H_0}} \tag{5.5}$$

In Figure 5.5, the monthly averages of the clearness index at Doha Airport are shown for the period from 2008 to 2012, with their standard deviations. It is noticed that the averaged K ranges from 0.58 to 0.65 and shows relatively small variations throughout the year. This is due to a balance between cloudy days in the winter and hazy and dusty days in the summer. Considering these more or less constant atmospheric conditions between seasons, H_0 and GHI change in parallel through the year (cf. Figures 5.11 and 5.4), and the monthly averages of K are relatively stable during a year period. It is also seen that the standard deviations vary from month to month, depending on the stability of the atmospheric conditions during each particular month.

On the same graph, the monthly K values obtained from the NASA-SSE database are also shown. This database consists of monthly data, average of 22 years of satellite measurements, from 1983 to 2005, provided for $1^\circ \times 1^\circ$ pixels. The averages of K as obtained by NASA range from 0.50 to 0.65, showing larger variations in a year period, in comparison with the ground-based K. Between April and September, both graphs are in good agreement. However, during the winter months from October to March the NASA-SSE values are lower. It must be noted that the NASA-SSE values are longer-term averages (22-year averages, from 1983 to 2005), while the ground values are derived from a 5-year period (2008 to 2012), lying outside the coverage period of NASA-SSE. Given that NASA-SSE values are modelled data, deviations from ground values are expected depending on the validity of the model in the conditions of the region. Moreover, the NASA-SSE value is the average over a region of $1^\circ \times 1^\circ$. This translates to approximately

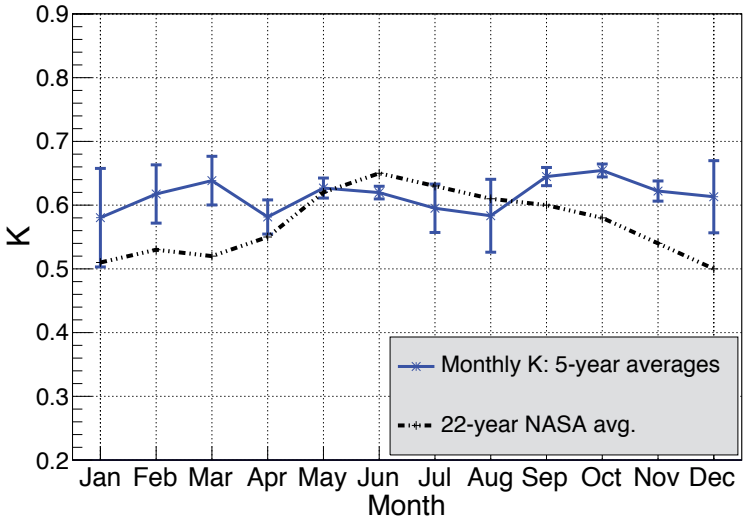

Figure 5.5: Comparison between ground-measured and NASA-derived monthly clearness index at Doha Airport throughout the year.

$110 \times 100\ km^2$ at Doha's latitude, which is almost the size of the country. For all these reasons, the disagreement between the two sets of data is expected, and one can rely on the ground-measured data, which are more representative of the conditions in Doha.

More details on the variation of K can be obtained from the daily clearness index values, shown in Figure 5.6. The daily clearness index is the ratio of a particular day's GHI to the extraterrestrial radiation (on a horizontal plane) for that day.

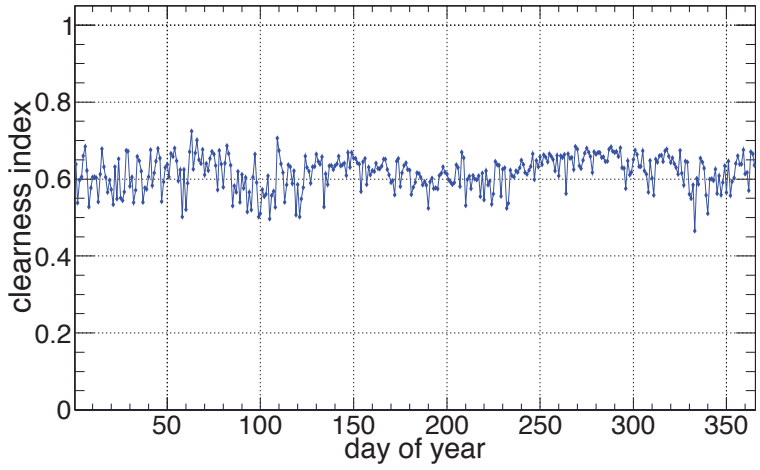

Figure 5.6: Averages of daily clearness index at Doha Airport throughout the year, for the period 2008 to 2012.

Figure 5.6 shows fairly constant values of daily clearness index in Doha throughout the year, although with more fluctuations in winter months due to the presence of varying clouds, while dust and haze are more constant in the summer.

The relation between sky conditions and daily values of clearness index has been studied by [142, 143] for example, but there is no consensus on sky condition classifications related to clearness index values. According to the European Solar Radiation Atlas report [144], the 5-year average of $K = 0.62$ found in Doha implies very sunny climatic conditions.

To have a point of reference and comparison with other values, Table 5.2 shows the annual averages of the monthly K for Doha and other cities in the world. The 5-year ground measurement-derived K for Doha is higher than the NASA-SSE value, while ground measurements for Abu Dhabi [145] (1-year average) are lower than the NASA value. Also included in the table are the year by year K values for Doha. As expected from the GHI yearly averages, year 2009 shows a lower K than other years.

City	K	year by year (2008 to 2012)
Doha, ground[a]	0.62	0.61, 0.60, 0.63, 0.62, 0.62
Doha[b]	0.57	
Abu Dhabi, ground[c]	0.58	
Abu Dhabi[b]	0.60	
Ankara[b]	0.53	
Cairo[b]	0.60	
Dammam[b]	0.61	
Athens[b]	0.53	
Tunis[b]	0.58	
Tehran[b]	0.57	

Table 5.2: Annual averages of clearness index for Doha and other cities; (a) 5-year average of ground measurements, and year by year, (b) 22-year averages by NASSA-SSE, and (c) 1-year ground measurements, 2007.

5.2 Solar radiation data analysis

In this section, the analysis of ground measurements of solar radiation collected at the QEERI site, 25.33°N, 51.43°E, is presented. The data was collected over one full year starting from the 1st of December, 2012, to the 30th of November, 2013. By the nature of the solar sensors used, the collected data are classified as DNI, GHI, and DHI (see Chapter 4 for more details on the experimental site and instruments). The three components were collected as 1-minute average irradiances (averages of samples taken every second). Considering no missing points in the data set, the total number of data per radiation

component for the year under study should be 525600 values. However, the actual total number of collected values per component was 514763 data points, which means that the data set has missing values equivalent to 7 days, 12 hours, 37 minutes, or 2% of the total. The missing values were distributed as follows: 4 minutes missing in December 2012, 7 minutes missing in February 2013, and 10826 consecutive minutes missing in April 2013. The missing data in April was due to a problem of the memory in the data logger. To avoid similar problems in the future, an external memory card was fitted to the data logger and is used as a backup for data recording. The missing data were ignored and no data gap filling procedure was implemented. Instead, the averages were calculated based on the actual collected data points.

5.2.1 Data quality control

Prior to any further data processing and analysis, quality control (QC) checks were performed on the recorded data, following the BSRN standards [137], as discussed in Section 4.2.6. The procedure consists of flagging the 1-minute data of each component according to checks on physical limits, extremely rare values and consistency tests among all components (see formulas in Tables 4.5 and 4.6). All data with flags indicating failed tests (from here on, called *flagged data*) detected by the QC procedure were then scrutinised in order to understand the reasons behind the erroneous values. The data analyses in the next sections are based on the data which passed the QC tests. Flagged data were ignored and not considered in the calculation of the averages shown in this chapter.

For the used data set, Table 5.3 summarises the number of flagged 1-minute data (the entries that failed the corresponding QC test) for the physically possible limits and the extremely rare limits, per irradiance component (DNI, GHI and DHI) and per test. Table 5.4 shows the number of entries which failed the comparison tests: consistency among the three components and the diffuse ratio test. Only data between sunrise and sunset were considered in these tables; sunrise and sunset are determined by a solar zenith angle of 90.83° according to the definition given by [146]; in order to check whether the data that fail the QC checks are close to the sunrise or sunset times, statistics of data points excluding moments close to sunrise and sunset are also shown: data with zenith angles less than 85°, 80° and 75°. Figures 5.7 and 5.8 show the sunrise and sunset times for this location in Doha through the year.

As a result of the quality control tests applied on the data set, the total number of flagged data, about 1%, is negligible relatively to the total number of available data. For the physical and extremely rare limits tests, the percentages of flagged data are greatly reduced when excluding data close to the sunrise and sunset times, as expected because

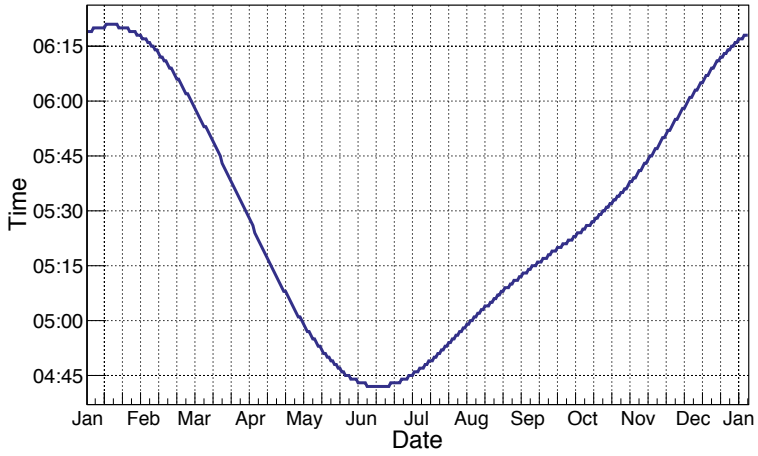

Figure 5.7: Sunrise time calculated day by day over a period of one year at the QEERI site in Doha, Qatar.

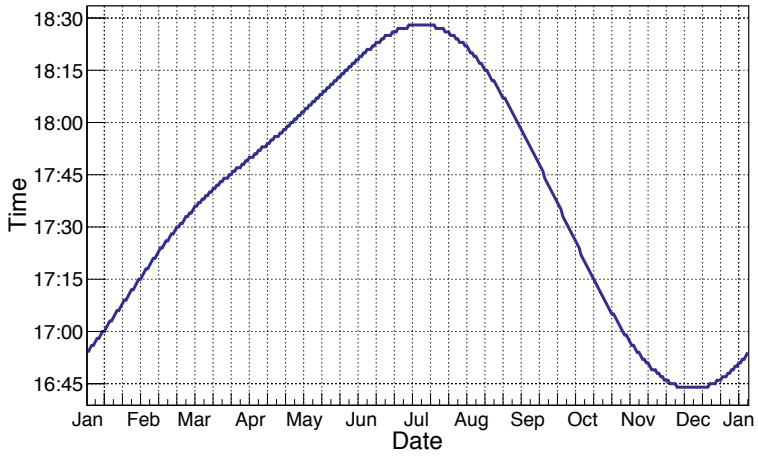

Figure 5.8: Sunset time calculated day by day over a period of one year at the QEERI site in Doha, Qatar.

of the lower performance of the sensors (pyranometers in particular) at low solar elevation angles. For the comparison tests, the flagged data were checked against the log book as discussed in Section 4.2.6, and it was found that for most of these flagged minutes, the reason was an intervention or activity such as the routine cleaning of the sensor domes.

An additional check was used as a quick test to verify the consistency of the data timestamps with respect to the sun's position through the year. For this test, the complete data sets, containing the values of DNI and GHI, collected as 1-minute averages over the year of 2013, are presented in Figure 5.9, in a way to show the 365 days of the year on the x-axis, and the 1440 minutes of each day on the y-axis, with a colour scale displaying the radiation level at each point. The colour-coded intensity axis is on the right of each

	SZA $\leq 90.83°$		SZA $\leq 85°$		SZA $\leq 80°$		SZA $\leq 75°$	
	phys	ext	phys	ext	phys	ext	phys	ext
DNI	1	51	0	50	0	46	0	43
GHI	1336	2943	55	67	38	39	16	17
DHI	2893	4229	51	79	38	48	16	24
Available entries	260484		241015		224236		207355	

Table 5.3: Number of entries which fail the physically possible limits (phys) and extremely rare limits (ext) tests, and the total number of collected entries in each solar zenith angle (SZA) interval.

	SZA $\leq 90.83°$	SZA $\leq 85°$	SZA $\leq 80°$	SZA $\leq 75°$
$GHI/(DNI\cos(SZA)+DHI)$	2456	2361	1517	1386
DHI/GHI	2	2	2	2
Available	260484	241015	224236	207355

Table 5.4: Number of entries which fail the comparison tests: the comparison among the three components and the diffuse ratio test. The total number of collected entries within every solar zenith angle (SZA) cut is also shown.

plot and represents the irradiance in W/m^2 for each minute, with violet representing the lowest levels of radiation, and red for the highest levels of radiation. Two red lines were drawn independently on top of each graph, and represent the calculated sunrise and sunset times through the year. The sunrise and sunset lines perfectly contain the evident daytime values throughout the year, which gives a quick verification that there is no shift in time and the data follow the expected temporal variations of solar radiation during each day. In addition, the mean y values, displayed in the statistics boxes on each figure, provide a verification of the local solar noon time in this location, which occurs around 11:30 am (deducted from the equation of time, see Section 1.2.1). The days with missing data in April are noted as discontinuities, around day 110. This test provides an initial assessment of the data set and serves as a quick overview of the quality of the collected data.

As expected and since DNI is measured normal to the sun's rays, it is noticed that the higher values of 1-minute DNI can be found all around the year. The highest peaks were found in winter; however, the minute values within a day in winter have larger fluctuations than in summer. GHI, on the other hand, being measured on a horizontal surface, depends

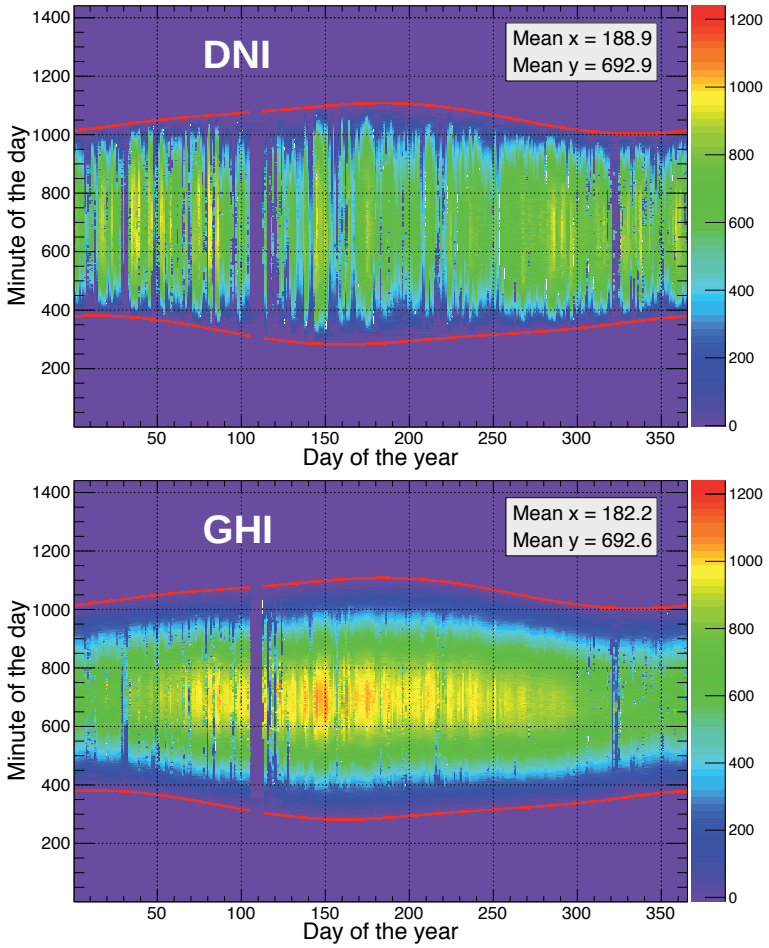

Figure 5.9: 1-minute values of solar irradiance, in W/m^2, through one year in Doha.

on the sun angles during the year and thus it is season-driven; the displayed minute values of GHI show a smoother distribution through the year, with higher values concentrated in the summer season. These behaviours are furtherly analysed in the following sections, by aggregating the data in terms of hourly, daily and monthly averages.

Data gap filling

In general, in Geosciences, several approaches can be applied in order to fill the gaps found in the data sets. These methods are either parametric (based on models) or non-parametric (depending only on the data) [147, 148, 149, 150]. In solar radiation, similar procedures could be implemented for filling the gaps. The length of the gap, i.e., hourly data missing in one day, or daily data missing in a year, etc. is one of the main factors to take into account when deciding on the data gap filling method. For instance, the National Solar Radiation Database (NSRDB) of the USA, uses the following methods for filling the gaps in the data set of measurements, taken between 1961 and 1990: for gaps of 5

hours or less, linear interpolation is used, for gaps from 6 to 47 hours, they substitute data from the same hours of adjacent days, and for gaps of 2 days to one year, the substitution of data is from the same calendar days from another similar year [151]. They have also investigated other methods such as filling the solar model input parameters and modelling the solar irradiance based on the filled input parameters. They also used modelled data for filling gaps in the measured data. Gap filling procedures for solar radiation data were also developed as part of the Solar Radiation Resource Assessment (SRRA) project in India, which describes the Indian experience in operating solar monitoring stations [152]. Their basic gap filling procedure relies on the availability of the three components of solar radiation (DNI, GHI and DHI) and on the duration of the gap, with gaps up to 3 hours, greater than 3 hours and gaps greater than 24 hours, and consist of using the equation relating the three components, modelled values, linear interpolation of clearness indices or by replacing data from neighbouring days. The standardisation of procedures for gap filling is also in the core activity of the IEA Task 46 "Solar Resource Assessment and Forecasting", which addresses the basic objectives and means to understand and improve the knowledge of solar energy resources [64].

In this thesis work, the missing values are due to two reasons: either the value was recorded but flagged by the quality control tests and therefore considered as missing, or the value was not recorded by the data acquisition system. As commented before, it was decided not to apply any gap filling for this work, so the averages represent the available minutes. The number of missing minutes in December and February was negligible, so they have no effect on the calculation of the averages; in April, although the number of missing minutes is not negligible, the decision of ignoring these days in the calculation of the averages was based on the fact that several years of measurements should be available in order to decide on and apply a procedure for filling the gaps, in particular when several days are missing, and such data is currently not available for Doha, or any part of Qatar.

5.2.2 Extraterrestrial solar radiation

As seen in Chapter 1, the radiation emitted by the sun and arriving at the top of the earth's atmosphere, known as the extraterrestrial radiation, is not constant through the year, changing by ±3.3% depending on the distance between the earth and the sun. Figure 5.10 shows how the extraterrestrial radiation varies throughout a year, because of the changes in the sun-earth distance. Equation 1.1 is used for the calculation of the direct, or beam, extraterrestrial radiation calculated on a plane perpendicular to the sun's rays at the top of the earth's atmosphere.

The extraterrestrial radiation on a horizontal surface (also at the top of the atmo-

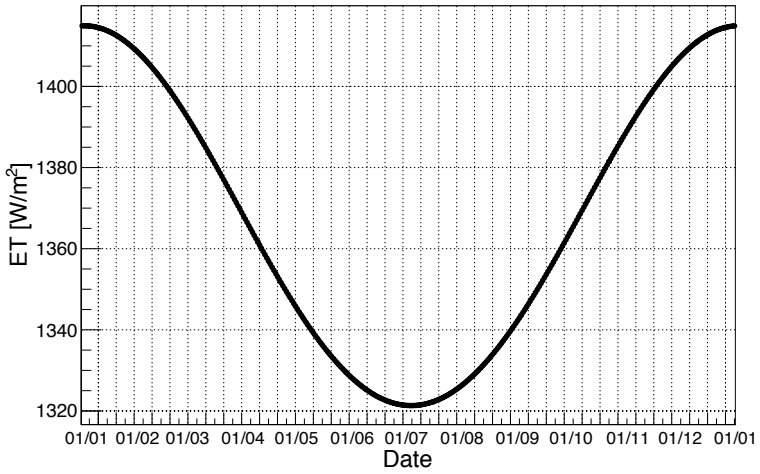

Figure 5.10: Variation of the beam extraterrestrial solar irradiance in a one-year period.

sphere) depends, in addition, on the position of the sun relative to the location on the earth's surface. At any time, it can be calculated from the direct extraterrestrial radiation modulated by $\cos\theta_z$, the cosine of the zenith angle of the sun (θ_z) at that time, and can be integrated over the period from sunrise to sunset in order to obtain the total daily extraterrestrial radiation on a horizontal surface, denoted as H_0. The term $\cos\theta_z$, given by Equation 1.3, takes into account the geometry and the position of the horizontal surface with reference to the angle of incidence of the solar radiation, that is, the declination angle of the sun (δ), the latitude of the surface of interest (ϕ) and the solar hour angle (h). H_0 can be calculated, in W/m^2, as follows [16]:

$$H_0 = I_0 \cdot \left[1 + 0.033 \cdot \cos\left(\frac{2\pi n}{365}\right)\right] \cdot \cos(\theta_z), \tag{5.6}$$

where I_0 is the solar constant (1367 W/m^2), n is the day of the year (1 to 365), and θ_z is the zenith angle of the sun. For more information on the sun geometric angles, refer to Section 1.2.1. Figure 5.11 shows the variation of the daily total extraterrestrial radiation on a horizontal surface throughout the year, for the location of the experimental site.

It is clear that the variation of the daily extraterrestrial radiation at this location is relatively large and the radiation is about 70% higher in summer than in winter. This is a crucial feature and is used in the study of the atmosphere when it comes to calculating the normalised level of radiation at ground level, that is, the amount of radiation at the surface of the earth compared to the amount of radiation at the top of the atmosphere.

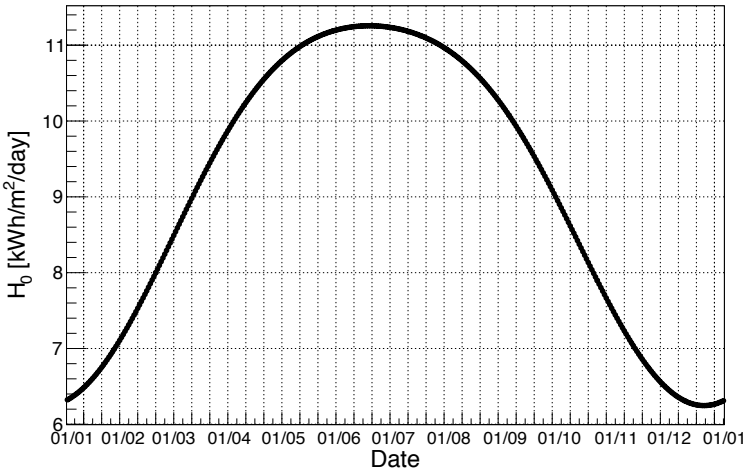

Figure 5.11: Variation of the daily extraterrestrial solar irradiation on a horizontal surface at the experimental site in Doha, in a one-year period.

5.2.3 Hourly, daily and monthly irradiances

An analysis of the ground-measured solar data at the location under study is given in this section. The goal is to study the characteristics of solar radiation in Doha over a one-year period, from December 2012 to November 2013.

The quality-controlled minute values of DNI, GHI and DHI in W/m^2 were used for the calculation of the hourly, daily and monthly averages. The month of April shows a gap in the data but no gap filling procedures were used, as discussed in Section 5.2.1, so April was represented by 23 days of data (around 77% of the month's possible values). For the calculation of the averages, only daytime (from sunrise to sunset) minute values which pass the quality control tests of physical limits and consistency were included. Night values, which are usually negative in the GHI and DHI signals due to the thermal offset of pyranometers (see Section 1.3), were set to zero for the 3 components and counted in the calculation of daily and monthly averages, i.e., these averages are normalised to days of 24 hours. For the calculation of the hourly averages, all minute values within the sunrise to sunset interval, regardless of their sign, were considered as long as they pass the quality checks. Close to the sunrise and sunset hours, the measured values are close to zero but both positive and negative values can be found. It was decided to include all in the calculation of hourly averages (note that this only affects the hours including the instants of sunrise and sunset) because of the measurement uncertainties.

The averages of hourly DNI, GHI and DHI are shown in Figure 5.12, considering the whole year. The averages are calculated in 24 bins of 1 hour each. The bin 12, for example, represents the average of the minutes from 11:01 am until 12:00 pm. The curves

present a more or less symmetrical shape centred around solar noon, the typical variation of the solar radiation during daytime, from sunrise to sunset. It is noticed in the graph, that shortly after solar noon the direct radiation tends to be slightly lower than just before solar noon. This is probably due to the stabilisation of the atmospheric conditions in the afternoon period, concentrating a higher amount of aerosols in the atmosphere. This is not the case of the global radiation, since the lower level of the direct component is compensated by an increase of the diffuse component at that time.

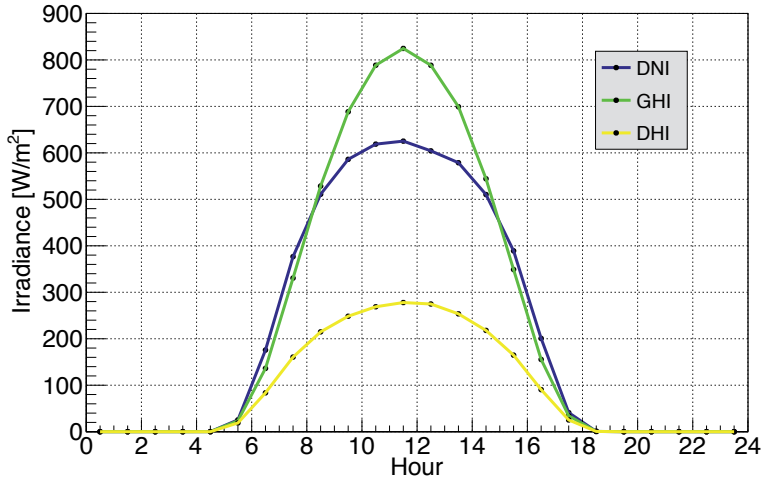

Figure 5.12: Hourly DNI, GHI and DHI in Doha, averaged over one year, from December 2012 to November 2013.

Note also that, as shown in Figures 5.7 and 5.8, the sunrise and sunset times change from day to day, and for the experimental site there is a maximum difference of around 1 hour and a half between winter and summer. For more clarity and in order to separate the averages along the year, the hourly averages were calculated for each month and are presented in Figure 5.13 for DNI, GHI and DHI. GHI hourly averages are higher in the summer months, and for hours close to solar noon one can distinguish two periods: one with higher level of radiation, including the months from March to October, and the second with relatively lower level of radiation, from November to February. This is not the same for the hourly averages of DNI, which do not exhibit a clear seasonal trend from month to month; the month of October shows the highest DNI levels and April shows the lowest levels of DNI during this year of data collection; although April was represented by 77% of its data points, little or no bias is expected to result from this and the calculated averages are estimated to be representative, since hazy and dusty conditions were present most of the days of this month, as the daily averages will indicate. Nevertheless, an accurate estimation of the bias is only possible by comparing with a different set of ground measurements of a nearby station, which is not available.

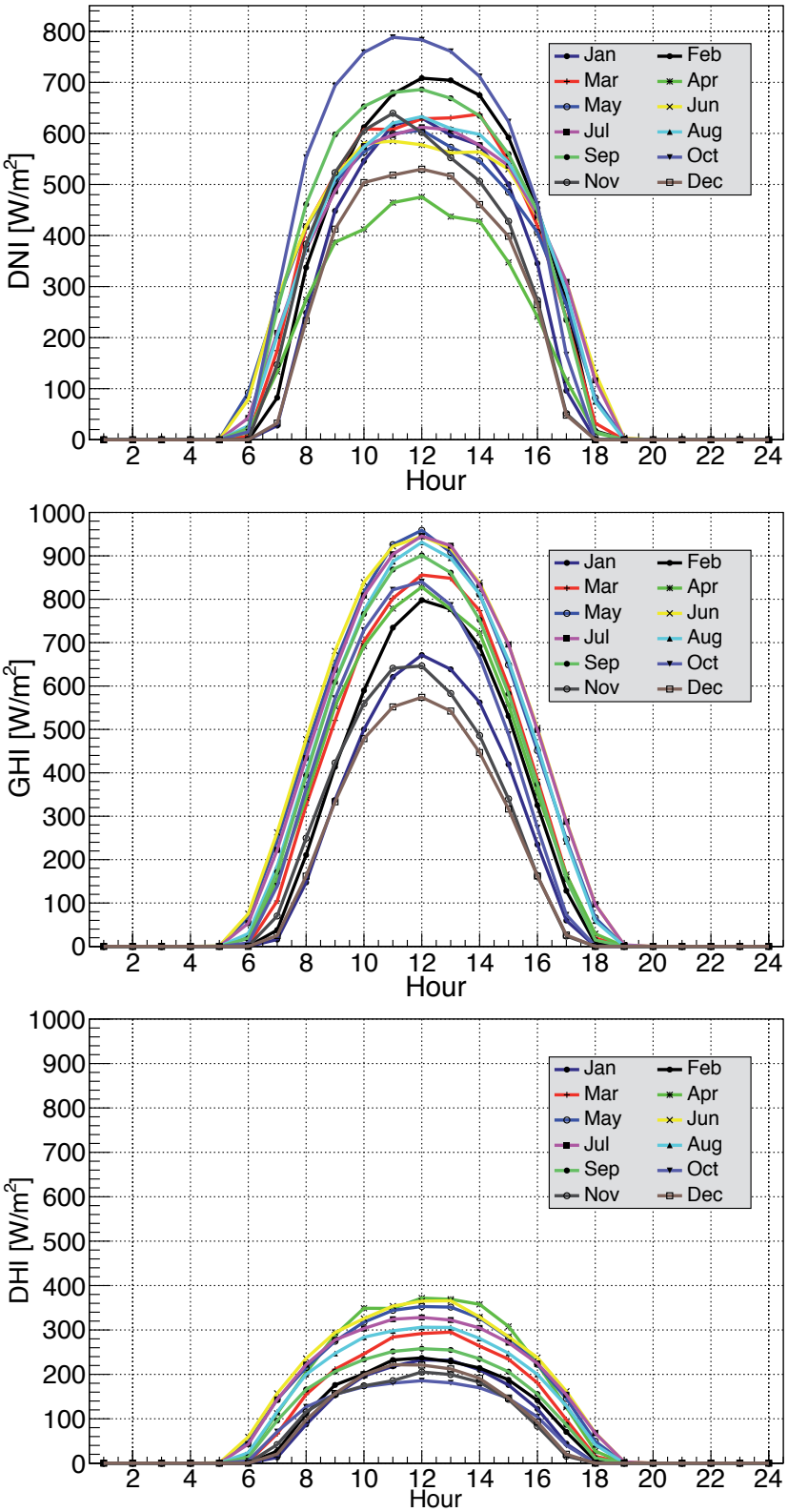

Figure 5.13: Hourly DNI, GHI and DHI in Doha, averaged per month, for all the months in a one-year period, from December 2012 to November 2013.

The daily averages of DNI, GHI and DHI are shown in Figure 5.14. The maximum 1-minute value of the day is shown in red. As discussed, these averages include the 24 hours of the day. For clarity in the graphs, to help differentiate visually between missing and actual low averages, missing days are shown as -50 W/m^2 (7 days in total) and days with more than 3.5 hours of missing data are shown as -60 W/m^2 (1 day). In general, it is noted that the daily values, and even the minute peaks, show larger fluctuations from November (last days in the plots) to June (around day 210), due to the occasional and intermittent cloudy conditions in these months, than from July to October, when days are mostly cloudless but often with a presence of haze and dust for days or weeks at a time.

The daily averages of DNI display large day to day fluctuations during this period with no evident seasonal changes through the year. This is due to the different atmospheric conditions encountered in the atmosphere of Doha from day to day, which can change from clear to cloudy (mainly in winter), hazy or dusty (mainly in summer), anytime during the year. The 1-minute peaks are in general higher during winter than in summer, due to higher aerosol levels in the summer that continuously decrease the level of direct radiation. The maximum daily average of DNI was calculated for 25 May with a value of 407.2 W/m^2, and the maximum measured minute DNI value was 987.5 W/m^2, on 22 March 2013.

The daily GHI averages show smaller day to day fluctuations in general and, as expected, values are higher during the summer months. The highest daily GHI average is found on 30 May with a value of 356 W/m^2 and the highest minute GHI value is 1231.5 W/m^2, measured on the first of May 2013.

Daily DHI averages show relatively constant values until March, when values started increasing because of more days with dust and haze, until around mid-August, when DHI started decreasing again. The highest daily DHI average value is 205.8 W/m^2, found in the summer, on 11 June, and the maximum minute DHI value is recorded for the first of May 2013, with the value of 757.7 W/m^2.

The monthly averages of DNI, GHI and DHI are shown in blue in Figure 5.15 and the maximum daily averages for each month are shown in red. The monthly averages are calculated from the 1-minute values of radiation.

The monthly DNI averages increased from December to February and remained almost constant from March until September, except for the low value observed in April. As discussed before, the low average in April is estimated to effectively represent the radiation level available during this month; while it is true that this month has missing values which were not counted in the calculation of the monthly average, it is unlikely that these days

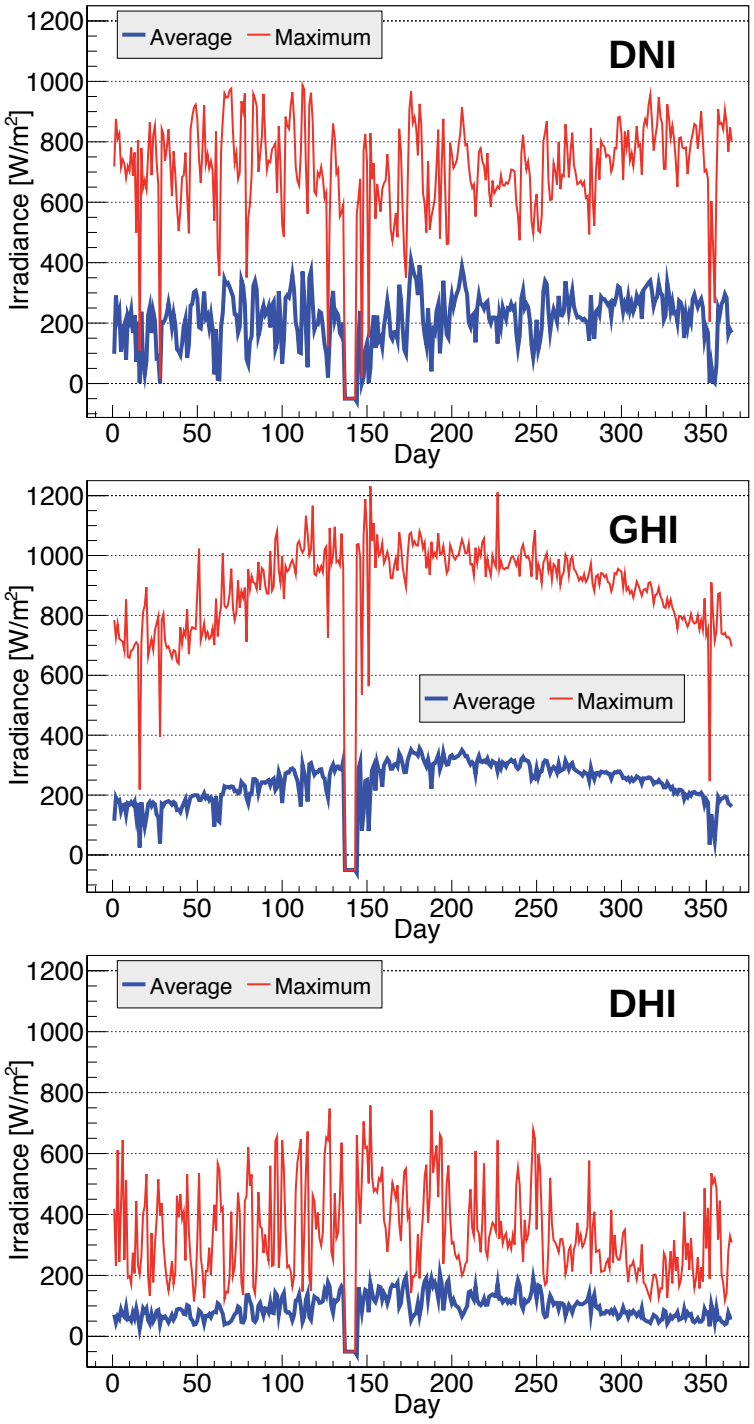

Figure 5.14: Daily averages and maximum minute values per day for DNI, GHI and DHI in Doha in one year, from Dec/2012 to Nov/2013. Values for missing days are set to negative (see text).

had high levels of radiation, because of the values seen around this period (cf. Figure 5.14) and because during the month of April there was a high frequency of cloudy days and days with dusty and/or hazy conditions, to which DNI is highly sensitive [5]. The month

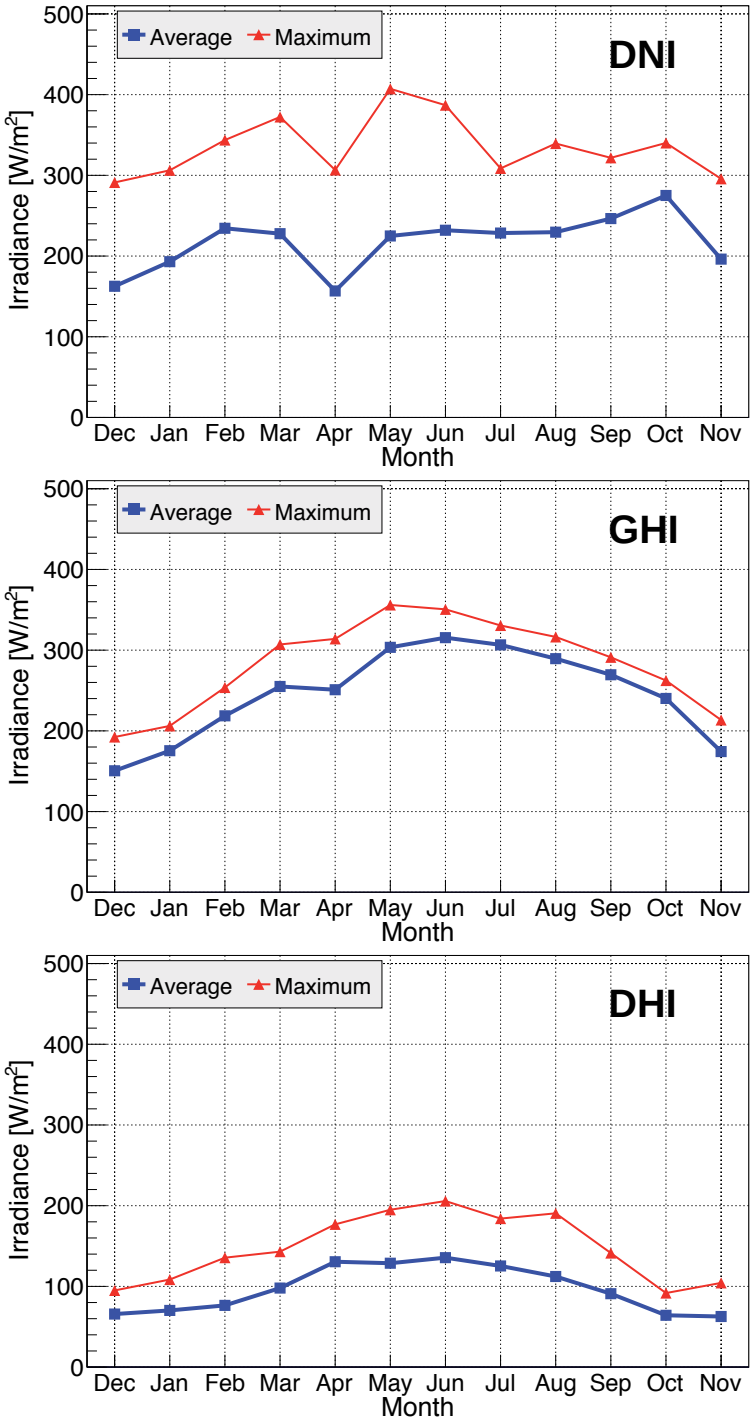

Figure 5.15: Monthly averages and maximum daily values per month for DNI, GHI and DHI in Doha during one year, from December 2012 to November 2013.

of October shows the highest average of DNI with a value of 275 W/m^2. Atmospheric conditions during this month were particularly clean and there were few days with dust or haze.

The monthly averages of GHI have high values in summer time, except from March

to April where the value remains almost constant. From May to July, GHI monthly averages are above 300 W/m^2, with the highest monthly average of 315.5 W/m^2 in June. The lowest value was observed in December with 165 W/m^2, which means that GHI values almost doubled between December and June.

DHI monthly averages show higher values in the summer, with the highest in June with 135.6 W/m^2. The lowest monthly averages of 65 W/m^2 were found in December 2012, October and November 2013.

The monthly averages of GHI calculated for the QEERI station were compared with the longer-term (5 years, 2008–2012) monthly averages calculated in Section 5.1.1, for the station at the Doha International Airport belonging to QMD. This is summarised in Table 5.5. The relative difference between the two data sets is less than ±10% for all months, which means that the current measurements are consistent with historical data observed in Doha. The relative difference in April is less than ±1%, which indicates that the low monthly average calculated for this month at the QEERI station is not biased by the missing values.

Month	QEERI	QMD	rDifference (%)
Dec	3.61	3.87	7.2
Jan	4.21	4.02	-4.5
Feb	5.24	4.80	-8.4
Mar	6.12	5.81	-5.1
Apr	6.02	6.05	0.5
May	7.28	6.92	-4.9
Jun	7.57	6.97	-7.9
Jul	7.36	6.65	-9.6
Aug	6.95	6.36	-8.5
Sep	6.47	6.17	-4.6
Oct	5.76	5.35	-7.1
Nov	4.18	4.30	2.9

Table 5.5: Comparison of monthly averages of GHI in Doha, in $kWh/m^2/day$: based on one year of data collected by the QEERI solar station and 5 years of data collected by the QMD station.

5.2.4 Frequency distributions

In addition to the aggregation of data in terms of hourly, daily and monthly averages, to have a more complete characterisation of the solar radiation at the location under study it is useful to present the frequency distribution of the data, specially since data are available at high temporal resolution (1-minute values). These distributions are considered an important statistical tool for the adaptation of modelled solar data to the measured values and for the validation of prediction models [7]. They are also useful for site selection, systems design and performance studies of solar energy plants [153]. Figure 5.16 shows the relative frequency distributions of minute DNI and GHI during daytime, for the period under study. Each bin is of 50 W/m^2, and each curve was normalised to 100%. The thin, coloured lines represent the frequencies in each month, and the added distributions for the year are depicted by the thick line.

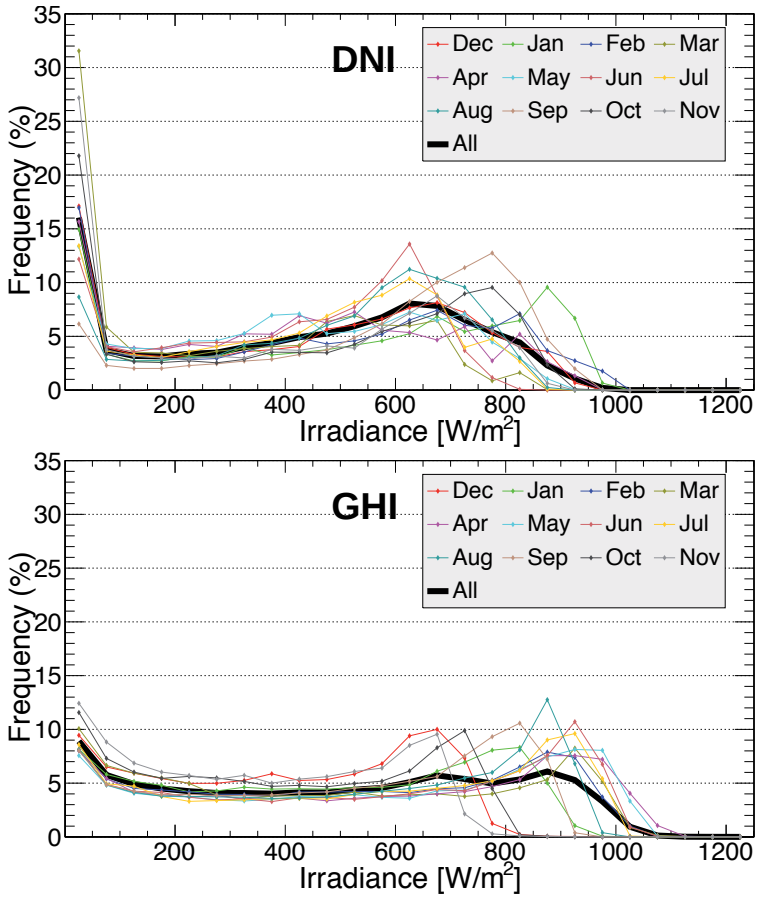

Figure 5.16: Frequency distributions of one-minute values of solar irradiance through one year in Doha. All distributions are normalised to 100% for comparison clarity.

One can notice that moderate values of DNI are measured for this location, having a frequency peak around 650 W/m^2 and a wide dispersion. DNI occurrence appears

not to follow a clear seasonal variation when comparing consecutive months; however, peaks of high radiation are more frequent in the winter season and peaks of lower level of radiation are common during the months with dust and haze such as April, May and June. In contrast, GHI has a clear seasonal variation; a frequency peak around 650 W/m^2 is seen for October, November and December and the distributions do not exceed 800 W/m^2; January and September are transition months towards higher radiation, and the rest of the months have frequency peaks around 900 W/m^2 with the radiation reaching more than 1000 W/m^2.

5.2.5 Atmospheric transmission

The atmospheric conditions play an important role in the variations of the solar radiation in Doha during a period of a year. These variations are seen at the different averaging levels shown previously, which give a broader view about how the radiation level is changing through the year from hour to hour, from day to day and from month to month. In order to give more details about the state of the atmosphere, the clearness index K_t and the diffuse ratio K_d were investigated. The clearness index is defined [16] as the ratio of GHI to extraterrestrial radiation on the horizontal surface (H_0). The diffuse ratio is the ratio of DHI to GHI. These two indices give good indication about the transmission of solar radiation in Doha's atmospheric conditions characterised by high aerosol loads most of the year, mainly due to desert dust and industrial emissions.

Figure 5.17 shows the monthly averages of clearness index and diffuse ratio in Doha for the period under study.

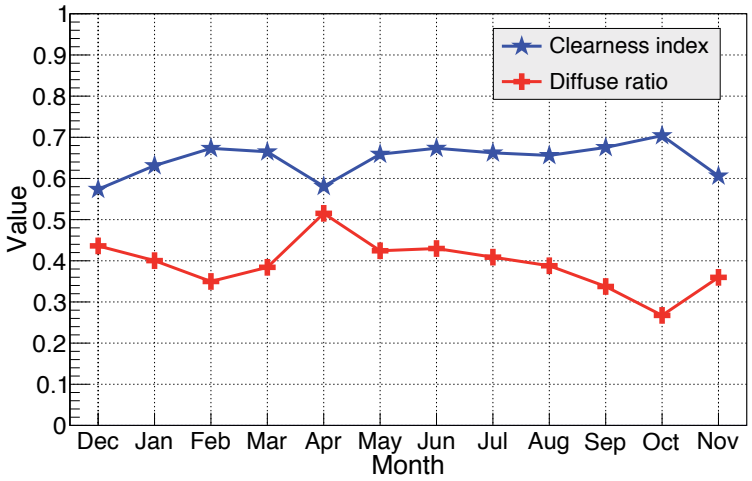

Figure 5.17: Monthly clearness index and diffuse ratio in Doha during one year, from Dec/2012 to Nov/2013.

K_t averages range from 0.57 to 0.70. The clearness index averages from February to

September are almost constant, except in April, as commented before; October had the highest clearness index, due to the clean atmosphere observed in October, as seen in the high level of DNI radiation in the monthly, daily and hourly averages. In contrast, K_d shows larger variations, ranging from 0.27 to 0.52, with the lowest diffuse ratio in October. As can be seen by comparing both graphs, these two indices are in general inversely related, i.e., low diffuse ratios correspond to clearer skies, and vice versa. This relationship is an essential feature in the modelling of solar radiation and has been extensively studied in the literature for the derivation of the solar radiation components.

Daily averages of both indices are shown in Figure 5.18. They show the same behaviour as the monthly averages, but with bigger fluctuations due to the higher resolution of the daily averages, with more details being smoothed in the monthly averages. The daily clearness index is also generally stable but shows some large drops which lower the monthly averages in December, April and November. The yearly averages of K_t and K_d in this period are 0.65 and 0.39, respectively. These values imply a generally sunny climate but with high levels of sunlight diffusion because of dust and aerosols in the atmosphere.

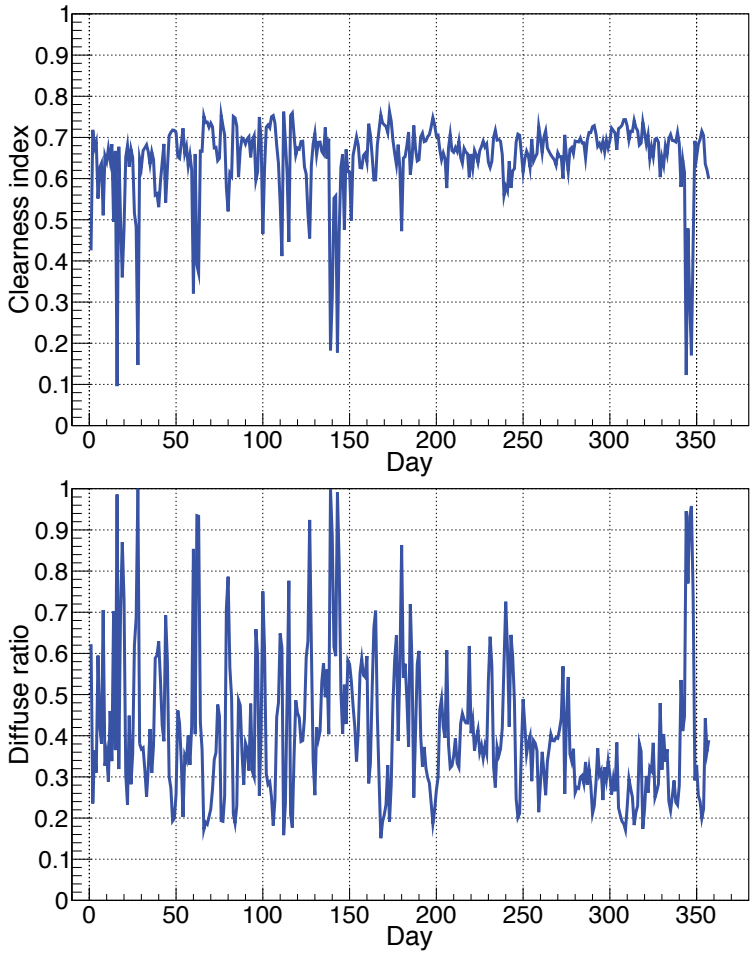

Figure 5.18: Daily clearness index and diffuse ratio in Doha during one year, from Dec/2012 to Nov/2013.

Chapter 6

Correlation of DNI with backscatter

This chapter is dedicated to the study of the lidar backscatter signals. This includes in particular the study of the noise imbedded in the signals measured by the lidar. The noise analysis was done to find a limit on the atmospheric height used for the integration of the lidar signal. The second part of the chapter, the ultimate goal of this thesis work, describes the methodology correlating the lidar backscatter profiles with solar radiation. A validation of the results is done through the use of solar data derived from two known satellite databases, acquired for the same location and time. Through the derived model, this study shows how aerosol data as assessed by the backscatter signal of a lidar ceilometer can provide relevant information about the state of the atmosphere in Doha. This information is directly related to the amount and quality of solar radiation available at ground level, in particular a decreased level of the direct radiation and an increased level of the diffuse radiation. Therefore, it can be deducted that aerosol information extracted from lidar measurements can be used as an alternative input for solar radiation modelling or for the calibration of satellite-derived solar data.

6.1 Ceilometer signal analysis

As described in Chapter 4, the signal processing by the data acquisition system of the CL51 ceilometer is performed in real time and consists of acquiring the backscatter signal, applying the range correction, subtracting the noise, calculating the first three cloud base heights or the vertical visibility from the attenuated backscatter signal, and displaying the results in terms of range-corrected (i.e., multiplied by the corresponding height) backscatter profiles or cloud height profiles. The raw data for the present study are the range-corrected backscatter coefficients recorded each 36 s with 10 m resolution, and a maximum height of 15 km. The study was limited to the clear days of the year, in

order to avoid wrong information that may arise, in the averaging or data analysis of the backscatter coefficients, from the presence of a cloud. A detailed explanation of the 'clear days' selection is given in Section 6.2.1.

In addition, the integration of the backscatter coefficients in the vertical column was limited to 5 km. This limit was found to be a good compromise between including the required information for the analysis and excluding the noise-dominated signal provided by the ceilometer during a period of one year. The selection of 5 km is the result of different analyses in a detailed study of the ceilometer signal, presented in the following subsections.

The ceilometer signal performance decreases with increasing altitudes and a noisier profile at higher altitudes is observed in the ceilometer measurements, as can be seen in Figure 6.1. This figure shows the variation of the hourly-averaged backscatter coefficients at solar noon (the hour from 11:00:01 am to 12:00:00 pm) versus the height in the atmosphere up to 10 km, for all the clear days during a period of one year. Each line represents the hourly backscatter coefficients of one day, and the height shown is limited to 10 km for visual clarity. This figure is similar to, but not the same as, the right-hand side graph in Figure 4.6. Pronounced aerosol layers can be distinguished at low altitudes as large, positive signals, and a noisier signal is seen at high altitudes as highly variable signals, randomly oscillating between negative and positive amplitudes. The main problem affecting the ceilometer signal around noon is the background noise from the sun, mainly during summer, when the sun is almost directly overhead and within the line of view of the lidar.

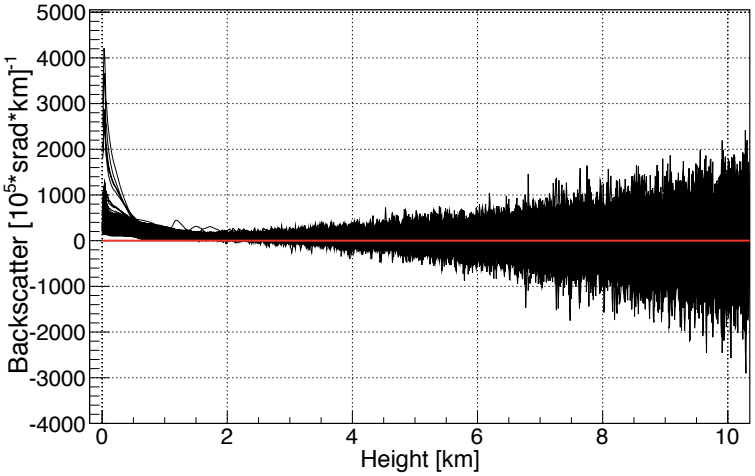

Figure 6.1: Variation of the hourly-averaged backscatter coefficients with height, at solar noon, for all the clear days through one year in Doha.

Several tests, presented in Sections 6.1.1 to 6.1.3, have been carried out to understand

the behaviour of the signal as a function of the height and from one day to another. This allows to understand the signal to noise ratio and to determine the maximum height in the atmosphere where the lidar signal has less level of noise. These tests include the study of the cumulative distribution, the average, the standard deviation, the frequency distribution, and the variability of the range of the hourly backscattered coefficients in binned heights. The objective was to obtain qualitative information about the nature and behaviour of the lidar signal in each bin of height and identify a height after which any real signals cannot be distinguished or separated from noise (in cloud-free conditions).

The tests were applied for each of the months of the year separately except for the last test in Section 6.1.3, which includes all the clear days together. This allows to spot any month or season dependency in the studied signal and to rely on the test which applies for all months, without any dependency on season or atmospheric contents. The hourly averages of the backscatter coefficient, hereby called beta coefficients, were obtained from the 36-s backscatter coefficients with height steps of 10 m, up to 15 km. In the plots shown in the following sections, the data were averaged in bins of 500 m. Several bin widths were tested and 500 m was found to be a good compromise between smoothing out the high resolution oscillations and keeping a good representativeness of the beta values for the analysis.

6.1.1 Cumulative beta

For each clear day, the hourly-averaged beta values, measured at noon, were grouped in bins of 500 m in height. The cumulative beta plots, shown in Figure 6.2, are presented as one line per day.

By studying the cumulative beta, it is expected to have the beta accumulation of the hourly coefficients increasing with height, until a certain height, at which the cumulative beta value becomes constant or very slowly-varying. This is because real signals are positive, and if after some height the signal becomes dominated by noise, the added signals should cancel by their alternating negative and positive amplitudes (see Figure 6.1).

As one can see, the cumulative beta in the plots stabilises at different heights depending on the month. This shows that the height where the cumulative beta reaches a stable value, is season- and month-dependent. It is also noted that cumulative beta starts to decrease after the so-defined stabilisation height. The dominance of negative values at high altitudes is most likely due to the noise cancellation method adopted by Vaisala. This method seems not to work effectively for all seasons under the conditions of this experiment. Indeed, the ceilometer's tilt option, meant to avoid the direct sun

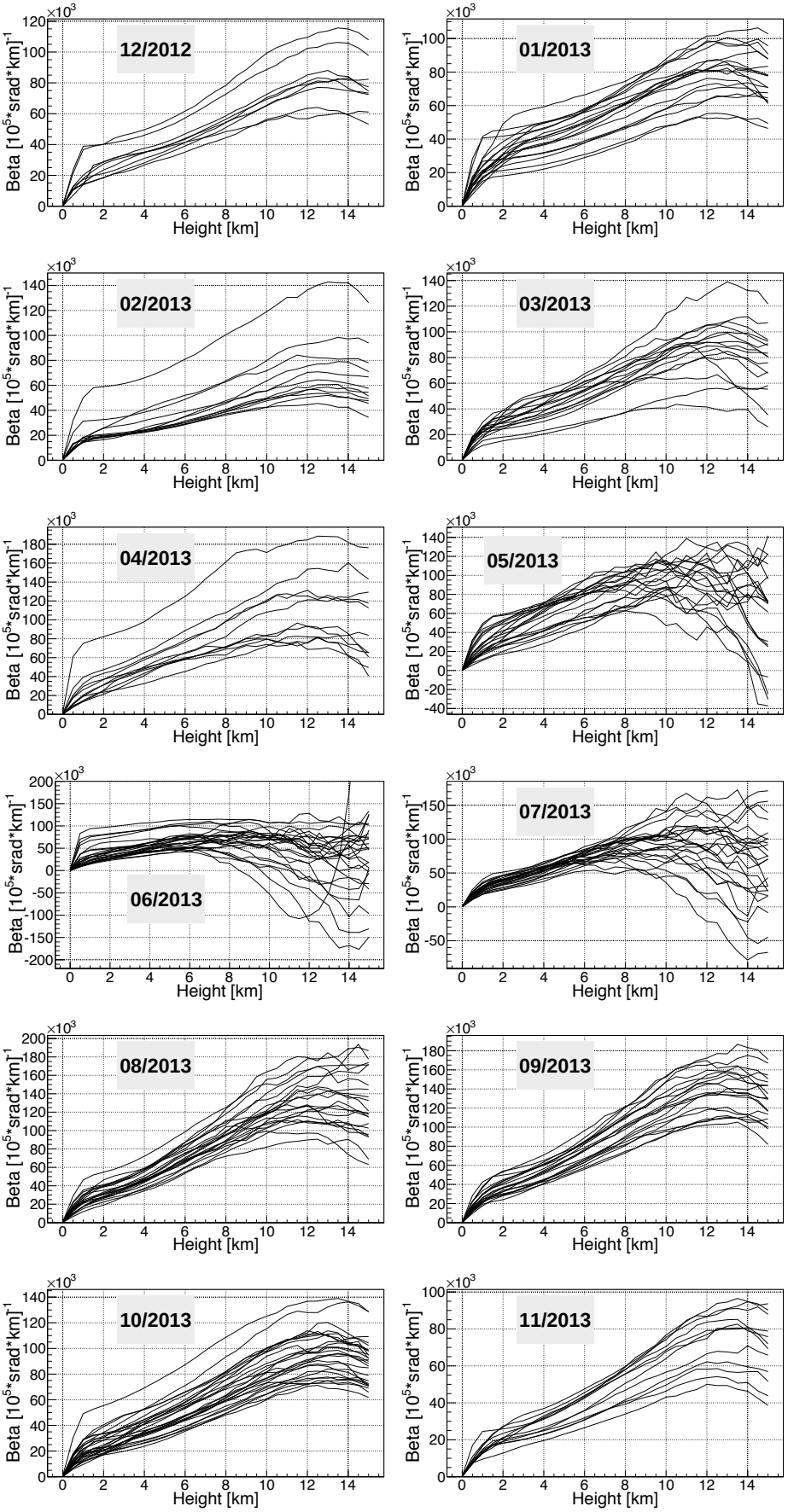

Figure 6.2: Cumulative beta in 500-m steps, at solar noon for the clear days of all the months of the year under study.

rays, was not used in the current setup of this experiment and the device was kept in its vertical position all through the year. Therefore, the background noise from the sun is sometimes affecting the lidar signal. With these conditions, the background noise is more pronounced in summer than in winter, since the position of the sun in the sky is very close to the line of view of the ceilometer in summer. Probably, this effect is not properly taken into account in the noise cancellation process. It should be noted that the information given by Vaisala regarding background noise cancellation is very brief and does not provide a precise understanding of the method. Another important feature seen in these plots is the abrupt increase of the cumulative beta at low heights, followed by a slower increase up to the stabilisation height. This is due to the highly changing constituents in terms of concentrations and species type between the different layers in the first few km of the atmosphere. The change continues with height, but with a slower rate due to the mixing happening on the way up to the top of the boundary layer, where the mixing is almost complete. The current test was useful to detect a month-dependent height from which the effect of the noise starts to affect the signal. However, and in order to have a unified height selection independent of the month, other tests were conducted, as described in the next subsections.

6.1.2 Day-to-day variability of beta

The constituents of the atmosphere within the range of the ceilometer change on daily basis. In order to understand up to which height in the atmosphere these changes are still discernible with the CL51, the average of the backscatter coefficients was calculated at each height for all the clear days of each month and month by month, then the values were averaged in bins of 500 m and plotted versus the height. This is useful to compare how, on average, the atmospheric conditions change between subsequent height bins in the atmosphere, as seen in Figure 6.3. It is expected that the average backscatter coefficients at heights where the noise is dominant should show lower values (close to zero) than those of real signals, due to the positive and negative amplitudes of noise. The figure shows that the average backscatter coefficient decreases rapidly as height increases, then remains roughly constant up to a certain height, and decreases again at higher altitudes. However, at even higher altitudes the signal deviates from zero, which indicates that at the highest altitudes the negative and positive values are not cancelling out.

What can be distinguished in these graphs, are the large variations of the average backscatter coefficient from one height bin to another in the first 4 to 5 km in comparison to the variations after these heights, and this is found in all the months. This gives indication that the observed atmospheric conditions after 4 to 5 km, as profiled by the

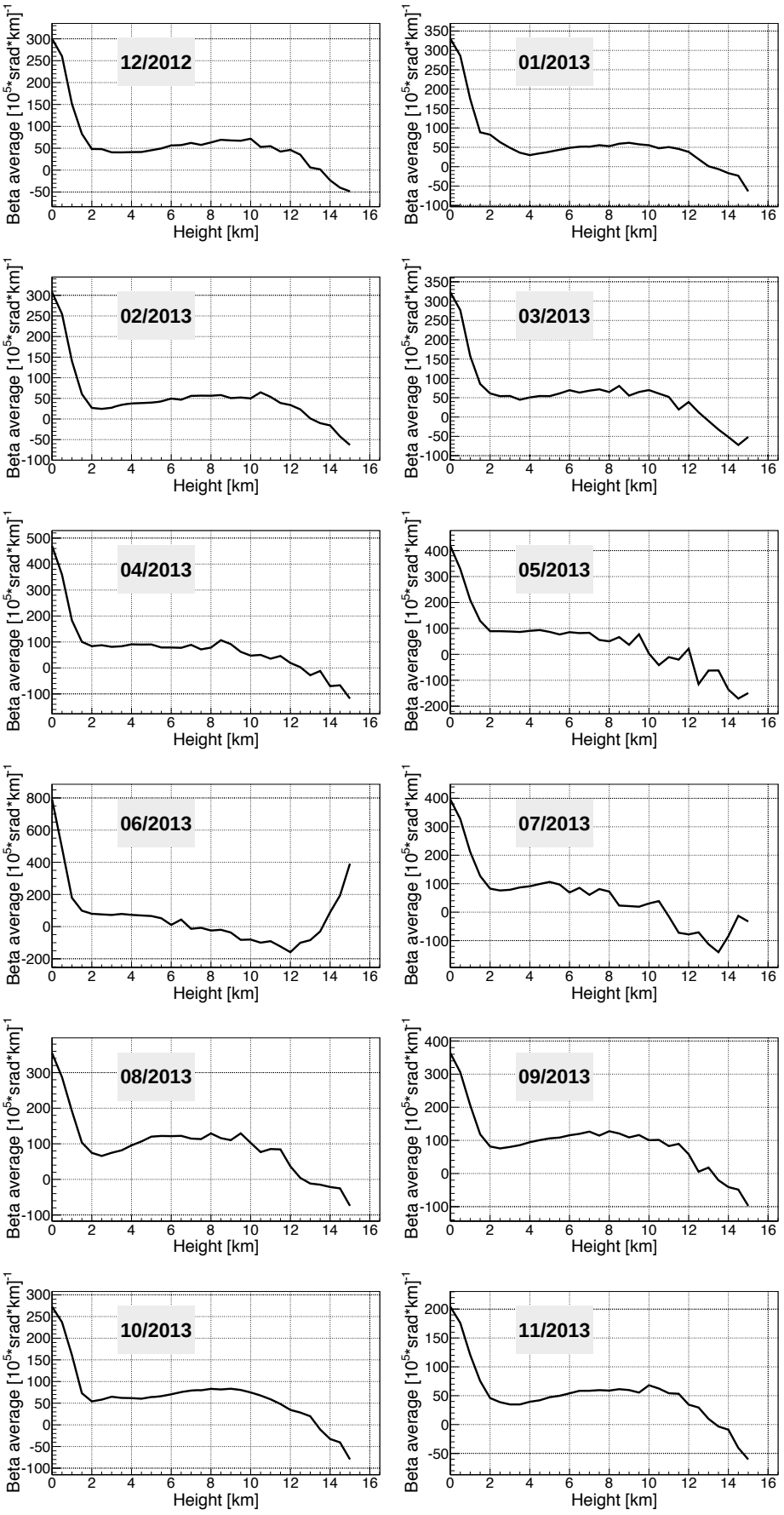

Figure 6.3: Average of beta for all clear days of the month versus height, at solar noon.

ceilometer (in the area of the experiment in Doha, Qatar), do not change drastically. This could be either because of dominance of the noise in the signal or because in reality the atmosphere is more stable.

Going further in the analysis, as a complement to the study of the averages, the standard deviation of the day-to-day backscatter coefficients measured at each height was calculated. This was necessary to quantify the variability of the backscatter coefficients during these days. The standard deviation averaged in bins of 500 m is shown versus the height in Figure 6.4. This figure shows that the degree of daily variation in the atmosphere is larger at low heights and decreases with height, until around 4 to 5 km. After those heights, an unexpected behaviour was observed: the standard deviation of the day-to-day backscatter coefficients starts to increase with height, as if the atmosphere at these altitudes exhibited large variations from day to day. This is not true since, by the definition of the boundary layer height, the atmospheric constituents are more variable in, and confined to, the first few km, and the free atmosphere above this layer presents more stable conditions. Therefore, the observed increase in the value of standard deviation of beta can be most probably attributed to the increasing level of noise with altitude. Indeed, any noise oscillations imbedded in the ceilometer signal, amplified by the range correction, result in larger variations.

For a better comparison of the standard deviations at different heights by avoiding the effect of the increasing levels of noise with height, it was decided to somehow normalise the standard deviation, by considering the range of the beta values at the corresponding height. This was done by calculating the range of the backscatter values at each height, i.e., the difference between the maximum and minimum values of beta found at each height, then dividing the standard deviation of the backscatter values at this height (shown in Figure 6.4) by the found range. Although there is not necessarily a definite expected value for this ratio, in statistical analysis it can be expected that the standard deviation is approximately equal to one fourth of the range of the data, for data following a normal distribution, as in the case of noise, for instance[i]. This is useful in detecting the variability between the data in different bins of height and helps in identifying the noise as the signal that best follows normality. This can be seen in Figure 6.5, showing the distribution of the ratio of the range to the standard deviation (the inverse of the ratio just described) versus height, averaged in bins of 500 m, for all the clear days of each month. As seen on the plots, the value of this ratio is randomly varying at lower

[i]Indeed, in a normal distribution that is symmetric and bell-shaped with mean μ and standard deviation σ, about 68% of the data fall within $\pm 1\sigma$ of the mean, 95% falls within $\pm 2\sigma$ of the mean, 99.7% falls within $\pm 3\sigma$ and approximately 4σ cover the range for a small number of data points and 5σ or 6σ cover the range in the case of a large number of data points.

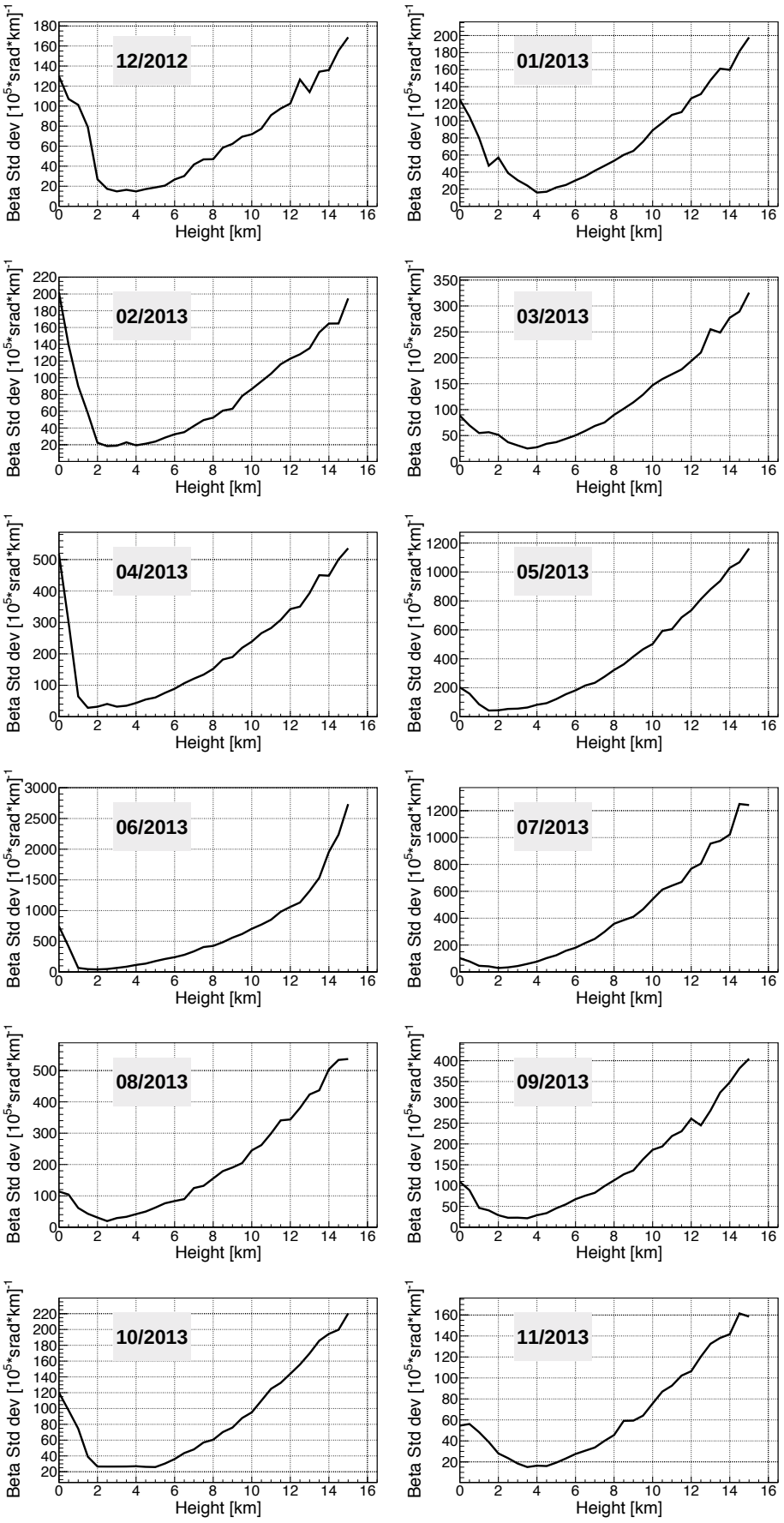

Figure 6.4: Standard deviation of beta for all clear days of the same month versus height, at solar noon.

heights, then stabilises and remains more or less constant afterwards with values between 3.5 and 4, from about 4 to 5 km, and up to 15 km. This observation, as previously explained, indicates that the signal at these heights exhibits a behaviour closer to a normal distribution and is therefore probably dominated by noise. In summer, and specifically in June, this behaviour is seen at even lower heights, which could be explained by the fact that during this month, although there are large aerosol loads in the atmosphere, the presence of these constituents is almost constant every day. Consequently, the daily variation is not as pronounced as in the winter season, leading to a stable ratio at these low heights and a signal close to normality. Moreover, the ratio in June remains stable up to around 11 km and then unexpectedly increases. This is because the noisy signal at high altitudes is more susceptible to extreme values and outliers which, depending on their magnitude and sign, greatly affect the value of the range and thus of the ratio of range to standard deviation. In summary, this test indicates once more that the lidar signal can be used, for the purposes of this work, up to 4 to 5 km for most of the months.

Another study shows the beta signal range variability with height. This is useful to show how the range of the signal is changing from day to day, among the different heights in the atmosphere. Indeed, due to the atmospheric dynamicity, the range of the beta values should present a relatively high variability from day to day. This is valid in height intervals where the beta values come from signals that are not dominated by noise. In contrast, at heights where the measured values are dominated by noise, the range of beta should remain more or less constant from day to day. This is translated to a larger standard deviation of the ranges of beta from day to day, within height bins corresponding to real signals, as compared to that of noise. Given that, as seen before, noise produces larger beta values at high altitudes, this comparison is also done by using a normalised form of the standard deviation. In this case, the relative standard deviation of the range is obtained by dividing the standard deviation of the ranges at each height bin (σ_{range}) by the average range in that bin. These relative standard deviations of the range are displayed in Figure 6.6, in bins of 500 m, for two seasons: "summer", including the months from March to September, and "winter", from October to February (see Section 6.1.3 for the reasoning leading to this definition of seasons). It is noted that in winter the relative standard deviations show larger variations in the first 4 to 5 km, while in summer the larger variations are confined to the first 3 to 4 km. After these heights, the standard deviation of the ranges of beta remain constant. This is another indication that, in general, above 4 or 5 km the CL51 signal may be in fact dominated by noise. However, an alternative explanation could still be given to a low variability in the range of beta values: low dynamicity of the atmosphere at these heights. To explore this possibility in

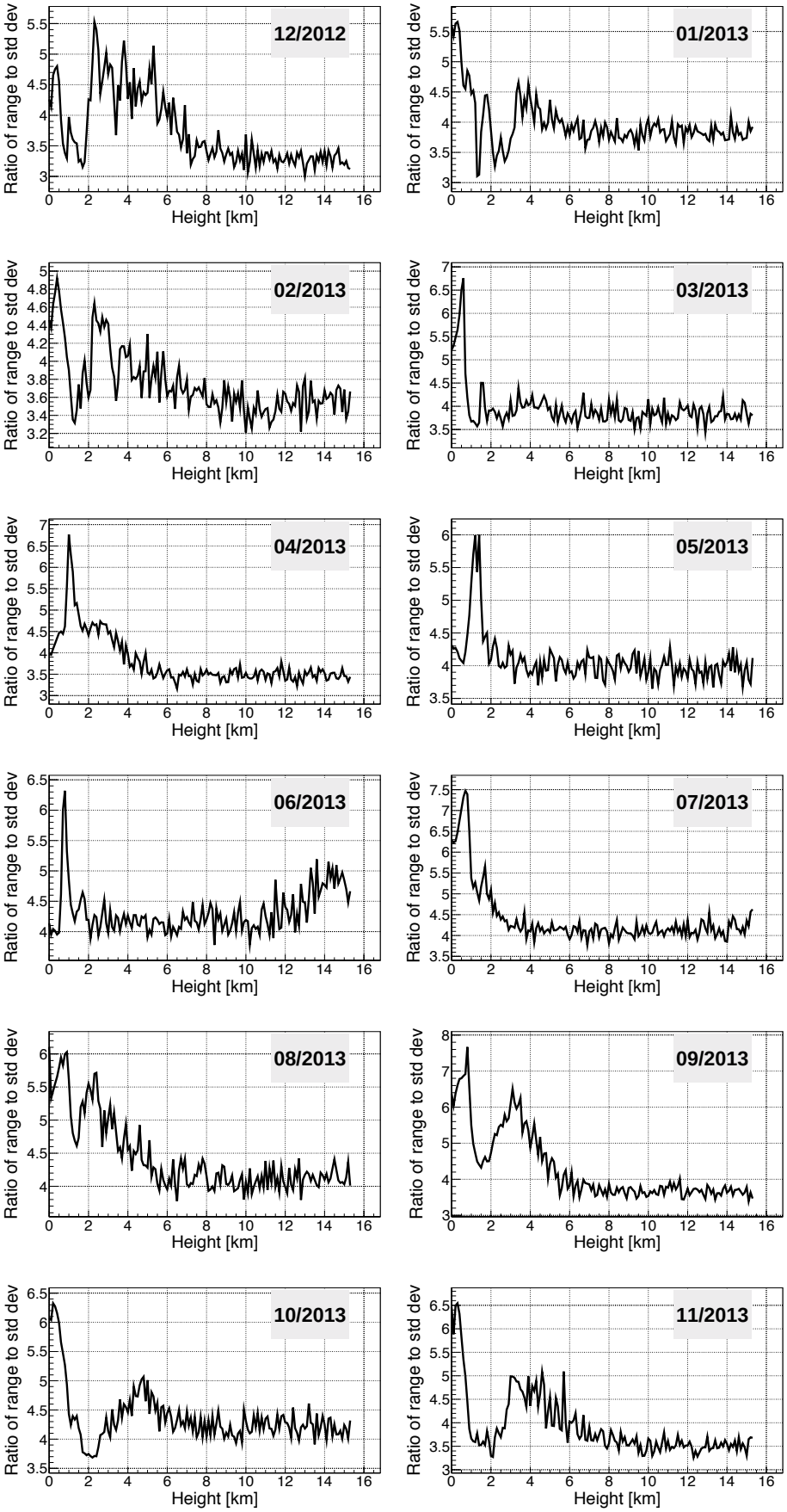

Figure 6.5: Variability of the ratio of range to standard deviation of beta calculated for all clear days of the same month versus height, at solar noon.

more detail, the frequency distributions of beta were studied.

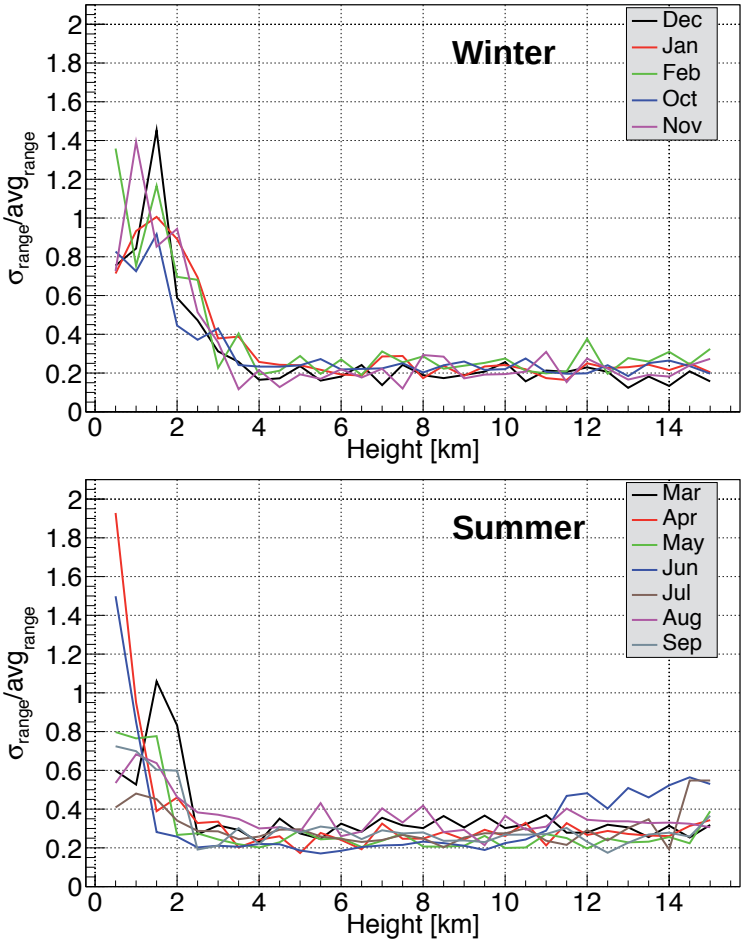

Figure 6.6: Relative variabilities in the day-to-day range of the beta values at noon, per height intervals of 500 m. Each line corresponds to one month. Winter includes from October to February, and summer includes the rest of the year.

6.1.3 Beta frequency distribution

This analysis shows how the backscatter coefficient values of all the clear days of a month are distributed within defined bins of height. From the studies above, it is expected that the frequency distributions of the beta values at the higher portions of the atmosphere follow a Gaussian, or look-alike distribution, indicative of noise. This analysis started by examining the frequency distribution of the 10-m beta values within the first km and comparing it to the distribution of the remaining heights together (1 to 15 km in this case). Then, the lower window was successively increased in steps of 1 km (i.e., inspecting the distribution of the first 2 km against 2–15 km, then of the first 3 km against 3–15 km, etc.) in order to identify any change in the trend of the frequency distribution, or spot

the height from which the signal starts to have a Gaussian-like shape. This was a lengthy process, since it was made with different height steps, always up to 15 km, repeating the process for each month separately. It was possible to distinguish two seasons following this analysis: one running from October to February while the other one covers the rest of the months (March to September). In the first season, the frequency distributions of the ceilometer signal were still random until around 7 to 8 km, with almost all the betas having positive values. At higher altitudes, the frequency distributions of the beta coefficient show a more Gaussian shape. In the other season, this critical or splitting height drops to 4 to 5 km. To illustrate this, a few samples of this analysis are shown in Figure 6.7 for the months of January and July, with splitting heights of 8 and 5 km, respectively.

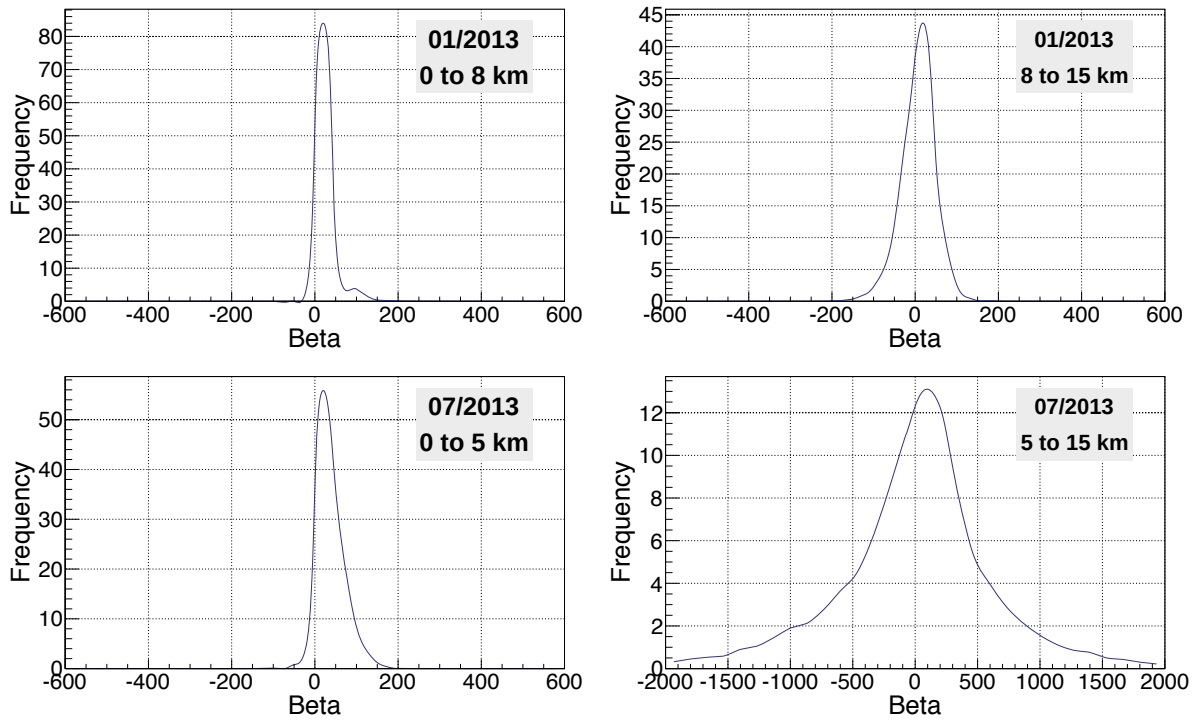

Figure 6.7: Frequency distribution of beta in terms of two height bins, at solar noon for the clear days in the months of January and July.

Going into more detail, and to find and a quantitative expression of the beta distributions, a similar analysis was made by studying the distribution of the 10-m beta values within height bins of 1 km (0–1 km, 1–2 km, ..., 14–15 km) independently of each other. It was found that the Cauchy-Lorentz distribution more closely approximates the noise affecting the lidar signal. Indeed, this distribution is more suitable for data with impulsive and non-symmetric characteristics [154]. It provides a better description of noise than the Gaussian distribution for cases where the analysed variable shows heavier

tails, which is the observed behaviour of the beta distributions. The tails of the beta distributions can be perfectly fitted with the Cauchy-Lorentz distribution, as shown in Figure 6.8. A fitting function was applied on the frequency distribution of the signal at each 1-km height step; a good fit means that the signal in that height bin is dominated by noise. The fitted function was:

$$p2 \cdot \frac{p1^2}{(x - p0)^2 + p1^2}, \tag{6.1}$$

where x is the beta value and the fit parameters are $p0$ (peak location), $p1$ (related to the width of the distribution) and $p2$ (related to the height of the peak).

The results of the fits are presented in Figure 6.8, where the frequency distributions of the beta values of all months are shown per height bin; the data are in blue and the fitted function is in red. As expected, at low altitudes the beta distribution is not well fitted by the noise distribution, and the fit improves with increasing height. This can be seen both visually, by comparing the lines, and quantitatively, by comparing the χ^2/ndf statistics[ii] at different heights in the atmosphere. To have more sense of the results of the fits, the χ^2/ndf values of these fits are plotted in Figure 6.9 as a function of height, in the same 1-km bins. It is clear that χ^2/ndf varies with height and it has relatively large values for heights up to 5 or 6 km; after that, it stabilises around a value close to 1, indicating that the data are well fitted by the noise distribution. From these results it was concluded that, considering all months, the beta values at heights above 5 or 6 km are indeed dominated by noise and no significant signals are seen by the ceilometer, in agreement with the results of the previously described studies.

6.1.4 Summary

Several tests were performed to study the ceilometer signal, and noise profiles in bins of height were done. The combined results shown in the previous sections led to the conclusion that the ceilometer signal in clear days is useful (for the purpose of this work) up to a height around 7 to 8 km during some months of the year and 4 to 5 km for the rest of the months. The analysis of the standard deviation and the frequency distribution of beta shows that the variability of the atmosphere from day to day is confined for all the months to the first 5 to 6 km in the atmosphere; this is a key result for the present work, since the main idea is the study of this variability and its effect on solar radiation.

Therefore, and being conservative, limiting the integration in the vertical column up to a height of 5 km was considered to be a good compromise between including all

[ii] As a rule of thumb, values of χ^2/ndf close to 1 are considered the result of a good fit.

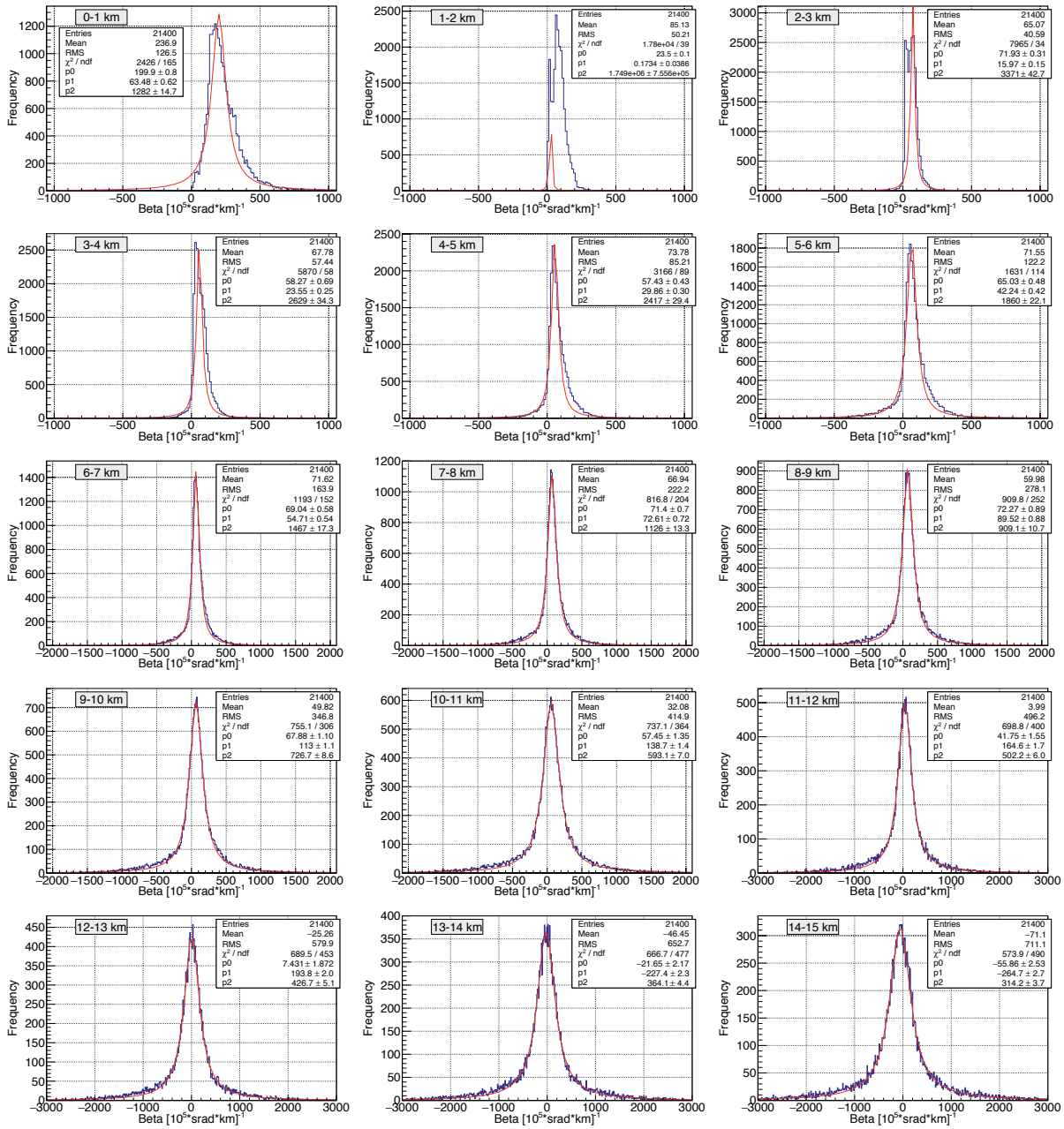

Figure 6.8: Distributions of beta fitted to noise for each *km* in height. See details in text.

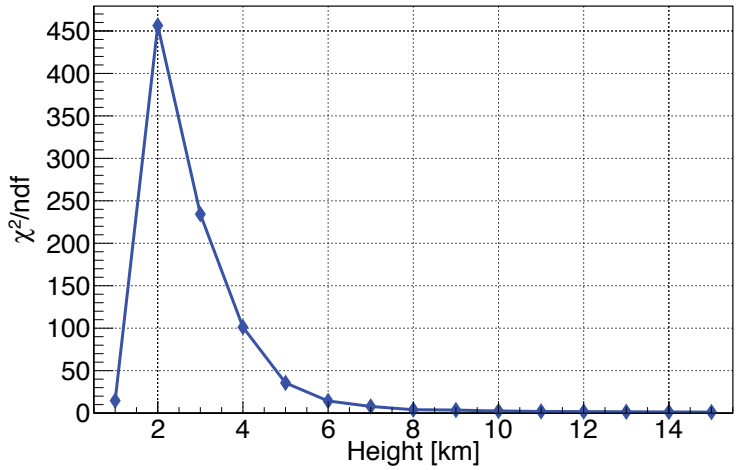

Figure 6.9: Goodness of the fit of the beta distribution to a noise distribution for each km in height. See details in text.

the needed information in the atmosphere and taking the most valid signal from the ceilometer and excluding the noise.

For this reason, the present study will be confined to the first 5 km, since the main intent of this work is to show how the atmospheric variations affect the solar radiation.

6.2 Modelling Direct Normal Irradiance with lidar

Very often, the direct normal irradiance is not measured directly due to practical reasons, and is derived instead from measurements of other readily available parameters such as global irradiance or by using models such as radiative transfer models or satellite-based models. However, the resulting modelled DNI data exhibits high discrepancies when compared to ground measurements [155, 156]. A large part of these uncertainties is attributed to inaccurate aerosol data used as input in the model. Aerosols play an important role in the attenuation of DNI [5]. Aerosol optical depth (AOD) is one of the most important parameters used to represent solar light extinction [6]. AOD can either be derived from satellite observations, for instance with the MODerate resolution Imaging Spectroradiometer (MODIS) of NASA [10] or the Multi-angle Imaging SpectroRadiometer (MISR) [9], or measured by ground-based sunphotometers, as done by NASA's Aerosol Robotic Network AERONET [8]. Chemical transport models such as MATCH (Model of Atmospheric Transport and Chemistry) [157] and numerical weather prediction models as used within the MACC (Monitoring Atmospheric Composition and Climate) project [11] are also used to estimate AOD. Lidar-ceilometer measurements provide information

about the evolution and intensity of aerosols in the atmosphere, obtained from the measurements of vertical backscatter profiles of the atmosphere. One of the main goals of this thesis work is the study of the potential use of aerosol information, extracted from the measurements of a lidar-ceilometer, for the assessment or the modelling of the direct normal irradiance.

In the following sections the data of the CL51 ceilometer is used for the estimation of DNI by establishing a relation between the daily variations of DNI and backscatter atmospheric extinction around solar noon, under cloud-free conditions. The experiment was carried out for a period of 12 months, from December 2012 to November 2013. Atmospheric backscatter profiles as measured by the ceilometer were acquired at the same time and location as the DNI measurements by a pyrheliometer, as described in Chapter 4. The methodology to obtain the correlation between both measurements is described below and consists of correlating the hourly DNI clearness index, K_n, to the hourly backscatter measurements integrated over a column of 5 km in height. The results of this technique were then compared to satellite-based model techniques and show the potential use of aerosol information as measured by lidar-ceilometer for solar radiation modelling.

6.2.1 Methodology

For the comparison of lidar backscatter measurements and DNI, only clear days in the time interval 10 am to 1 pm, Doha local time, were selected. Clear days were chosen because the purpose of this thesis is to study the effects of aerosols (and not clouds), as measured by a lidar-ceilometer, on solar radiation. Moreover, eliminating cloudy days avoids any inconsistencies arising from the possible presence of clouds above one instrument and not the other. By clear day it is meant that, during the period between 10 am and 1 pm, the sky around the sun's disk and along the lidar-ceilometer's line of view was free of visible clouds. The method used for selecting clear days was based on the CL51 algorithm, visualised through Vaisala's CL-VIEW software [158], which reports cloud height information when detected. In addition, each individual DNI profile was visually scrutinised and a comparison between both results (cloud reports and DNI) was made to improve the correctness of the selection. Following this method and including only days where both measurements were available, 214 clear days were selected, during the period from Dec/2012 to Nov/2013. The Beta-model presented in this study is derived using this sample of selected clear days.

The purpose of this study is to show how the dynamicity of the atmosphere as measured by a lidar-ceilometer is reflected in the variability of DNI. To detect these changes

in the atmosphere, the method adopted here consists of comparing, at a specific time of the day, the day-to-day variation of the hourly averages of a normalised form of DNI, the K_n index, which is the ratio of DNI to the extraterrestrial DNI at the top of the atmosphere, with the day-to-day variation of the hourly-averaged backscatter lidar signal integrated over the vertical column up to 5 km in height. This integrated backscatter signal is hereby called for simplicity the Betatot coefficient; the limit of the maximum height up to 5 km is discussed in Section 6.1. The extraterrestrial DNI for day n of the year, in W/m^2, was calculated following Equation 1.1.

The comparison was made in the hour that includes solar noon, from 11 am to 12 pm Doha local time (UTC+3 hours), so that the zenith angle of the sun is as close as possible to the vertical direction of the lidar beam, thus having as similar amounts of air mass as possible. Solar noon occurs for this location in Doha around 11:30 am, more precisely between 11:16 and 11:48 am, depending on the time of the year; the solar zenith angle at solar noon varies from about 2° in summer to about 48° in winter because of the seasonal changes in solar declination angle. The use of K_n in the model, instead of DNI, provides a sort of normalisation by taking into account the seasonal variations of DNI due to changes in the sun-earth distance, allowing for better comparison of different times of the year. To better understand the impact of different air masses throughout a year, all possible sun zenith angles in a year period, at around solar noon, are depicted in Figure 6.10 for the site of the experiment. This angle varies slowly from day to day. However, the variation is large through the year, which means that the amount of air mass seen by the ceilometer is not always the same as that seen by the pyrheliometer, specially in the winter season where the sun elevation is lower and thus sunlight traverses a longer path. In this section, this additional distance is assumed to have a negligible effect. Indeed, and as seen in Section 6.1, the variability of atmospheric contents is mostly confined to lower heights, and therefore all the relevant information, which is contained in these heights, is considered as included in the 5 km integration of the vertical column considered here.

6.2.2 Lidar-ceilometer measurements

As stated before, backscatter intensities were measured by a CL51 ceilometer, pointing vertically upwards and operating continuously for the acquisition of backscatter profiles and detection of aerosol structures in the atmosphere. As also discussed, aerosol information is represented by a backscatter coefficient reported each 36 s up to 15 km, in 10-m steps. Betatot, the integrated hourly average of the backscatter coefficient up to 5 km, was obtained by calculating first the hourly-averaged backscatter coefficients for each height step, from the 36-s backscatter coefficients acquired by the lidar, and then the

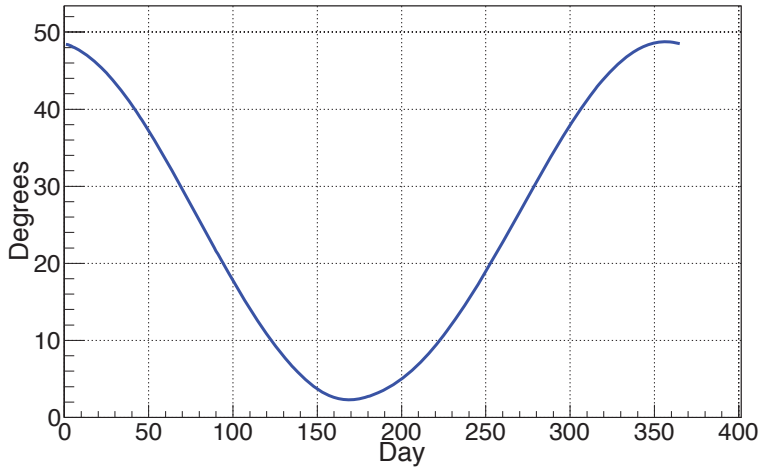

Figure 6.10: Daily variation of the zenith angle of the sun around solar noon, from 1 January to 31 December for Doha, Qatar.

averaged coefficients were summed from ground level up to 5 km. The plot of the daily variation of this sum at the noon hour, i.e., from 11 am to 12 pm, is displayed in Figure 6.11 for the 214 selected clear days. The variations in Betatot show the dynamicity of the atmosphere in Doha. It is observed that Betatot has higher values in the summer season. This is mainly due to the atmospheric conditions in Doha during summer (more precisely, from April to September), when the atmosphere is more highly loaded with aerosols and dust events are more prone to occur. The highest values of Betatot observed in the figure are related to dust storm events, as will be discussed in Section 6.2.3.

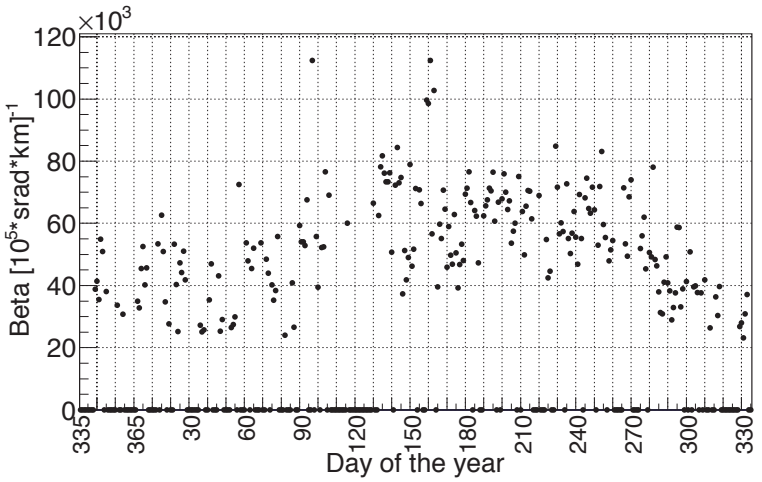

Figure 6.11: Daily variation of integrated backscatter around solar noon for cloud-free days in a one-year period. Non-clear days are shown with Betatot=0.

6.2.3 DNI measurements

For the calculation of hourly averages of DNI, only one-minute DNI data which pass the quality control tests were considered. Gap-filling was not needed, because in all the selected clear days, there were no values missing or failing the quality tests, so all hourly averages used here were obtained from 60 one-minute values. In Figure 6.12, DNI hourly averages for all the selected clear days around solar noon are shown. DNI exhibits large day-to-day fluctuations with no obvious seasonal changes during the year, depending mainly on the atmospheric extinction of solar radiation. Therefore, within one month one can find days with high DNI hourly average at noon while the next day shows a much lower value. The hourly DNI averages fall mostly within a band from 600 to 900 W/m^2, except in periods where dust storms occur and significantly reduce the amount of DNI. A qualitative inverse relation can be seen between the Betatot and DNI graphs. For instance, the lowest DNI (under 200 W/m^2) values in Figure 6.12 correspond to the highest Betatot values in Figure 6.11. The correlation is more clearly shown and discussed in the next section. During summer, lower values of DNI are found due to higher aerosol levels. The maximum hourly average of DNI around solar noon was 969.1 W/m^2, found on 22 March, and the minimum was 75.5 W/m^2, found on 6 April. As mentioned in Section 6.2.1, DNI was not used directly for the development of the model, but through the normalised DNI clearness index K_n.

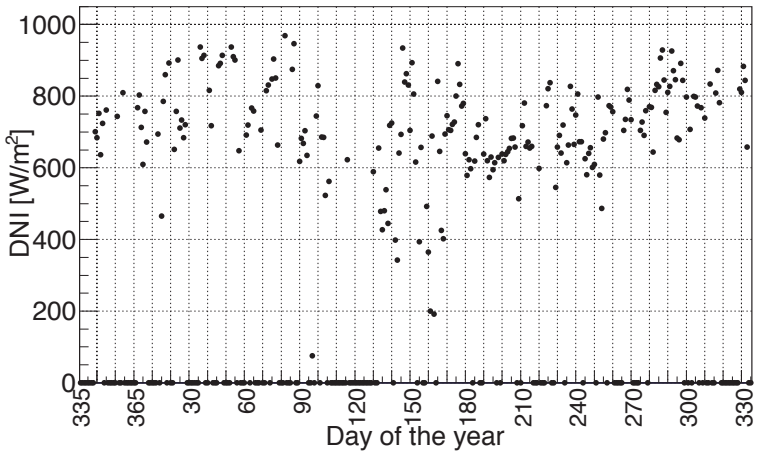

Figure 6.12: Daily variation of hourly averages of DNI around solar noon for cloud-free days in a one-year period. Non-clear days are shown with DNI=0.

6.2.4 Correlation of DNI and ceilometer signal

In general and all through the year, the atmosphere in Qatar is highly loaded with aerosols, mainly due to desert dust, high humidity and the occurrence of dust storms, but also because of industrial emissions. The direct and indirect effects of aerosols on the extinction of solar radiation are widely studied in the literature [159, 160, 161]. In this thesis work, the correlation between aerosols as extracted from lidar-ceilometer backscatter measurements and DNI measurements is shown in an attempt to quantify this effect, resulting in a model for the derivation of DNI from ceilometer measurements only. For the rest of this chapter, this model is referred to as the Beta-model.

Figure 6.13 shows the relation between hourly K_n and the Betatot coefficient in Doha following the method described in Section 6.2.1. It is observed from the experimental data that K_n seems to decrease exponentially with Betatot and an exponential function is found to fit well both measurements, a behaviour similar to the Lambert-Beer exponential law [100], which describes the decrease of radiation traversing a medium. The fitted equation can be written as follows:

$$K_n = \exp(slope \cdot Betatot + const), \tag{6.2}$$

where Betatot is the sum of the hourly-averaged backscatter lidar signals at noon, up to a height of 5 km; *slope* and *const* are parameters obtained from the fit and are shown on the statistics box of Figure 6.13.

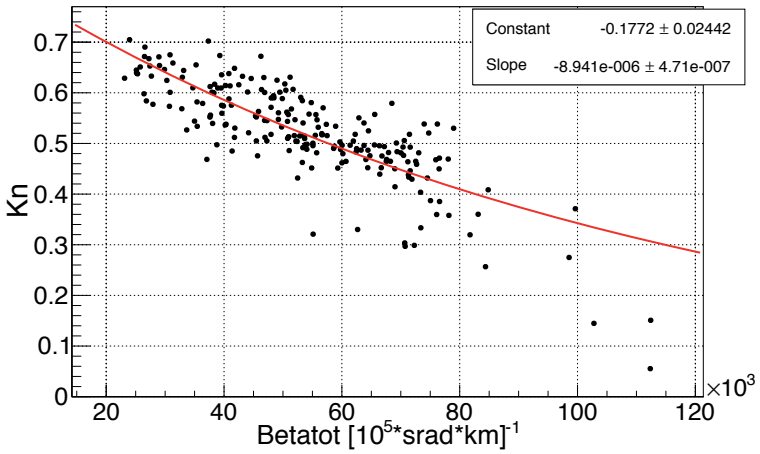

Figure 6.13: Correlation between K_n and integrated backscatter at solar noon in Doha.

The presented exponential function fits well the K_n measurements as a function of Betatot. The relative bias and RMSE, as defined in Section 6.2.5 and calculated between the fit function and the ground measurements are (all values in %) 0.0695 and 11.164 for

K_n, and 0.156 and 11.101 for DNI, respectively. Despite the limited integration height of 5 km, a close correlation is found between both measurements and this is emphasised in the next paragraphs, where the proposed Beta-model is shown to provide good statistical measures when validated against ground-measured DNI.

6.2.5 Model validation

In order to validate the Beta-model, results from different data sets and different periods of time are discussed in the following.

Three validations were made using ground measurements acquired by the same solar radiation monitoring station, at QEERI's solar resource assessment site; two of them were performed using the same sample of the selected clear days from December 2012 to November 2013, but at different hours, and the third validation was made with a new sample of clear days selected for the next twelve months, i.e., from December 2013 to November 2014:

- The first validation was done from December 2012 to November 2013, with the hour preceding the one used to derive the Beta-model, that is, K_n at 11 am (from 10 to 11 am).
- The second validation was done from December 2012 to November 2013, with the hour after, that is, K_n at 1 pm (from 12 to 1 pm).
- The third validation was made for a different period (the following year), from December 2013 to November 2014, for the same hour used to derive the Beta-model, at 12 pm (from 11 am to 12 pm).

Validating the Beta-model using 2 different hours in the day tests the validity of the model at a slightly wider interval of solar zenith angles or, equivalently, air masses. The clear days for the second year were selected following the same methodology described in Section 6.2.1.

As seen in Section 1.5, solar radiation at ground level can also be derived from satellite observations, with data currently available for all sky conditions, from several commercial providers such as GeoModel Solar and SoDa services, or for free such as from the NASA-SSE database; models and databases also exist for clear sky conditions [162, 144]. In order to have an independent reference for comparison, three sets of additional analyses were done; the first set uses the SolarGIS database to derive hourly K_n at 11 am and 1 pm, from December 2012 to November 2013. The second and third ones use McClear-derived hourly K_n data, at 11 am and 1 pm from December 2012 to November 2013, and 12 pm for the data from December 2013 to November 2014.

All these tests are summarised in Table 6.1.

Period:	Dec/2012 – Nov/2013			Dec/2013 – Nov/2014		
Hour:	11	12	13	11	12	13
Beta-model vs. ground	✓	✗	✓	✗	✓	✗
SolarGIS model vs. ground	✓	✗	✓	✗	✗	✗
McClear model vs. ground	✓	✗	✓	✗	✓	✗

Table 6.1: Validations of the different models with ground measurements.

Validations at 11 am and 1 pm, December 2012 to November 2013

For these validations, K_n and DNI were derived from the Beta-model for all the selected clear days by using Equation 6.2 and the Betatot values obtained for hour 11 am and hour 1 pm. Figure 6.14 shows the scatter plot comparison between the Beta-model-estimated hourly DNI (bottom) and K_n (top) and the corresponding averages of DNI and K_n calculated from DNI measurements at 11 am (left plots) and at 1 pm (right plots).

To provide a basis for comparing the statistical results of the previous validation, the hourly values of K_n were calculated using satellite data and validated against the same ground measurements. Figures 6.15 and 6.16 show the comparison with ground measurements of calculated hourly K_n and DNI from the SolarGIS satellite service and the McClear database, respectively, for 11 am and 1 pm.

Validation at 12 pm, from December 2013 to November 2014

The third validation of the Beta-model was made at 12 pm, with data of the next twelve months. Using a different year allows to test the validity of the model under different atmospheric cloudless conditions from those used for the derivation of the model. The results are compared with the validation of the McClear-derived hourly K_n with ground measurements. The left-hand side graph in Figure 6.17 shows the scatter plot comparison between the Beta-model-estimated hourly K_n and the corresponding averages of K_n calculated from DNI measurements. The right-hand side graph shows a similar comparison, for McClear-derived hourly K_n.

It is noted that the scatter plots of modelled against measured DNI, on the bottom rows of Figures 6.14 to 6.17, are almost identical to the K_n scatter plots on the top row of the same figures.

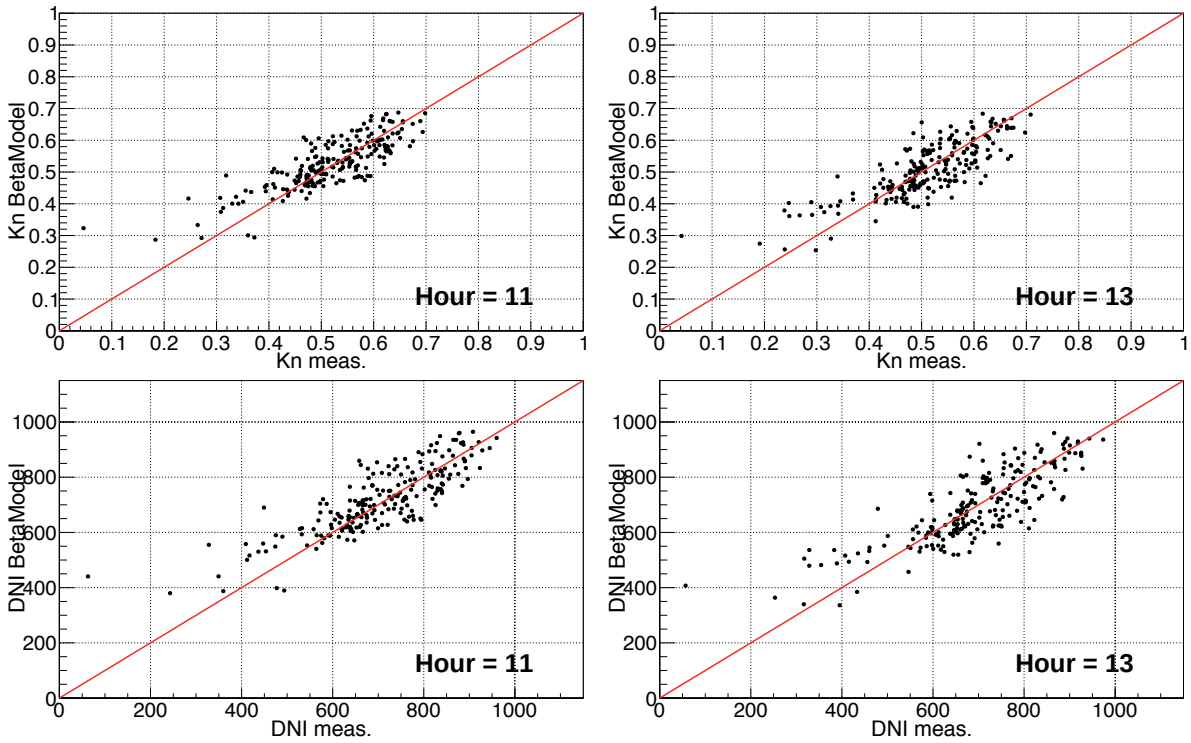

Figure 6.14: Comparison of the hourly values of K_n (top) and DNI (bottom) obtained through the Beta-model *vs.* the values calculated from DNI measurements, at the hour from 10 to 11 am (left), and from 12 to 1 pm (right). The one-to-one line is shown in red. See Tables 6.2 and 6.3 for the statistical results.

Results

In clear-sky conditions, aerosols are the main factor affecting the extinction of DNI. Errors in the estimation of aerosol data used as input in solar radiation models, may result in DNI uncertainties in the range of 15% to 20%, specifically in regions like the Arabian Peninsula, where dust storms strike occasionally and contribute to changes in the aerosol regime [5].

In the SolarGIS calculation scheme, aerosols are represented by the AOD derived from a chemical-transport model, the MACC database lead by ECMWF (European Centre for Medium Range Weather Forecast) [11], which characterises the overall radiative effect of aerosols in terms of daily AOD values (summarised from 6-hourly) at 550 nm, with a spatial resolution of 125 km. It was demonstrated in [163] that using daily AOD data from the MACC database, instead of monthly, significantly improves the calculation of DNI. The SolarGIS model has demonstrated good results when compared to ground measurements in atmospheric conditions similar to the ones encountered in Qatar [164].

McClear is a fully physical clear-sky model to estimate solar radiation at ground level under clear sky conditions. Its inputs of aerosols, ozone column and water vapour come

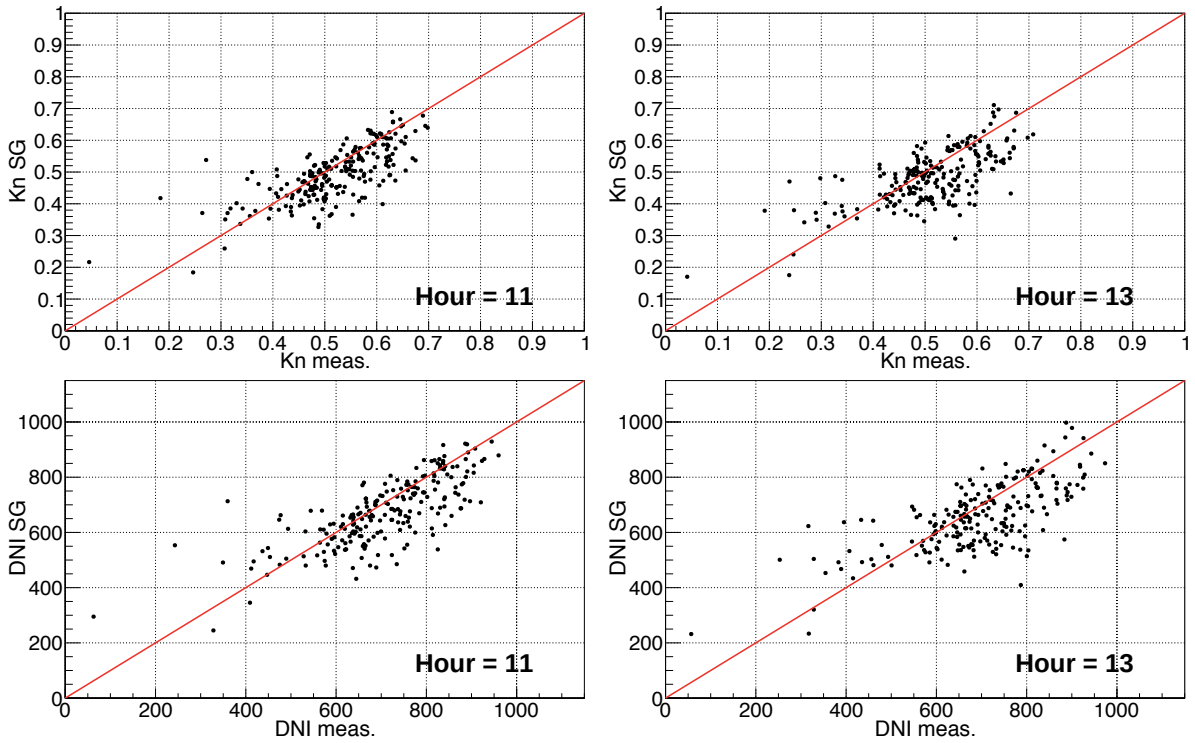

Figure 6.15: Comparison of the hourly values of K_n (top) and DNI (bottom) obtained from SolarGIS *vs.* the values calculated from DNI measurements, (left) at the hour from 10 to 11 am and (right) at the hour from 12 to 1 pm. The one-to-one line is shown in red. See Tables 6.2 and 6.3 for the statistical results.

primarily from the MACC project. It is mainly based on the use of the abaci approach (tables for computation) and interpolation functions, which enable the model to reproduce data as estimated by the radiation transfer model libRadtran, but in a much faster way for use in real-time routine applications. Aerosol information as used by the McClear model consists of aerosol optical depth at 550 nm, Ångström coefficient, and aerosol type: urban, continental clean, continental polluted, continental average, maritime clean, maritime polluted, maritime tropical, antarctic, and desert. The McClear model has been validated at several BSRN stations giving good results [162].

To obtain a quantitative comparison between the performance of these models and the Beta-model, the following statistical indicators were calculated:

- The mean bias error (MBE), which is the difference between the mean value of the modelled values (K_n or DNI) and the mean value of the corresponding measurements, is given in radiation units by the formula:

$$MBE = \frac{1}{Np}\sum_{i=1}^{Np}(M_i - G_i) \tag{6.3}$$

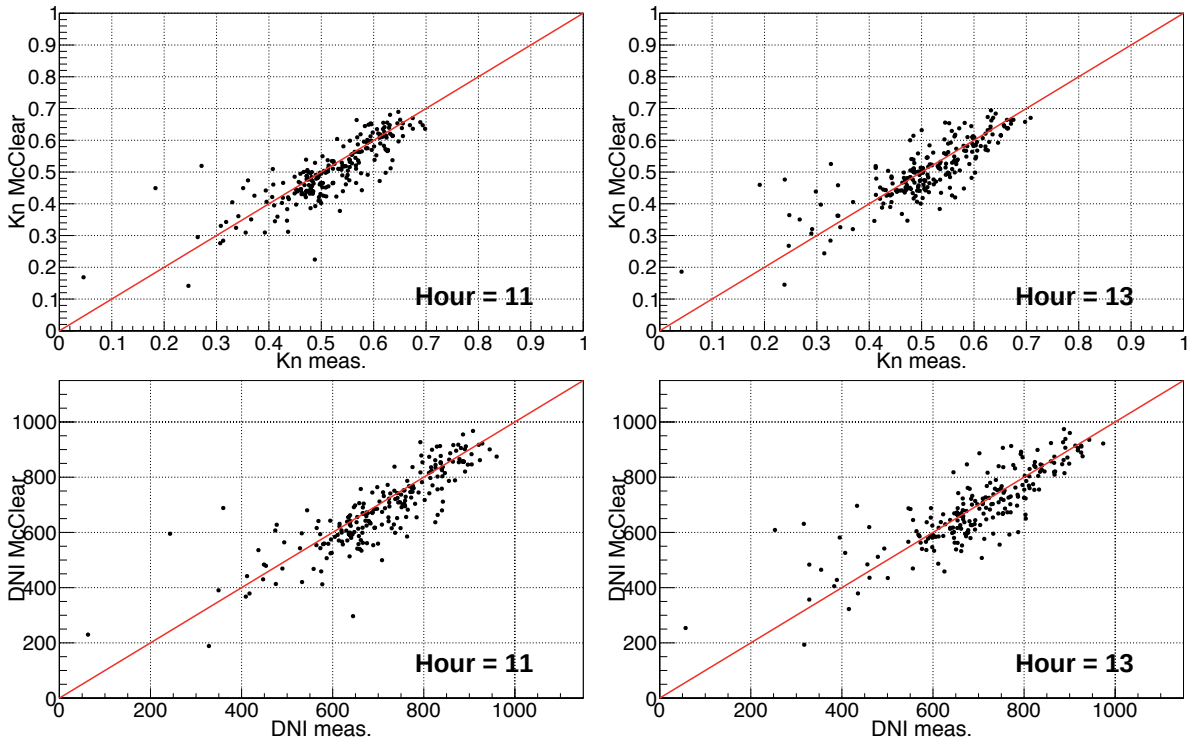

Figure 6.16: Comparison of the hourly values of K_n (top) and DNI (bottom) obtained from McClear *vs.* the values calculated from DNI measurements, (left) at the hour from 10 to 11 am and (right) at the hour from 12 to 1 pm. The one-to-one line is shown in red. See Tables 6.2 and 6.3 for the statistical results.

where Np is the total number of data pairs (in this case, one for each selected day), M_i are the modelled values and G_i are the reference (ground-measured) values. MBE allows to identify systematic errors.

- The root-mean-square error (RMSE) is also given in radiation units and compares time-coincident modelled and measured data pairs, and is calculated as

$$RMSE = \sqrt{\frac{\sum_{i=1}^{Np}(M_i - G_i)^2}{Np}} \tag{6.4}$$

where Np is the total number of data pairs (in this case, 214, one for each selected day), M_i are the modelled values and G_i are the reference (measured) values.

- The relative MBE (rMBE) and relative RMSE (rRMSE), which are the MBE and RMSE divided by the mean value of the measured quantity (K_n or DNI) and usually presented as percentage.

- The correlation factor measures the strength and direction of a linear relationship between the modelled and corresponding measured data points. If the relationship

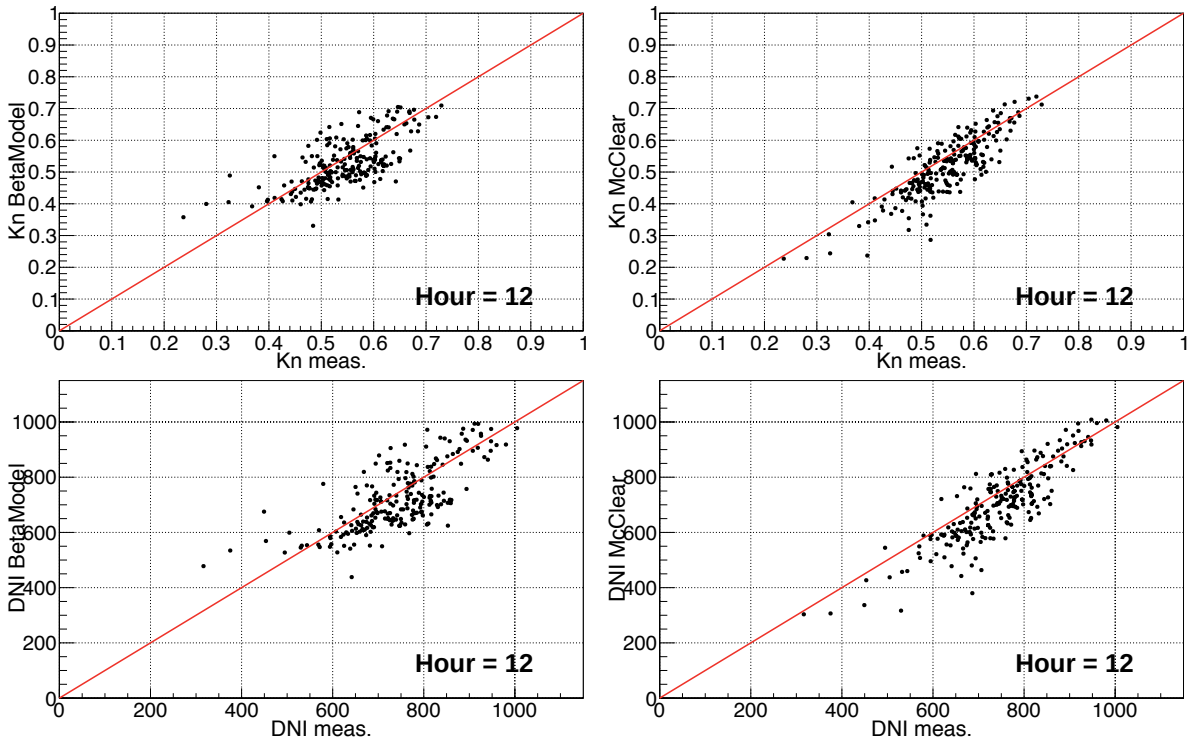

Figure 6.17: (Left) Comparison at the hour from 11 am to 12 pm of the hourly values of K_n (top) and DNI (bottom) obtained through the Beta-model *vs.* the values calculated from DNI measurements, from December 2013 to November 2014. (Right) Same comparison, but for McClear-derived data. The one-to-one line is shown in red. See Table 6.4 for the statistical results.

is strong and positive (negative), this factor is close to 1 (-1). A weak or non-exitent correlation results in a factor close to 0. The formula is:

$$Correl. = \frac{Np\sum(M_i G_i) - (\sum M_i)(\sum G_i)}{\sqrt{Np(\sum M_i^2) - (\sum M_i)^2}\sqrt{Np(\sum G_i^2) - (\sum G_i)^2}} \tag{6.5}$$

Tables 6.2 and 6.3 present the overall statistical comparison results of both K_n and DNI at 11 am and 1 pm, respectively, for the same selected clear days that were used to derive the model (from December 2012 to November 2013), whereas Table 6.4 shows the same, but at 12 pm, for the data set of the next twelve months (December 2013 to November 2014). Hourly K_n and DNI are derived from each of the three models (Beta-model, SolarGIS and McClear) and compared against the corresponding ground-measured values. From these tables, it is evident that the Beta-model's statistical results are indeed good, comparable to the results of the McClear-derived values and even improving the MBE, RMSE and correlation factor with respect to the results from the SolarGIS-derived values. The validation of the Beta-model using an independent set of data derived from values collected the following year, also shows good results comparable to those of the

McClear model, a result which demonstrates the validity of the Beta-model in different aerosol load conditions. It must be noted, as well, that for the validation made at one hour before and one hour after the hour for which the model was derived, even though the solar zenith angles during both hours mostly overlap through the year, a difference still remains, yet the model provides good results, supporting the use of K_n as a normalised parameter for the model and giving evidence that the Beta-model works for a relatively wide range of solar zenith angles.

Model	Np	MBE	rMBE	RMSE	rRMSE	Correl.
K_n						
Beta-model	214	0.010	1.861	0.056	10.826	0.819
SolarGIS model	214	-0.024	-4.663	0.071	13.794	0.732
McClear model	214	-0.015	-2.951	0.058	11.277	0.831
DNI						
Beta-model	214	13.957	1.979	76.673	10.869	0.832
SolarGIS model	214	-32.882	-4.661	96.708	13.710	0.754
McClear model	214	-20.327	-2.882	78.301	11.100	0.849

Table 6.2: Statistical indicators of the comparison of modelled against measured K_n (dimensionless) and DNI (W/m^2), at the hour from 10 to 11 am, from Dec/2012 to Nov/2013. rMBE and rRMSE are in %.

Model	Np	MBE	rMBE	RMSE	rRMSE	Correl.
K_n						
Beta-model	213	-0.001	-0.285	0.061	11.916	0.796
SolarGIS model	213	-0.027	-5.351	0.081	15.850	0.672
McClear model	213	-0.004	-0.813	0.060	11.738	0.813
DNI						
Beta-model	213	-1.024	-0.147	82.568	11.873	0.817
SolarGIS model	213	-37.424	-5.382	109.99	15.817	0.698
McClear model	213	-5.404	-0.777	80.609	11.592	0.832

Table 6.3: Statistical indicators of the comparison of modelled against measured K_n (dimensionless) and DNI (W/m^2), at the hour from 12 to 1 pm, from Dec/2012 to Nov/2013. rMBE and rRMSE are in %.

Although the comparisons between the hourly satellite data as derived from SolarGIS and hourly ground measurements (seen in Tables 6.2 and 6.3) show fairly good statistical

Model	Np	MBE	rMBE	RMSE	rRMSE	Correl.
K_n						
Beta-model	213	-0.017	-3.083	0.063	11.443	0.689
McClear model	213	-0.032	-5.768	0.060	11.007	0.849
DNI						
Beta-model	213	-21.562	-2.900	84.765	11.400	0.737
McClear model	213	-42.112	-5.663	81.198	10.920	0.869

Table 6.4: Statistical indicators of the comparison of modelled against measured K_n (dimensionless) and DNI (W/m^2), at the hour from 11 am to 12 pm, for the data set of the period December 2013 to November 2014. rMBE and rRMSE are in %.

results, the observed errors may be attributed to the low spatial as well as temporal resolution of the aerosol data; daily AOD data, as used in the SolarGIS model, may not be sufficient to capture the high fluctuations and variability of aerosols in Doha, specially in dust storm events. Improvement in the chemical transportation model for the derivation of the aerosol data, considering the spectral sensitivity of AOD, and increasing the spatial and temporal resolution may be needed to achieve better results for modelling DNI using satellite observations in the Arabian Peninsula. In contrast, the McClear model uses higher temporal resolution data of aerosols (3-hourly), hence the better comparison results. The Beta-model, even though it is only based on one input, uses aerosol data (backscatter) with an even higher temporal resolution of one hour, measured on-site, reflecting the actual local conditions; these improved spatial and temporal resolutions contribute to its good performance when compared with ground measurements.

6.2.6 BetaCos-model

Although the Beta-model shows good results when its validation is compared to satellite validation, it is still presenting errors which could be mostly attributed to the different viewing angles between the two devices, measuring the backscatter on the one hand and DNI on the other hand. This observation is more noticeable during the winter season, where the sun around solar noon exhibits low elevation angles in the sky, as seen in Figure 6.10. In an attempt to improve the statistical results of the Beta-model, another model, called here BetaCos-model, was developed by using the same methodology described in Section 6.2.1, but instead of using the Betatot coefficient for DNI derivation, it was decided to use an hourly average of a modified Betatot coefficient, 'BetaCos', defined

here as the Betatot coefficient modified by the zenith angle as follows:

$$BetaCos = \frac{\sum_{min=1}^{Nmin} \frac{beta_{min}}{\cos\theta_z}}{Nmin}, \tag{6.6}$$

where BetaCos is the modified hourly Betatot, $beta_{min}$ is the 1-minute-averaged beta coefficient and θ_z is the zenith angle at that same minute; the sum runs over all the minutes with data within the hour (a maximum of 60).

The idea behind the use of this modified Betatot, is to add an additional scattering volume to the lidar beam's path equivalent to the extra path traversed by the solar radiation, which depends on the zenith angle and is more pronounced in the winter season. The resulting BetaCos-model relating the hourly K_n and the BetaCos coefficient, for the selected clear days at around solar noon, is shown in Figure 6.18. It is observed that K_n seems also to decrease exponentially with BetaCos and an exponential function is fitted to the data, similarly to Equation 6.2. The fitted equation is written as follows:

$$K_n = \exp(slope \cdot BetaCos + const), \tag{6.7}$$

where *slope* and *const* are parameters obtained from the fit and are shown on the statistics box of Figure 6.18.

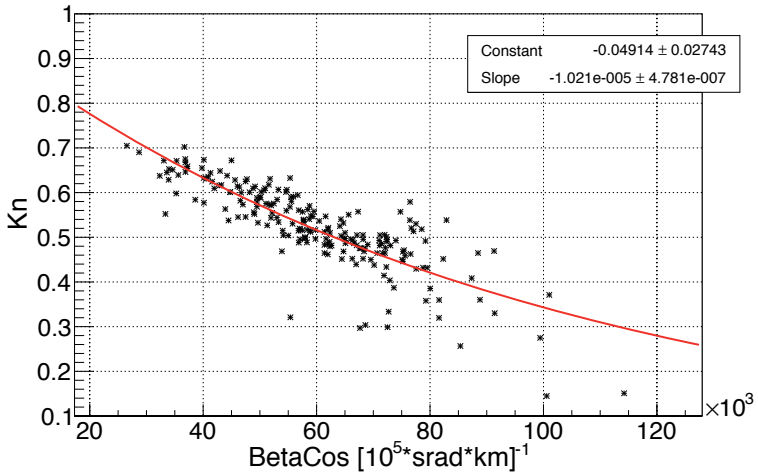

Figure 6.18: Correlation between K_n and the modified Betatot coefficient, BetaCos, at solar noon in Doha.

For comparison with the Beta-model, the relative bias and RMSE were calculated between the fit function and the ground measurements and give (all values in %) 0.032 and 10.330 for K_n, and 0.0059 and 10.231 for DNI, respectively. These results are slightly better than those of the Beta-model shown in Section 6.2.4.

BetaCos-model validation

As in the case of the Beta-model, the BetaCos-model was validated against ground measurements. K_n and DNI are derived from the BetaCos-model and compared against the corresponding ground-measured values, as shown in the DNI and K_n scatter plots in Figures 6.19 and 6.20, for the hours 11 am and 1 pm of the same selected clear days that were used to derive the model (from December 2012 to November 2013), and at 12 pm for the data set of the next twelve months (December 2013 to November 2014).

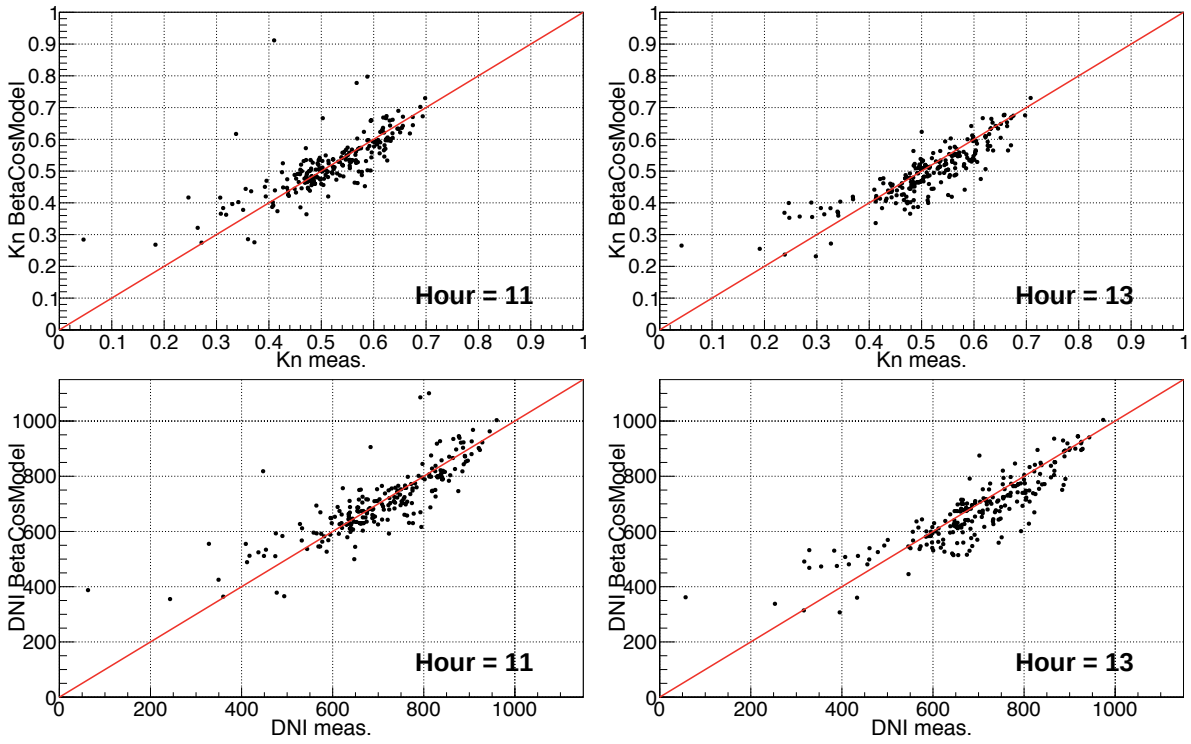

Figure 6.19: Comparison at two hours: from from 10 am to 11 am (left) and from 12 pm to 1 pm (right) of the hourly values of K_n (top) and DNI (bottom) obtained through the BetaCos-model *vs.* the values calculated from DNI measurements, from December 2012 to November 2013. The one-to-one line is shown in red. See Tables 6.5 and 6.6 for the statistical results.

Tables 6.5 and 6.6 include the overall statistical comparison results of both K_n and DNI at 11 am and 1 pm from December 2012 to November 2013. Table 6.7 shows the same, but at 12 pm, for the data set of the period from December 2013 to November 2014. The statistical results of the Beta-model are also shown in these tables for comparison. It is evident that the BetaCos-model's results are indeed good, but no clear improvement over the Beta-model is seen for the ranges of zenith angles tested here.

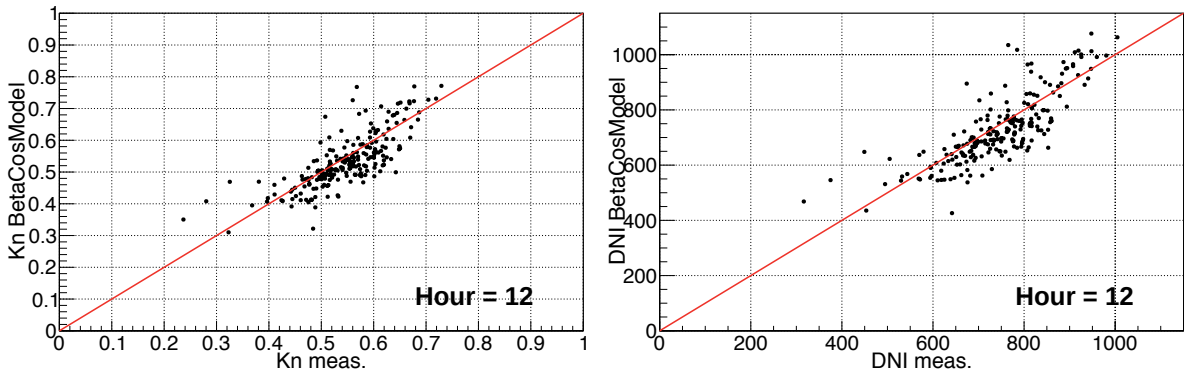

Figure 6.20: Comparison at the hour from 11 am to 12 pm of the hourly values of K_n (left) and DNI (right) obtained through the BetaCos-model *vs.* the values calculated from DNI measurements, from December 2013 to November 2014. The one-to-one line is shown in red. See Table 6.7 for the statistical results.

Model	Np	MBE	rMBE	RMSE	rRMSE	Correl.
K_n						
BetaCos-model	214	0.005	0.871	0.064	12.441	0.766
Beta-model	214	0.010	1.861	0.056	10.826	0.819
DNI						
BetaCos-model	214	6.265	0.888	88.436	12.537	0.781
Beta-model	214	13.957	1.979	76.673	10.869	0.832

Table 6.5: Statistical indicators of the comparison of modelled against measured K_n (dimensionless) and DNI (W/m^2), at the hour from 10 am to 11 am, for the data set of the period December 2012 to November 2013. rMBE and rRMSE are in %.

Model	Np	MBE	rMBE	RMSE	rRMSE	Correl.
K_n						
BetaCos-model	213	-0.014	-2.799	0.052	10.259	0.864
Beta-model	213	-0.001	-0.285	0.061	11.916	0.796
DNI						
BetaCos-model	213	-19.235	-2.766	70.718	10.169	0.876
Beta-model	213	-1.024	-0.147	82.568	11.873	0.817

Table 6.6: Statistical indicators of the comparison of modelled against measured K_n (dimensionless) and DNI (W/m^2), at the hour from 12 to 1 pm, for the data set of the period December 2012 to November 2013. rMBE and rRMSE are in %.

Model	Np	MBE	rMBE	RMSE	rRMSE	Correl.
K_n						
BetaCos-model	213	-0.012	-2.141	0.056	10.300	0.776
Beta-model	213	-0.017	-3.083	0.063	11.443	0.689
DNI						
BetaCos-model	213	-15.250	-2.051	76.289	10.260	0.803
Beta-model	213	-21.562	-2.900	84.765	11.400	0.737

Table 6.7: Statistical indicators of the comparison of modelled against measured K_n (dimensionless) and DNI (W/m^2), at the hour from 11 am to 12 pm, for the data set of the period December 2013 to November 2014. rMBE and rRMSE are in %.

6.2.7 BetaCos-model in a wider zenith angle range

It was shown that the performance of the BetaCos-model is comparable to the Beta-model. The reason is that the BetaCos-model was developed based on data resulting from the selection of clear days around solar noon. In order to expand the applicability of this model, clear days for the period Dec/2012 to Nov/2013 were selected using the methodology described in Section 6.2.1, but in a wider window of time, that is, from 7 am to 4 pm. The data based on this selection is used for the derivation of the new BetaCos-model, following the same reasoning as in Section 6.2.6: a model relating the hourly K_n and the BetaCos coefficient as shown in Figure 6.21. For all the hours from 7 am to 4 pm, K_n and BetaCos are fitted with an exponential function, written as follows:

$$K_n = \exp(slope \cdot BetaCos + const), \tag{6.8}$$

where BetaCos is calculated from Equation 6.6 for all the hours between 7 am and 4 pm, and *slope* and *const* are parameters obtained from the fit and are shown on the statistics box of Figure 6.21.

Validation

The BetaCos-model presented in 6.2.7 was validated against ground measurements. K_n and DNI are derived from the BetaCos-model and compared against the corresponding ground-measured values, as shown in the DNI and K_n scatter plots in Figures 6.22 for the hours from 7 am to 4 pm, using a newly selected set of clear days from the next twelve-month period (December 2013 to November 2014). In order to have a reference for the comparison, the same validation (using the same data set) is performed with data derived from the McClear database and shown in the same figure.

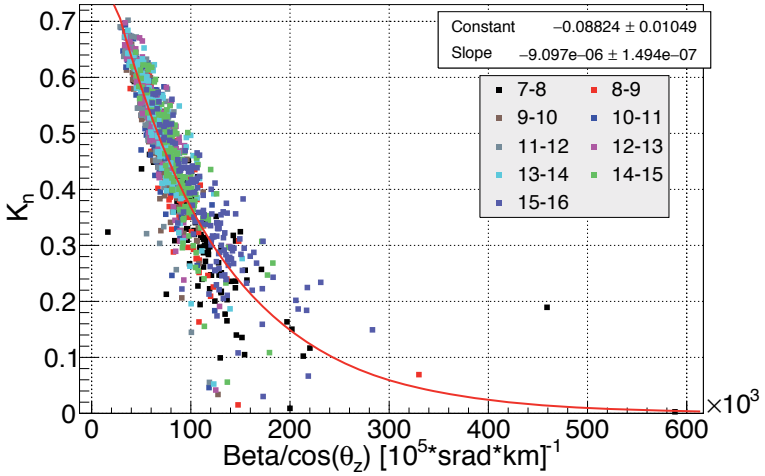

Figure 6.21: Correlation between K_n and the modified Betatot coefficient BetaCos for all the clear days from 7 am to 4 pm, for the period Dec/2012 to Nov/2013 in Doha.

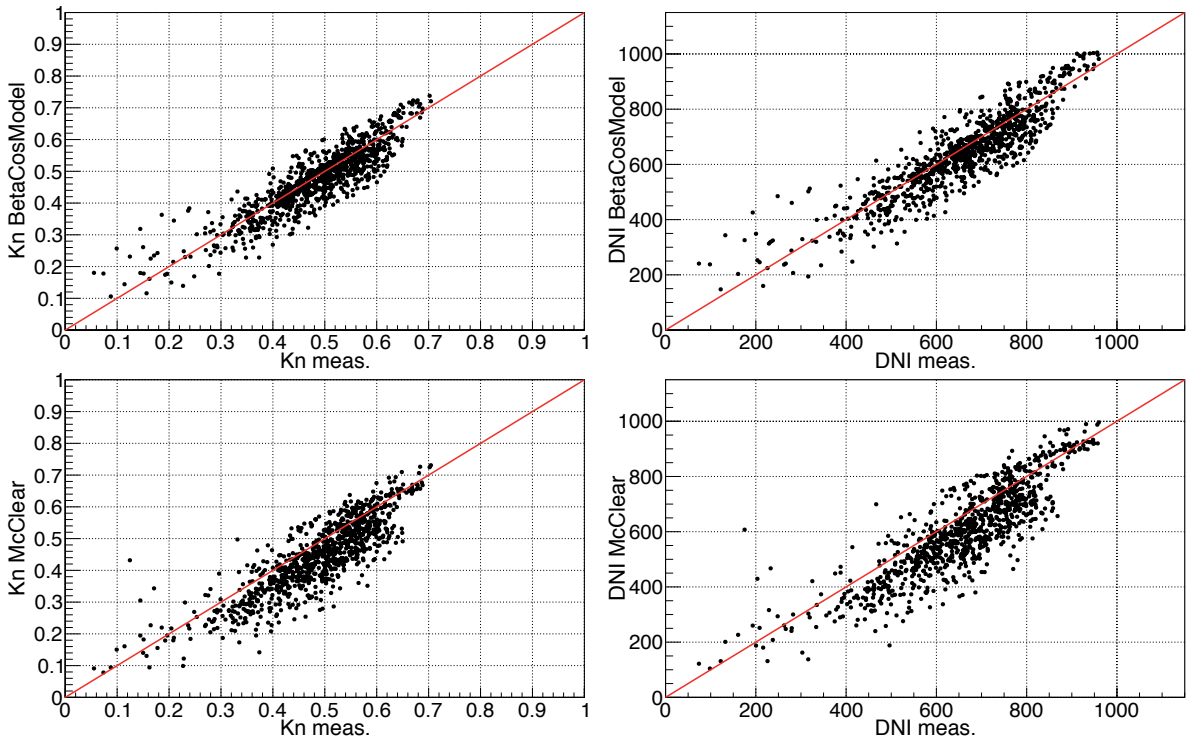

Figure 6.22: Comparison of the hourly values of K_n (left) and DNI (right) obtained through the BetaCos-model (top figures) and the McClear model (bottom figures) *vs.* the values calculated from DNI measurements, from December 2013 to November 2014, for hours 8 to 16 (from 7:01 to 16:00). The one-to-one line is shown in red. See Table 6.8 for the statistical results.

Table 6.8 presents the overall statistical comparison results of both K_n and DNI for the BetaCos-model and the McClear model, for the hours from 7 am to 4 pm, for the

period from December 2013 to November 2014. It is evident that the BetaCos-model's results are indeed good, and the errors are even better than those of the McClear model, which demonstrates the validity of the BetaCos-model for the wider range of zenith angles tested here, corresponding to hours 7 am to 4 pm during one year in Doha, covering the zenith angle range from 1.877° to 82.89°.

Model	Np	MBE	rMBE	RMSE	rRMSE	Correl.
K_n						
BetaCos-model	891	-0.013	-2.641	0.051	10.407	0.894
McClear model	891	-0.043	-8.943	0.074	15.325	0.856
DNI						
BetaCos-model	891	-16.839	-2.562	68.254	10.386	0.899
McClear model	891	-57.919	-8.814	100.176	15.244	0.865

Table 6.8: Statistical indicators of the comparison of modelled against measured K_n (dimensionless) and DNI (W/m^2), at the hours from 7 am to 4 pm, for the data set of the period December 2013 to November 2014. rMBE and rRMSE are in %.

6.3 Application: calibration of McClear

It was seen in Section 6.2.5 that the estimation of DNI using the Beta-model is possible and is even comparable to more advanced models based on satellite observations, currently available for routine use and applications. This result gives indication that lidar devices can potentially be used for DNI estimation under clear sky conditions and in a somewhat wide range of zenith angles.

A related application for the backscatter coefficient, on which the Beta-model was based, consisting of a calibration of satellite-derived solar radiation data, is suggested in the following lines, applicable under high aerosol loads.

In the following analysis, it was decided to use satellite data derived by the McClear database only, to have a better understanding of how aerosols as extracted by the lidar signal can be used to calibrate satellite data. Indeed, by its concept, McClear is a clear sky model and its estimation of DNI is made directly using physical equations under clear sky conditions, whereas in the SolarGIS model, all-sky DNI is estimated using empirical relations with GHI. Therefore, using DNI derived from McClear is more straightforward in the calibration suggested below, since DNI under clear sky and as extracted from a physical model is strongly dependent on the composition of the atmosphere, namely aerosols, which is the parameter to be looked at in the lidar backscatter coefficient.

By looking to the scatter plots of the McClear model *vs.* ground measurements, there is no clear difference between days with high aerosol loads and clean days. In order to go deeper in the analysis and study how the performance of the McClear model behaves with an increasing load of aerosols in the atmosphere, the plot of the ratio of the hourly DNI derived from the McClear database to the hourly DNI calculated from ground measurements, *vs.* Betatot (which is directly related to aerosol loads), is shown in Figure 6.23 for the hour from 11 am to 12 pm, for the selected clear days from December 2012 to November 2013. The McClear model performs quite well, evidenced by the closeness of the data points to a ratio of 1, up to a certain value of Betatot; after that value of Betatot, it is clear that the performance of the McClear model decreases, as the DNI ratio departs from 1: higher Betatot values, i.e., higher aerosol contents, lead to an overestimation of the DNI as modelled by McClear.

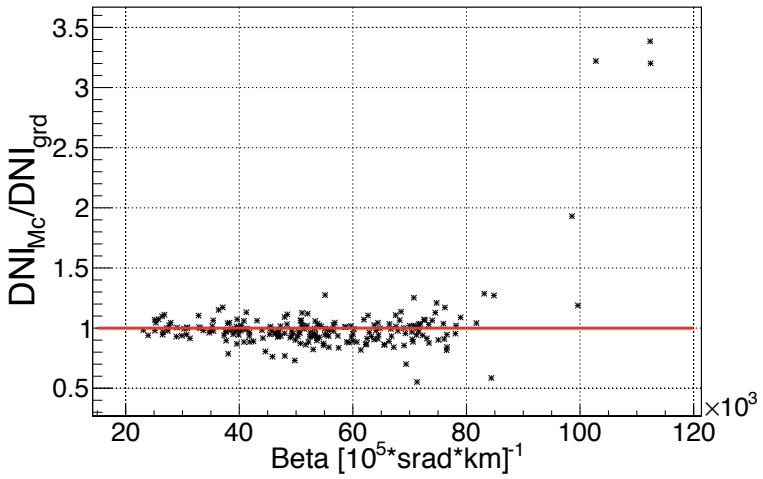

Figure 6.23: Study of the performance of the McClear model represented by the ratio $DNI_{McClear}/DNI_{ground}$, *vs.* Betatot, at the hour from 11 am to 12 pm, where $DNI_{McClear}$ and DNI_{ground} are, respectively, the hourly values of DNI obtained from McClear and calculated from DNI measurements.

In order to quantify the decrease in performance at high Betatot values, an exponential function was fitted to the ratios corresponding to Betatot values around $70000 \cdot [10^5\ srad \cdot km]^{-1}$ and higher, where the McClear model shows a poor performance. The equation of the fit is:

$$DNI_{McClear}/DNI_{ground} = CF = \exp(slope \cdot Betatot + const), \tag{6.9}$$

where Betatot is the sum of the hourly-averaged backscatter lidar signals at noon, up to a height of 5 km; $DNI_{McClear}$ is the hourly value of DNI derived by McClear and DNI_{ground} is the hourly value of DNI derived from the ground measurements also at

noon. CF stands for calibration function, and *slope* and *const* are parameters obtained from the fit and are shown on the statistics box of Figure 6.24.

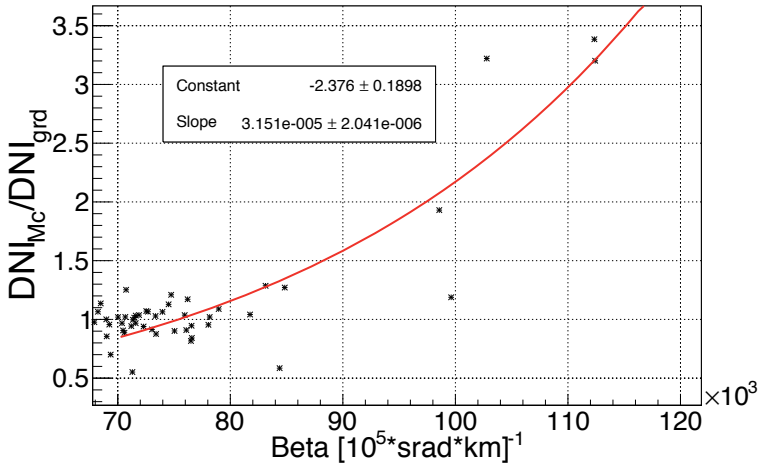

Figure 6.24: Fit applied to the performance of the McClear model for Betatot values exceeding $70000 \cdot [10^5\ srad \cdot km]^{-1}$.

The fitted function is then used to correct the DNI values derived from the McClear model, for Betatot values higher than $70000 \cdot [10^5\ srad \cdot km]^{-1}$. The correction uses Equation 6.9 as follows:

$$DNI_{McClear,corr} = DNI_{McClear}/CF, \tag{6.10}$$

where $DNI_{McClear,corr}$ is the corrected value of $DNI_{McClear}$.

Equation 6.10 represents a calibration method of the McClear database, as a function of Betatot. In order to demonstrate the validity of this calibration, the performance of the McClear model was studied for different periods of time. Figure 6.25 shows the performance of the McClear model *vs.* Betatot at 11 am (from 10 to 11 am), and Figure 6.26 shows the performance of the McClear model *vs.* Betatot at 1 pm (from 12 to 1 pm). Both figures present on the left side the actual McClear performance, and on the right the performance of the corrected McClear, after applying the function in Equation 6.10. The graphs on the right side confirm the effect of the calibration.

In order to evaluate the effect of the suggested method on the calibration of the McClear model, the relative bias and RMSE were calculated between the DNI ratio (hourly DNI McClear/hourly DNI measurements) and the ideal value of 1, at the hours 11 am and 1 pm. The results are listed in Table 6.9, and show that the calibrated dataset has lower RMSE values but higher biases than the original McClear dataset. This bias increase, however, is due to the fact that no calibration was applied here to the DNI

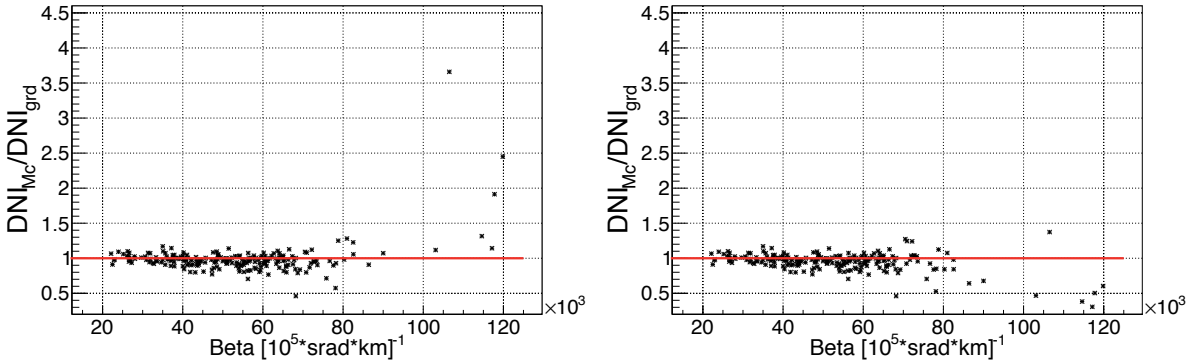

Figure 6.25: Validation of the calibration of the McClear model, at the hour 11 am, from 10 to 11 am. On the left, the uncalibrated DNI ratio; on the right, the same ratio after correcting the McClear DNI.

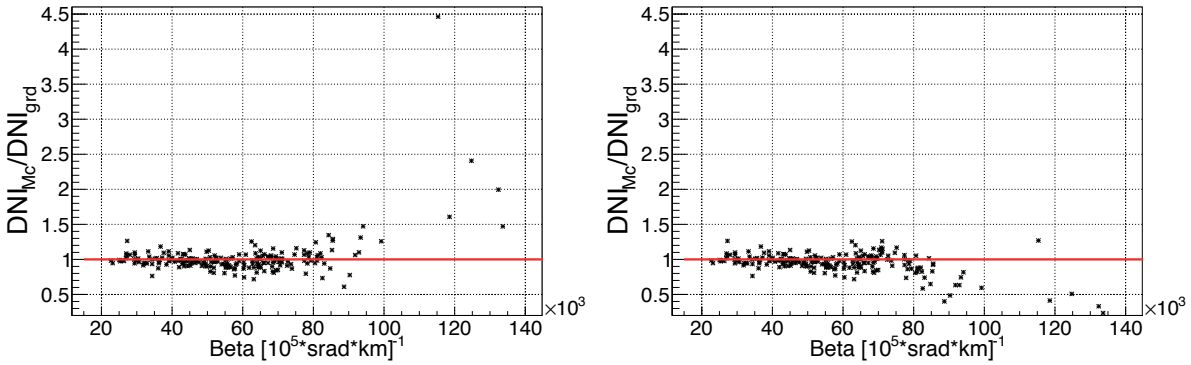

Figure 6.26: Validation of the calibration of the McClear model, at the hour 1 pm, from 12 to 1 pm. On the right, the uncalibrated DNI ratio; on the left, the same ratio after correcting the McClear DNI.

ratios at Betatot below $70000 \cdot [10^5\ srad \cdot km]^{-1}$, where McClear generally underestimates DNI.

Model	Np	rMBE	rRMSE
$Hour = 11$			
McClear	214	-1.05	24.2
Calibrated McClear	214	-5.11	14.2
$Hour = 13$			
McClear	213	1.96	29.22
Calibrated McClear	213	-5.1	15.53

Table 6.9: Statistical indicators of the comparison of McClear against McClear calibrated using the Betatot coefficient, for the data set of the period December 2013 to November 2014, for the hours 11 am and 1 pm. rMBE and rRMSE are in %.

The same calibration process was attempted for the selected clear days of the next twelve months, from December 2013 to November 2014. However, very few Betatot values in this selection were large enough (greater than $70000 \cdot [10^5\ srad \cdot km]^{-1}$) to apply the calibration function obtained here. The reason for that is the large number of missing data acquired by the lidar this year due to problems in the data acquisition system; most of the missing data were confined to the summer season, from May to September, which represents the higher percentage of dusty and hazy days, conditions where the Betatot value is high. It should be noted that, similarly, the first selection of clear sky moments (from December 2012 to November 2013) does not include days with missing lidar data, which might have been classified as clear days as well, and could have provided more days with high Betatot values. Another constraint in the selection of clear days is that the clear moments had to be selected in a window of 3 hours (from 10 am to 1 pm) instead of only the hour required to derive the model (from 11 am to 12 pm); this reduces the number of clear days, but was necessary in order to eliminate possible moments of a passing cloud which may be unnoticed but blocking one instrument and not the other, because of their different viewing angles.

In view of these results, it can be deducted that, in general, the McClear model performs quite well when compared to ground measurements. The low performance seen in high aerosol regimes is expected since the spatial resolution of the aerosol databases used as inputs to the McClear model is greater than 100 km (1.125° for the reanalysis model MACC). Thus, the use of the lidar ceilometer for extracting aerosol information is a sort of downscaling of the aerosol information to a local adjustment, and allows to improve the accuracy in the estimation of solar radiation by McClear. Nevertheless, the calibration technique could be better elaborated, by including more statistics in the production of the correction function. This may be possible through a more accurate and automated approach for selection of clear moments. Two clear-sky identification methods, found in the literature, will be explored in the future. The first one filters the clear-sky periods by their diffuse ratio values and uses a modified clearness index [162] for clear-sky classification, and the other method was developed by [165] as a series of tests on 1-minute measurements of global and diffuse radiation accounting for magnitude, variability, and change in magnitude with time.

Chapter 7

Conclusions

Given its geographic location and its favourable climatic conditions, Qatar could be expected to have high solar resources in terms of direct radiation, making it suitable for solar energy applications, and in particular, the concentrating technologies. Ground measurements of DNI are in general scarce, and not yet available for Qatar. The existing information in this regard consists of solar maps calculated for the country, based on models and satellite observations. Modelled DNI data generally have high uncertainties and are not accurate enough, one of their main limitations being the determination of the inputs to the model. Under clear sky conditions, aerosols represent the critical input in solar radiation modelling, and are usually determined in terms of Aerosol Optical Depth, AOD, which is best measured at ground level, with sunphotometers. Alternatively, when ground measurements are missing, as is the case in Qatar, spaceborne measurements are used, albeit with higher uncertainties than ground measurements. In any case, it is vital to determine aerosol information with high accuracy, in order to improve DNI modelling in regions of high potential for solar power generation.

This research work focused largely on the analysis of ground-measured solar radiation data and backscatter profiles of the atmosphere in Doha, Qatar. The goal is to address the unavailability of ground-truth data of DNI and to determine aerosol information in a direct and efficient way. This is important to evaluate the reliability of the existing solar resource information in Qatar, available until now only as modelled data. The study was possible through a correlation between lidar-ceilometer and solar radiation measurements, taken at the same location in Doha during a one-year period, from December 2012 to November 2013. As a result, two models for deriving DNI data in clear-sky conditions were developed and show good results and some improvement when compared to existing models. At the same time, a method for calibrating satellite-derived solar data in extreme conditions was suggested, demonstrating the potential use of lidar-ceilometer devices for

estimating the radiative effect of aerosols. This application is of particular interest in a region like Qatar, and also for any other location characterised by dusty and highly aerosol-loaded atmospheric conditions.

For the analysis of the solar radiation components, one-minute quality-controlled averages of DNI, GHI and DHI were measured with a high precision monitoring station located in Doha. Hourly, daily and monthly averages of solar irradiance as well as two atmospheric indices, the clearness index and the diffuse ratio, were derived and studied. The yearly-averaged DNI, GHI and DHI were 218.7, 245.8 and 96.0 W/m^2, totalling 1916, 2153 and 841 $kWh/m^2/year$, respectively. The monthly DNI averages ranged from 157 to 275 W/m^2, GHI varied between 151 and 315 W/m^2, and DHI ranged from 63 to 136 W/m^2, with the highest monthly averages of DNI = 275.0 W/m^2 in October, GHI = 315.5 W/m^2 in June, and DHI = 135.6 W/m^2 also in June, for the year under study. The mean values of GHI and DHI increased notably from winter to summer, having a peak in June, whereas DNI had only a small increase and remained, on average, almost constant throughout the year. This DNI behaviour is due to a balance between cloudy days in the winter season and haze and dust during the summer. The clearness index and the diffuse ratio show yearly averages of 0.65 and 0.39, respectively. The high diffuse fraction of almost 40% indicates the high level of aerosols in the atmosphere of Doha. These results reflect the solar conditions in the city of Doha, and are limited to a period of one year of measurements. However, it could be expected to find more or less similar solar conditions in other coastal and populated cities of Qatar.

In parallel, the backscatter measurement profiles of the atmosphere in Doha were also studied. On a daily basis, the intensity of the backscatter as a function of the time of the day was acquired by a lidar-ceilometer device, each 36 s for each 10 m in height. This measured signal reflects the amount of constituents of the atmosphere at the corresponding height, and was used in the analysis presented here. The lidar-ceilometer device is capable of profiling the atmosphere in a vertical direction up to 15 km in height. However, a height limit of 5 km was found to be a good compromise between excluding the noisier signals and including the dynamicity of the atmosphere. This limit in height was used for the integration of the backscatter signal in the vertical column, giving the parameter used for the correlation between the ceilometer and the solar radiation measurements.

As a result of the correlation study, two models, the Beta-model and the BetaCos-model, were derived and elaborated for estimating DNI in clear sky conditions. The Beta-model was tested and validated against ground-measured data for DNI derivation in the zenith angle range of 1.877° to 53.79°. Considering the selected clear days from

December 2012 to November 2013 and for the hours from 10 am to 1 pm, the bias and the RMSE of the Beta-model are 0.67% and 11.28%, respectively. When compared to results of two advanced satellite models for the same days, it was found that the Beta-model performs at least as well as the SolarGIS (-4.85% bias and 14.73% RMSE), and the McClear model (-1.74% bias and 11.46% RMSE). The BetaCos-model was developed in an attempt to improve the errors observed in the Beta-model, resulting in better performance. The BetaCos-model takes into account the difference in air masses sensed by the two instruments. The results of the BetaCos-model show an improvement (-2.56% bias and 10.39% RMSE) compared the McClear model (-8.81% bias and 15.24% RMSE), with a zenith angle coverage ranging from 1.877° to 82.89°.

In addition to the derived models and despite the limited available statistics, an example calibration of the McClear method was also suggested. This calibration applies to data corresponding to high aerosol loads and results in an improvement in the performance of the McClear method during extreme conditions.

Considering one year of measurements, it is found that in general Doha has a sunny climate, but with high levels of diffuse solar radiation, mostly due to dust and other aerosols. These atmospheric properties are expected to increase uncertainties in the estimation of DNI from satellite-based models. The BetaCos-model, developed and validated here, is shown to have a performance comparable to a physical clear-sky model. This indirectly indicates that the integrated backscatter signal over the vertical column, can be used to evaluate the radiative effect of aerosols, as an alternative to the commonly used AOD parameter. Moreover, it highlights the potential usefulness of lidar-ceilometer devices in the solar resource assessment field.

In summary, the analysis and the results presented in this thesis work make available invaluable information, spanning from high precision ground measurements of solar radiation, to lidar-ceilometer data measuring the magnitude of the variations of aerosol loads in the atmosphere of Doha, Qatar. This precious information was used for the elaboration of a novel method for DNI derivation and for the validation and calibration of existing modelled DNI data. The ground-measured solar radiation data used in this work, could be used to validate other existing databases that are not accurate enough, and can contribute to the reduction of their uncertainties. A physical model could be expected to be derived from the correlation study between lidar-ceilometer and solar radiation measurements, an approach to be elaborated as future perspectives for this thesis work.

Chapter 8

Future work

8.1 Beta-model improvement

The Beta-model introduced in this work describes the variations of DNI through the year as a function of the day-to-day changes in Betatot, around solar noon, for clear days. This restriction to a temporal window around noon was chosen to ensure that both DNI and backscatter were measured roughly along the same direction in the sky. In order to test whether the Betatot changes through the day, measured vertically with the CL51 ceilometer, can be related to changes in DNI at the corresponding hours of the day, the first step is to study how Betatot is changing through the day, i.e., its hour-to-hour variations. Such a study requires the use of a selection of clear days, in which there are no visible clouds in the line of sight of both the ceilometer (vertically upwards) and the pyrheliometer (following the sun) through the day. A window of time was chosen from hours 7 (average of 6 to 7 am) to 18 (5 to 6 pm). Figure 8.1 shows preliminary results of this study, using the new selection of clear days, from December 2012 to November 2013. Betatot is calculated for each hour of the day and displayed as a function of the hour, averaged by month (dashed lines in the figure) and by season (summer and winter as defined in Section 6.1.3).

As seen in the figure, the hourly averages of Betatot change as the day evolves, for all the months, with the highest values usually around 1–2 pm. It is also seen that the months previously defined as summer show higher hourly averages and range of variations through all these hours, with respect to the winter months. It should be noted, however, that for this study the clear days were selected based on a day free of clouds from 6 am to 6 pm, as seen only by the CL51 ceilometer (no DNI selection). This selection was also limited by the missing lidar data, giving a total of 136 days identified as cloud-free. Although clear days were found in all months, some months have a noticeably lower

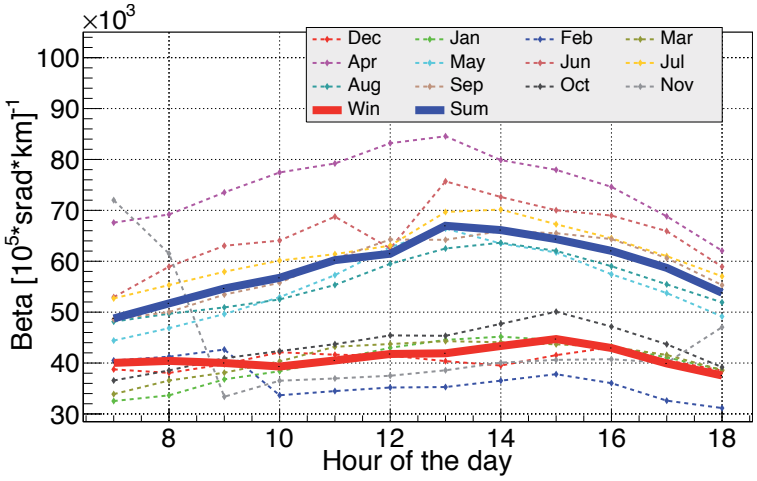

Figure 8.1: Beta values for each hour from 6 am to 6 pm, averaged by month (thin dashed lines) and by season (winter and summer, thicker lines), for the new selection of clear days, from December 2012 to November 2013.

number of clear days compared to other months. Therefore, not all monthly averages are well represented and this study is still to be better elaborated with more statistics and more accurate averages. This can be seen in the averages at hours 7 and 8 for the month of November, which are dominated by the high values of one day, since only 4 clear days were selected for this month.

As additional consideration, and in order to be able to relate the changes in Betatot seen throughout the day with DNI, it is important to remove the zenith angle dependence of DNI. The K_n index used for the Beta-model in the previous sections does not remove this angular dependence for all sun positions through the day; however, it is valid for the angles used for the derivation and validation of the Beta-model, that is, for zenith angles in the range 1.877° to 53.79°. Two approaches can be thought of in this regard:

- A possible analysis, expected to allow a wider zenith angle coverage, is to define a model based on the suggested Beta-model, but with an additional degree of freedom: the zenith angle. This is possible through the definition of different exponential functions to fit K_n *vs.* Betatot (see Equation 6.2) for every time slot of the day, i.e., in different ranges of zenith angles. The slope and constant parameters would then be different for each slot of time, in a way to fit the corresponding data points; a correlation is expected to be found between each of these constant parameters and the zenith angle, which will result in the final model:

$$K_n = \exp\left[slope(\theta_z) \cdot Betatot + const(\theta_z)\right], \tag{8.1}$$

where $slope(\theta_z)$ and $const(\theta_z)$ are functions of the zenith angle θ_z.

This analysis is currently under study and the preliminary results are promising. In Figure 8.2, K_n is shown *vs.* Betatot, in several time slots of the day represented by different colours in the graph, from 8 am to 4 pm. For comparison, the red line represents the values of K_n that follow the Beta-model equation. It should be noted that the data points in this figure correspond to the new selection of clear days, as explained in this paragraph.

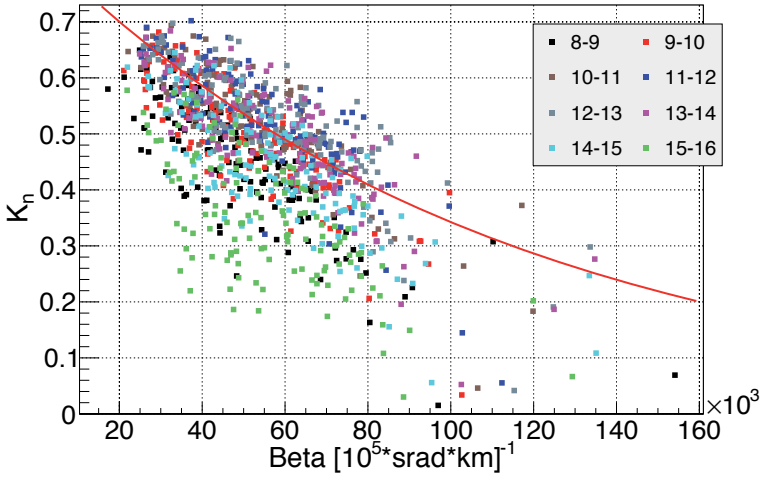

Figure 8.2: Hourly values of measured K_n *vs.* Betatot from 8 am to 4 pm for the new selection of clear days, from December 2012 to November 2013. For illustration purposes only, the red line representing the K_n values derived from the Beta-model is also shown.

- Another possible methodology to expand the zenith angle coverage is to use a modified clearness index, K'_n. This modified index, proposed by [166] to remove most of the zenith angle dependence of DNI, may be a good parameter to correlate with Betatot, for all the daytime zenith angles. The derivation of K'_n requires the calculation of the air mass m for a given zenith angle as follows:

$$m = \frac{1}{\cos(\theta_z) + 0.50572 \cdot (96.07995 - \theta_z)^{-1.6364}}, \tag{8.2}$$

where θ_z is the solar zenith angle in degrees. K'_n is then calculated as:

$$K'_n = \frac{K_n}{0.1 + 1.031 \cdot \exp\left(\frac{-1.4}{0.9 + 9.4/m}\right)}, \tag{8.3}$$

where K_n is the DNI clearness index defined before.

Figure 8.3 shows a comparison between the hourly variations of K_n and K'_n throughout the day, for all the clear days selected in this paragraph. It is seen that K'_n as

compared to K_n is somewhat flatter on a wider range of time during the day, and thus allows to cover a slightly wider range of zenith angles.

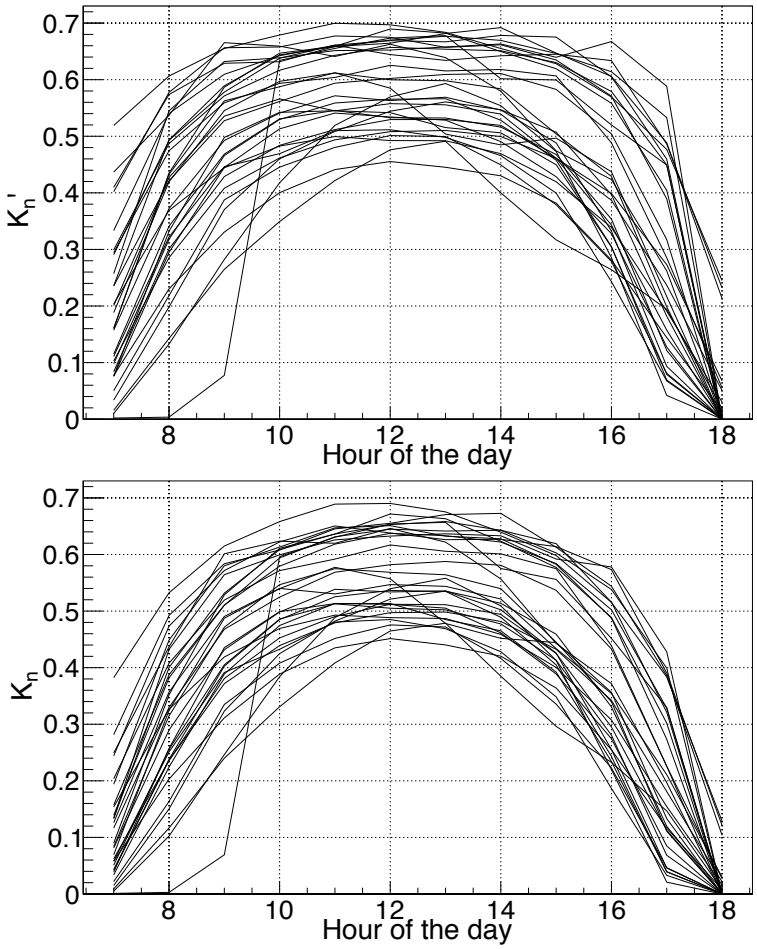

Figure 8.3: Hourly variations of K'_n (top) and K_n (bottom) through the day, for the new selection of clear days from December 2012 to November 2013.

8.2 Physical model development

The Beta-model is an empirical equation correlating the backscatter measurements with the DNI measurements. However, the concept from which the Beta-model was derived is related to the attenuation of the solar radiation at the top of the atmosphere after traversing a certain distance in the atmosphere, before reaching the ground. This is also described by the Lambert-Beer equation, defined previously, which can be written as follows:

$$DNI = DNI_0 \cdot \exp[-(\tau_a + \tau_{WV} + \tau_{ozone} + \tau_{Rayleigh}) \cdot m], \tag{8.4}$$

where DNI_0 is the DNI at the top of the atmosphere defined in Equation 1.1; τ_a, τ_{WV}, τ_{ozone} and $\tau_{Rayleigh}$ are the optical depths of aerosols, water vapour, ozone molecules and gas molecules in the atmosphere, respectively; and m is the air mass.

Assuming that aerosols are the only changing parameter in the atmosphere, Equation 8.4 can be written as:

$$K_n = \exp[-(\tau_a + \tau_{others}) \cdot m] \tag{8.5}$$

In order to remove the dependency of this equation on m, a new modified clearness index (K_n'') can be defined as:

$$K_n'' = -\frac{1}{m}\ln(K_n) = (\tau_a + \tau_{others}) \tag{8.6}$$

If a linear relation can be found between K_n'' and Betatot as follows:

$$K_n'' = a \cdot Betatot + b, \tag{8.7}$$

where a and b are constants, then the aerosol optical depth τ_a can be directly related to Betatot.

Since in reality water vapour is also a changing parameter in the atmosphere of Doha, another physical approach of using the Betatot coefficient would be to consider T_l, the Linke turbidity factor in the atmosphere, and deduct a new formulation of this factor using ceilometer measurements. The Linke turbidity has been used to estimate solar radiation by considering the properties and quantity of air molecules and aerosols in the atmosphere. It is defined as the number of Rayleigh atmospheres that would lead to the observed attenuation of the direct normal radiation, and is given by the equation [140]:

$$DNI = DNI_{TOA} \cdot \exp(-T_l \cdot \tau_{Rayleigh} \cdot m) \tag{8.8}$$

By equating Equations 8.8 and 6.2, the hourly Linke turbidity factor could be determined from the Beta-model.

These possibilities of quantifying aerosol and turbidity parameters from the Betatot coefficient, if validated, will widen the scope for the use of lidar-ceilometers. Instead of only being used for determining the boundary layer height or cloud height (standard uses) or for deriving clear-sky DNI and empirically calibrating satellite-derived solar data in high aerosol loads regimes (as discussed in this thesis work), lidar-ceilometers could also be used to give quantitative values of aerosol optical depths in the atmosphere, a parameter of high importance in the solar resource assessment field, and for which measurements are not currently available for Qatar.

Bibliography

[1] Y.A.G. Abdalla and M.K. Baghdady. Global and diffuse solar radiation in Doha (Qatar). *Solar and Wind Technology*, 2(3-4):209–212, 1985.

[2] QNDS. Qatar National Development Strategy, 2001-2016. Technical report, General Secretariat For Development Planning, 2011.

[3] C. Gueymard, W.T. Gustafson, G. Bender, A. Etringer, and P. Storck. Evaluation of procedures to improve solar resource assessments: Optimum use of short-term data from a local weather station to correct bias in long-term satellite derived solar radiation time series. In *Proceedings of World Renewable Energy Forum, Denver, CO*, 2012.

[4] M. Suri, J. Remund, T. Cebecauer, C. Hoyer-Klick, D. Dumortier, T. Huld, P.W. Stackhouse, Jr., and P. Ineichen. Comparison of direct normal irradiation maps for europe. In *Proceedings of SolarPACES International Conference*, 2009.

[5] C.A. Gueymard. Uncertainties in modeled direct irradiance around the Sahara as affected by aerosols: Are current datasets of bankable quality? *J Sol Energy Eng*, 133(3):031024, 2011.

[6] C.A. Gueymard and R. George. Gridded aerosol optical depth climatological datasets over continents for solar radiation modeling. In *Solar World Congress, Orlando, USA*, 2005.

[7] T. Cebecauer, M. Suri, and C.A. Gueymard. Uncertainty sources in satellite-derived direct normal irradiance: how can prediction accuracy be improved globally? In *Proceedings of SolarPACES International Conference*, 2011.

[8] B.N. Holben, T.F. Eck, I. Slutsker, D. Tanré, J.P. Buis, A. Setzer, E. Vermote, J.A. Reagan, Y.J. Kaufman, T. Nakajima, F. Lavenu, I. Jankowiak, and A. Smirnov. AERONET - A federated instrument network and data archive for aerosol characterization. *Remote Sensing of Environment*, 66(1):1–16, 1998.

[9] J. Keller, S. Bojinski, and A.S.H. Prevot. Simultaneous retrieval of aerosol and surface optical properties using data of the Multi-angle Imaging SpectroRadiometer (MISR). *Remote Sensing of Environment*, 107(1-2):120–137, 2007.

[10] P.G. Kosmopoulos, D.G. Kaskaoutis, P.T. Nastos, and H.D. Kambezidis. Seasonal variation of columnar aerosol optical properties over Athens, Greece, based on MODIS data. *Remote Sensing of Environment*, 112(5):2354–2366, 2008.

[11] MACC. http://www.gmes-atmosphere.eu/about/project/details, 2014. Last accessed April 2015.

[12] P.G. Kosmopoulos, D.G. Kaskaoutis, P.T. Nastos, and H.D. Kambezidis. Assessment of the level-3 MODIS daily aerosol optical depth in the context of surface solar radiation and numerical weather modeling. *Atmospheric Chemistry and Physics*, 13:675–692, 2013.

[13] J. Polo and G. Estalayo. Impact of atmospheric aerosol loads on Concentrating Solar Power production in arid-desert sites. *Solar Energy*, 115:621–631, 2015.

[14] A.A. Kokhanovsky, F.-M. Breon, A. Cacciari, E. Carboni, D. Diner, W. Di Nicolantonio, R.G. Grainger, W.M.F. Grey, R. Holle, K.-H. Lee, Z. Li, P.R.J. North, A.M. Sayer, G.E. Thomas, and W. von Hoyningen-Huene. Aerosol remote sensing over land: A comparison of satellite retrievals using different algorithms and instruments. *Atmospheric Research*, 85:372–394, 2007.

[15] NASA Facts. The balance of power in the earth-sun system. NASA Publication Number: FS-2005-9-074-GSFC, 2005.

[16] J.A. Duffie and W.A. Beckman. *Solar Engineering of Thermal Processes. Fourth edition.* John Wiley & Sons, Inc., 2013.

[17] C. Fröhlich. Solar constant, construction of a composite total solar irradiance (TSI) time series from 1978 to present. Physikalisch-Meteorologisches Observatorium Davos, World Radiation Center, Davos, Switzerland, 2014.

[18] C.A. Gueymard. The sun's total and spectral irradiance for solar energy applications and solar radiation models. *Solar Energy*, 76:423–453, 2004.

[19] G. Kopp and J.L. Lean. A new, lower value of total solar irradiance: Evidence and climate significance. *Geophysical Research Letters*, 38(1-16):L01706, doi:10.1029/2010GL045777, 2011, 2011.

[20] F. Tendeku. Retrieval of atmospheric turbidity coefficient and water column density from solar irradiance data. *Proceedings of Arkansas Academy of Science*, 49, 1995.

[21] M. Paulescu, E. Paulescu, P. Gravila, and V. Badescu. *Weather Modeling and Forecasting of PV Systems Operation*. Springer, 2013.

[22] WMO 2008. Guide to meteorological instruments and methods of observation. WMO-No. 8, World Meteorological Organization, Geneva, Switzerland. 7th edition, 2008.

[23] R. Rösemann. *A guide to solar radiation measurement*. Gengenbach Messtechnik, 2011.

[24] M.A. Martinez, J.M. Andujar, and J.M. Enrique. A new and inexpensive pyranometer for the visible spectral range. *Sensors*, 9:4615–4634, 2009.

[25] C. Fröhlich. History of Solar Radiometry and the World Radiometric Reference. *Metrologia*, 28:111–115, 1991.

[26] D.R. Myers. Quantitative analysis of spectral impacts on silicon photodiode radiometers. In *American Solar Energy Society Solar Conference Proceedings; Raleigh, North Carolina. Boulder, CO*, 2011.

[27] I. Reda, T. Stoffel, and D. Myers. Calibration of a solar absolute cavity radiometer with traceability to the world radiometric reference. Tech. Rep. NREL TP-463-20619 National Renewable Energy Laboratory, Golden, CO, 1996.

[28] ASTM 2005a. Standard test method for calibration of pyrheliometers by comparison to reference pyrheliometers. Standard ASTM E816-05, American Society for Testing and Materials, West Conshohocken, PA, 2005.

[29] ASTM 2005b. Standard test method for calibration of a pyranometer using a pyrheliometer. Standard ASTM G167-05, American Society for Testing and Materials, West Conshohocken, PA, 2005.

[30] ISO 9846:1993. Solar energy – calibration of a pyranometer using a pyrheliometer. ISO catalogue ISO 9846:1993, 1993.

[31] ISO 9846:1992. Solar energy – calibration of field pyranometers by comparison to a reference pyranometer. ISO catalogue ISO 9846:1992, 1992.

[32] ISO 9059-1990. Solar energy – calibration of field pyrheliometers by comparison to a reference pyrheliometer. ISO catalogue ISO 9059-1990, 1990.

[33] ISO 9060-1990. Solar energy – specification and classification of instruments for measuring hemispherical solar and direct solar radiation. ISO catalogue, ISO 9060-1990, 1990.

[34] S. Cros and L. Wald. Survey of the main databases providing solar radiation data at the ground level. In *23rd EARSeL Annual Symposium "Remote Sensing in Transition", Ghent, Belgium*, 2003.

[35] G. König-Langlo, R. Sieger, H. Schmithüsen, A. Bücker, F. Richter, and E.G. Dutton. The Baseline Surface Radiation Network and its World Radiation Monitoring Centre at the Alfred Wegener Institute. WMO WCRP-24/2013. http://www.bsrn.awi.de/, 2013. Last accessed April 2015.

[36] WRDC. http://wrdc-mgo.nrel.gov/, 1964. Last accessed April 2015.

[37] A.S. Ångström. Solar and terrestrial radiation. *Q. J. Roy. Met. Soc.*, 50:126, 1924.

[38] A.K. Katiyar and C.K. Pandey. A review of solar radiation models, Part I. *Journal of Renewable Energy*, 2013, 2013. 10.1155/2013/168048.

[39] C.A. Gueymard, P. Jindra, and V. Estrada-Cajigal. A critical look at recent interpretations of the Ångström approach and its future in global solar radiation prediction. *Solar Energy*, 54:357–363, 1995.

[40] J. Almorox. Estimating global solar radiation from common meteorological data in aranjuez, spain. *Turk. J. Phys.*, 35:53–64, 2011.

[41] J.M. Gordon and M. Hochman. On correlations between beam and global radiation. *Solar Energy*, 32:329–336, 1984.

[42] G.F. Orgil and K.G. Hollands. Correlation equation for hourly diffuse radiation on a horizontal surface. *Solar Energy*, 19:357–359, 1977.

[43] D.G. Erbs, S.A. Klein, and J.A. Duffie. Estimation of the diffuse radiation fraction for hourly, daily, and monthly-average global radiation. *Solar Energy*, 28:293, 1982.

[44] D.T. Reindl, W.A. Beckmann, and J.A. Duffie. Diffuse fraction correlations. *Solar Energy*, 45(1):1–7, 1990.

[45] E.L. Maxwell. A quasi-physical model for converting hourly global horizontal to direct normal insolation. Technical Report No. SERI/TR-215-3087, Golden, CO: Solar Energy Research Institute, 1987.

[46] P. Ineichen. Comparison and validation of three global-to-beam irradiance models against ground measurements. *Solar Energy*, 82:501–512, 2008.

[47] C.A. Gueymard. Direct solar transmittance and irradiance predictions with broadband models. Part I: detailed theoretical performance. *Solar Energy*, 74:355–379, 2003.

[48] F. Vignola, J. Michalsky, and T. Stoffel. *Solar and Infrared Radiation Measurements*. CRC Press, 2012.

[49] M.A. Behrang, E. Assareh, A. Ghanbarzadeh, and A.R. Noghrehabadi. The potential of different artificial neural network (ANN) techniques in daily global solar radiation modeling based on meteorological data. *Solar Energy*, 84:1468–1480, 2010.

[50] J. Mubiru and E.J.K.B. Banda. Estimation of monthly average daily global solar irradiation using artificial neural networks. *Solar Energy*, 82:181–187, 2008.

[51] A. Linares-Rodriguez, J.A. Ruiz-Arias, D. Pozo-Vazquez, and J. Tovar-Pescador. An artificial neural network ensemble model for estimating global solar radiation from meteosat satellite images. *Energy*, 61:636–645, 2013.

[52] Y. Eissa, P.R. Marpu, I. Gherboudj, H. Ghedira, T.B.M.J. Ouarda, and M. Chiesa. Artificial neural network based model for retrieval of the direct normal, diffuse horizontal and global horizontal irradiances using SEVIRI images. *Solar Energy*, 89:1–16, 2013.

[53] D. Cano, J.M. Monget, H. Guillard, M. Albuisson, N. Regas, and L. Wald. A method for the determination of the global solar radiation from meteorological satellite data. *Solar Energy*, 37:31–39, 1986.

[54] R. Perez, P. Ineichen, K. Moore, C. Chain, M. Kmiecik, R. George, and F. Vignola. A new operational satellite to irradiance model: description and validation. *Solar Energy*, 73(5):307–317, 2002.

[55] C. Rigollier, M. Lefèvre, and L. Wald. The method Heliosat-2 for deriving shortwave solar radiation from satellite images. *Solar Energy*, 77:159–169, 2004.

[56] A. Zelenka, R. Perez, R. Seals, and D. Renné. Effective accuracy of the satellite-derived hourly irradiance. *Theor Appl Climatol*, 62:199–207, 1999.

[57] K. Yang, G.W. Huang, and N. Tamaig. A hybrid model for estimating global solar radiation. *Solar Energy*, 70(1):13–22, 2001.

[58] K.G. Karlsson, A. Riihel, R. Muller, J.F. Meirink, J. Sedlar, M. Stengel, M. Lockhoff, J. Trentmann, F. Kaspar, R. Hollmann, and E. Wolters. CLARA-A1: a cloud, albedo, and radiation dataset from 28 yr of global AVHRR data. *Atmos. Chem. Phys.*, 13:5351–5367, 2013.

[59] J. Polo, L.F. Zarzalejo, and L. Ramírez. Solar radiation derived from satellite images. In M. Paulescu, E. Paulescu, P. Gravila, and V. Badescu, editors, *Weather Modeling and Forecasting of PV Systems Operation*. Springer, 2013.

[60] L. Diabate, H. Demarcq, N. Michaud-Regas, and L. Wald. Estimating incident solar radiation at the surface from images of the Earth transmitted by geostationary satellites: the Heliosat project. *International Journal of Solar Energy*, 5:261–278, 1988a.

[61] C. Rigollier, O. Bauer, and L. Wald. On the clear sky model of the ESRA – European Solar Radiation Atlas – with respect to the heliosat method. *Solar Energy*, 68:33–48, 2000.

[62] L. Wald. Heliosat-4 use of ground albedo and MSG parameters. MACC-II Deliverable D_123.3, 2014.

[63] C. Schillings, H. Mannstein, and R. Meyer. Operational method for deriving high resolution direct normal irradiance from satellite data. *Solar Energy*, 76:475–484, 2004.

[64] IEA/SHC task 36. Solar resource knowledge management, IEA/SHC task 36. International Energy Agency Solar Heating and Cooling Programme.

[65] M. Šúri and T. Cebecauer. SolarGIS: New web-based service offering solar radiation data and PV simulation tools for Europe, North Africa and Middle East. In *EUROSUN 2010 Conference, Graz, Austria*, 2010. http://www.geomodelsolar.eu. Last accessed April 2015.

[66] P. Blanc, B. Gschwind, M. Lefèvre, and L. Wald. The HelioClim project: Surface solar irrradiance data for climate applications. *Remote Sensing*, 3:343–361, 2011. http://www.helioclim.org. Last accessed April 2015.

[67] Irsolav. http://irsolav.com/, 2015. Last accessed April 2015.

[68] 3Tier. http://www.3tier.com/en/, 2015. Last accessed April 2015.

[69] R. Meyer, C. Hoyer, C. Schillings, F. Trieb, E. Diedrich, and M. Schroedter. SOLEMI: A new satellite-based service for high-resolution and precision solar radiation data for Europe, Africa and Asia. In *ISES Solar World Congress 2003*, 2003. http://www.dlr.de/tt/desktopdefault.aspx/tabid-2885/4422_read-6581. Last accessed April 2015.

[70] W.S. Chandler, J.M. Hoell, D. Westberg, C.H. Whitlock, T. Zhang, and P.W. Stackhouse Jr. NASA's Prediction of Worldwide Energy Resource (POWER) Web services. In *AMS 91st Annual Meeting, Seattle, Washington*, 2011. http://eosweb.larc.nasa.gov/sse. Last accessed April 2015.

[71] M. Fontoynont, D. Dumortier, D. Heinemann, A. Hammer, J.A. Olseth, A. Skartveit, P. Ineichen, C. Reise, J. Page, L. Roche, H.G. Beyer, and L. Wald. SATELLIGHT: A www server which provides high quality daylight and solar radiation data for western and central Europe. In *9th Conference on Satellite Meteorology and Oceanography in Paris*, 1998. http://satel-light.com/core.htm. Last accessed April 2015.

[72] T. Stoffel, D. Renné, D. Myers, S. Wilcox, M. Sengupta, R. George, and C. Turchi. Concentrating Solar Power. Best practices handbook for the collection and use of solar resource data. Technical Report NREL/TP-550-47465, http://www.nrel.gov/docs/fy10osti/47465.pdf, 2010. Last accessed April 2015.

[73] Fraunhofer ISE. Photovoltaics Report. Fraunhofer Institute for Solar Energy System ISE, 2014.

[74] S.P. Philipps, A.W. Bett, K. Horowitz, and S. Kurtz. Current status of concentrator photovoltaic (CPV) technology. Fraunhofer Institute for Solar Energy System ISE and National Renewable Energy Laboratory NREL, 2015.

[75] W.B. Stine and M. Geyer. Power from the sun. Version of 'Solar Energy Systems Design' by W.B. Stine and R.W. Harrigan (John Wiley & Sons, Inc. 1986), 2001.

[76] V. Quaschning. Solar thermal power plants, technology fundamentals. *Renewable Energy World*, 6:109–113, 2003.

[77] IRENA/CSP. Concentrating Solar Power, technology brief, IEA-ETSAP, January 2013, 1983.

[78] J.M. Wallace and P.V. Hobbs. *Atmospheric Science. An introductory survey.* Elsevier, 2006.

[79] R.B. Stull. *An Introduction to Boundary Layer Meteorology*. Kluwer Academic Publishers. Springer, 1988.

[80] J.C. Kaimal and J.J. Finnigan. *Atmospheric boundary layer flows: their structure and measurement*. Oxford University Press, New York, NY, 1994.

[81] W. Jiang, X. Yumao, and Y. Hongbin. *Base of Boundary-layer Meteorology*. Nanjing: Nanjing University Press, 1994.

[82] J.R. Garratt. *The Atmospheric Boundary Layer*. Cambridge University Press, Cambridge, 1992.

[83] T.F. Stocker, D. Qin, G.K. Plattner, M. Tignor, S.K. Allen, J. Boschung, A. Nauels, Y. Xia, V. Bex, and P.M. Midgley. *IPCC, 2013: Climate Change 2013: The Physical Science Basis*, volume 29. Cambridge University Press, Cambridge, United Kingdom and New York, NY, USA, 2013.

[84] W.C. Hinds. *Aerosol Technology. Properties, Behavior, and Measurement of Airborne Particles*. John Wiley & Sons, Inc., 1999.

[85] R. Jaenicke. Atmospheric aerosol size distribution. In R.M. Harrison, editor, *Atmospheric Particles*, pages 543–596. John Wiley & Sons, Inc., 1998.

[86] C. Weitkamp. *Lidar, Range-Resolved Optical Remote Sensing of the Atmosphere*. Springer, 2005.

[87] K.Y. Kondtratyev. *Climatic effects of Aerosol and Clouds*. Springer, 1999.

[88] I. Tegen and A.A. Lacis. Modeling of particle size distribution and its influence on the radiative properties of mineral dust aerosol. *J. Geophys. Res.*, 101(19):237–244, 1996.

[89] F. Li, A.M. Vogelmann, and V. Ramanathan. Saharan dust aerosol radiative forcing measured from space. *Journal of Climate*, 17(13):2558–2571, 2004.

[90] N. Bellouin, O. Boucher, J. Haywood, and M.S. Reddy. Global estimate of aerosol direct radiative forcing from satellite measurements. *Nature*, 438:1138–1141, 2005.

[91] J. Zhang, S.A. Christopher, L.A. Remer, and Y.J. Kaufman. Shortwave aerosol cloud-free radiative forcing from Terra II: Seasonal and global distributions. *J. Geophys. Res*, 110, 2005.

[92] F. Marenco, V. Santacesaria, A.F. Bais, D. Balis, A. di Sarra, A. Papayannis, and C. Zerefos. Optical properties of tropospheric aerosols determined by lidar and spectrophotometric measurements (Photochemical Activity and Solar Ultraviolet Radiation Campaign). *Appl. Opt.*, 36(27):6875–6886, 1997.

[93] E.J. Welton, K.J. Voss, P.K. Quinn, P.J. Flatau, K. Markowicz, J.R. Campbell, J.D. Spinhirne, H.R. Gordon, and J.E. Johnson. Measurements of aerosol vertical profiles and optical properties during INDOEX 1999 using micropulse lidars. *J. Geophys. Res.*, 107:8019–8039, 2002.

[94] M.I. Mishchenko, L.D. Travis, and A.A. Lacis. *Scattering, Absorption and Emission of Light by Small Particles*. Cambridge University Press, 2002.

[95] C.F. Bohren and D.R. Huffman. *Absorption and Scattering of Light by Small Particles*. John Wiley & Sons, Inc., 1983.

[96] H.C. van de Hulst. *Light scattering by small particles*. Dover Publications, Inc., 1981.

[97] G. Mie. Beiträge zur Optik trüber Medien, speziell kolloidaler Metallösungen. *Annalen der Physik*, 330(3):377–445, 1908.

[98] M.I. Mishchenko. Calculation of the amplitude matrix for a nonspherical particle in a fixed orientation. *Appl. Opt.*, 39:1026–1031, 2000.

[99] E.M. Purcell and C.R. Pennypacker. Scattering and absorption of light by nonspherical dielectric grains. *Astrophysical Journal*, 186:705–714, 1973.

[100] V. Kovalev and W. Eichinger. *Elastic Lidar. Theory, Practice, and Analysis Methods*. John Wiley & Sons, Inc., 2004.

[101] D.I. Cooper and W.E. Eichinger. Structure of the atmosphere in an urban planetary boundary layer from lidar and radiosonde observations. *Journal of Geophysical Research*, 99:22937–22948, 1994.

[102] B.A. Holmen, W.E. Eichinger, and R.G. Flocchini. Application of elastic lidar to PM10 emissions from agricultural nonpoint sources. *Environmental Science Technology*, 32:3068–3076, 1998.

[103] C.A. Gueymard. Stable analytical inversion solution for processing lidar returns. *Applied Optics*, 20(2), 1981.

[104] British Petroleum Company. BP Statistical Review of World Energy June 2014, 63 edition. London, British Petroleum Co., 2014.

[105] The World Bank. CO2 emissions (metric tons per capita). Technical report, World Development Indicators, 2014.

[106] Kahramaa. Statistics report 2012. Technical report, Qatar General Electricity and Water Corporation KAHRAMAA, Corporate Planning and Business development, 2013.

[107] QNV 2030. Qatar National Vision 2030. Technical report, General Secretariat For Development Planning, 2008.

[108] Pan-Arab renewable energy strategy 2030, roadmap of actions for implementation. IRENA, 2014.

[109] Supreme Committee. Qatar Foundation stadium. http://www.sc.qa/en/stadiums/qatar-foundation-stadium. Last accessed April 2015.

[110] M.M. Haruni. The solar pilot project in Qatar. *Solar and Wind Technology*, 1(2):93–108, 1984.

[111] Qatar Foundation Magazine. The Foundation, issue 73, January 2015. Qatar Foundation, Doha, Qatar, 2015.

[112] Total. A new energy future with solar energy. Total Marketing services, New Energies, Paris, France, 2013.

[113] N. May. *Eco-balance of a Solar Electricity Transmission from North Africa to Europe*. PhD thesis, Technical University Of Braunschweig, Faculty for Physics and Geological Sciences, 2005.

[114] J. Beták, M. Súri, T. Cebecauer, and A. Skoczek. Solar resource and photovoltaic electricity potential in EU-MENA region. In *EUPVSEC2012 Conference*, 2012.

[115] Concentrating solar power for the Mediterranean region, final report. Institute of Technical Thermodynamics, Sections system analysis and technology assessment, DLR, 2005.

[116] Feasibility study on combined CSP-seawater desalination technology. 6th World Water Forum, Marseille, France, 2012.

[117] High-quality renewable energy resource data for the Kingdom of Saudi Arabia. King Abdullah City for Atomic and Renewable Energy (K.A.CARE), Renewable Resource Monitoring and Mapping (RRMM) Program, 2013.

[118] The UAE solar atlas. The Research Center for Renewable Enregy Mapping and Assessment (ReCREMA), Masdar Institute, 2013.

[119] D. Bachour and D. Perez-Astudillo. Ground-measurement GHI map for Qatar. *Energy Procedia*, 49:2297–2302, 2014. Proceedings of the SolarPACES 2013 International Conference.

[120] S. Emeis and K. Schäfer. Remote sensing methods to investigate boundary-layer structures relevant to air pollution in cities. *Bound.-Lay. Meteorol.*, 121:377–385, 2006.

[121] C. Münkel, S. Emeis, and K. Schäfer. Aerosol concentration measurements with a lidar ceilometer: results of a one year measuring campaign. *Proc. SPIE 5235*, pages 486–496, 2004.

[122] C. Münkel. Boundary layer and air quality monitoring with a commercial lidar ceilometer. *Proc. SPIE 6367*, 2006.

[123] C. Münkel, K. Schäfer, and S. Emeis. Investigation of boundary layer dynamics, dust and volcanic ash clouds with laser ceilometer. *Proc. SPIE 8890, Remote Sensing of Clouds and the Atmosphere XVIII; and Optics in Atmospheric Propagation and Adaptive Systems XVI*, 2013.

[124] R.C. Muñoz and R.I. Alcafuz. Variability of urban aerosols over Santiago, Chile: Comparison of surface PM10 concentrations and remote sensing with ceilometer and lidar. *Aerosol and Air Quality Research*, 12:8–19, 2012.

[125] C. Münkel and J. Rasanen. New optical concept for commercial lidar ceilometers scanning the boundary layer. *Proc. SPIE 5571*, pages 364–374, 2006.

[126] V.R. Morris. Vaisala ceilometer (VCEIL) handbook. U.S. Department of Energy, Office of Science, Office of Biological and Environmental Research, Atmospheric Research, 2012.

[127] C. Münkel. Mixing height determination with lidar ceilometers – results from Helsinki Testbed. *Meteorol. Z.*, pages 451–459, 2007.

[128] C. Münkel. Automatic monitoring of boundary layer structures with ceilometer. *WMO Technical Conference on Meteorological and Environmental Instruments and Methods of Observation, Helsinki, Finland*, pages 2–17, 2010.

[129] D. Bachour and D. Perez-Astudillo. Boundary layer height measurements over Doha using lidar. *Energy Procedia*, 57:1086–1091, 2014. Proceedings of the SolarPACES 2013 International Conference.

[130] J.J. Michalsky. The astronomical almanac's algorithm for approximate solar position (1950-2050). *Solar Energy*, 40:227–235, 1988.

[131] I. Moradi. Quality control of global solar radiation using sunshine duration hours. *Energy*, 34:1–6, 2009.

[132] S. Younes, R. Claywell, and T. Muneer. Quality control of solar radiation data: present status and proposed new approaches. *Energy*, 30:1533–1549, 2005.

[133] T. Muneer and F. Fairooz. Quality control of solar radiation and sunshine measurements – lessons learnt from processing worldwide databases. *Building Services Eng. Res. Technol.*, 23:151–166, 2002.

[134] W. Tang, K. Yang, J. He, and J. Qin. Quality control and estimation of global solar radiation in China. *Solar Energy*, 84:466–475, 2010.

[135] M. Journee and C. Bertrand. Quality control of solar radiation data within the RMIB solar measurements network. *Solar Energy*, 85:72–86, 2011.

[136] G. Maxwell, S. Wilcox, and M. Rymes. User's manual for SERI QC software – Assessing the quality of solar radiation data. NREL/TP-463-5608, National Renewable Energy Laboratory, Golden, Colorado, 1993.

[137] C.N. Long and E.G. Dutton. BSRN global network recommended QC tests, v2.0. Technical report, BSRN Technical Report, 2002.

[138] B. Espinar, B. Gschwind, L. Wald, and C. Thomas. An OGC web processing service for assessing the quality of solar radiation measurements. *27th International Conference on Informatics for Environmental Protection, Hamburg, Germany*, 2013.

[139] F. Vejen, C. Jacobsson, U. Fredriksson, M. Moe, L. Andresen, E. Hellsten, P. Rissanen, T. Palsdóttir, and T. Arason. Quality control of meteorological observations. Automatic methods used in the Nordic countries. Norwegian Meteorological Institute, 2002.

[140] P. Ineichen. Global irradiation: average and typical year, and year to year annual variability. Research report of the Institut of the Environnemental Sciences, University of Geneva, 2011.

[141] S. Lohmann, C. Schillings, B. Mayer, and R. Meyer. Long-term variability of solar direct and global radiation derived from ISCCP data and comparison with reanalysis data. *Sol Energy*, 80:1390–1401, 2006.

[142] D.H.W. Li and J.C. Lam. An analysis of climatic parameters and sky condition classification. *Building and Environment*, 36(4):435–445, 2001.

[143] J. Calbó, J.A. González, and D. Pagès. A method for sky condition classification from ground-based solar radiation measurements. *J Appl Meteorol*, 40:2193–2199, 2001.

[144] K. Scharmer and J. Greif. *The European Solar Radiation Atlas*. Les Presses de l'École des Mines, Paris, 2000. (1:24).

[145] M.D. Islam, I. Kubo, M. Ohadi, and A.A. Alili. Measurement of solar energy radiation in Abu Dhabi, UAE. *Applied Energy*, 86:511–515, 2009.

[146] NOAA. http://www.esrl.noaa.gov/gmd/grad/solcalc/. Last accessed April 2015.

[147] R.W. Reynolds and T.M Smith. Improved global sea-surface temperature analysis using optimum interpolation. *J Climate*, 7:929–948, 1994.

[148] T.M. Smith, R.W. Reynolds, R.E. Livezey, and D.C. Stokes. Reconstruction of historical sea-surface temperatures using empirical orthogonal functions. *J Climate*, 9:1403–1420, 1996.

[149] R. Mendelssohn, F.B. Schwing, and S.J. Bograd. Spatial structure of subsurface temperature variability in the California Current. *J. Geophys Res*, 108(C3):3093, 2003.

[150] D. Kondrashov and M. Ghil. Spatio-temporal filling of missing points in geophysical data sets. *Nonlin Processes Geophys*, 13:151–159, 2006.

[151] E.L. Maxwell. Final Technical Report, National Solar Radiation Data Base (1961-1990), NREL/TP-463-5784 DE9500262, 1995. National Renewable Energy Laboratory. Golden, Colorado, USA.

[152] A. Kumar, S. Gomathinayagam, G. Giridhar, I. Mitra, R. Vashistha, R. Meyer, M. Schwandt, and K. Chhatbar. Field experiences with the operation of solar radiation resource assessment stations in India. In *Energy Procedia, Proceedings of the SolarPACES International Conference*, volume 49, pages 2351–2361, 2013.

[153] G. Vijayakumar, S.A. Klein, and W.A. Beckman. Analysis of short-term solar radiation data. *Solar Energy*, 79(5):495–504, 2005.

[154] R.E. Carrillo, T.C. Aysal, and K.E. Barner. A generalized Cauchy distribution framework for problems requiring robust behavior. *EURASIP Journal on Advances in Signal Processing*, 2010:312989, 2010.

[155] R. Meyer, C. Gueymard, and P. Ineichen. Standardizing and benchmarking of modeled DNI data products. In *Proceedings of SolarPACES International Conference*, 2011.

[156] M. Súri, J. Remund, T. Cebecauer, C. Hoyer-Klick, D. Dumortier, T. Huld, P.W. Stackhouse Jr., and P. Ineichen. Comparison of direct normal irradiation maps for Europe. In *Proc SolarPACES Conf Berlin, Germany*, 2009.

[157] W.D. Collins, P.J. Rasch, B.E. Eaton, B.V. Khattatov, J.-F. Lamarque, and C.S. Zender. Simulating aerosols using a chemical transport model with assimilation of satellite aerosol retrievals: Methodology for INDOEX. *J Geophysical Research: Atmospheres*, 106(D7):7313–7336, 2001.

[158] CLVIEW. http://www.vaisala.com/en/products/ceilometers/Pages/CL-VIEW.aspx, 2015. Last accessed April 2015.

[159] C.D. Papadimas, N. Hatzianastassiou, C. Matsoukas, M. Kanakidou, N. Mihalopoulos, and I. Vardavas. The direct effect of aerosols on solar radiation over the broader Mediterranean basin. *Atmos Chem Phys*, 12:7165–7185, 2012.

[160] V. Ramanathan, P.J. Crutzen, J.T. Kiehl, and D. Rosenfeld. Aerosol, climate and the hydrological cycle. *Science*, 294:2119–2124, 2001.

[161] N. Hatzianastassiou, C. Matsoukas, E. Drakakis, P.W. Stackhouse Jr., P. Koepke, A. Fotiadi, K.G. Pavlakis, and I. Vardavas. The direct effect of aerosols on solar radiation based on satellite observations, reanalysis datasets, and spectral aerosol optical properties from Global Aerosol Data Set (GADS). *Atmos Chem Phys*, 7:2585–2599, 2007.

[162] M. Lefèvre, A. Oumbe, P. Blanc, B. Espinar, B. Gschwind, Z. Qu, L. Wald, M. Schroedter-Homscheidt, C. Hoyer-Klick, A. Arola, A. Benedetti, J.W. Kaiser, and J.-J. Morcrette. McClear: a new model estimating downwelling solar radiation at ground level in clear-sky conditions. *Atmos. Meas. Tech.*, 6:2403–2418, 2013.

[163] T. Cebecauer and M. Suri. Accuracy improvements of satellite-derived solar resource based on GEMS re-analysis aerosols. In *Proc. Conf. SolarPACES 2010, Perpignan, France*, 2010.

[164] GeoModel. http://www.geomodelsolar.eu/_docs/various/SolarGIS_validation_SaudiArabia_2013-02.pdf, 2013. Technical report. Last accessed April 2015.

[165] C.N. Long and T.P. Ackerman. Identification of clear skies from broadband pyranometer measurements and calculation of downwelling shortwave cloud effects. *Journal of Geophysical Research*, 105 (D12):15609–15626, 2000.

[166] R. Perez and P. Ineichen. Making full use of the clearness index for parameterizing hourly insolation conditions. *Solar Energy*, 45(2):111–114, 1990.